Technische Universität München

Physikalische Chemie

Conformations and Fragmentation of Biologically Relevant Molecules and their Binary Complexes with Water Probed by High Resolution UV and Mass Analyzed Threshold Ionization Spectroscopy

Rosen Karaminkov

Vollständiger Abdruck der von

der Fakultät für Chemie

der Technischen Universität München

zur Erlangung des akademischen Grades eines

DOKTORS DER NATURWISSENSCHAFTEN

genehmigten Dissertation.

Vorsitzender: Univ.-Prof. Dr. St. J. Glaser

Prüfer der Dissertation:

> 1. Univ.-Prof. Dr. H. J. Neusser
> 2. Univ.-Prof. Dr. Dr. h. c. A. Laubereau

Die Dissertation wurde am 09.11.2009 bei der Technischen Universität München eingereicht und durch die Fakultät für Chemie am 07.12.2009 angenommen.

To my lovely daughters,

Vanessa and Plamena,

and to my beloved wife,

Evelina

Preface

Since the dawn of humanity the permanent desideration for knowledge and understanding of the surrounding world has been the driving force that evolved the ancient studies and promoted the science over the ages to its modern thrive with its complexity and variety of research fields. Nowadays the macroscopic properties and functionality of chemical and biological systems have been ultimately related to the microscopic properties of the their constituents thus giving rise to research areas such as spectroscopy, microbiology, nanoscience, etc., with their realms of interest, which are closely interwoven. A nice example of collaboration between the rapidly developing branches of science is the connection between stereochemistry and spectroscopy. While the former deals with spatial arrangements of atoms in molecules and the effects of these arrangements on the physical and chemical properties of substances, spectroscopy provides insight into the structure and bonding of the most abundant isomers of a chemical compound.

The unique conditions obtained during the supersonic expansion of molecules from higher pressure into vacuum results in the formation of cold molecules and small complexes which sometimes have been referred to as those of a fourth state of matter. Furthermore, in molecular beams, the species concerned can be investigated under conditions that removed pressure broadening and much of Doppler broadening from the resulting spectra. When molecules are injected into the carrier gas, they attain very low rotational temperatures, higher vibrational temperatures of the order of 100 K and translational temperatures down to 0.1 K. Therefore, the so-called 'fourth state of matter' consists of molecules which are generally cold and which have different translational, rotational and vibrational temperatures. These conditions are an excellent environment for molecular spectroscopy and result in several major advantages. First, weakly bound species, such as van der Waals and hydrogen-bonded complexes and clusters, are held together at the typically low vibrational temperature, which allows a high precision spectroscopic studies and second advantage is that spectra of large molecules can be rotationally resolved. The development of lasers and the refinement of the mass resolution techniques have been proved to be an extremely important tool in investigation of the spectroscopy, conformations, fragmentation and dynamics of molecules in supersonic jets or pulsed beams. The mass analyzed threshold ionization and resonance enhanced two photon ionization techniques, used in this work, have demonstrated the ability to obtain beautiful electronic spectra even for the very low concentra-

tions typical of biological species in cold supersonic jets. Because the samples are so cold and the laser resolution so high the spectra of even quite complex organic molecules become simple enough to analyze in detail.Conformers stabilized trough the formation of *intra*molecular hydrogen bonds and hydrogen bonded complexes are of interest particularly in biochemical systems and also for a variety of other reasons; for example, they may be intermediates in *inter*molecular reactions. It is significant that in the past 30 years, a detailed picture of hydrogen bonding has merged from high-resolution and mass selective spectroscopy investigations of weakly bounded complexes.

Contents

Part I

Introduction

Chapter 1

Introduction

1.1 Molecular conformers

The positions of the atoms define the molecular geometry, which is an important property of molecules and is directly connected to their reactivity. Historically, this led to the establishment of the stereochemical principles connecting molecular shape with functionality. An important contribution was made by the French physicist Biot (1815) who discovered the rotation of the plane of polarization of linearly polarized light by certain organic molecules in solution or in gaseous phase, a phenomenon referred to as optical activity. This event was followed by works of Louis Pasteur (1848), who ascribed this property to the presence of some *asymmetric* grouping of atoms in a molecule, and later on van't Hoff and Le Bel (1874) added a third dimension to the two-dimensional chemistry of earlier days. It was not till the early nineteen-fifties when Barton and Hasel introduced the concept of conformational analysis. This concept added another dimension, a time-dependent (temporal) one to the three-dimensional stereochemistry and extended its scope to reaction processes. That gives a more realistic description of the molecules, which exhibit *intra*molecular motions such as deformation of bond angles, bond stretching and contraction, and rotation about one or more single bonds. As a consequence, a chemical compound exists in a dynamic equilibrium with a number of continuously changing energy-preferred conformations which differ from each other in the degree of rotation about one or more single bonds (dihedral angles) and in some cases also in bond angles and bond lengths. They are distinct molecular species separated by energy barriers and are called *conformers* or *isomers* (from *Greek īsomerēs, having equal share : īso-, iso- + meros, part, share*). Although incapable of independent existence at room temperatures, they are detectable at low temperatures and gaseous phase by certain physical methods. Depending on their relative population and energy barriers separating them, the conformers influence the physical and chemical properties of a compound. The importance of the molecule's conformeric structures involved in chemical reactions either

as reactants or products has been discussed in modern chemistry textbooks. F. A. Carey and R. J. Sundberg in their organic chemistry textbook [1] show explicitly the relationship between reactivity and stereochemistry introducing terms such as *stereoselectivity* and *stereoscpecifity*. A chemical *stereoselective* reaction is one in which a single reactant forms two or more conformeric products. When two or more conformeric reactants each provide stereoisomeric products, the reaction is called *stereospecific*. An example for *stereospecific* reactions is the S$_N$2 substitution that results in the inversion of the configuration. The *R*-reactant gives the *S*-product and the *S*-reactant gives the *R*-product. Another example is the epoxidation of *E*-2-butene that gives *trans*-2,3-dimethyloxirane, whereas *Z*-2-butene gives *cis*-2,3-dimethyloxirane. This and other
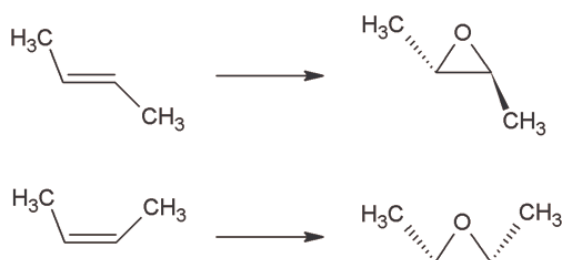
Figure 1.1: *Epoxidation of E-2-butene*

examples [1] manifest the paramount importance of the molecular architecture and the need of a reliable assignment of the conformeric structures.

It is well known that neurotransmitters are the chemical bridging structures that transfer information between neighboring nerve cells [2]. The region through which the neurotransmitter must pass from one cell to the other is called the synaptic gap. Suitable neurotransmitters pass this way in milliseconds and transfer their information by binding to the host cell. This highly selective process is explained by the "key-lock-principle" [3]. It is unclear whether only certain conformers of these neurotransmitters are able to bind to the docking site or the conformation is adapted during docking. In order to understand these processes in more detail it would be necessary to know the conformational landscape of the neurotransmitters. It is plausible to assume, that however, the conformational preferences are influenced from the molecular environment and solvation, but knowing the conformational landscapes of the isolated neurotransmitters would be a first step. A second step would then be the investigation of small complexes with solvent molecules. This information can be obtained from investigations of cold, isolated molecules.

Towards this end, the present work describes new results on model biologically relevant flexible molecules and their hydrated clusters, obtained through the combination of high-resolution UV spectroscopy and high-level *ab initio* calculations. These results elucidate the preferable conformations of isolated molecular species in the gas phase, stabilized by weak interactions, and may

serve as an input information for a chemical synthesis of novel compounds.

1.2   Hydrated complexes

Once the monomer's conformeric landscape is determined, the next level of evaluation of the molecular shape of flexible molecules is to investigate their behavior in a realistic environment. Water, the most abundant nature's solvent has attracted a lot of attention in the last two decades. The strength of water as a solvent lies in its ability to form H-bonded networks that strongly influence the properties of the solutes. When a solute molecule possesses two hydrogen bonding sites: donor and acceptor, the water may select one of them or fill in the gap between them forming a bridge structure. In the process, the shape of the host molecule can be vastly modified. Additionally, a production and a stabilization of a higher-energy conformer can be observed [4]. Small clusters of water molecules in the gas phase are formed using supersonic jet expansion method [5] and are probed by various spectroscopic techniques in a size-controlled manner. When the potential energy surface (PES) is characterized by several energy potential minima separated by a relatively high potential barriers in the conditions of expansion cooling, the respective conformations are trapped and their populations are cooled to ground state levels. During the expansion the clusters are collisionally cooled to low rotational temperatures and most of the vibrational hot bands are removed. This reduces the congestion and complexity of an optical spectrum, aiding the assignment of the observed spectral features. Detailed information about *inter*molecular binding structures in these clusters provides substantial fundamental data for a microscopic view reflecting H-bonding networks in condensed phases and can serve as a calibration point for theoretical models.

Some of the molecules whose complexes (*c.1652, "composed of parts," from French complexe, from Latin complexus "surrounding, encompassing"*) with water molecules have been extensively studied are benzene [6], phenol [7, 8], cresol [9], tropolone [7], benzonitrile [10] indole [10–13], 3-methylindole [14,15] and 2-phenylethanol [16]. To date many systems have been studied, showing a clear trend for shifting the focus from small model molecular species to investigating larger, more complex and realistic systems with biological relevance. Therefore, we investigated the formation of singly hydrated clusters in 2-phenylethanol and its fluoro substituted derivatives by the combination of low- and high-resolution UV resonance-enhanced two-photon spectroscopy, genetic-algorithm-based rotational fitting technique and high-level quantum chemical calculations. Detailed and comprehensive discussions on the observed spectroscopic features are presented in Chapters 3 and 7.

1.3   Photofragmentation of biomolecules

In the last decades, the fragmentation (*c.1531, from Latin fragmentum "a fragment, remnant," from root of frangere "to break."*) of biomolecular ions has become a rapidly developing field of exploration since it is an indispensable part of the proteomic technology. There exist a large variety of methods to explore this fundamentally and intrinsically interesting phenomenon. The fragmentation can be induced by collisions, light or some kind of charge exchange process that leads to the cleavage of just one or two bonds out of the numerous chemical bonds that hold the biomolecule together (for review, see [17]). The final goal of such experiments is the production of fingerprint reference mass spectra for the identification of small organic molecules. In these applications it is usually the fragmentation pattern rather than the nominal masses that provides definitive markers and leads to compound identification. Aromatic amino acids and their derivatives play a key role in the near-UV absorption of proteins which causes a considerable effort towards the understanding of their spectroscopy, structure, photophysics and excited-state dynamics [18]. Recently Rizzo and coworkers reported in interesting fragmentation behavior of protonated aromatic amino acid in a cold, 22-pole ion trap. In protonated tyrosine, different conformers excited with similar energy exhibit different fragmentation patterns, which suggests a conformer-specific excited-state dynamics [19]. The biomolecular ion production of the protonated species is realized by an electrospray ion source (ESI). The so-produced ions are trapped in electrostatic ion traps and photofragmented by fixed in energy UV laser pulses. As a next step one can either record an infrared-ultraviolet double resonance spectrum of the photofragments [19] or probe the dynamics and the mechanisms of the photofragmentation [18]. In our group we use UV resonance-enhanced multiphoton ionization spectroscopy for the excitation of neutral nonprotonated biomolecules and subsequent generation of biomolecular ions. Usually, this is a gentle and nondestructive technique for exploration of the spectroscopic features of the studied molecular systems in the first excited, S_1, electronic state. The molecules under consideration, consist of a chromophore part and a hydroxyl or an amino groups (or both) situated in the side chain. This facilitates charge transfer process along the backbone of the molecule and a successive breaking of the C_α—C_α bond [18]. In this work, a similar situation was observed for the neurotransmitter ephedrine, where the specific fragmentational behavior is explained as a consequence of vibrationally induced photodissociation. This interesting case is discussed in detail in Chapter 8 of the present work. Another case of a specific fragmentational behavior is the photofragmentation of pseudoephedrine, where we recorded a high-resolution spectra of the charged fragments and found evidences for a conformer-dependent photodissociation. The results are presented in Chapter 9.

In this thesis a number of high-resolution and threshold-ionization mass selective UV experiments are described covering most of the aforementioned topics. The studied molecular systems are two types: *i*) biological, such as ephedrine used in the drug synthesis and *ii*) biologically rel-

evant compounds such as 2-phenylethanol that mimic the interactions in real neurotransmitters (2-phenylethylamine).

$$*****$$

In Chapter 3, a spectroscopic study of 2-phenylethanol (2-PE) and its complex with water is presented. Both the vibrationally and rotationally resolved spectra of the first electronically excited state have been observed when the masses of the monomer and the singly hydrated cluster are detected. All vibronic bands in the resonance enhanced two-photon ionization (R2PI) spectrum of the monomer blue-shifted up to 220 cm^{-1} have been measured at high resolution of 70 MHz. Comparing the fits of the experimental data with the results from the high-level *ab initio* calculations an assignment of the spectroscopic features is made, which proofs the existence of two conformeric structures in the cold molecular beam. For the water cluster, an identification of one of the vibronic bands is made which implies that the water is connected to the terminal hydroxyl group of the most stable conformer of the monomer with a single hydrogen bond as a proton donor.

Chapter 4 describes the effects of fluorination on the conformational landscape of 2-PE. The stability of the noncovalent OH $\cdots$ π bond of the unperturbed system is tested with a substitution on the *para*-positon of the benzene ring. The results of the fitted high-resolution spectra in conjunction with the computational findings show that the presence of an electronegative atom at the *para*-positon does not influence the conformational preferences and the rovibrational spectral profiles of 2-*para*-fluorophenylethanol (2-*p*-FPE) yield conformers similar to those of 2-PE.

The same experimental approach combined with even higher level of quantum chemistry *ab initio* calculations have been used for the investigation of the geometrical isomers of the *ortho*-fluorinated derivative of 2-PE. In this case, the proximity of the F atom to the flexible ethanol tail favors a formation of a σ-hydrogen bond and a distortion of the stabilizing OH $\cdots$ π bond of the most abundant conformation of the nonfluorinated 2-PE, resulting in a formation of new conformations of 2-*ortho*-fluorophenylethanol (2-*o*-FPE). Indeed, the rotationally resolved spectrum of one of the vibronic bands of the intermediate electronic, S_1, state was completely different from the profiles of the other vibronic features in the low-frequency region of the $S_1 \longleftarrow S_0$ electronic transition, which we ascribe to a presence of a second conformer with a terminal hydroxyl group rotated towards the position of the F atom. The other high-resolution spectra were assigned as originating from a similar conformer as in the case of 2-PE and 2-*p*-FPE. The experimental results supported by a high-level *ab initio* calculations are shown in Chapter 6.

The analysis of the cationic state of the prototype flexible molecule 2-*p*-FPE by mass analyzed threshold ionization spectroscopy (MATI) and by supporting *ab initio* calculations brought forward some of the modern aspects of application of the MATI technique as a conformer distinguishing tool and a probe method for the existence of stabilizing hydrogen bonds in the neutral species. The results of this research are presented in Chapter 5.

Part II

Experimental Details

Chapter 2

Experimental Techniques

The combination of Low- and High-Resolution Doppler-free resonance enhanced two-photon ionization (R2PI) spectroscopy with mass selection of jet-cooled (2-12 K) molecular species in the gas phase is a powerful experimental technique for studying of isolated biologically relevant molecules, their molecular complexes, and fragmentation behavior. It allows partially rotationally resolved (FWHM = 70 MHz) spectra of the vibronic bands of the $S_1 \longleftarrow S_0$ electronic transition of the studied molecular systems to be measured at their mass channel. The so-obtained spectra are analyzed by a specially designed computer-assisted fitting routine based on genetic algorithms. Thus accurate rotational constants in the ground, S_0 and the first excited, S_1 electronic state, and the transition moment ratio of the observed species can be determined. The R2PI technique together with mass analyzed threshold ionization spectroscopy (MATI) of flexible cationic molecules, can be used as a sensitive tool for conformational assignment of neutral molecular conformers in the S_1, electronic state.

v_1 $v_2=const$

v_1 v_1

(a) One- and two-color ionization

(b) Two-color ionization with fragmentation
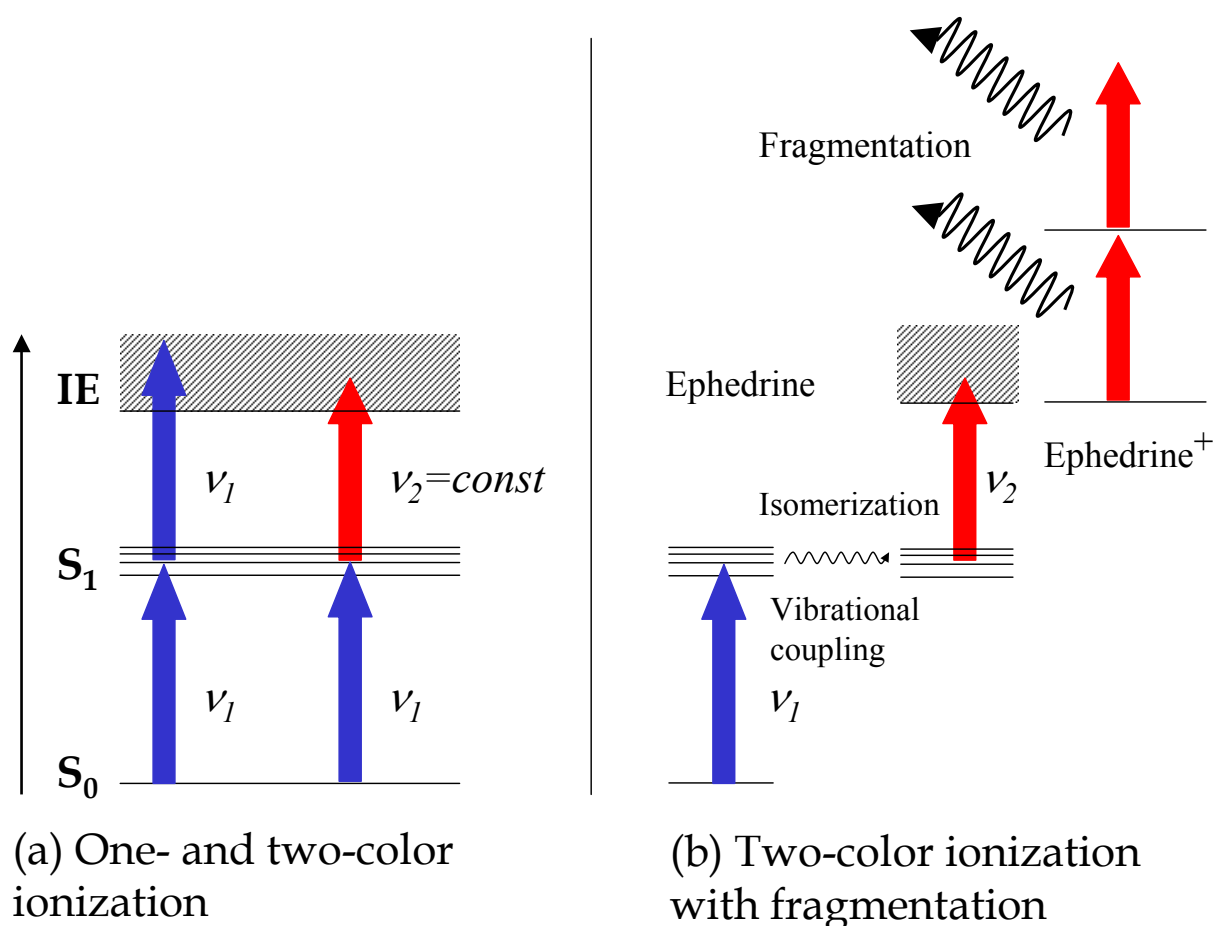
Figure 2.1: *Resonant two-photon ionization (R2PI) scheme.*

2.1 Resonance Enhanced Two-Photon Ionization (R2PI) UV Laser Spectroscopy

The excitation scheme for producing UV R2PI spectra employs promotion of jet-cooled molecular species from their ground, S_0, electronic state to the first excited, S_1, electronic state and a subsequent ionization. The energy scheme is presented in Fig. 2.1a. The recording of the highly resolved UV R2PI spectrum of a rovibronic transition is preceded by the identification of the vibronic bands in the $S_1 \longleftarrow S_0$ spectrum. The latter is obtained when two photons with the same energy (v_1) from a single laser source are used both for the excitation and ionization steps. The so called one-color ionization scheme has the disadvantage that when scanning a broad region in the S_1 electronic state, the total photon energy ($2v_1$) may exceed the dissociation energy in the ion and thus lead to an undesired fragmentation of the studied species, especially in case

of weakly bound complexes. The other drawback is the lower resolution of the scanning laser, which cannot resolve the rotational profile of the vibronic bands. This technique is used mainly for finding the position of the vibronic transitions. The above shortcomings are overcame by using a two-color ionization scheme, in which one photon with energy ν_1 is employed to excite the molecules from their electronic ground state to the first excited electronic state and a second photon with a constant energy ($\nu_2 = const$) is used to ionize the already excited molecules. The energy of the excitation photon is scanned and the one of the ionization photon is fixed to a value which exceeds (typically by 100 cm^{-1}) the ionization limit but is below the dissociation energy of the cluster ion (see Fig. 2.1a). For the production of highly resolved rovibrational UV R2PI spectra a scanning laser with a linewidth of around 70 MHz is used (ν_1). The excitation and the subsequent ionization occur only if the resonance condition is fulfilled (see Eq. 2.1).

$$\Delta E = h\nu_1 = E_n - E_m \tag{2.1}$$

where, E_n and E_m are the energies of the starting and ending levels of the transition. As mentioned above, one of the consequences of the multiphoton ionization is the presence of fragmentation of the excited species. Such a peculiar case is shown for the flexible biological molecule ephedrine (see Fig. 2.1b). Here even at very low energies of the second photon [20], the fragmentation of the parent ion cannot be avoided. This interesting behavior is discussed in detail in Chapter 8.

2.2   R2PI Experimental Set up

The experimental set up consists of three main components:

- Molecular beam vacuum apparatus with pulsed heatable nozzle for production of jet-cooled molecular species [5, 21, 22] and a coupled time-of-flight (TOF) with an ion detector

- Laser system for low- and high- resolution spectroscopy

- Data acquisition system

Only the main features of these functional units will be described here, together with some new implementations. For a complete description see the diploma works of Holvan [23], Helm [24], Siglow [25], Gerthner [26] and the PhD theses of Sussmann [27] and Chervenkov [28].

2.2.1   Molecular beam apparatus

The supersonically jet-cooled molecules and molecular complexes are produced by adiabatic expansion through a pulsed nozzle into vacuum. The vacuum chamber consists of two differ-
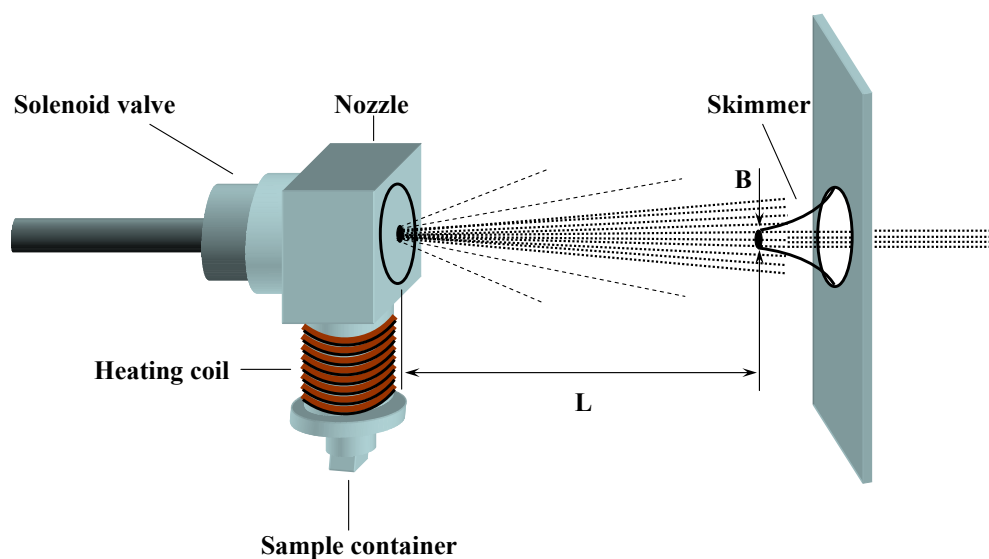
Figure 2.2: *Schematic drawing of the heatable nozzle for production of molecular beams.*

entially pumped subchambers: a forechamber and an interaction chamber (see the enlargement in Fig. 2.4). The forechamber contains the pulsed nozzle (see Fig. 2.2), and the cold molecular beam is produced there. The interaction chamber is connected to the forechamber through a skimmer with a clearance of 1.5 mm, through which the molecular beam passes. The interaction chamber is the place where the interaction between the molecules and the laser pulses takes place. It is also the receptacle of the time-of-flight mass spectrometer. The two chambers are evacuated by two turbomolecular pumps (Balzers TPU 2200, 3200 l/s and Balzers TPU 510, 510 l/s) that maintain vacuum of 9.10^{-9} mbar in nozzle-nonoperating regime. The cold molecular beam [5, 21, 22] is produced by expansion of the investigated species entrained in a carrier gas through a heatable (up to $120°$ C) nozzle with an orifice diameter of 300 μm. The sample is contained in a small cup inside the nozzle, just before the orifice. This allows for the vapors of the sample to mix with the carrier gas prior to the expansion. The container can be heated and the temperature can be maintained stable (within $0.5°$ C) by a programmable electronic thermocontroller (HENGSTLER GRADO 901). The sample holder consists of two compartments, which allow the introduction of two molecular species. The simultaneous heating provides better vapor mixing conditions, hence and an increased cluster formation before the interaction with the buffer gas. The carrier gas is usually Ar since it favors the collisional cooling of large molecules due to its large atomic mass. Ne can also be used, though the cooling process in this case is not very efficient. The stagnation pressure of the carrier gas inside the nozzle is typically in the range 2-4 bar. The molecular beam is laced through a conical skimmer (see the enlargement in Fig. 2.4).

The skimmer position is fixed but the nozzle position is adjustable so that the nozzle to-skimmer distance can be optimized as a trade-off between the ion signal intensity and the Doppler broadening. The reduced Doppler broadening $\Delta\nu_D$ for a transition with Frequency ν is depends on several parameters [29]:

$$\Delta\nu_D = \frac{\nu}{c}\frac{B}{Lu_\infty} = \frac{\nu}{c}Ku_\infty \tag{2.2}$$

where L denotes the distance between nozzle and skimmer, u_∞ the thermal velocity of the expanding gas and B the diameter of the skimmer (see Fig. 2.2). The ratio B/L=K is also known as the collimation ratio. Usually, the Doppler broadening is reduced to 40-50 MHz. This is a very important parameter, since it is included in the total frequency of the spectrum:

$$\Delta\nu_{tot} = \sqrt{\Delta\nu_L^2 + \Delta\nu_D^2} \tag{2.3}$$

where $\Delta\nu_L$ is the frequency width of the laser light. This relation holds under the conditions of Gaussian-shaped line broadenings.
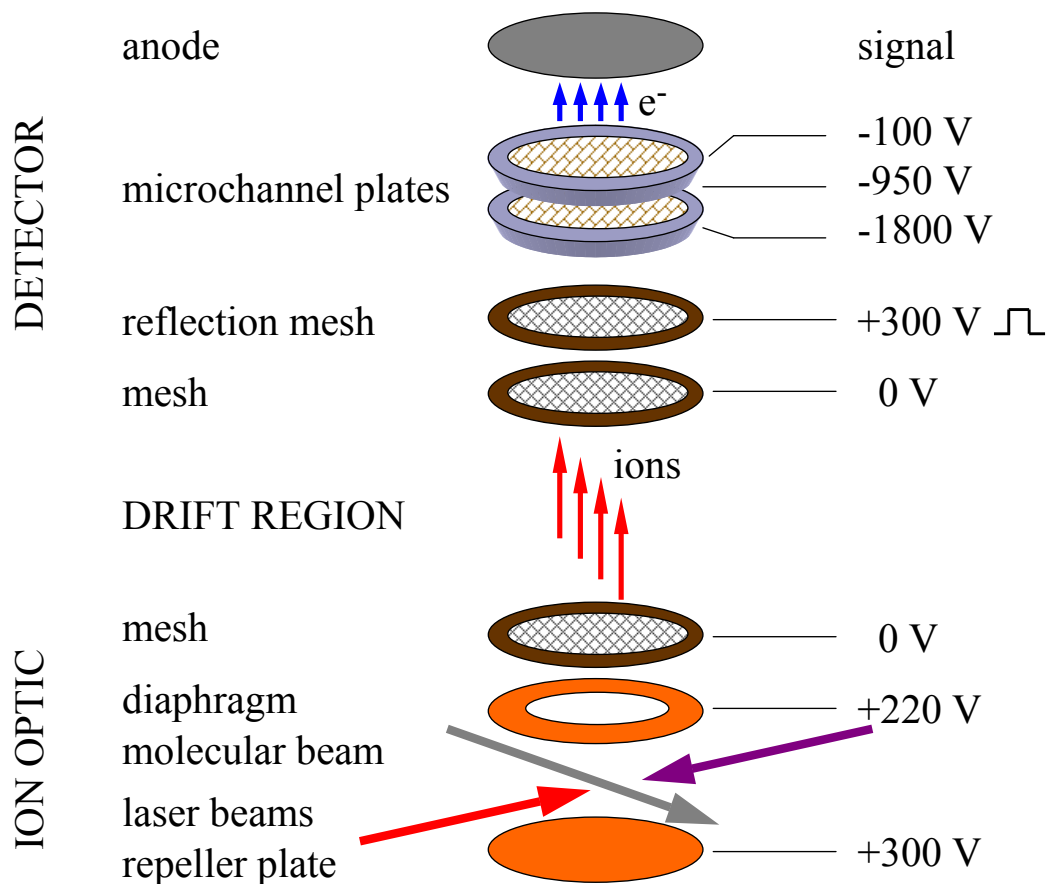
Figure 2.3: *Schematic drawing of the Ion optic.*

The ions produced as a result of the interaction between the molecular beam and the laser pulses are mass selected with a homebuilt [30,31] linear Wiley-McLaren [32] time-of-flight (TOF) mass spectrometer (see Fig. 2.3). The ion optics of the spectrometer consists of three elements deflectors, which create an electric field deflecting the ions from the initial straight trajectory of the molecular beam in a direction perpendicular to the plane defined by the molecular beam and the path of the laser pulses. Thus, the ions are targeted at the detector, which is on top of the interaction chamber. The deflector comprises two regions: the ion extraction region and the ion steering region. The laser-generated ions are extracted by the electric field created between the *repeller plate* (bottom plate in Fig. 2.3) with a potential of +300 V, and the *diaphragm* with a potential of +220 V. The upward trajectory of the extracted ions is corrected by the weaker electric field between the diaphragm and the *mesh* (grounded). The ions pass through a drift region of 20 cm and then are detected by *microchannel plates* whose amplification ranges between 10^6 and 10^8. It is well-known that the nonrelativistic kinetic energy of charged particles is proportional to the charge and the potential difference. Mathematically, this relationship is expressed by the equation:

$$\frac{1}{2}mv^2 = eU \tag{2.4}$$

Since the R2PI experiments are concerned with singly ionized molecules and molecular complexes and the applied electric field in the TOF is the same for all ions, the above equation can be recast to demonstrate that the arrival time of the ions at the detector is proportional to the square root of their mass:

$$t \propto \sqrt{m} \tag{2.5}$$

Thus, the measured arrival time can be easily transformed into ionic mass. By using referent molecular systems (e. g. C_6H_6), the proportionality constant has been determined to be 2.70 μs.u^{-2}.

2.2.2 Laser System

The laser equipment consists of two functional laser units, presented schematically in Fig. 2.4.

- *pulsed broadband tunable dye laser*, which is used as a source both for the excitation and ionization photons in one-color low-resolution experiments, and as a source for the ionization photons in two-color high-resolution experiments.

- *pulsed amplified narrow-band single-mode continuous wave* (cw) *ring dye laser*, which provides the excitation photons for the two-color high-resolution measurements.
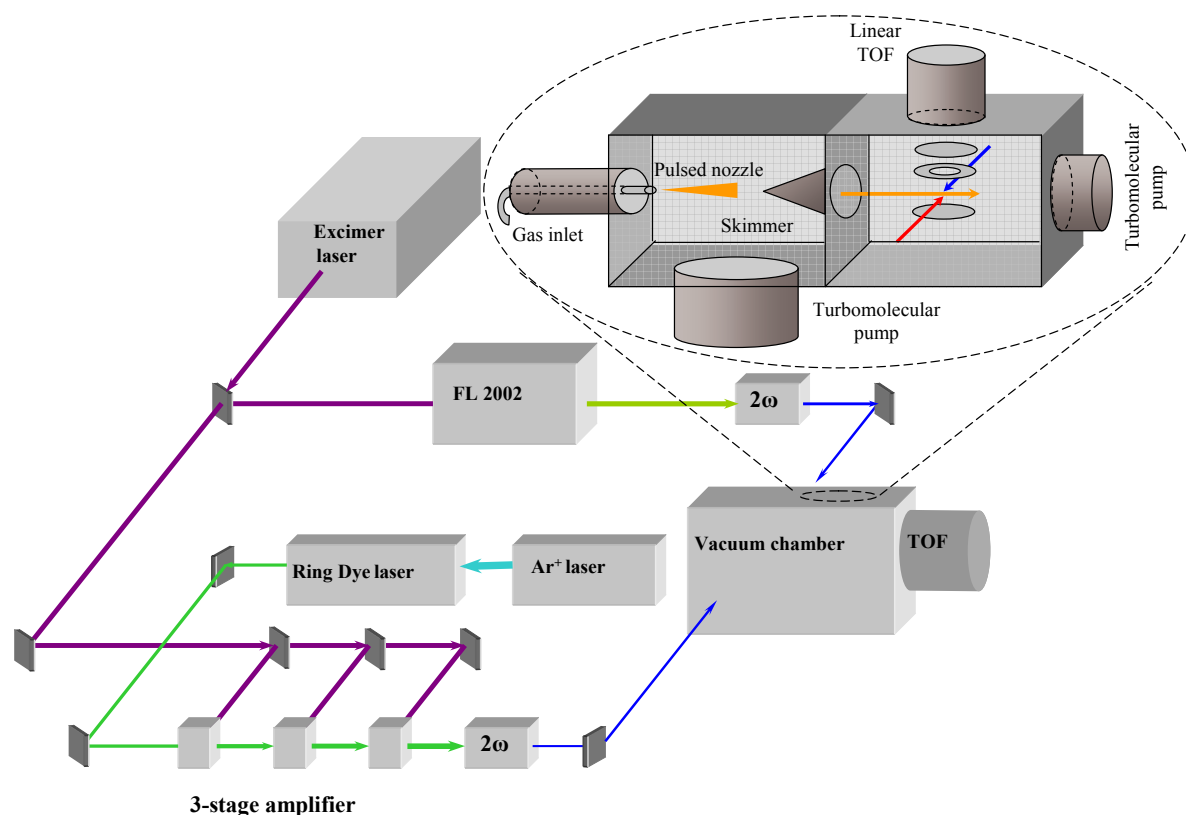
Figure 2.4: *Schematic representation of the laser system for low- and high-resolution resonance enhanced two-photon ionization experiments. Enlargement: Schematic view of the molecular-beam set up.*

Ionization Laser

The ionization photons are produced by frequency doubling in a Beta-Barium-Borate (BBO) or Potassium-Dihydrophosphate (KDP) crystal of the output pulses of a commercial tunable broadband dye laser (LAMBDA PHYSIK FL2002) with a linewidth of 0.4 cm^{-1} (FWHM) . This laser has an *oscillator* and an *amplifier*. The frequency tuning is performed by tilting of a diffraction grating, which plays also the role of a high-reflective rear mirror of the oscillator. Both oscillator and amplifier are pumped transversely by a XeCl excimer laser (LAMBDA PHYSIK EMG 203 MSC) generating pulses at 308 nm with an energy of 230 mJ and duration of *ca*. 20 ns (FWHM). The frequency-doubled dye laser pulses have an energy of the order of 1 mJ. The so-produced UV laser pulses pass through a telescopic system before they enter the vacuum chamber. This allows us to control the laser spot size at the interaction point with the molecular beam.

Single Mode cw Ring Dye Laser

The narrow-band single-mode cw laser is a ring dye laser (Coherent CR-699-21) operating with Coumarin 6 and Coumarin 521 in the wavelength range between 510 and 550 nm. It generates a cw laser beam with a bandwidth of 2 MHz and an output power ranging from 200 to 400 mW, depending on the pump laser power and the dye used. Single continuous scans within 30 GHz (1 cm^{-1}) are routinely performed. The pump source for the ring laser is an Ar$^+$ ion laser (Coherent Innova 400) operating at one of its strongest line at 488 nm (for Coumarin 521). The pump power varies between 4 W and 6 W.

Pulsed Amplification

Pulsed amplification of a cw single mode laser was invented by Hänsch and Wallenstein [33, 34], first realized by Salour [35], and applied to molecular spectroscopy by Riedle et *al*. [36]. The output of the single-mode ring laser is pulsed amplified in a three-stage homebuilt amplifier. The latter consists of three dye cells. The seeding cw beam propagates through the three cells where it is amplified by the pump pulses of the excimer laser described above in a transversal pumping geometry (see Sec. 2.2.2). The energy of the excimer-laser pulses is not distributed uniformly at the three cells but in proportion 10:20:70 starting from the first one. There are pinholes and interference filters down the seeder beam path to prevent generation of amplified spontaneous emission in the second and third amplifiers. The so-amplified high-resolution laser pulses are coupled into a doubling crystal (BBO or KDP) for *second harmonic generation* (SHG). The frequency-doubled pulses are nearly Fourier-transform-limited [37–39]. Their frequency bandwidth is *ca*. 70-100 MHz, pulse duration 10-13 ns and maximum energy 0.5-1.0 mJ. They are then laced through a telescopic system, similar to the one used for the broadband laser pulses (see Sec. 2.2.2), prior to being steered into the vacuum chamber (see Sec. 2.2.1 and Fig. 2.4) where they counterpropagate with the pulses from the broad-band dye laser and overlap with them in space and time at the crossing point with the molecular beam.

Pulse Stretching

The amplified pulses are nearly Fourier-transformed limited. For such pulses there exists a relationship between their duration and the spectral width, referred to as (*time-bandwidht product*) [37]. For Gaussian-shaped pulses in the time domain this relation is given by the formulae:

$$\Delta t \Delta \nu = \frac{2 \ln 2}{\pi} = 0.441 \tag{2.6}$$

For rectangular pulses this product is close to 1 [40]. Our amplified pulses are close to rectangular with a pulse duration of *ca*. 20 ns. (FWHM). This corresponds to a spectral width of
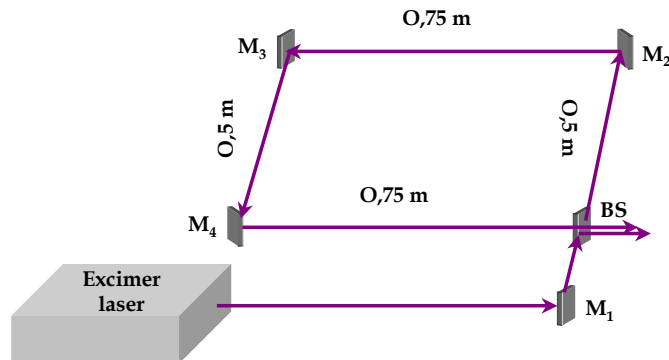
Figure 2.5: *Schematic view of the laser pulse delay line.*

ca. 50 MHz (FWHM). A possible approach to decrease this linewidth is to elongate the pulse in the time domain. Towards this end, we constructed a pulse stretcher, schematically depicted in Fig. 2.5. The pump pulses produced by the excimer laser are split by a 50/50 beamsplitter. The transmitted component is directed towards the amplifier, while the reflected component of the pulse is routed along a delay line with a total length of 2.5 m.
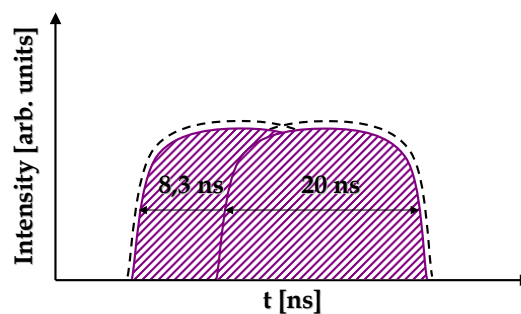
Figure 2.6: *Graphical representation of the elongated excimer laser pulse. The time width is measured at FWHM.*

This results in a delay of *ca.* 8.3 ns. Then the delayed and the non-delayed pulses are concatenated. The delay line is optimized in such a way that the two pulses partially overlap, this leading to a longer pulse with a duration of *ca.* 28 ns. (see Fig. 2.6). This pulse duration corresponds to a linewidth of *ca.* 36 MHz. The so-produced pulses are used to pump the dye cells of the three-stage amplifier. The amplified pulses, however, have a duration of *ca.* 14 ns, and, correspondingly, a bandwidth of *ca.* 70 MHz. The undesired broadening of the bandwidth is brought about most likely by fast fluorescence in the amplifier's cells, which is an intrinsic property of the lasing dyes.

Thus we have demonstrated that the pulse stretcher alone does not lead to the desired spectral width of the amplified pulses, but indeed it improved our laser resolution.

2.2.3   Control of the Experiment. Data Acquisition System

For the laser pulses and the cooled molecules to arrive simultaneously at the interaction point, the opening of the nozzle and the excimer laser pulse generation must be synchronized. This is realized by a master trigger sending trigger pulses to the nozzle controller (it can control the nozzle opening of typically 50 μs and hence, the quantity of the ejected molecular species) and a delay generator (Stanford Research Systems DG 535). The latter determines the time after the nozzle opening at which the excimer laser must be fired. This is the time necessary for the molecules to drift the distance from the nozzle to the interaction point with the laser pulses. This delay can be manually controlled and optimized for every particular case. To minimize the effect of the temporal jitter of the excimer laser, its pulses activate a photodiode, which serves as a trigger setting time zero for the TOF and the data acquisition system.

The data acquisition system consists of three gated integrators (Stanford research systems SR 280) and a personal computer (PC). The gated integrators integrate the ion signal within the selected time gate whose width is usually 50 ns or 100 ns. The signal is then digitized and recorded on a PC.

The laser scan (both for low- and high resolution experiments), the recording of the absolute frequency markers, the relative calibration with a Fabry-Perot interferometer, and the data acquisition system are controlled by a homemade software operating in LabVIEW environment.

2.3   Computer-Aided Rotational Fit Based on Genetic Algorithms

The rotational structure of vibronic bands in large flexible molecules and their clusters is more complicated and congested than in rigid smaller-sized species. This is due to the larger mass of

the molecule or cluster, their lower symmetry, and the additional internal degrees of freedom. This makes the interpretation of the rotational structure more complicated; an assignment of the large number of overlapping rotational transitions is a lengthy procedure, and in most cases individual lines are no longer resolved so that an assignment is impossible. For these reasons it is useful to apply pattern recognition methods for the simulation and interpretation of the complex spectra of these molecular species. This has become possible by the use of modern computers after the fast development of computational power and advanced algorithms. In our group a fitting procedure with implemented *genetic algorithms* (GA) [20, 41–46] has been developed by J. E. Braun. The details of the algorithm of the fitting procedure have been described elsewhere. [28] Here only the basic features of the data analysis are demonstrated.

As an initial step, the program generates several trial solutions based, in most cases, on arbitrary values of the participating parameters. Any trial solution is referred to as an *individual*. Any set of trial solutions is termed *population*. The size of the population, i.e., the number of solutions in a given set, is a free parameter and it can be user-defined. Normally, this number depends on the particular problem and varies between several tens to several hundreds. After a population has been created, there comes the second step, the *evaluation*. The quality can be ranked and a special number called *fitness* is used as an indicator for the quality. Usually, the fitness is normalized and it takes on values in the range between zero and one. As a figure of merit for the quality of the trial solutions, a comparison of any of the simulated spectra with the experimental one is used. The comparison is based, usually, either on cross correlation or on least squares fit. Experience shows, however, that cross correlation yields better results. The experimental spectrum is cross correlated with different calculated spectra and the maximum of the so-obtained cross correlation is a criterion for the quality of the simulation. The calculation includes a simulation of the spectrum and convolution of the simulated stick spectrum with a Gaussian line shape function. The cross correlation can be taken as a value for area overlap between theoretical and experimental spectra as a function of their relative position.When the spectra are completely different, the fitness tends to zero, and vice versa, when the spectra are very similar, the fitness converges to one. When the quality estimation is over there comes the *selection* step, in which of all initially generated spectra only the fittest ones are selected and subjected to a further treatment. The number of selected and preserved spectra is a free parameter. The selected spectra are allowed to bring forth a new generation through the processes of *reproduction* [41]. This process generates two new solutions; each of them having features from either of the parent ones. Some *mutations* using *random number generator* are applied to the new generation. This operation is necessary since it exploits the whole multidimensional space and prevents clinging of the solution to a local maximum. When the described procedure is repeated iteratively, it ultimately yields the best solution. Very often, it is necessary that the contribution of the peaks in P and R branches, respectively, be emphasized. For this purpose, the experimental spectrum is multiplied by a specially designed weighting function prior to being cross correlated with any of the synthesized spectra. This approach has turned out to be successful in many cases. To augment the efficiency of the fitting

routine, the explored multidimensional volume can be restricted by imposing some constraints to the possible values of the fitted parameters (rotational constants, transition moment (TM) ratio, rotational temperature, etc.). The procedure has been successfully applied to the analysis of highly resolved spectra with densely spaced peaks or with a low signal-to-noise ratio of flexible biologically relevant molecules and their complexes [20, 46].

2.4 Mass-Analyzed Threshold Ionization (MATI)

The excitation scheme of the pulsed-field threshold ionization combined with the resonance-enhanced two-photon excitation is shown in Fig. 2.7. The first laser pulse with a fixed wavelength and energy $h\nu_1$ promotes the molecules to a vibronic band in the S_1 electronic state. The second laser with photon energy $h\nu_2$ is scanned across the ionization thresholds of ionic vibrational states above the adiabatic ionization energy (AIE).
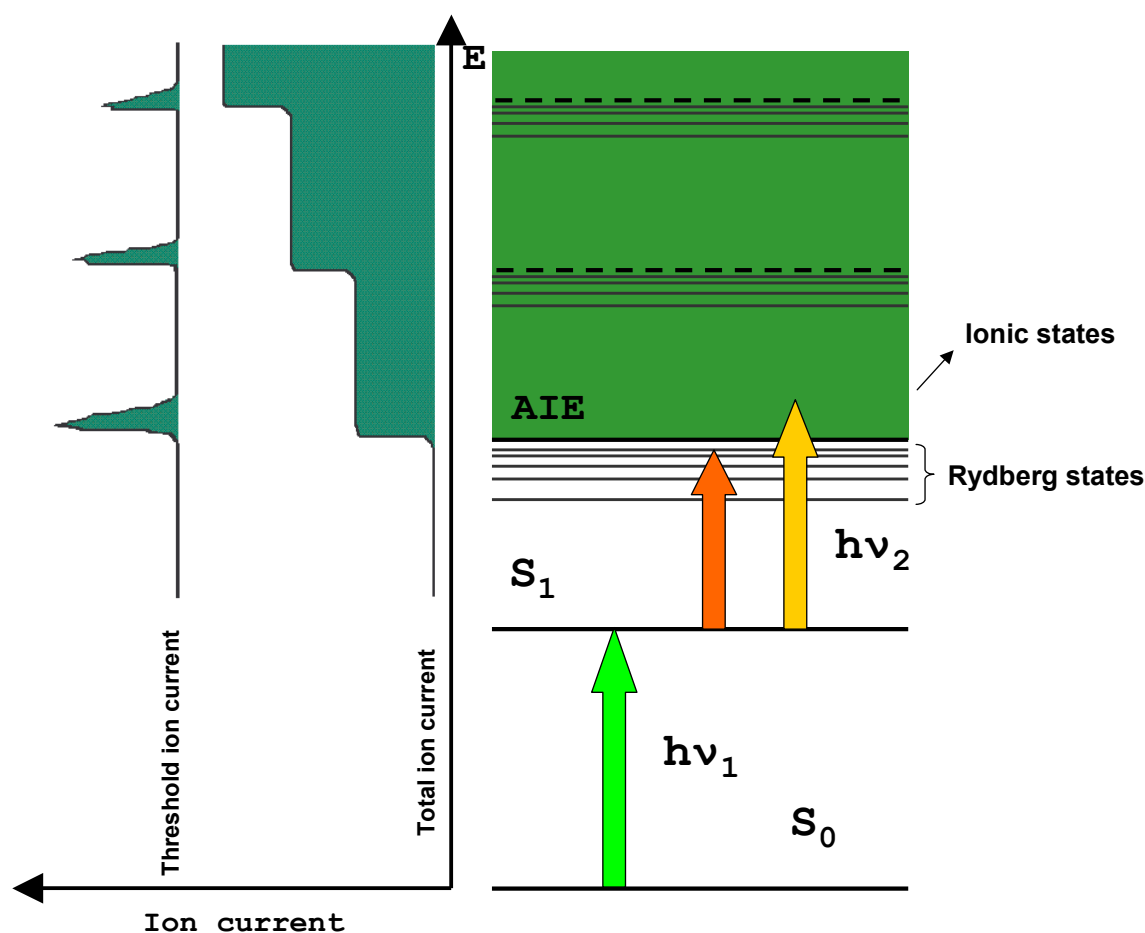
Figure 2.7: *Mass-analyzed threshold ionization (MATI) scheme.*

Recording the total ion current yields a photoionization curve with steps at the individual lowest thresholds (see left side of Fig. 2.7). Together with the prompt ions, molecules in long-lived high (*n,l*)-Rydberg states [47–50] are excited, which are separated from the prompt ions by a suitable separation process. They are ionized by a delayed pulsed field (t≈10μs and U≈+1000 V), and the resulting threshold ions are detected solely after the MATI separation process, described in details elsewhere [51–53]. As a result, sharp peaks with no background are observed at the individual thresholds. This leads to a vibrational spectrum of the molecular ions as shown schematically on the left side of Fig. 2.7. The ionization thresholds are slightly lowered by the presence of a weak separation field necessary for the separation process (U≈-0.3 V). It causes a shift of the individual thresholds (i.e., of the peaks in the ion spectrum) towards lower energies of about 10 cm^{-1}, but does not affect their relative energy distance, yielding a characteristic vibrational frequency pattern, we are interested in. This technique was first developed by Zhu & Johnson [51] as a complementary method of the zero kinetic energy photoelectron spectroscopy (ZEKE) [54], where the weakly bound Rydberg electrons are detected and monitored as a function of the ionization laser wavelength. The ZEKE spectroscopy has a somewhat higher resolution and sensitivity than the MATI spectroscopy because during the separation and pulsed field ionization process in MATI experiments many of the highest Rydberg states that contribute to most of the signal in ZEKE experiments are destroyed. It has been shown by our group [47] that Rydberg states in the region of 40≤n≤110 can be resolved in high-resolution optical double resonance experiments. The advantage of the MATI technique is its mass selectivity, which becomes essential when cluster dissociation experiments are performed. In this work, high Rydberg states are excited by the two-photon excitation scheme via various intermediate vibronic S_1 states originating from different conformers.

2.4.1 MATI Experimental Set up

The experimental set up comprises three functional units: vacuum equipment with pulsed heatable nozzle for production of jet-cooled molecular species [5, 21, 22] and a coupled linear reflecting time-of-flight mass spectrometer (RETOF) with an ion detector [55], a laser system for one-color resonance-enhanced multiphoton ionization (REMPI) and MATI, and a data acquisition system. They are described in detail in the PhD thesis of BRAUN [56]. Here just the main features will be presented.
The MATI experiment consists of two dye lasers yielding ≈10 ns light pulses with a bandwidth of ≈ 0.3 cm^{-1} (Lambda Physik, FL 3002 and Lambda Physik, LPD 3000), which are used for the excitation of molecules to high Rydberg levels or for the production of ions in a resonantly enhanced one- and two-color two-photon ionization (see Fig. 2.8). Both dye lasers are pumped synchronously by an XeCl excimer laser (Lambda Physik, EMG 1003i). The two counterpropagating laser beams intersect a skimmed supersonic molecular beam perpendicularly 15 cm down-

stream the nozzle orifice. The cold molecular beam is produced by the supersonic expansion of a gas mixture into vacuum.The mixture of the sample vapors with the buffer gas argon at 3 bar was expanded into the vacuum through a pulsed-operated heatable nozzle (General Valve) with an orifice diameter of 500 μm. The light pulses overlap in time and space in the center of the first stage of a double-stage acceleration configuration [53] formed by three metal disks with holes. This results in a production of threshold ions, which are accelerated into a linear reflecting TOF mass spectrometer [55].
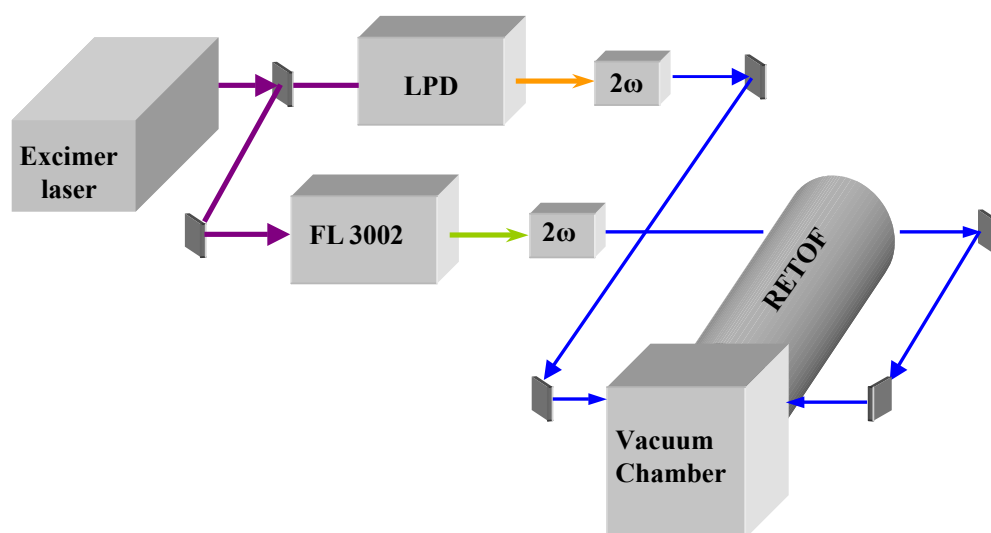
Figure 2.8: *Schematic representation of the laser system for mass-analyzed threshold ionization (MATI) experiments.*

After reflection, ions with different masses reach a multichannel plate detector at different times. The detector signal is recorded with gated integrators (STANFORD RESEARCH SYSTEMS SR 280), then digitized and processed in a microcomputer system with a homemade software operating in LabVIEW environment.

Part III

Results and Discussion

Chapter 3

Identification of Conformational Structures of 2-Phenylethanol and its Singly Hydrated Complex by Mass Selective High-Resolution Spectroscopy and *ab initio* Calculations

The flexible prototype molecule, 2-phenylethanol (2-PE), and its singly hydrated complex have been investigated in a cold supersonic beam by combination of high-resolution two-color R2PI spectroscopy and quantum chemistry ab initio calculations. The existence of two monomer structures separated by a high potential energy barrier, gauche and anti ones, was proven. Higher-energy conformers are supposed to relax to the observed ones during the jet expansion process. We have identified the conformational structure of the complex between 2-PE and water, which corresponds to water binding to the most stable gauche conformer. No detectable structural changes of the host 2-PE molecule have been observed upon attachment of a single water molecule. A conformational relaxation mechanism is suggested also for the 2-PE·H_2O complex.

3.1   Introduction

Many biological processes are regulated by relatively small, flexible molecules. A typical example for such molecules are neurotransmitters, [57, 58] which play an important role in the human body. The properties and functionality of neurotransmitters depend significantly on their conformational structure, which is determined by a subtle interplay between weak *intramolecular* interactions and *intermolecular* interactions with the solvent. The importance of these interactions has been realized, and their detailed exploration has attracted a lot of scientific interest over the past decade. In recent investigation the combination of various spectroscopic techniques in the gas phase with advanced quantum chemistry computations has allowed first retrieval of structural information on a number of neurotransmitters, including 2-phenylethylamine, [59–64] phenylalanine, [65] ephedrine, [20, 66–68] norephedrine, [69] pseudoephedrine, [67] adrenaline. [69] 2-phenylethanol (2-PE) (see Scheme with atom labels) is the hydroxy analog of the neurotransmitter molecule, 2-phenyl-ethylamine. It has been extensively studied over the last years [16, 46, 61, 63, 70–73] as a neurotransmitter prototype molecule. The *gauche* structure of the most stable conformer of the 2-PE monomer has been conclusively established by microwave [70] and our high-resolution resonant two-photon ionization (R2PI) [46] experiments combined with quantum chemistry *ab initio* calculations. Yet, however, there exist several unclear issues and controversies on the conformational structures of the bare molecule and the structure of its singly hydrated complex. The present work presents a detailed analysis of the existing conformers of the 2-PE monomer and discusses possible processes leading to interconversion of conformers in the jet expansion. The experimental findings from mass selective high-resolution UV two-photon resonance enhanced ionization spectroscopy of all pronounced bands in the vicinity of the strongest origin band are reconciled with the theoretical predictions on rotational constants, transition moment ratios, and vibrational frequencies from high-level *ab initio* quantum chemistry calculations. Through a confident assignment of all the observed vibronic bands in the vicinity of the strongest 0_0^0 origin band in the spectrum of the 2-PE monomer, we have concluded that two conformers, *gauche* and *anti* ones are observed under the conditions of adiabatic expansion in a cold supersonic beam. The analysis of the theoretical potential energy surface corroborates the assumption that the higher-energy conformers that presumably exist in the preexpansion region relax to the observed ones, the latter being separated by a high potential barrier. We also extended the study of 2-PE to its singly hydrated complex. This investigation renders itself as a natural extension of our previous study on the 2-PE·Ar complex, [46] where the structure is determined by the interplay between the *intramolecular* hydrogen bond and the *intermolecular* dispersion interactions. This is to our knowledge the first application of mass resolved high-resolution UV spectroscopy to studying hydrated complexes of flexible biologically relevant molecules, which are a subject of intense research over recent years. [4, 73–78] The important issues addressed are whether and how solvent molecules affect the conformational
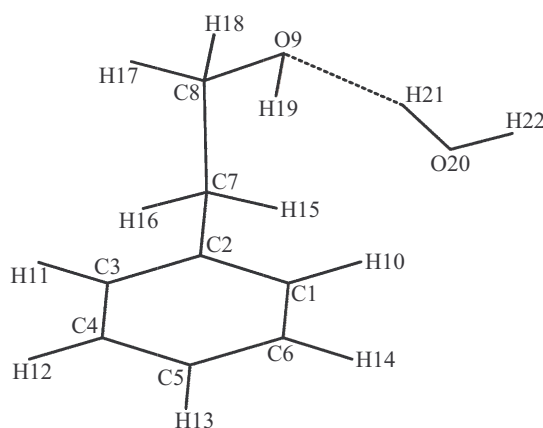
Figure 3.1: *Atom labels of the 2-PE·H_2O complex*

structure of the flexible solute molecule and how the flexible molecule adapts its structure to the local environment under the combined action of *intra-* and *intermolecular* hydrogen bonds. Another interesting aspect is whether water stabilizes particular conformers thus acting as an efficient conformational selector. The complex between 2-PE and water is a prototype system for microsolvation and is expected to reveal the binding pattern and the influence of water on the conformational shape and stability of the host flexible molecule.

3.2 Experiment and Data Processing

The experimental setup used to measure the one- and two-color resonance enhanced two-photon ionization spectra of 2-PE has been described in Chapter 2.2 and following publications [10, 46, 79, 80]. Briefly, the 2-PE vapor is mixed with Ar at a pressure of 3.0 bar and expanded into vacuum through a pulsed-operated heatable nozzle with orifice diameter of 300 μm. To increase the vapor concentration of 2-PE in the nozzle the substance was heated to 96 °C. To reduce the Doppler broadening a skimmer with an orifice of 1 mm in diameter is used. The molecular beam is intersected perpendicularly by two counterpropagating laser pulses.

The analysis of the highly resolved spectra has been performed using our homemade rotational fit computer routine based on genetic algorithms. [20, 44, 46, 81] Cross correlation was employed as a fitness function. The typical number of generations was 200 with 200 individuals in a generation.
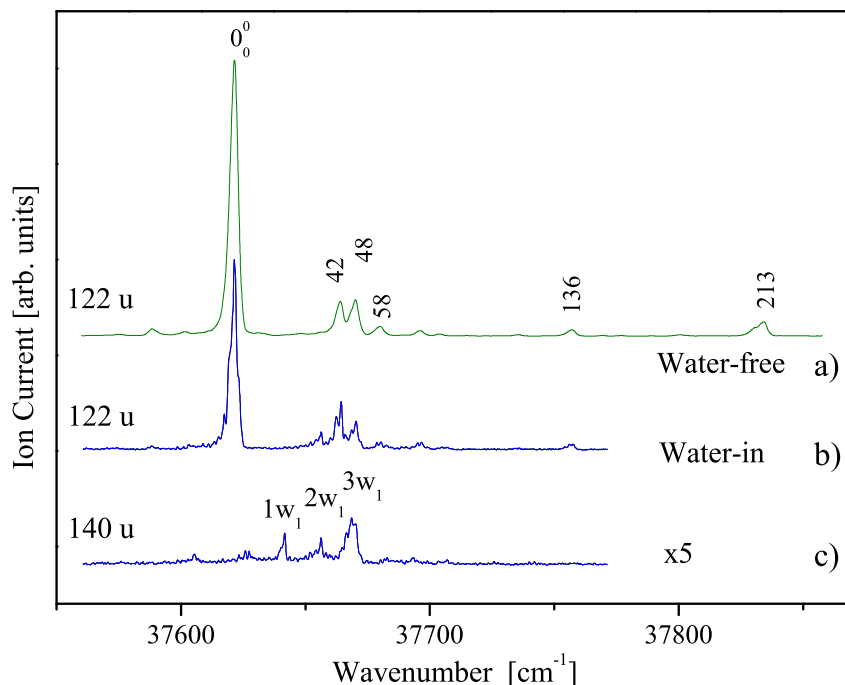
Figure 3.2: *One-color R2PI spectra of the $S_1 \leftarrow S_0$ electronic transition of the 2-PE monomer measured at the monomer (m/z = 122) mass channel under water-free (a), water-present (b) conditions, and of the 2-PE· H_2O complex (c) recorded at its parent (m/z = 140) mass channel.*

3.3 Experimental Results

3.3.1 Low Resolution Spectrum

We have recorded low-resolution one-color resonant two-photon ionization(R2PI) spectra monitoring three different mass channels in the vicinity of the $S_1 \leftarrow S_0$ electronic transition of 2-PE under two different experimental conditions. In the first case, the spectrum was measured under water-free conditions by selecting the ion signal at the parent mass channel at m/z=122. The spectrum is presented in Fig. 3.2(a). The 0_0^0 vibronic band and the small redshifted band at 30 cm^{-1} have been discussed in our previous paper. [46] Here we discuss the blueshifted vibronic features in the spectrum at +42, +48, +58, +136, and +213 cm^{-1}. The second set of spectra was recorded under water-in conditions monitoring both parent mass channel at m/z=122 and the mass channel of the singly hydrated 2-PE at m/z=140. The two resulting spectra are shown in Fig. 3.2(b, c).

The three most intense vibronic bands measured at the mass channel of the 2PE-water cluster are labeled with $1w_1$, $2w_1$ and $3w_1$, respectively. It has been found that the positions of peak $+48$ cm^{-1} in the monomer mass channel and peak $3w_1$ in the 2PE-water cluster mass channel coincide. Therefore, peak $+48$ cm^{-1} is likely to originate from fragmentation of the 2-PE-water cluster. However, adding water does not change the relative intensity of this band. This leads us to the conclusion that $3w_1$ is a mixture of two close lying bands: one of the 2-PE monomer, and the other one of the 2-PE·H_2O complex. A clear evidence for the nature of this band is provided only by high-resolution spectroscopy, and is presented below. There is a stronger fragmentation behavior of band $2w_1$ in comparison with the other bands ($1w_1$ and $3w_1$) observed at this mass channel. This may be tentatively explained by the existence of 2-PE·H_2O cluster conformers of different stability. The remaining smaller vibronic bands in the spectrum of Fig. 3.2(c) measured at mass channel m/z=140 do not correspond to any of the bands in Fig. 3.2(b) measured at the mass channel of the monomer. As a next step, to elucidate the conformational structures giving rise to the above-described vibronic bands of 2-PE and its singly hydrated cluster, we measured the bands under discussion with a much higher resolution.

3.3.2   High Resolution Spectra

3.3.3   Monomer Bands

The highly resolved UV spectra of all blue shifted bands recorded at the monomer mass channel under water-free conditions are shown in Figs. 3.3- 3.5. In all bands, a well-pronounced rotational structure covering a range from 3 to 5 cm^{-1} is resolved. The rotational structure of the bands at $+42$, $+136$ and $+213$cm^{-1} is similar to the that of the published 0_0^0 band. [46] It is characterized by a central dip, a small Q branch on the red side of the dip, and well defined P and R branches. The spectra of these three bands manifest a hybrid a-, b-, and c-type character with prominent b contribution. They do not consist of single rotational lines but we observe peaks produced by aggregation of several rotational lines resulting in a minimum value for the peak width of 250 MHz FWHM.
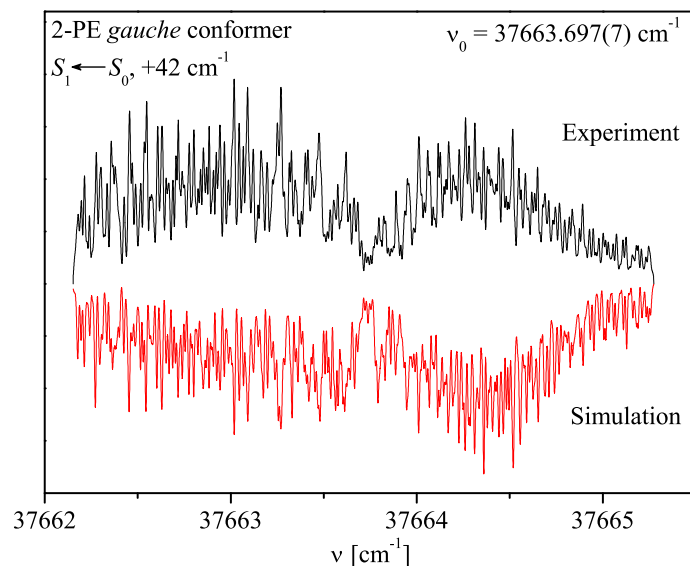
Figure 3.3: *High-resolution two-color UV R2PI spectrum of vibronic band +42 cm^{-1} in Figure 3.2, recorded at m/z = 122. The band is assigned as a progression of the gauche conformer **2** of the 2-PE monomer with its rotationless transition centered at 37663.697(7) cm^{-1}. Upper trace: experimental spectrum. Lower inverted trace: the best-fit simulated spectrum yielding the parameters in Table 3.1 (for details, see text).*

To find the rotational constants for the ground, S_0, and the first excited, S_1, electronic states, the transition moment ratio, the rotational temperature, and the origin position, v_0, we used the computer-assisted rotational fit procedure based on genetic algorithm described earlier. [20, 44, 81] (see also Sec. 2.3)As starting values for our fits, we used the values resulting from ab inito calculations of the ground state rotational constants for the *anti* and *gauche* conformers. To minimize the number of simultaneously fitted parameters, we used a stepwise approach to determine the experimental values of all parameters. As a first step, we constrained the ground state rotational constants within 0.5% of their initial value and let the search space for the excited state rotational constants and for the other parameters relatively broad. In a second step, we used the values obtained in the first step and fixed the transition moment ratios but letting the other parameters free. The produced theoretical stick spectrum was convoluted using a Gaussian line shape with a FWHM of 150 MHz. The best-fit results for the bands are shown in the inverted spectra in Figs. 3.3- 3.5. The simulated spectra (the lower inverted part) agree well in both peak positions and peak intensities with the experimental ones (upper trace). The achieved cross correlation between the experimental and simulated spectra is as high as 95%. The experimentally obtained values of the rotational constants, the transition moment ratios, and the rotational temperatures

Figure 3.4: *High-resolution two-color UV R2PI spectra of vibronic bands +48 cm^{-1} and +58 cm^{-1} in Figure 3.2, recorded at m/z = 122. The bands are assigned as a vibrational progressions of the anti conformer **5** of the 2-PE monomer with the rotationless transitions centered at 37669.601(2) cm^{-1} and 37679.516(7) cm^{-1}, respectively. Upper traces: experimental spectra. Lower inverted traces: the best-fit simulated spectra yielding the parameters in Table 3.1 (for details, see text).*

are summarized in Table 3.1. Comparing the experimental values for the rotational constants with the results from the *ab initio* calculations we can clearly assign the bands at +42 cm^{-1}, +136 and +213cm^{-1} to the most stable *gauche* structure. However, differences are observed for the measured transition moment ratio of the + 42 cm^{-1} band from the +136 and +213cm^{-1} bands and from theory. The experimental values for the +136 and +213 cm^{-1} bands (18:74:8) are the same as the ones of the 0_0^0 band [46] but differ from the theoretically predicted one at the MP2/cc-pVDZ level of theory (1:96:3). The measured mixed *a* and *b*-type spectrum with transition moment ratio (42:50:8) of the +42 cm^{-1} band yields a transition moment orientation which is not predominantly along the *b* principal axis of inertia as is theoretically expected. On the other hand, the experimental rotational constants for both ground and excited state are close to the ones of conformer **2**. We used the above-described procedure to assign the spectra of the +48 and +58cm^{-1} vibronic bands in Fig. 3.4 fitting with a differing rotational band structure characterized by a minor central dip, a very small Q branch on the red side of the dip, and well resolved P and R branches. Again, there is a good match in peak positions and peak intensities of measured and simulated spectra with achieved cross correlation of 96% and 95%, respectively. There is a good agreement between the values of rotational constants *B* and *C* in Table 3.1 and those found by our *ab initio* calculations of the *anti* conformer **5** for the ground, S_0, and the first excited, S_1, electronic states (cf. Table 3.3). Only the experimental and calculated values for the ground rotational constant *A* are somewhat different. In addition, the experimental values for the transition moment ratios of the two bands (4:96:0 and 8:92:0, respectively) are very close to the one calculated (0:100:0) for conformer **5**.

3.3.4   Water Complex Bands

Two of the vibrational bands, 1w$_1$ and 3w$_1$, measured at the parent mass channel (*m/z* = 140) of the singly hydrated complex of 2-PE (see Fig. 3.2) have also been measured under high resolution. The low intensity of band 2w$_1$ did not allow this band to be rotationally resolved. Band 3w$_1$ yields relatively high intensity when measured by two-photon two-color ionization and spans over a fairly broad (ca. 4 cm^{-1}) range. The band is superimposed on a high background and its overall profile is characterized by two pronounced P and R branches and a shallow central dip with a weak Q branch. It is worth pointing out that though its high intensity band 3w$_1$ does not feature resolved rotational microstructure. This precluded its rotational fit analysis. The experimental highly resolved spectrum of band 1w$_1$ is presented in Fig. 3.6 (upper trace). The spectrum covers a relatively narrow frequency range of ca. 1.5 cm^{-1}. It has a well-resolved structure built up of separate peaks with a linewidth of 250 MHz resulting from aggregations of closely spaced single rotational lines. The spectrum lies on a small background, and features a prominent Q branch in the center and less intense P and R branches with irregular but resolved structure. We fitted the spectrum by the computer-aided routine based on genetic algorithms
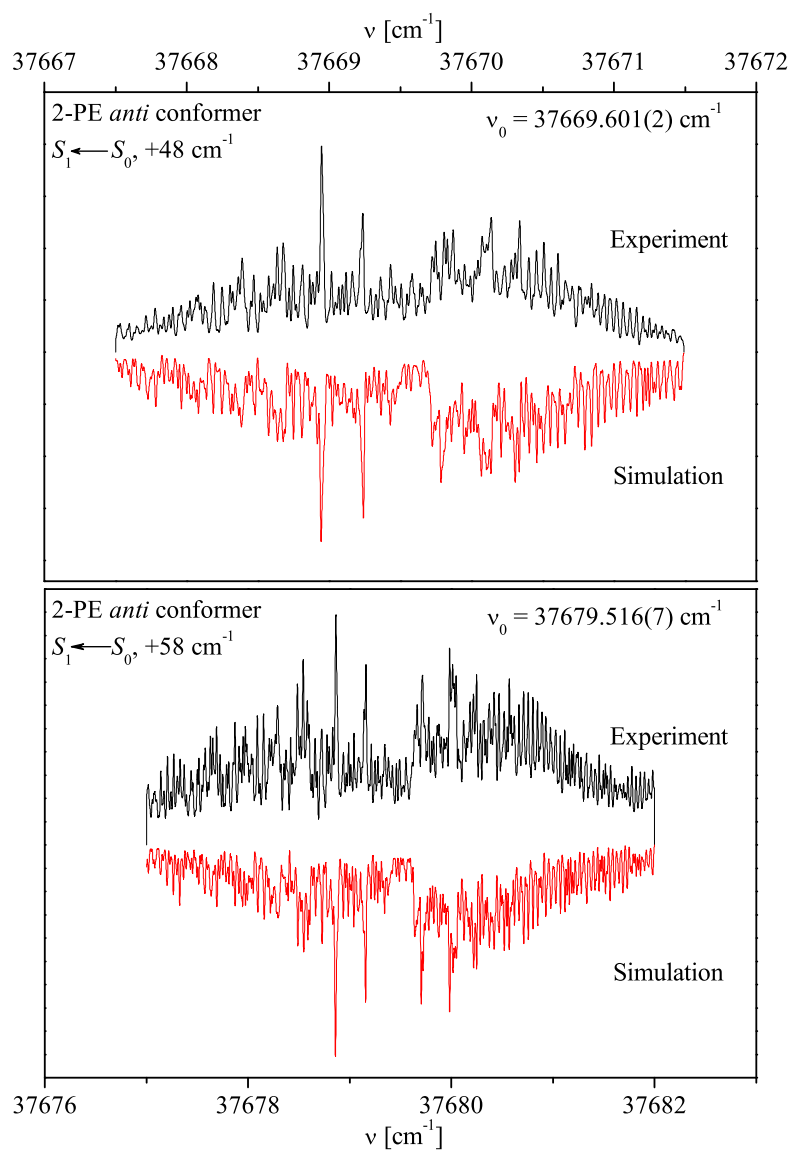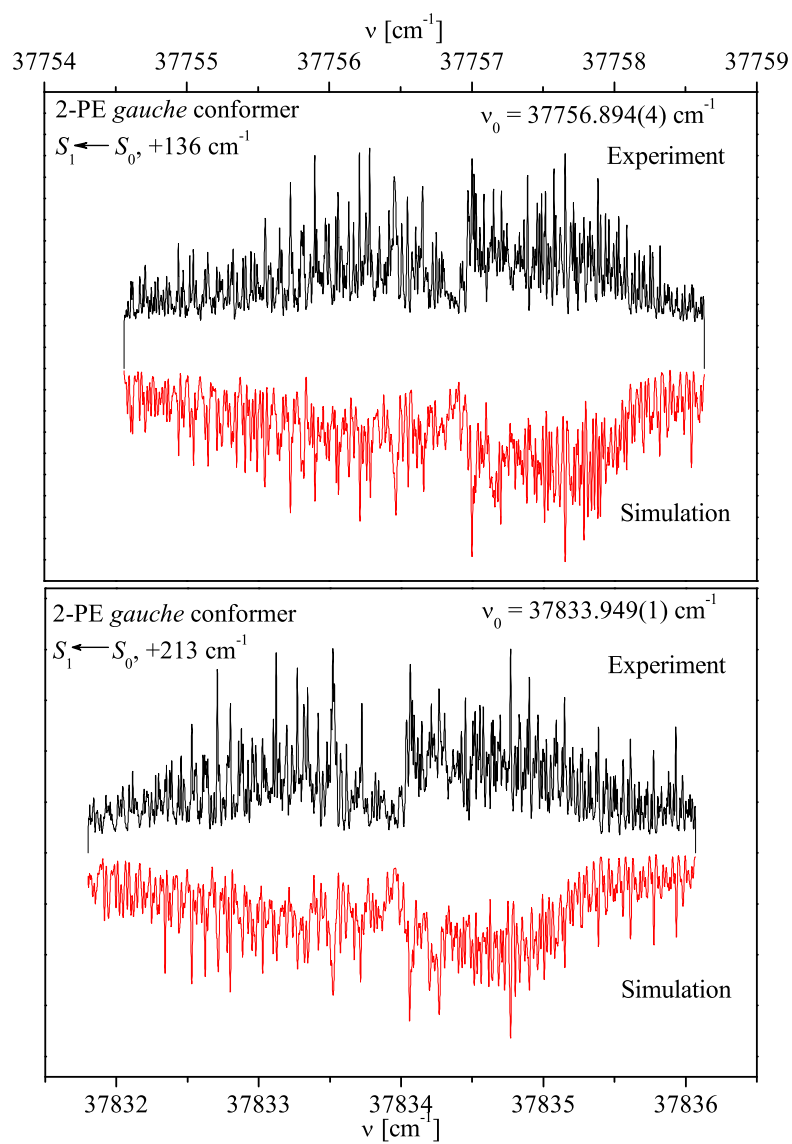
Figure 3.5: *High-resolution two-color UV R2PI spectra of vibronic bands +136 cm^{-1} and +213 cm^{-1} in Figure 3.2, recorded at m/z = 122. The bands are assigned as a vibrational progressions of the gauche conformer **2** of the 2-PE monomer with the rotationless transitions centered at 37756.894(4) cm^{-1} and 37833.949(1) cm^{-1}, respectively. Upper traces: experimental spectra. Lower inverted traces: the best-fit simulated spectra yielding the parameters in Table 3.1 (for details, see text).*

Parameter	Band				
	$+42$ cm^{-1}	$+48$ cm^{-1}	$+58$ cm^{-1}	$+136$ cm^{-1}	$+213$ cm^{-1}
A''	0.1116(11)	0.14765(19)	0.14785(30)	0.1113(22)	0.1118(25)
B''	0.03605(32)	0.02841(9)	0.02857(34)	0.03620(63)	0.03611(63)
C''	0.3211(28)	0.02527(8)	0.02558(41)	0.3203(35)	0.03192(33)
A'	0.1083(14)	0.14118(14)	0.14122(27)	0.1080(32)	0.1086(26)
B'	0.03538(33)	0.02803(7)	0.02818(39)	0.03560(49)	0.03550(56)
C'	0.03128(45)	0.02513(9)	0.02513(42)	0.03110(47)	0.03109(34)
$\mu_a^2 : \mu_b^2 : \mu_c^2$	42:50:8	8:92:0	4:96:0	19:74:9	19:74:9
ν_0 , cm^{-1}	37663.697(7)	37669.601(2)	37679.516(7)	37756.894(4)	37833.949(1)
T(K)	8.5(2)	8.6(3)	9.9(2)	11.3(5)	11.2(1)
Best-fit cross correlation (%)	94.5	95.6	95.2	94.7	95.6

Table 3.1: *Experimental rotational constants for the ground,S_0 (A'', B'', C''), and for the first excited,S_1 (A', B', C'), electronic states, the transition moment ratio, $\mu_a^2 : \mu_b^2 : \mu_c^2$, the band origin frequency, ν_0, the rotational temperature, T, and the best-fit cross correlation obtained from the rotational fit of bands $+42$, $+48$, $+58$, $+136$, and $+213$ cm^{-1}, shown in Figures 3.3- 3.5. The numbers in parentheses represent one standard deviation in units of the least significant quoted digit. The uncertainty for the relative values of μ_a^2, μ_b^2, and μ_c^2 in the transition moment ratio does not exceed 5(%).*

outlined above and derived the molecular parameters of the species producing it. The simulated stick spectrum was convoluted by a Gaussian profile with a linewidth of 150 MHz. The resulting best-fit simulated spectrum is depicted in Fig. 3.6 (lower inverted trace). The simulation reproduces fairly well both overall profile and peak positions. The so-obtained rotational constants for the ground, S_0, and the first excited, S_1, excited state, the transition moment ratio, the band origin position, ν_0, and the rotational temperature, T, are summarized in Table 3.3.4.

3.4   *Ab initio* Calculations

Ab initio quantum chemistry calculations for various conformations of the 2-PE monomer and its singly hydrated complex have been performed using GAUSSIAN 03 program package. [82] Five different conformations of the 2-PE monomer and six different conformational structures of the 2-PE·H2O complex have been considered.

3.4.1   2-PE Monomer

To find the stable conformations of the 2-PE monomer we performed a potential-energy grid search at the MP2/cc-pVDZ level of theory. The grid search was realized by scanning the
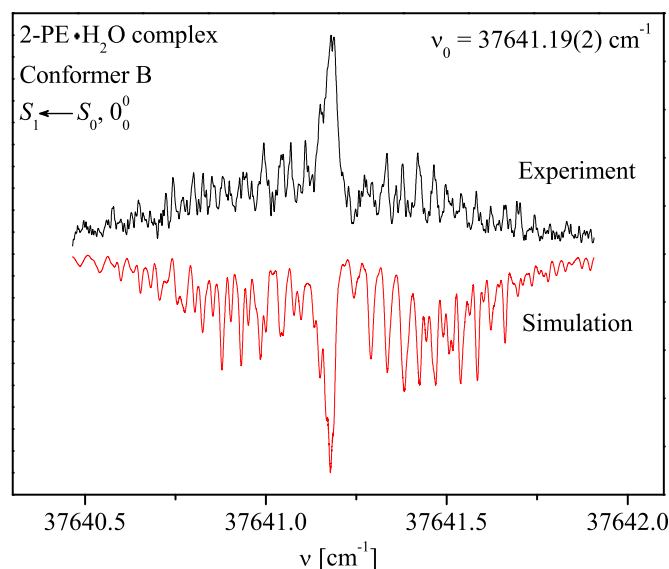
Figure 3.6: *High-resolution two-color UV R2PI spectrum of vibronic band $1w_1$ in Figure 3.2, recorded at $m/z = 140$. The band is assigned as the 0_0^0 origin band of conformer conformer **B** of the 2-PE·H_2O complex with the rotationless transition centered at 37641.19(2) cm^{-1}. Upper trace: experimental spectrum. Lower inverted trace: the best-fit simulated spectrum yielding the parameters in Table 3.5 (for details, see text).*

C2C7C8O9 and C7C8O9H19 dihedral angles of the 2-PE molecule. The so-obtained potential-energy surface is depicted in Fig. 3.7 (for the sake of clear visualization the potential-energy surface is inverted). Five potential-energy minima have been predicted. The deepest one (global minimum) corresponds to the *gauche* conformer (conformer **2**) in which the terminal OH group of the side chain points to the π electrons of the aromatic ring. Other two higher-energy structures (conformer **1** and conformer **3**) separated from each other, and from the main minimum, by low potential barriers correspond also to *gauche* conformations but with different orientations of the OH group (different C7C8O9H19 dihedral angles). The conformations with the side chain pointing away from the benzene ring (conformer **4** and conformer **5**) are referred to as *anti* conformers, and they give rise to the other two potential energy minima. The two structures in question are separated by a low potential barrier from each other, and by a high barrier along the C2C7C8O9 angle coordinate from the *gauche* conformers. The conformational structures corresponding to the potential-energy minima have been subjected to a further full structural optimization and calculation of their energetics at the MP2/cc-pVDZ level of theory for the ground, S_0, electronic state, and at the CIS/cc-pVDZ level of theory for the first, S_1, electronic state. In addition, a frequency analysis for both ground, S_0, and first excited, S_1, electronic state has been performed at the same level of theory, respectively. The presence of only positive frequencies is a verification

Paramter	Band $1w_1$
A''	0.0671(9)
B''	0.0270(3)
C''	0.0224(10)
A'	0.0654(14)
B'	0.0268(3)
C'	0.0221(1)
$\mu_a^2 : \mu_b^2 : \mu_c^2$	69:31:0
ν_0 , cm^{-1}	37641.19(2)
T(K)	1.4(1)
best-fit cross correlation (%)	91

Table 3.2: *Experimental rotational constants for the ground,S_0 (A″, B″, C″*

, and for the first excited,S_1 (A′, B′, C′), electronic states, the transition moment ratio, $\mu_a^2 : \mu_b^2 : \mu_c^2$, the band origin frequency, ν_0, the rotational temperature, T, and the best-fit cross correlation obtained from the rotational fit of the 0_0^0 origin band of the $S_1 \leftarrow S_0$ electronic transition of conformer **B** of the 2-PE·H$_2$O complex shown in figure 3.6. The numbers in parentheses represent one standard deviation in units of the least significant quoted digit. The uncertainty for the relative values of μ_a^2, μ_b^2, and μ_c^2 in the transition moment ratio does is 9(%).

that the optimized structures indeed correspond to potential-energy minima. The rotational constants of the discussed conformations for both ground and excited electronic states along with the energies without and with the zero-point vibrational energy corrections for the ground state, and the transition moment ratios for the first excited electronic state, as well as some typical interatomic distances, planar, and dihedral angles are summarized in Table 3.3. The fully optimized conformations are also shown in Fig. 3.7 atop of their corresponding point on the potential-energy surface. The vibrational frequencies for the first excited, S_1, electronic state are detailed in Table 3.4. In addition to the above-described calculations, structural optimizations, energy calculations, and vibrational analysis of conformers **4** and **5** at the MP2/aug-cc-pVTZ level of theory have been performed as well. The use of this very extended basis set significantly accounting for the electron correlation was expected to resolve the existing controversy [59,63,70] on the energy ordering of conformer **4** and conformer **5**, and to theoretically substantiate our experimental results. No noticeable structural changes occur upon extending the basis set from cc-pVDZ to aug-cc-pVTZ but at the augmented basis set conformer **5** is more stable than conformer **4** by 53 cm^{-1}. This result does not include the ZPVE since the vibrational analysis of the two conformations at this basis set is computationally very expensive. The inclusion of the ZPVE, however, is not expected to alter the relative energy ordering of the two conformers.
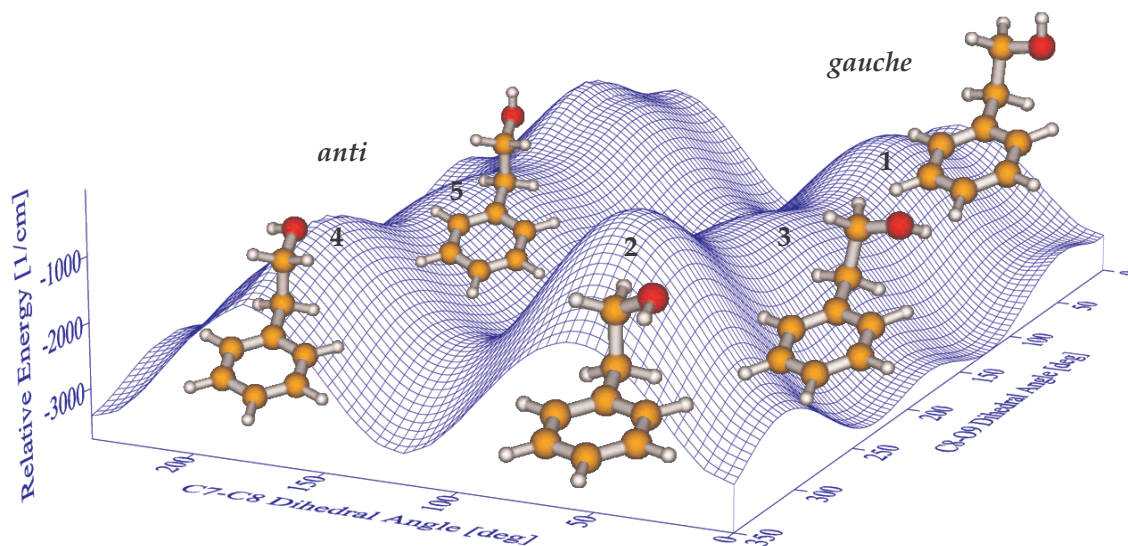
Figure 3.7: *Potential energy surface (inverted for the sake of a better visualization) as a function of the C2C7C8O9 and C7C8O9H19 dihedral angles of the 2-PE monomer. The gauche and anti conformations are separated by a high potential barrier in the C7C8 coordinate. The five energetically most favorable conformations of the 2-PE monomer have been fully geometrically optimized in their ground, S_0, electronic state at the MP2/ccpVDZ level of theory. The fully optimized structures are depicted on their corresponding minima on the potential energy surface.*

3.4.2 2-PE·H$_2$O Complex

As an initial step we performed structural optimizations for the ground, S_0, and the first excited, S_1, electronic state at the MP2/6-31G* and CIS/6-31G* level of theory, respectively, of various conformations of the 2-PE·H$_2$O complex. The starting geometries of the hydrated complexes were conceived by attaching the water moiety to different plausible binding sites of the three lowest-energy conformations (conformers **2**, **4**, and **1**) of the 2-PE monomer. In this way, 6 different conformations of the 2-PE·H$_2$O complex were produced and optimized (Fig. 3.8). The theoretically predicted inertial parameters for the ground and excited state and the transition moment ratio were used to simulate theoretical spectra, which were visually compared with the experimental highly resolved spectrum of the 2-PE·H$_2$O complex (see Fig. 3.6, upper trace). The apparent disagreement between the experimental spectrum and the simulated spectra corresponding to the two hydrated complexes when involving the *anti* conformer of the 2-PE monomer (conformer **4**) was a clear indication that the experimental spectrum does not originate from any
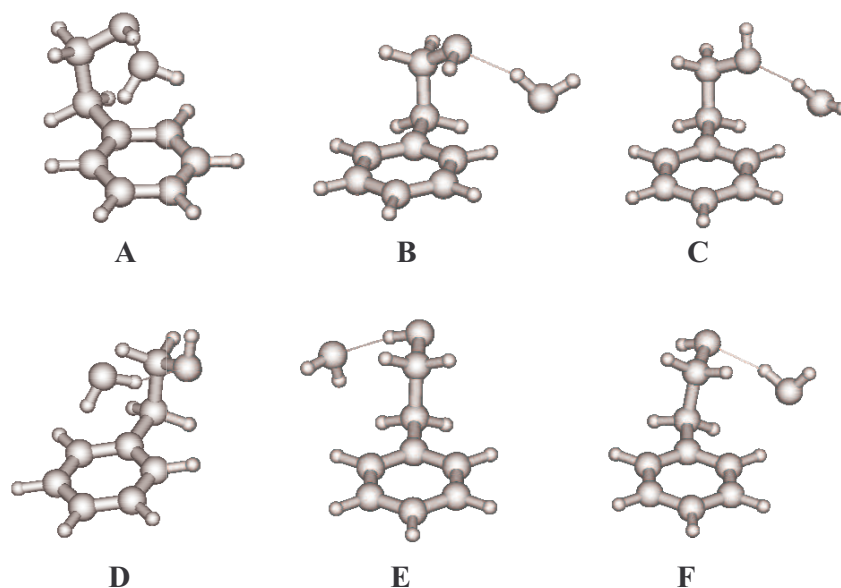
Figure 3.8: *Electronic ground state, S_0, structures of the 2-PE·H_2O complex optimized at the MP2/cc-pVDZ (conformers A, B, C, and D) and MP2/6-31G* level of theory, respectively. Typical angles, bond lengths, inertial parameters, and binding energies for these structures are listed in Table 3.5*

of these two complexes. For this reason the latter were ruled out from a further consideration. The remaining four structures of the 2-PE·H_2O complex were subjected to further full geometrical optimizations and vibrational analysis for both ground, S_0, and first excited, S_1, electronic states at the MP2/cc-pVDZ and CIS/cc-pVDZ level of theory, respectively, thus improving the electron correlation. In this way various binding patterns have been thoroughly theoretically explored, in which water plays either the role of a proton donor or of a proton acceptor forming σ or π weak *intermolecular* hydrogen bonds. The found vibrational frequencies of all optimized conformers are positive, which is a verification that indeed those structures correspond to minima on the potential energy surface. We also calculated the binding energies without and including the basis set superposition error (BSSE) and zero-point vibrational energy (ZPVE). The absolute binding energies depend essentially on the inclusion of the corrections accounting for the BSSE and ZPVE but the energy ordering of the conformations remains always the same. The rotational constants for both ground and first excited electronic state, binding energies for the ground state, and the transition electronic dipole moment of all conformations are summarized in Table 3.5. The optimized conformational shapes are depicted in Fig. 3.8, where conformers **A**, **B**, **C**, and **D** have been optimized at the MP2/cc-pVDZ level of theory, and conformers **E** and **F** (presented for completeness) have been optimized at the MP2/6-31G* level of theory The most stable con-

former (the one with the highest binding energy) is conformer **A** in which the water molecule inserts between the benzene ring and the side chain of the most stable 2-PE monomer (conformer **2**). In this bridging structure the water molecule acts both as a proton donor and a proton acceptor forming a weak π hydrogen bond with the benzene ring, and σ bond with the hydrogen atom of the terminal hydroxyl group of 2-PE. The second-in-energy conformer is conformer **B** in which the water moiety binds sideways to 2-PE through the formation of a single σ bond wherein the water molecule donates a proton to the oxygen atom of the OH group of 2-PE. The higher-energy conformers of the 2-PE·H_2O complex involve conformer **1** of the 2-PE monomer.

3.5   Discussion

3.5.1   Monomer conformers

In our *ab initio* calculations of the 2-PE monomer at the MP2/cc-pVDZ level of theory, we have considered five of the most stable 2-PE monomer structures which have been discussed in previous works. [16, 61, 70, 72, 73] The most stable conformer is the one with the hydroxyl hydrogen positioned above the benzene ring, and designated hereinafter as conformer **2**. The next two conformations are the *anti* conformer **4**, and the *gauche* conformer **1**, separated from the most stable species by 586 cm^{-1} and 685.86 cm^{-1}, respectively. The energy gap between them, however, is very small, and therefore the above ordering may be changed upon improving the used computational method and basis set. The most unstable conformations are the *gauche* conformer**3** , and the *anti* conformer **5**, distanced by 783.30 cm^{-1} and 788.35 cm^{-1} away from the lowest-energy conformer **2**. We unambiguously assign bands + 136 and +213 cm^{-1} to conformer **2** where the agreement of the theoretical and experimental values for the rotational constants of the ground, S_0, and the first excited, S_1, electronic states and the transition moment ratio is the best. This is the conformer that produces also the strongest band (see Fig. 3.2). [46] In the case of band +42 cm^{-1}, where the transition moment ratio differs form the one predicted for conformer **2**, the assignment is based on the rotational constants' match only. A similar to our (42:50:8) change of the transition moment ratio has been predicted (42:36:22) by Mons et al. [16] We support their explanation for the origin of this phenomenon: the + 42 cm^{-1} band may gain intensity through vibronic coupling to another excited electronic state, which leads to a strong dependency of the transition moment ratio on the nature of the vibration. An additional argument that conformer **2** produces the bands at +42 cm^{-1}, +136 cm^{-1}, and +213 cm^{-1} is the good agreement between the band positions and the theoretically predicted fundamental vibrational frequencies for this conformer (see Table 3.4). On the basis of the above vibrational analysis, we tentatively conclude that the very weak band at +90 cm^{-1} also originates from conformer **2** of the 2-PE monomer. The other unassigned weak band at +75 cm^{-1} is very likely to stem from fragmentation of a water

Conformer	Gauche						Anti			
	Conformer 1		Conformer 2		Conformer 3		Conformer 4		Conformer 5	
	S_0	S_1	S_0	S_1	S_0	S_1	S_0	S_1	S_0	S_1
d (H15-C1), Å	3.78	3.89	2.54	2.78	3.41	3.53	-	-	-	-
α_1 (C1C2C7), deg	120.8	120.9	120.5	120.6	121.1	122.1	120.5	120.4	120.7	120.6
α_2 (C2C7C8), deg	112.7	114.7	110.8	113.8	113.3	116.8	111.2	113.3	111.0	113.1
α_3 (C7C8O9), deg	107.7	108.9	112.3	113.0	113.1	114.1	112.8	112.0	107.5	107.5
α_4 (C8O9H15), deg	106.9	109.5	105.6	109.0	105.9	109.2	106.1	109.3	106.7	109.4
τ_1 (C3C2C7C8), deg	10.4	105.1	90.0	90.6	109.9	140.8	89.4	90.3	88.5	89.3
τ_2 (C2C7C8O9), deg	69.3	70.6	60.5	64.8	67.4	71.6	176.7	177.3	0	0
τ_3 (C7C8O9H19), deg	-168.6	-170.7	-61.6	65.3	66.5	63.1	66.3	67.0	0	0
A, cm^{-1}	0.11622	0.11716	0.11023	0.11200	0.11707	0.12553	0.14449	0.14457	0.14570	0.14542
B, cm^{-1}	0.03577	0.03481	0.03677	0.03524	0.03526	0.03374	0.02831	0.02812	0.02840	0.02819
C, cm^{-1}	0.02975	0.02909	0.03176	0.03047	0.02921	0.02740	0.02533	0.02508	0.02541	0.02516
$\mu_a^2 : \mu_b^2 : \mu_c^2$	-	18:77:5	-	1:96:3	-	23:77:0	-	0:100:0	-	0:100:0
E_{rel}, cm^{-1}	652.78	-	0	-	703.59	-	649.69	-	769.00	-
E_{rel} (incl. ZPVE), cm^{-1}	685.86	-	0	-	783.30	-	586.00	-	788.35	-

Table 3.3: *Theoretical interatomic distances, d, planar angles, α, dihedral angles, τ, and rotational constants for the ground, S_0, and the first excited, S_1, electronic state of the gauche and anti conformers of the 2-PE monomer calculated at the MP2/cc-pVDZ and CIS/cc-pVDZ level of theory, respectively. The electric dipole transition moment (TM) ratio $\mu_a^2 : \mu_b^2 : \mu_c^2$ has been obtained from CIS/cc-pVDZ calculation of the optimised geometry of the 2-PE monomer. Relative energies, E_{rel} of the five most stable conformational structures of the 2-PE monomer without and with inclusion of the zero-point vibrational energy have been obtained from MP2/cc-pVDZ level of theory.*

Conformer **1**		Conformer **2**		Conformer **3**		Conformer **4**		Conformer **5**	
v, cm^{-1}	Mode	v, cm^{-1}	Mode	v, cm^{-1}	Mode	v, cm^{-1}	Mode	v, cm^{-1}	Mode
31	torsion	45	torsion	26	torsion	42	torsion	40	torsion
102	stretching	89	stretching	120	bending	88	bending	89	bending
129	torsion	135	torsion	148	torsion	99	torsion	96	torsion
226	bending	230	stretching	232	bending	230	bending	232	bending

Table 3.4: *Theoretical lowest vibrational frequencies for the first excited, S_1, electronic state of the gauche and anti conformations of the 2-PE monomer, calculated at the CIS/cc-pVDZ level of theory. The applied scale factor is 0.94.*

complex of 2-PE. The calculated inertial parameters of conformers **4** and **5** are very similar with exception of rotational constant A. This is not surprising noting that these two structures differ from each other only by the orientation of the terminal OH group of the side chain. Notwithstanding the similarity of the theoretically predicted rotational constants of the discussed conformers, the rotational fit of our high-resolution spectra unambiguously demonstrates that both vibrational bands at +48 and +58 cm^{-1} originate from structure 5. This assignment is in agreement with the finding of Mons et al. [16] based on UV-UV hole burning and infrared spectroscopy. The assignment of band +48 as originating from conformer **5** is corroborated also by dispersed fluorescence experiments. [73] Both close-lying bands with similar rotational structures, +48 and +58, may result from transitions from conformer **5** in the electronic ground, S_0, state to conformers **4**and **5** in the first excited, S_1, electronic state due to the torsional potential for the hydroxyl hydrogen in the electronically excited state favoring these transitions. [16] This is a plausible explanation since in the *anti* conformers **4** and **5**, the behavior of the OH group is almost negligibly perturbed by the rest of the molecule and, for this reason, its properties are expected to bear resemblance to the ones of the OH group in ethanol, and hence the OH potential energy model for ethanol [83] can be applied to the *anti* 2-phenylethanol as well. A like phenomenon has been observed also for p-tyrosol. [84]

All vibrational bands measured under high resolution have been successfully assigned to conformers **2** and **5**, respectively. No evidences for the existence of the other three conformers have been found. This puts forward the following issues: i) why only two out of five theoretically predicted conformational structures have been experimentally observed; ii) why the highest-energy conformer **5** is observed in the cold molecular beam rather than any of the low-lying structures. The explanation of the first question requires cognizance of the potential-energy surface and discussion of the relaxation dynamics during the process of the adiabatic expansion presuming that in the preexpansion region of the nozzle there exist several different conformational structures at room temperature that relax during the process of the adiabatic cooling. As seen from the shape of the potential energy surface depicted in Fig. 3.7, the *gauche* conformers are separated from the *anti* conformers by a high potential barrier, whereas the potential barriers between the

gauche and between the *anti* conformers, respectively, are very low. Therefore we may conclude that the high potential barrier precludes the interconversion between *gauche* and *anti* conformers on one hand, and on the other hand the low potential barriers between the *gauche* and *anti* conformers, respectively, favor the relaxational intraconversion within the two groups of species during the expansion. Thus, it is plausible to assume that under such circumstances the *gauche* conformers relax to the most stable *gauche* conformer, which is the most stable conformer as well, and the *anti* conformers relax to the lowest-energy *anti* conformer. It is not clear, however, why the experimentally observed *anti* conformer is conformer **5**, which is less stable by 202.35 cm^{-1} than conformer **4** as predicted at the MP2/cc-pVDZ level of theory. Experimental evidences for the existence of conformer **5** have been presented also by microwave spectroscopy. [70] To clarify this question, we performed additional *ab initio* quantum chemistry calculations with a very extended basis set for these two conformers. Augmenting the basis set, we have found that at the MP2/aug-cc-pVTZ level of theory with an improved electron correlation conformer **5** is energetically more stable than conformer **4** by 45 cm^{-1}. This fact combined with the presumed low potential barrier between the two conformers also at the MP2/aug-cc-pVTZ level of theory favors a fast and efficient relaxation of conformer **4** to conformer **5**, and hence, the experimental observation of the latter.

3.5.2   2-PE·H$_2$O Conformer

Comparing the rotational constants for the ground, S_0, and the first excited, S_1, electronic state and the transition moment ratio obtained from the fit of the highly resolved two-photon two-color spectrum measured at the parent (*m/z* = 140) channel of the singly hydrated complex of 2-PE with the respective theoretically predicted inertial parameters and transition moment ratios of the optimized structures of the complex, we have concluded that band 1w$_1$ originates from the 2-PE·H2O conformer **B** where water binds sideways to the most stable (conformer **2**) conformer of 2-PE through the formation of a strong single 3c3 hydrogen bond (bond length 1.9 Å) wherein water donates a proton to the oxygen atom of the side-chain hydroxyl group of 2-PE. The theoretically predicted distance between the O atom of the water moiety and the nearest hydrogen atom from the benzene ring is 2.44 Å, which is likely to suggest the existence of an additional weak σ hydrogen bond in which the water molecule is a proton acceptor. This assumption is somewhat justified by the well resolved structure of this band, which is typical for rigid or almost rigid complexes where the position of the attached species is fixed and the relative motions of the two moieties are strongly constrained. Since the two hydrogen bonds are almost perpendicular to each other, the existence of the above-mentioned additional weak σ hydrogen bond is supposed to hinder the tumbling motion of the water moiety about the strong σ hydrogen bond thus preventing complication of the rotational structure of the spectrum. The relatively small theoretically predicted energy gap of 94 cm^{-1} from the most stable conformer (conformer **A**) can

Conformer	Conformer **A** (Conformer **2**)		Conformer **B** (Conformer **2**)		Conformer **C** (Conformer **1**)		Conformer **D** (Conformer **1**)	
	S_0	S_1	S_0	S_1	S_0	S_1	S_0	S_1
d (H15-C1), Å	2.93	3.17	2.52	2.86	4.02	4.19	3.95	4.11
α_1 (C1C2C7), deg	120.4	120.5	120.2	120.4	120.4	120.7	120.6	120.7
α_2 (C2C7C8), deg	111.0	114.1	110.6	113.6	112.1	114.4	112.0	114.4
α_3 (C7C8O9), deg	112.1	112.9	112.1	112.9	107.9	104.2	107.4	108.8
α_4 (C8O9H15), deg	105.8	109.3	105.3	108.9	107.2	109.6	106.5	109.2
τ_1 (C3C2C7C8), deg	88.7	84.3	87.5	85.2	88.8	82.9	93.2	90.9
τ_2 (C2C7C8O9), deg	58.9	63.7	58.3	63.2	63.6	67.0	63.8	66.0
τ_1 (C7C8O9H19), deg	-88.2	-87.0	-57.7	-65.5	-177.8	-172.9	176.9	177.0
d (O9-H21) Å,	1.87	2.01	1.91	2.05	1.89	2.02	2.04	2.18
α_5 , deg	101.9	109.4	162.5	159.3	167.3	170.8	150.6	146.2
τ_4, deg	-0.6	-26.8	62.9	61.3	-160.2	174.3	67.0	59.1
A, cm^{-1}	0.06383	0.06038	0.06748	0.06438	0.06673	0.06198	0.06437	0.05907
B, cm^{-1}	0.03272	0.03118	0.02763	0.02660	0.02691	0.02666	0.03120	0.02992
C, cm^{-1}	0.02898	0.02717	0.02256	0.02125	0.02181	0.02077	0.02870	0.02653
$\mu_a^2 : \mu_b^2 : \mu_c^2$	-	24:1:75	-	71:29:0	-	85:10:5	-	14:2:84
E_{rel}, cm^{-1}	0	-	216	-	463	-	391	-
E_{rel} (BSSE), cm^{-1}	0	-	460	-	725	-	628	-
E_{rel} (BSSE + ZPVE), cm^{-1}	0	-	94	-	240	-	131	-

Table 3.5: *Theoretical interatomic distances, d, planar angles, α, dihedral angles, , and rotational constants for the ground, S_0, and the first excited, S_1, electronic state of the singly hydrated complexes of 2-PE calculated at the MP2/cc-pVDZ and CIS/cc-pVDZ level of theory, respectively. The electric dipole transition moment (TM), $\mu_a^2 : \mu_b^2 : \mu_c^2$, ratio has been obtained from CIS/cc-pVDZ calculation of the optimized geometry of the 2-PE·H_2O complex. The relative energies of the four most stable conformational structures of the singly hydrated complex of 2-PE without and with inclusion of the basis set superposition error (BSSE) correction and zero-point vibrational energy have been obtained from MP2/cc-pVDZ calculations. The parent conformations of 2-PE giving rise to the respective hydrated complexes are reported in parentheses in the header of the table. For details, see text.*

also be attributed to the assumed additional hydrogen bond. Comparing the geometrical parameters (interatomic distances, planar and dihedral angles) of the 2-PE molecule (conformer **2**) in bare state (see Table 3.3) and in the complex with water (see Table 3.5), one can infer that no appreciable structural changes or deformations of the 2-PE species take place upon complexation with water. This demonstrates that the backbone of the host *gauche* 2-PE conformer is stabilized by an *intramolecular* hydrogen bond between the terminal OH group and the π electrons of the benzene ring, which is stronger than the *intermolecular* hydrogen bonds responsible for the water attachment. A conspicuous difference, however, is observed between the transition moment ratios of 2-PE monomer (conformer **2**) and its singly hydrated complex (conformer **B**). Since in the latter the π electrons of the aromatic chromophore are not involved in the interaction with the water moiety it is very unlikely that there is an alteration of the transition moment vector relative to the benzene ring. We attribute the observed drastic change of the transition moment ratio as a pure mass effect descending from reorientation of the principal axes of inertia due the attachment of a water molecule. It is important to note that after excitation of band $1w_1$, the 2-PE·H_2O does not fragment under the water-in conditions of two-photon one-color experiments as no trace of a signal has been observed at the parent mass channel of the monomer ($m/z = 122$), this pointing to a stable complex.

An interesting issue is the search for the theoretically predicted most stable conformer of the 2-PE·H_2O complex (conformer **A**). Since conformer **A** is predicted to be the most stable one, this suggests that it must yield a high intensity band. This is, however, not the case for band $2w_1$, and we tentatively assign band $3w_1$ as originating from conformer **A**. The high intensity of this band is in line with the above discussion. The unresolved rotational structure of this band can be explained by a tumbling motion of the intercalated water moiety about the π *intermolecular* hydrogen bond. Unlike the case of conformer **B** where the two *intermolecular* bonds are almost perpendicular, in this case, the two *intermolecular* bonds, the OH$\cdots\pi$ and the H-O σ bonds lie almost on a straight line, and the rotation of the water molecule about the π hydrogen bond is not hindered, which leads to a broadening and smearing of the rotational structure of the spectrum. Our assignment is in line with the one of Hockridge et al., [64] and we also observe fragmentation of band $3w_1$ into the mass channel of the 2-PE monomer ($m/z = 122$). Hockridge et al. [64] have assigned band $2w_1$ to conformer **B**, and band $1w_1$ does not appear at the mass channel of the singly hydrated complex of 2-PE ($m/z =122$). We have performed a one-color experiment monitoring the mass channel of the doubly hydrated complex of 2-PE but we did not observe any peaks. It is very unlikely that on one hand the abundance of doubly hydrated complexes of 2-PE in the molecular beam be high, and on the other hand they fragment completely to singly hydrated complexes so as to yield an intensity commensurate to the intensity of the most stable conformer **A** (band $3w_1$).

3.6   Summary and Conclusions

2-PE, the hydroxy analog of the simplest aromatic neurotransmitter, 2-phenylethylamine, and its singly hydrated complex have been investigated by combination of mass selective high-resolution two-color R2PI spectroscopy combined with quantum chemistry *ab initio* calculations. All prominent blueshifted vibronic bands of the 2-PE monomer up to 220 cm^{-1} have been measured under high-resolution of 70 MHz. On the basis of comparison of the inertial parameters obtained from the analysis of the highly resolved spectra and those resulting from the structural optimizations of the lowest-energy conformations of 2-PE, we were able to assign all 5 bands as resulting from two conformers, the lowest-energy *gauche* conformer and the second-in-energy *anti* conformer of 2-PE. This structural assignment is corroborated by the fair agreement between the theoretically predicted vibrational frequencies for the *gauche* and *anti* conformers and the vibrational band positions. The observation of only two out of 5 theoretically predicted conformations under the conditions of molecular jet expansion in conjunction with a detailed theoretical study of the potential energy surface of 2-PE has put forward the issue of conformational interconversion. Our calculations demonstrate that different members in the *gauche* manifold and in the *anti* manifold are separated from one another by only low potential barriers, while the *gauche* conformers are separated from the *anti* conformers by a significant potential barrier. On this basis we conclude that in the process of adiabatic jet expansion all *gauche* conformers relax to the most stable *gauche* conformers, which is also the lowest-energy conformers of 2-PE, and the *anti* conformers relax to the most stable *anti* conformer. The high potential energy barrier between them, however, precludes the *anti* conformers from a further relaxation to the most stable *gauche* geometry of conformer **2**. This corollary implies that energy considerations alone are not sufficient for an adequate explanation of the observed structures. It is important also the relaxational kinetics in the expansion process to be considered.

It is known that the properties of many biologically relevant molecules depend substantially on their environment. To elucidate this issue, as a first step, we investigated the complexation of 2-PE with a single water molecule. Comparing the results from the high-resolution experiment with those from *ab initio* calculations, we have found that the most stable conformers of the singly hydrated complex of 2-PE belong to the most stable structure of the monomer. The relatively scarce vibronic spectrum of the 2-PE·H$_2$O complex (only three bands) implies that the many different conformations of the singly hydrated complex of 2-PE which are theoretically supposed to exist in the preexpansion region either dissociate or relax to two stable conformation presumably separated by a high potential barrier which precludes the interconversion of the higher-lying conformer to the most stable one. We did not observe significant structural changes of the 2-PE monomer upon its complexation with a single water molecule within our experimental resolution, which is an indication that in the case of the *gauche* conformer of 2-PE the *intramolecular* hydrogen bond still dominates over the *intermolecular* hydrogen bonds responsible for the water

attachment. From this we can conclude that a more complete solvation shell is necessary to bring about structural changes of the host molecule, and a systematic investigation of the influence of increasing number of solvent molecules on the structure of flexible biologically relevant species is intended.

Chapter 4

Fluorine Substitution and Nonconventional OH···π Intramolecular Bond: High-Resolution UV Spectroscopy and *ab initio* Calculations of 2-(*p*-fluorophenyl)ethanol

The para-fluorinated flexible neurotransmitter analog 2-phenylethanol has been investigated by highly resolved resonance-enhanced two-photon ionization two-color UV laser spectroscopy with mass resolution and ab initio structural optimizations and energy calculations. Two stable conformations, gauche and anti, separated by a high potential barrier have been identified in the cold molecular beam by rotational analysis of the vibronic band structures. The theoretically predicted higher-lying conformations most likely relax to these two structures during the adiabatic expansion. The lowest-energy gauche conformer is stabilized by an intramolecular nonconventional OH···π-type hydrogen bond between the terminal OH group of the side chain and the π electrons of the phenyl ring. The good agreement between the experimental and theoretical results demonstrates that even the substitution with a strongly electronegative atom of 2-phenylethanol at the para position has no noticeable effect on the strength and orientation of the OH···π bond.

4.1   Introduction

Molecular shape and charge distribution play an important role in the selectivity and functionality of biologically relevant molecules (for review, see ref. [3] and ref. 4423). It has been found that the conformational structures of flexible molecules are stabilized by a subtle balance between various nonconventional weak interactions involving neighboring functional groups and localized charges. [3, 60, 85–89] OH· · ·π bonds constitute a particular class of noncovalent weak hydrogen bonds. The importance of OH· · ·π bonds has been demonstrated in a large number of publications on model systems over recent years. [46, 59–63, 65, 73, 90] An interesting issue is how molecular substituents influence the strength of OH· · ·π bonds and hence the shape and stability of the respective molecular conformations. Fluorine substitution brings about a significant rearrangement of the electron density of the host molecule and, for this reason, fluorine substituted molecules can be used as convenient model systems to investigate the effect of electronegative groups and atoms on the conformational preferences of the studied species. To shed light on the delicate interplay between a substituted electronegative atom and a nonconventional OH· · ·π bond and the resulting conformational structure, we have investigated 2-(*p*-fluorophenyl)ethanol (2-*p*FPE) (Scheme 1), which is the para-fluoro derivative of the extensively studied [16, 46, 61, 63, 70, 72, 73, 84] neurotransmitter analog molecule 2-phenylethanol (2-PE). (see also previous Chapter)

Figure 4.1: *Atom labels of 2-pFPE*
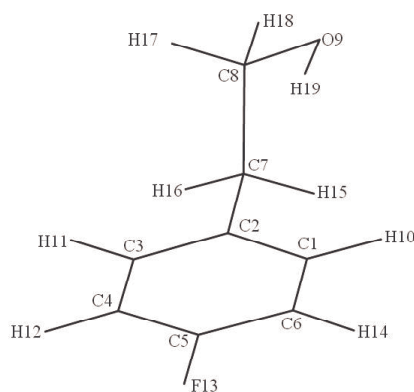
The molecule's skeleton is composed of a flexible side chain with a hydroxyl group at the end and an aromatic ring with a para-fluoro substitution. The parent molecule, 2-phenylethanol, has attracted a great interest in the recent years due to its conformational preferences in the gas phase and the presence of a nonclassical π-hydrogen intramolecular bond. Therefore it is important

to identify the most stable molecular geometries and, in particular, to understand the effect of electronegative substituents on the geometrical structure of the flexible molecule. The first experimental results from dispersed emission spectroscopy and theoretical data on 2-*p*FPE have been published recently by Chakraborty and co-workers. [91] In this work we present what is, to the best of our knowledge, the first investigation by high-resolution UV spectroscopy on the effect of the electron-attracting fluorine substitution on the stability of the most favorable conformers of this flexible molecule. In chapter 3, we have shown that the nonfluorinated most stable *gauche* geometry of 2-phenylethanol is stabilized by a π-hydrogen bonding of the alcoholic hydrogen of the side chain with the phenyl ring but the higher-energy *anti* structure is also present under molecular-beam conditions. [90] Here, we used the high-resolution mass-selective spectroscopy to determine unambiguously and directly the origin of most of the rovibronic bands in the $S_1 \longleftarrow S_0$ spectrum of 2-*p*FPE.

4.2 Experiment and Data Processing

The set up used for mass-selected resonant two-photon ionization (R2PI) in the present work has been described in detail in Sec. 2.2. Liquid 2-*p*FPE (97%) obtained from Aldrich was used without further purification, and vaporized at 100 °C in a gas stream of argon at a pressure of about 3.5 bars. The gas mixture was expanded in a free-jet expansion into vacuum through a pulsed-operated heatable nozzle with orifice diameter of 300 μm. To reduce the Doppler broadening the jet was skimmed before entering the interaction region with the counterpropagating laser beams that were perpendicularly focused onto the molecular beam 130 mm downstream of the nozzle. The low-resolution spectra of 2-*p*FPE as well as its high-resolution spectrum were measured by R2PI with mass selectivity in a supersonic molecular beam. The spectral resolution of about 70 MHz of the narrowband UV laser pulses is not sufficient for single rotational line resolution in the congested spectra of a molecule of this size. For this reason, we used a computer-based method for fitting of the rotational structure of the experimental highly resolved spectra. The method is based on genetic algorithms, which has proven to be a decisive tool in the determination of the molecular parameters(see Sec. 2.3). Cross correlation is employed as a figure of merit for match between the simulated and the experimental spectra. For the production of the synthetic spectra of the 2-*p*FPE monomer, we ran the program using 300 generations with 500 individuals in a generation. [20, 46]

4.3   Experimental Results

4.3.1   Low Resolution Spectrum

The vibronic structure of the $S_1 \longleftarrow S_0$ spectrum of 2-pFPE was investigated by low-resolution mass-selected one-colour R2PI. The resulting spectrum is depicted in Fig. 4.2. It was measured by monitoring the monomer parent mass (140 u) and the mass of the most prominent fragment (109 u) appearing in the R2PI mass spectrum. There is a dominating 0_0^0 band and several blueshifted vibronic bands, the strongest ones being at +42, +80 and +120 cm^{-1}. On the red side of the strongest band, there are only two weak bands, which are probably due to hot bands, fragmenting dimers of 2-pFPE, or complexes of 2-pFPE and Ar.
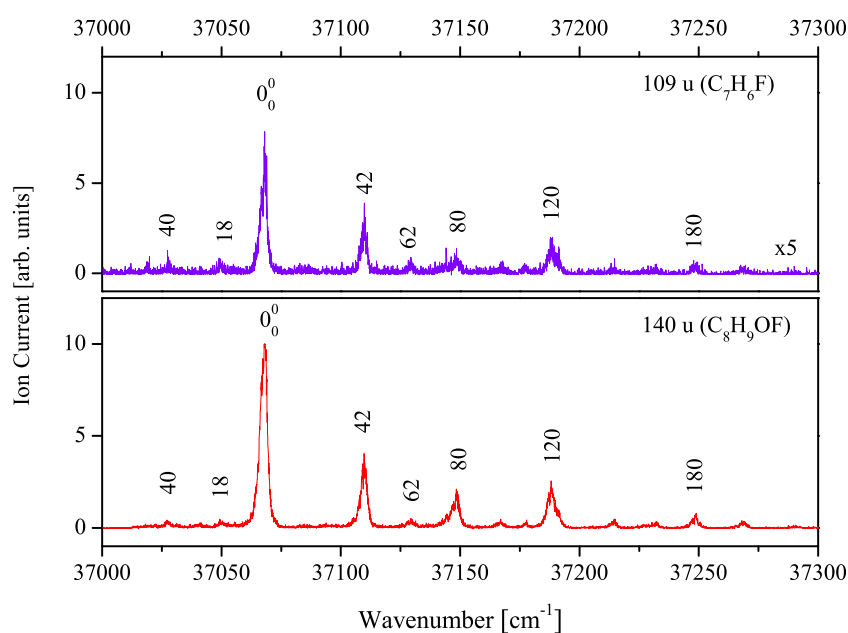
Figure 4.2: *One-color R2PI spectra of the $S_1 \leftarrow S_0$ electronic transition of the 2-pFPE monomer measured at the monomer C_8H_9OF (m/z = 140) mass channel (a) and the fragment mass channel C_7H_6F recorded at m/z = 109 mass channel (b).*

We identify the fragment at 109 u as originating from the detachment of CH_2OH from the side chain of the molecular cation. Most likely this occurs after the absorption of a further photon in the 2-pFPE cation. This results in the formation of the charged fragment $(C_7H6F)^+$ with an unchanged localization of the charge. This is different from the situation, *e.g.* in ephedrine, where

a charge transfer occurs before fragmentation of the cation because of the presence of a nitrogen atom with a lone electron pair in the side chain. [68] An analysis of all vibronic bands in the low-resolution one-color R2PI spectra shows a slightly different fragmentation ratio for the band at +80 cm^{-1} observed at the monomer and the fragment mass channels. A possible explanation for this will be given by rotational-band structure analysis of this band in the next section. To estimate an upper limit of the ionization energy (IE), we performed two-color R2PI experiments fixing the excitation photon to the 0_0^0 band in the $S_1 \longleftarrow S_0$ spectrum and decreasing the energy of the second photon stepwise to the lowest possible limit (35 026 cm^{-1}) so that the parent ion signal still could be observed. Thus we obtained an upper limit for the IE of 72 100 cm^{-1}, which is somewhat higher than the one for 2-phenylethanol [71] of 71 500 cm^{-1}. No fragmentation was observed in the case of the 2-phenylethanol cation. [46] Most likely this is due to a less efficient photon absorption in the cation after ladder switching of the multiphoton absorption from the neutral molecule to the cation. [92] To reveal possible conformations of 2-pFPE, we performed high-resolution experiments for resolution of the rotational band structure together with *ab initio* calculations employing extended basis sets.

4.3.2   High Resolution Spectra

The high-resolution UV spectrum of the strongest monomer band 0_0^0 and the spectra of the next two pronounced blueshifted vibronic features (+42 and +80 cm^{-1}) are presented in Fig. 4.3- 4.5 (upper traces). All spectra were recorded at the monomer mass channel 140 u. The 0_0^0 and the +42 cm^{-1} bands (Fig. 4.3 and 4.4) have a similar appearance of their rotational structure thus indicating that they originate from the same conformer. They will be discussed first.
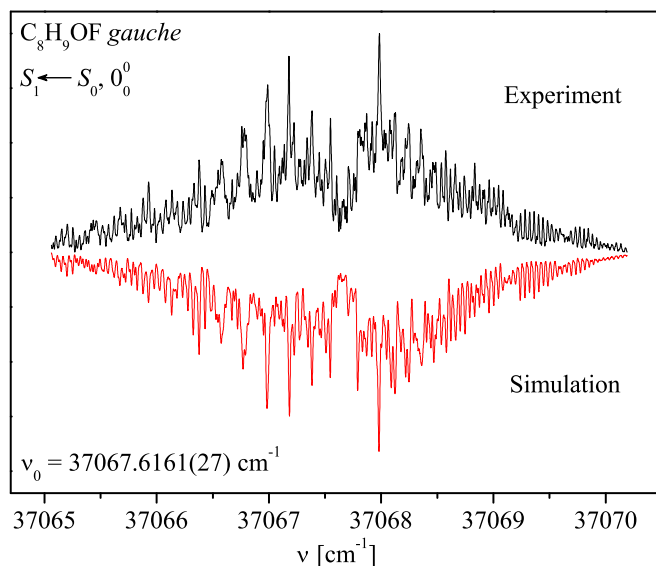
Figure 4.3: *High-resolution two-color UV R2PI spectrum of the 0^0_0 band recorded at m/z = 140. The band is assigned as the origin of the gauche conformer **1** (see Fig. 4.6) of the 2-pFPE monomer with its rotationless transition centered at 37 067.6161(27) cm^{-1}. Upper trace: experimental spectrum. Lower inverted trace: best-fit simulated spectrum yielding the parameters in Table 4.1 (for details, see text).*

The rotational constants and the transition-moment ratios were determined with the computer-assisted routine described above and in more detail in Section 2.3 To facilitate the fitting procedure and to shorten both search time and space, we used as starting values the ones received from low-level (MP2 6-311++G**) *ab initio* calculations. The resulting bestfit simulated spectra are also shown in Fig. 4.3 and 4.4 (lower inverted trace). The best agreement was obtained by convoluting the theoretical stick spectra with a Gaussian linewidth of 210 MHz FWHM. The simulated spectra agree very well both in peak positions and in intensities with the experimental ones, with an achieved cross correlation of 97.5% for the 0^0_0 vibronic band and 95.5% for the +42 cm^{-1} vibronic band. The experimentally found values for the rotational constants, the transition-moment ratios and the rotational temperatures are summarized in Table 4.1. The fits demonstrate that both experimental rotational spectra consist of prominent P and R branches in the wings and a minor contribution from the Q branch in the center. The two spectra are assigned as $a-, b-$,and c-type hybrids with a significant b-type contribution. They do not exhibit single rotational lines but regularly spaced peaks with a FWHM of approximately 250 MHz formed by aggregation of several rotational lines. A comparison of the experimental values for the rotational constants with the results from the *ab initio* computations determines the two observed
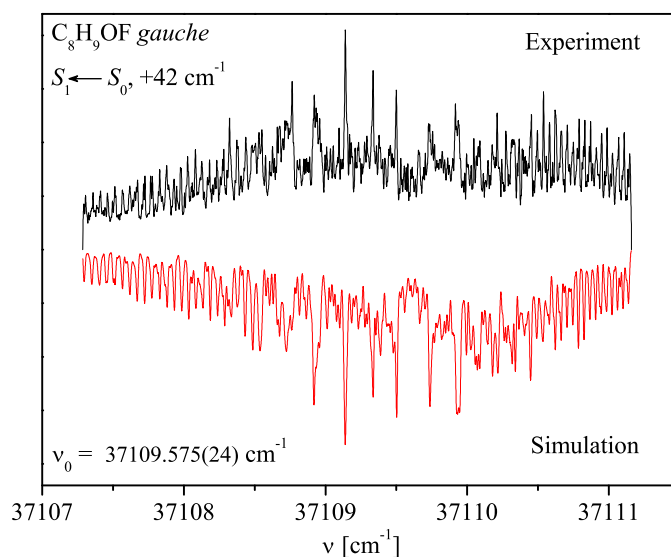
Figure 4.4: *High-resolution two-color UV R2PI spectrum of vibronic band at +42 cm^{-1} recorded at m/z=140. The band is assigned to the lowest-frequency fundamental torsional mode of the gauche conformer **1** with its rotationless transition at 37 109.575(24) cm^{-1}. Upper trace: experimental spectrum. Lower inverted trace: the best-fit simulated spectrum yielding the parameters in Table 4.1 (for details, see text).*

Parameter	Band		
	0_0^0 cm^{-1}	+42 cm^{-1}	+80 cm^{-1}
A''	0.10571(74)	0.1059(23)	0.14984(45)
B''	0.02409(36)	0.02414(38)	0.01986(41)
C''	0.02218(36)	0.02186(56)	0.01809(37)
A'	0.10165(77)	0.1020(18)	0.14215(38)
B'	0.02409(39)	0.02400(19)	0.01939(43)
C'	0.02188(31)	0.02147(36)	0.01853(40)
$\mu_a^2 : \mu_b^2 : \mu_c^2$	28:56:16	11:58:31	9:71:20
ν_0 , cm^{-1}	37067.6161(27)	37109.575(25)	37147.621(4)
T(K)	8.5(5)	8.9(1)	24(4)
Best-fit cross correlation (%)	97.5	95.4	92

Table 4.1: *Experimental rotational constants for the ground,S$_0$ (A$''$, B$''$, C$''$), and for the first excited,S$_1$ (A$'$, B$'$, C$'$), electronic states, the transition moment ratio, $\mu_a^2 : \mu_b^2 : \mu_c^2$, the band origin frequency, ν_0, the rotational temperature, T, and the best-fit cross correlation obtained from the rotational fit of bands 0_0^0, +42 and +80 cm^{-1}, shown in Figures 4.3- 4.5. The numbers in parentheses represent one standard deviation in units of the least significant quoted digit. The uncertainty for the relative values of μ_a^2, μ_b^2, and μ_c^2 in the transition moment ratio does not exceed 5(%).*
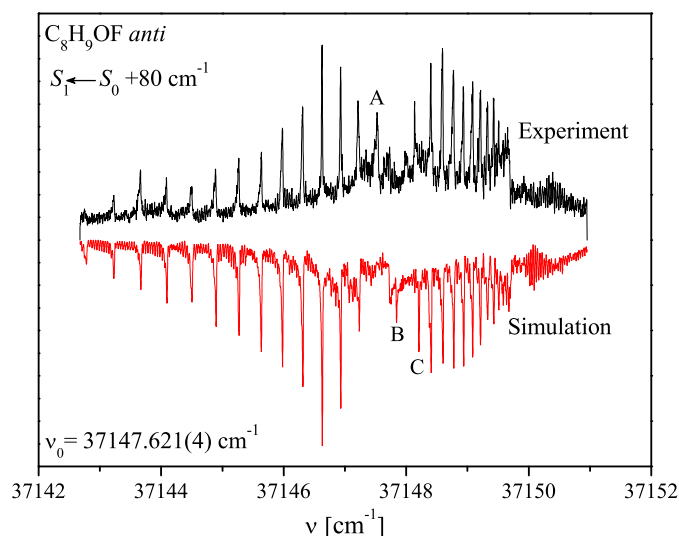
Figure 4.5: *High-resolution two-color UV R2PI spectrum of the +80 cm^{-1} band recorded at m/z = 140. The band is assigned as the origin of the anti conformer **4** (see Fig. 5) of the 2-pFPE monomer with its rotationless transition centered at 37 147.621(4) cm^{-1}. Upper trace: experimental spectrum. Lower inverted trace: best-fit simulated spectrum yielding the parameters in Table 4.1 (for details, see text).*

vibronic features as belonging to the most stable *gauche* conformer. The only observed difference between the experimental and theoretical results originates from the exchanged values of the *a*- and *c*-contributions in the transition-moment ratios of the bands (see Table 4.1). The structure of the highly resolved spectrum of the band at +80 cm^{-1} is completely different from that of the other discussed bands. The spectrum features nicely structured P- and R-branches with regularly spaced sharp peaks. From its appearance, the spectrum can be assigned as predominantly b-type with small contributions also from both a- and c-types. A peculiar trait of the spectrum is the converging series of peaks in the right side terminating with an abrupt cut-off at 37 149.7 cm^{-1}. To obtain the rotational constants for the ground, S_0, and the first excited, S_1, electronic states, the transition-moment ratio and the rotational temperature, we employed the above-mentioned computer-aided fit routine. Because of its different appearance, presumably the molecular parameters giving rise to this spectrum have to be different from the ones of the other bands. Therefore as initial values for the rotational constants, we employed the theoretically predicted values corresponding to the *anti* conformers, which do not differ much from each other as can be seen from Table 4.2. The resulting best-fit simulation is shown in Fig. 4.5 (lower inverted trace) and the molecular parameters bringing forth this fit are summarized in Table 4.1. The fit was able to reproduce excellently both the peak positions and peak intensities in the P- and R-branches and, in particular, the converging behavior and the fall off of the right side of the spectrum. Some discrepancies between the experimental and the simulated spectra are observed, however, in the central part. This is an indication that some phenomena not accounted for by the theoretical model of a rigid asymmetric- top Hamiltonian employed for the simulation of the
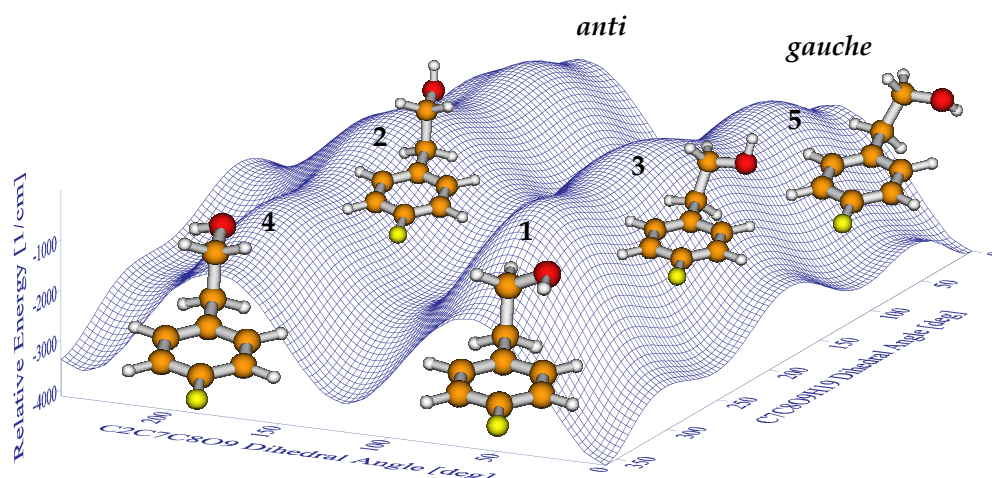
Figure 4.6: *Potential-energy surface (inverted for the sake of a better visualization) as a function of the C2C7C8O9 and C7C8O9H19 dihedral angles of the 2-pFPE monomer. The gauche and anti conformations are separated by a high potential barrier in the C7C8 coordinate. The five energetically most favorable conformations of the 2-pFPE monomer have been fully geometrically optimized in their ground, S_0, electronic state at the MP2/ccpVDZ level of theory. The fully optimized structures are depicted on their corresponding minima (maxima in the Figure) on the potential-energy surface.*

spectrum are involved, which lead to spectral shifts or broadening of the peaks. A more involved comment on this issue is presented in the discussion section.

4.3.3 *Ab initio* Calculations

Ab initio quantum-chemistry calculations using the Gaussian 03 programs package [82] have been performed to study theoretically the conformational structure, vibrational modes, and energetics of the 2-pFPE monomer. To identify the stable conformations of the 2-pFPE monomer, we performed a grid search exploring the energy corresponding to the various shapes of the side chain of 2-pFPE. The grid search was carried out at the MP2/cc-pVDZ level of theory, and included a scan of the C2C7C8O9 and C7C8O9H19 dihedral angles. The C3C2C7C8 dihedral angle was kept fixed at 90°. The three-dimensional potential-energy surface (PES) is depicted in Fig. 4.6 (for the sake of a better visualization, the PES is inverted). It features six potential minima pointing to six stable conformations of the 2-pFPE monomer corresponding to three *gauche* and three *anti* structures. The deepest (global) minimum belongs to the *gauche* conformer (conformer **1**), in which the terminal OH group of the side chain faces the π electrons of the benzene ring. The two energy minima separated from each other and from the global minimum by low

potential barriers correspond also to *gauche* structures but with a different orientation (different dihedral angle C7C8C9H19) of the OH group of the side chain. These conformations are designated as conformer **3** and conformer **5**, respectively. In all *anti* geometries, the side chain is extended away from the benzene ring (dihedral angle C2C7C8O9 = 180°), the difference between them being only the orientation of the OH group (dihedral angle C7C8C9H19). Two of the *anti* structures, however, with dihedral angles C7C8C9H19=63.91°and C7C8C9H19=-63.91°respectively, are completely symmetrical with respect to the C2C7C8O9 symmetry plane and give rise to two equivalent potential energy minima. That is why hereinafter only one of these structures, the conformer with dihedral angle C7C8O9H19 = -63.91°, will be considered. It is referred to as conformer **4**.The other differing *anti* structure is conformer **2** with a fully extended side chain in which the dihedral angle C7C8O9H19 = 180°. It is interesting to point out that the *anti* conformations are separated by low potential barriers from each other and by a high barrier along the C2C7C8O9 coordinate from the *gauche* structures. The so-identified five conformations have been further subjected to a full structural optimisation, frequency analysis and calculation of their energetics in the ground, S_0, electronic state at the MP2 level of theory employing the cc-pVDZ basis set. Full structural optimisation and frequency analysis have also been performed for the first excited, S_1, electronic state at the CIS/cc-pVDZ level of theory. The values of the typical interatomic distances, planar and dihedral angles defining the conformational shape, the rotational constants, the transition-moment ratio and the energies with and without inclusion of the zero-point vibrational energy (ZPVE) of the 5 stable conformations calculated using the cc-pVDZ basis set are summarized in Table 4.2. In the calculation of the zero-point vibrational energies, pertinent scale factors have been used. [93, 94] All calculated vibrational frequencies are positive, this being evidence that the optimized structures indeed correspond to potential minima. The fully optimized conformational structures are depicted in Fig. 4.6 atop their corresponding point on the potential-energy surface.

4.4   Discussion

The most stable calculated geometry of the conformers, without and with the inclusion of the ZPVE, corresponds to the *gauche* conformer **1** with its terminal OH group of the side chain pointing to the π electrons of the benzene ring. This structure is assumed to be stabilized by an intramolecular OH$\cdots\pi$ hydrogen bond, as is also the case in the 2-phenylethanol monomer. [16, 46, 70] The next-in-energy structure lies 446 cm^{-1} above (see Table 4.2) the most stable geometry and belongs also to a *gauche* conformer **3**, which differs from conformer **1** only by the orientation of the OH group, in this case pointing upwards. The third-in-stability conformation corresponds to the *anti* structure with its terminal OH group pointing sideways (conformer **4**) which is distanced by 556cm^{-1} from the lowest-energy conformation, and by 110 cm^{-1} from

Parameter	Conformer **1** gauche		Conformer **2** anti		Conformer **3** gauche		Conformer **4** anti		Conformer **5** gauche	
	S_0	S_1	S_0	S_1	S_0	S_1	S_0	S_1	S_0	S_1
r (H19Cl), Å	2.55	2.76	-	-	3.77	3.87	-	-	3.45	3.45
r (C5F13), Å	1.35	1.32	1.35	1.32	1.35	1.32	1.35	1.32	1.35	1.35
α_1 (C1C2C7), deg	120.6	120.0	120.9	120.0	120.9	120.3	120.7	119.8	121.4	121.4
α_2 (C2C7C8), deg	111.0	113.7	111.1	113.0	112.8	114.6	111.4	113.2	114.1	114.1
α_3 (C7C8O9), deg	112.3	113.1	107.5	107.3	107.6	109.0	112.8	111.7	113.2	113.2
α_4 (C8O9H19), deg	105.7	109.2	106.8	109.4	107.0	109.6	106.2	109.4	105.9	105.9
τ_1 (C3C2C7C8), deg	90.8	92.5	88.5	89.1	106.7	107.0	89.3	90.6	119.3	119.3
τ_2 (C2C7C8O9), deg	60.4	66.3	-180.0	-180.0	69.0	72.1	176.6	177.2	69.4	69.4
τ_3 (H19O9C8C7), deg	-63.3	-66.7	-179.9	-180.0	-169.4	-170.8	-63.9	-68.4	66.1	66.1
A, cm_{-1}	0.10414	0.10510	0.14011	0.13817	0.10873	0.10938	0.13867	0.13715	0.11107	0.11539
B, cm_{-1}	0.02429	0.02383	0.01951	0.01971	0.02377	0.02356	0.01947	0.01968	0.02330	0.02302
C, cm_{-1}	0.02198	0.02146	0.01814	0.01825	0.02080	0.02061	0.01810	0.01822	0.02012	0.01960
$\mu_a^2 : \mu_b^2 : \mu_c^2$	-	1 : 94 : 5	-	0 : 100 : 0	-	4 : 91 : 5	-	0 : 100 : 0	-	11 : 89 : 0
E_{rel}, cm_{-1}	0	-	712.2	-	517.2	-	614.8	-	594.2	-
E_{rel} (incl. ZPVE), cm_{-1}	0	-	617.4	-	446.2	-	556.0	-	572.0	-

Table 4.2: *Theoretical interatomic distances, d, planar angles, α, dihedral angles, τ, and rotational constants for the ground, S_0, and the first excited, S_1, electronic state of the gauche and anti conformers of the 2-pFPE monomer calculated at the MP2/cc-pVDZ and CIS/cc-pVDZ level of theory, respectively. The electric dipole transition moment (TM) ratio $\mu_a^2 : \mu_b^2 : \mu_c^2$ has been obtained from CIS/cc-pVDZ calculation of the optimized geometry of the 2-pFPE monomer. Relative energies, E_{rel} of the five most stable conformational structures of the 2-pFPE monomer without and with inclusion of the zero-point vibrational energy have been obtained from MP2/cc-pVDZ level of theory.*

the preceding structure. Conformer **4** is followed by the *gauche* conformer **5**, the energy gap between them, however, being very small at only 16 cm^{-1}. Because of the very small energy difference, it is very likely that the latter energy ordering may alter upon changing the employed model theory and basis set. The highest-energy conformation at +617 cm^{-1} is the *anti* conformer **2** with a completely extended side chain away from the benzene ring. We assign the strongest peak to the 0_0^0 origin band of the most stable *gauche* conformer **1**. The same conformer gives rise also to band +42 cm^{-1}. The assignment has been made on the basis of the very good agreement of the theoretically predicted rotational constants for this conformer (see Table 4.2) with the ones obtained from the fit of the highly resolved spectra both for the ground, S_0, and the first excited, S_1, electronic states (see Table 4.1). The vibrational analysis performed for the first excited electronic state, S_1, of conformer **1** shows that the lowest-frequency vibrational mode is at 47 cm^{-1} and corresponds to a torsion of the side chain about the C2C7 bond. This result is in a good accord with the position of the band at +42 cm^{-1} which provides a confident argument to assign this band to the fundamental torsional mode of conformer **1**. Some discrepancy between theory and experiment, however, is observed in the transition-moment ratio for both bands. This might be due to the limited accuracy of the excited state calculation at the CIS/cc-pVDZ level of theory. The rotational structure of the band at +80 cm^{-1} differs significantly from the structure of the strongest band (0_0^0) and the band at +42 cm^{-1}. Comparing the rotational constants for the ground and the first excited electronic states obtained from the fit of the spectrum with the ones theoretically predicted, we have convincingly established that this band descends from an *anti* conformer. This implication is in accord with the results from the dispersed fluorescence experiments of Panja *et al.*, [91] demonstrating that this band does not originate from the conformer bringing forth the main band and the band at +42 cm^{-1}. It is worth pointing out, however, that the theoretically predicted values of the rotational constants for the *anti* conformers **2** and **4** are very close, which is not surprising in view of the very similar structures of the two conformers differing only by the orientation of the terminal OH group, which presumably does not significantly affect the principal moments of inertia and hence the rotational constants of the two conformers. The experimental value of constant A differs somewhat from the calculated values for this constant for both *anti* conformers, **2** and **4**. Constraining the rotational fit in the vicinity of the theoretically predicted value of constant A did not yield acceptable results. Good fits were produced only after lifting the constraints on constant A whereupon its values drifted away from the theoretically predicted ones. Comparing the rotational constants for band +80 cm^{-1} alone in this case allows for the assignment of the band to an *anti* structure, but precludes a decisive assignment of band +80 cm^{-1} to one of the two *anti* conformers **2** or **4**. Energy consideration provides a tentative favour for conformer **4** as it is theoretically predicted to be more stable by 45 cm^{-1} compared to conformer **2**. These results, however, should not be regarded as a rigorous argument since the energy gap is very small and, as we have demonstrated for the 2-PE monomer [46] (see previous Chapter) the energy ordering may change upon changing the level of theory. It has been noted above that despite the excellent agreement between the experimental

and the simulated spectra in Fig. 4.5 in both peak positions and peak intensities in the wings (P- and R-branches), the central part of the spectrum could not be fitted satisfactorily: two of the peaks in the simulated spectrum (peaks B and C in Fig. 4.5) are shifted while another one (peak A in the experimental spectrum in Fig. 4.5) is very broadened and spread out. Due to the increased background in this region, it is very likely that some spectral contamination is present that may derive from fragmentation of hydrated complexes. This is a plausible assumption in view of the observed at this position band of the singly hydrated complex of 2-pFPE measured at its mass channel under low-resolution conditions. [95] The observed spectral shift of peak C by 0.07 cm^{-1} from the theoretical position is an indication that a localized perturbation is present in the central part of the spectrum. We performed an analysis of the rotational structure of the central region of the highly resolved spectrum of band +80 cm^{-1}. Using the parameters producing the fit shown in Fig. 4.5, we generated a stick spectrum using the PGOPHER program package [96] and in the so-produced spectrum, we made a Fortrat analysis and an assignment of the rotational transitions associated with the sharp peak C appearing to the right of the central dip just before the onset of the R-branch. All rotational lines under the envelope of this peak turned out to originate from transitions to small J' ($J' < 10$)-value rotational levels with identical value of K_a' ($K_a' = 3$) in the excited electronic state. This finding points to a coupling of rotational levels with small quantum number J and with the same value of $K_a' = 3$ as other, dark, levels, [97] while the other rotational levels with higher values of J and different values of K_a (giving rise to the majority of the spectral lines) remain unaffected, which leads to a good fit in the wings. Since this band is assigned to the vibrationless 0_0^0 band of the *anti* conformer, the question arises as to what the identity of the coupled states is. The terminal OH group in both *anti* conformers, **2** and **4**, does not form hydrogen bonds (as is the case for the most stable *gauche* conformer **1**) and, for this reason, the two conformations are separated by a small potential barrier (estimated from the PES depicted in Fig. 4.6 to be *ca.* 570 cm^{-1}) thus favoring the internal rotation of the OH group about the C8O9 bond. In this case, it is very likely that a coupling between the internal rotation of the OH group and the overall rotation of the molecule occurs for certain rotational energy levels which are in resonance with each other. This coupling may lead to shifting and pushing apart the individual rotational lines, the latter leading to a slight broadening of the observed peaks. Another plausible type of coupling leading to similar spectral shifts of only 0.07 cm^{-1} and broadening may descend also from the interaction between the above-discussed rotational energy levels of the *anti* conformer with higher rovibronic levels of the lowest-energy *gauche* conformer **1**. Though in this case the expected coupling is weak, this does not contradict the observed spectral shift of only 0.07 cm^{-1} of the resulting eigenstates. An interesting issue that merits discussion is why only two conformers have been observed out of 5 theoretically predicted stable structures which differ little in energy. The answer to this question can be found in the shape of the potential-energy surface and the resulting relaxation dynamics of the cooling process. The PES in Fig. 4.6 shows that the *gauche* conformations are separated from each other by only small potential energy barriers of less than 600 cm^{-1}. The same is true also for

the *anti* conformers. On the other hand, however, the *gauche* conformers are separated from the *anti* conformers by a high potential barrier of *ca.* 2000 cm^{-1}. Even if in the pre-expansion region all conformers are populated, upon adiabatic expansion the higher lying conformers relax to the lowest-energy ones within the *gauche* and the *anti* manifolds, respectively, because of the low potential barriers between the *gauche* and the *anti* species, respectively. Thus the higher-energy *gauche* conformers relax to the most stable *gauche* conformer **1**, the process of relaxation being favored by the low potential barriers between the *gauche* species. An identical mechanism can explain the relaxation of the *anti* conformers to the most stable *anti* structure. The interconversion between the *anti* and the *gauche* structures, however, is hindered by the high barrier along the C7C8 coordinate (see Fig. 4.6). This precludes a further relaxation of the lowest-energy *anti* conformer to the most stable *gauche* conformer **1** prior to photoexcitation and thus the former remains trapped in its local minimum at the low temperature of the molecular beam and we observe only two conformers: one *gauche* and one *anti*. On the other hand, the observed local perturbation of band +80 cm^{-1}, which corresponds to an *anti* conformation, demonstrates that after photoexcitation, an isomerization process may occur. At the low excess energy of the 0_0^0 band, however, the observed local perturbation of this band leading to a small shift (less than 0.1 cm^{-1}) of special rotational lines would result in a slow isomerization occurring in the range of 1 ns in the statistical limit. At higher excess energies, faster isomerization can be expected. If this occurs before the absorption of the ionization photon, this may lead to a different isomerization pathway and to a selective different fragmentation, similar to the one of our recent observations in ephedrine. [68] Furthermore, it is surprising to observe that the rotational temperature of the *anti* conformer (band +80 cm^{-1}) resulting from the fit is twice as high as that of the *gauche* conformer (the main band and the band at +42 cm^{-1}) (see Table 4.1). An interesting aspect that deserves special attention is the comparison between 2-phenylethanol (2-PE) [16, 46, 61, 70](see previous Chapter) and 2-*p*FPE. In both species the most stable conformer is the *gauche* one whose conformational structure is stabilized by an intramolecular nonconventional OH$\cdots\pi$ bond between the terminal OH group and the benzene ring. The potential-energy surface is very similar for both species, though their ordering according to the energy is different: in 2-PE the ordering is *gauche*, *anti*, *gauche*, *gauche*, *anti*, whereas for 2-*p*FPE the ordering is *gauche*, *gauche*, *anti*, *anti*, *gauche*. The energy gap between the most stable *gauche* structure and the next-in-energy one is also slightly different though of the same order of magnitude: 586 cm^{-1} for 2-PE *vs.* 446 cm^{-1} for 2-*p*FPE. The different ordering of the conformations may be a result of the redistribution of the π electron density of the benzene ring caused by the fluorine atom. The covalently bound fluorine atom brings about a significant breaking of the symmetry of the π electron density of the benzene ring, which is more pronounced than the one caused by the side chain, and leads to an excess of π electron density in the vicinity of the fluorine atom and a depletion of this density in the area close to the side chain. This different distribution of the π electron density is not expected to significantly influence the binding strength and the stability of the most stable *gauche* conformer in which the side chain is bent to the aromatic ring and stabilized by a non-

conventional OH$\cdots\pi$ bond. But on the other hand, the depleted π electron density close to the side chain affects the stability of the side chain itself and hence the energy ordering of the other conformations in which the OH group points away form the ring. In this case the reduced π electron density of the aromatic ring next to the side chain induces a redistribution of the electronic density within the side chain of the latter and hence affects its conformational stability and the ordering of the conformations.

4.5   Summary and Conclusions

The *para*-fluorinated flexible molecule 2-phenylethanol, the hydroxy analogue of the simplest neurotransmitter, 2-phenylethylamine, has been investigated by combination of high-resolution R2PI two-color mass-selective laser spectroscopy and quantum-chemistry *ab initio* calculations on its structure and energetics. In this work, all prominent vibronic bands in the low-resolution spectrum of the 2-*p*FPE monomer up to 120 cm^{-1} have been measured under high resolution of 70 MHz. Comparing the values of the rotational constants obtained from the fits of the highly resolved spectra with the theoretically predicted ones for the 5 lowest-energy conformations, we were able to convincingly assign all of these vibronic bands to two conformational geometries: the lowest-energy *gauche* structure and a higher lying *anti* structure of 2-*p*FPE. The observation of only two out of five theoretically predicted conformations requires a close inspection of the potential energy surface. The latter clearly demonstrates that the *gauche* conformers are separated from each other by low potential barriers and the same holds also for the *anti* conformers. The *gauche* conformations, however, are separated from the *anti* structures by a high potential barrier. This favors the relaxation of all originally produced *gauche* conformers to the most stable conformer in the *gauche* manifold and the relaxation of all initially produced *anti* conformers to the most stable structure within the *anti* manifold. The high barrier between the most stable *gauche* conformer and the higher-energy *anti* conformation, however, precludes the further relaxation of the *anti* structure to the most stable *gauche* one. We have observed local perturbations in the rotational structure of the higher-lying *anti* conformer. This points to a coupling of special rotational levels of the *anti* conformer to rovibronic states of a lower-energy conformation in the first excited electronic state, S_1. At higher excess energy in the S_1 state, this may result in isomerization processes in the statistical limit. From our investigation, we have found evidence that the fluorination at the *para* position of 2-phenylethanol does not alter the shape of the *gauche* conformer stabilized by an intramolecular OH$\cdots\pi$ bond and that this conformer remains the lowest-energy one. This implies that even upon the considerable change of the π-electron-density distribution in the aromatic ring brought about by the attachment of a strongly electronegative atom, the intramolecular nonconventional OH$\cdots\pi$ bond is not weakened appreciably. This result demonstrates the significance and robustness of this type of bond for the

stabilization of the conformational structures of flexible molecules.

Chapter 5

Mass Analyzed Threshold Ionization Spectroscopy of Flexible 2-*para*-fluorophenylethanol Conformers with and without an Intramolecular OH···π Bond

The cationic state of the prototype flexible molecule 2-para-fluorophenylethanol has been investigated by combination of mass-analyzed threshold-ionization (MATI) spectroscopy and quantum chemistry ab initio density functional theory (DFT) calculations employing two different functionals: the B3LYP functional and the new hybrid functional M05. The MATI spectra measured via vibronic bands in the S_1 intermediate state belonging to the most stable gauche conformer stabilized by an intramolecular OH···π hydrogen bond are structureless, while the spectra recorded via bands of the anti conformer feature well-resolved peaks. This result is in a good accord with our theoretical predictions showing that upon ionization, the anti conformer retains its structure, while the lowest-energy gauche conformer undergoes a significant structural change resulting in a break of the OH···π bond. This and the good agreement between the measured band positions and the theoretically predicted frequencies for the cationic anti conformer confirm the conformational assignment. The result for the cation provides clear evidence for the existence of a nonclassical intramolecular OH···π hydrogen bond if the electron density in the aromatic ring is sufficiently high as is the case only for the neutral molecule.

5.1 Introduction

In recent years, a variety of spectroscopic techniques [3, 20, 70, 85, 87, 98–100] have been used to deduce the conformational landscape of flexible prototype molecular systems of biological relevance. An important model system is 2-phenylethanol (2-PE), the hydroxyl analogue of the neurotransmitter 2-phenylethylamine, whose most stable conformer in the ground, S_0, and first excited, S_1, electronic states is stabilized by a non-conventional OH$\cdots\pi$ bond. [46, 90] In order to explore the stability and the strength of this noncovalent weak hydrogen interaction, we introduced perturbation of the π-electron system of the benzene ring by fluorine substitution at the *para* position, and analyzed its effect on the conformational structures.(See Chapter 4.) Spectroscopic data on 2-(para-fluorophenyl)ethanol (2-*p*FPE) (see Scheme 1) were published by Chakraborty et al. [91] and complemented by a study from our group (see Chapter 4) with a clear assignment of the *gauche* and *anti* structures by high resolution UV spectroscopy. The two conformers are separated by a relatively high potential barrier of about 20_0^0 cm^{-1} in the ground neutral state,(see Fig. 4.6) which under molecular beam conditions precludes the relaxation of the higher lying *anti* conformer (ca. 570 cm^{-1}) to the lowest energy *gauche* conformer, stabilized by a π-hydrogen bonding of the terminal hydroxyl group of the side chain with the phenyl ring. An even stronger perturbation of the p-electron density is caused by the ionization of the molecule. Dessent et al. have studied the ionization-induced conformational changes of aromatic molecules with a side chain by threshold ionization techniques. [101] In this work, for the first time we have applied the mass-analyzed threshold-ionization (MATI) spectroscopy to investigate the fate of an OH$\cdots\pi$ bonding that exists in the neutral molecule, after the ionization process taking a π electron out of the ring. Furthermore, existence and stability of *gauche* and *anti* conformers after ionization are investigated. The obtained MATI spectra provide information on the conformer-specific ionization-induced geometry changes and yield additional data for the spectroscopic identification of these conformers.

5.2 Experimental

The two-photon excitation scheme in a MATI experiment employs promotion of the molecules from their ground, S_0, state to a selected vibronic state in the first excited, S_1, electronic state and subsequent excitation to very high Rydberg states which are finally ionized by a delayed pulsed electric field. [51–53] The experimental setup of the MATI experiment is described in detail in Sec. 2.4.1 and our previous publications. [102, 103] Briefly, liquid 2-*p*FPE (purity 97%) was purchased from Sigma-Aldrich, used without further purification, and heated to 110 . A mixture of the sample vapor with the buffer gas argon at 3 bar was expanded into vacuum through a pulsed-operated General Valve nozzle with an orifice diameter of 500 μm. The so-produced

molecular beam was skimmed before entering the interaction region with two counterpropagating laser beams that were perpendicularly focused onto the molecular beam 150 mm downstream of the nozzle. The excited Rydberg molecules are separated from the directly produced photoions in the first stage of the acceleration region of a linear reflecting time of flight mass spectrometer (RETOF) by a weak electric field (*ca.* 0.18 0.22 V cm^{-1}) and ionized by a strong electric field of 1000 V cm^{-1} in the second stage. The resulting threshold ions are accelerated and injected by the same electric field into the drift region of the linear RETOF mass spectrometer. [55] The mass resolved signals are detected at different mass channels and recorded with gated integrators, digitized, and finally processed in a personal computer under LabVIEW environment.

5.3   Results

5.3.1   REMPI spectra

The one-color resonance enhanced multi-photon ionization (REMPI) spectrum of the excited, S_1, electronic state of 2-*p*FPE is shown in Fig. 5.1. It complements the already shown spectrum in the previous chapter with an extended scan to the blue side. In addition to the vibrations in the neighborhood of the strong band at 37067.6 cm^{-1}, a strong band shifted by 553 cm^{-1} to the blue is seen, which corresponds to the false origin ν_6 vibronic band in benzene. [97] In the preceding chapter we have identified the pronounced band at 37067.6 cm^{-1} as the origin of the *gauche* conformer, which is stabilized by an OH· · ·π hydrogen bond. The rotational structure of the weak band at 80 cm^{-1} to the blue of the strongest band was found to be completely different and assigned to the origin of the *anti* conformer by a fit of the rotational structure. Using the typical experimental vibrational frequencies found for the *gauche* conformer, we tentatively assign the weak bands at +147 cm^{-1} and +632 cm^{-1} to progression bands of the *anti* conformer (see below). To shed light on the identity of these bands and to examine the behavior of the *gauche* and the *anti* conformers after ionization, we performed MATI scans after two-photon excitation via various intermediate vibronic states in the first excited, S_1, electronic state.

5.3.2   MATI spectra

As a first step, in Fig. 5.2 the total ion current is shown as a function of the two-photon excitation energy measured by fixing the first photon energy to either origin in the S_1 intermediate state at 37067.6 cm^{-1} or 37147.6 cm^{-1} of the recently identified two conformers under consideration, and scanning the second photon energy. The total ion current in Fig. 5.2b, measured via the 0_0^0 band of the *anti* conformer in S_1 intermediate state shows a step-like behavior with two steps
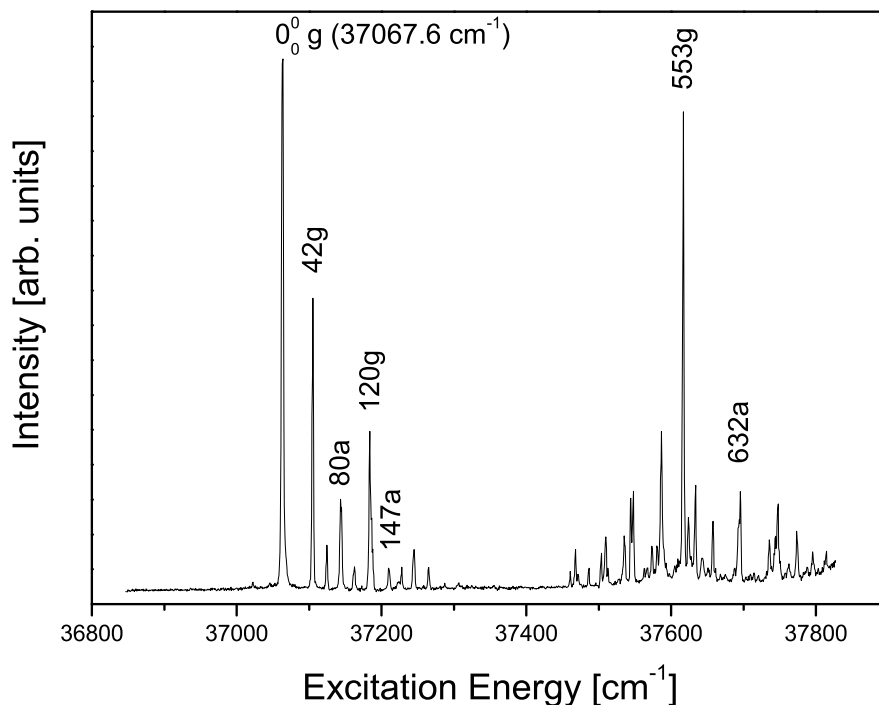
Figure 5.1: *One-colour* $S_1 \leftarrow S_0$ *REMPI spectrum of 2-pFPE, recorded at the monomer mass channel m/z = 140. Conformer assignments and relative peak positions are included in the spectrum. Bands originating from* gauche *and* anti *conformers are designated by (g) and (a), respectively.*

separated by only 40 cm^{-1}, while the total ion current spectrum via the strong peak at 37067.6 cm^{-1} (the 0_0^0 band of the *gauche* conformer) does not show a step-like behaviour but a gradually increasing total ion current (Fig. 5.2a). Next, using the two-color excitation scheme, only threshold ions are detected. The resulting MATI spectrum of the *gauche* conformer of 2-pFPE measured via the S_1, 0_0^0 origin at 37067.6 cm^{-1} as a function of the two-photon energy is shown in Fig. 5.3a. The spectrum is featureless and noisy with a smooth onset at around 71 200 cm^{-1} and an increasing intensity for higher excitation energies. In Fig. 5.3b, the MATI spectrum is shown when measured via the S_1, 0_0^0 band at 37 147.6 cm^{-1}, which has been assigned to the origin of the *anti* conformer of 2-pFPE. [104] It displays a well-resolved vibronic structure. No peak is observed on the red side of the strong peak at 71 238 cm^{-1}. This allows us to determine the adiabatic ionization energy (AIE) as 71 238 ±5 cm^{-1} (ionization energies are given without field correction [49]). In addition to the MATI spectra via the S_1 origins of the observed two conformers of 2-pFPE, we have recorded MATI spectra via two other vibronic bands in the S_1
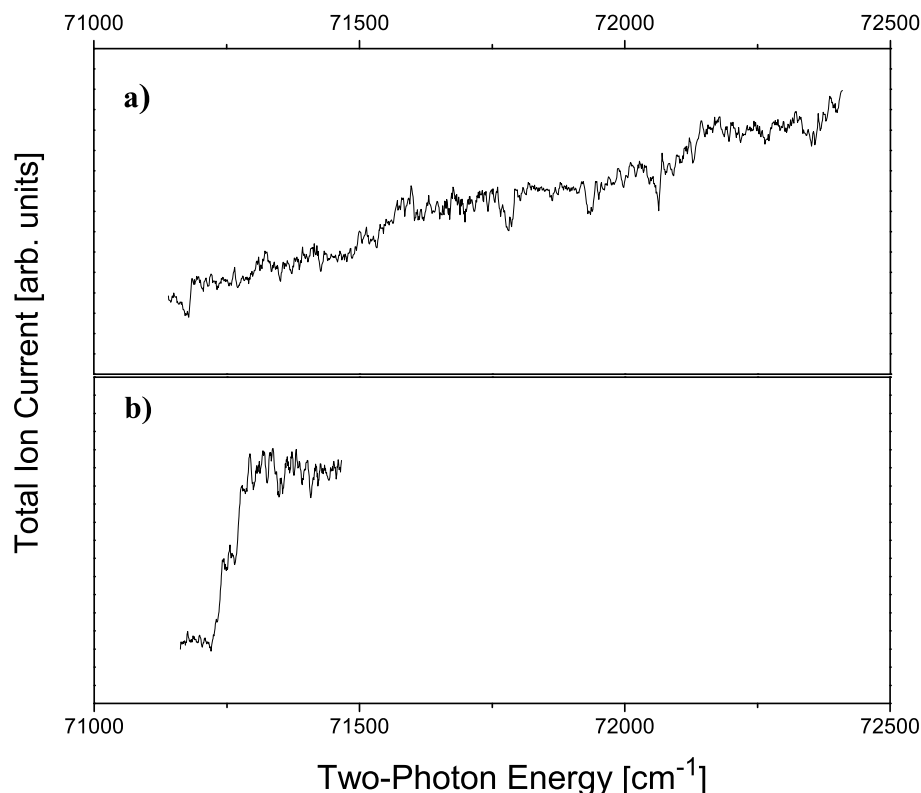
Figure 5.2: *Total ion current spectra of 2-pFPE measured via gauche (a) and anti (b) origins of the two conformers in the S_1 electronic state.*

intermediate state. The resulting spectra via the bands at +632 cm^{-1} and +147 cm^{-1} in the S_1 intermediate state are shown in Fig. 5.4a and b and the spectrum measured via the origin of the *anti* conformer in the S_1 intermediate state is shown in Fig. 5.4c with an extension up to 864 cm^{-1} excess energy. Each of the two spectra in Fig. 5.4a and b consists of several well-pronounced peaks, which are shifted to higher energy by 574 cm^{-1} and 66 cm^{-1}, respectively, from the AIE at 71 238 cm^{-1}. These shifts are similar to the respective blue shift of the vibronic S_1 intermediate states. The corresponding positions of the low frequency vibronic MATI peaks measured via different intermediate states are marked with dotted lines in Fig. 5.4b and c. The presence of a similar vibronic structure in the D_0 cationic state means that the spectra originate from the *anti* conformer of the 2-*p*FPE molecule and assigns the corresponding intermediate state bands to the *anti* conformer.
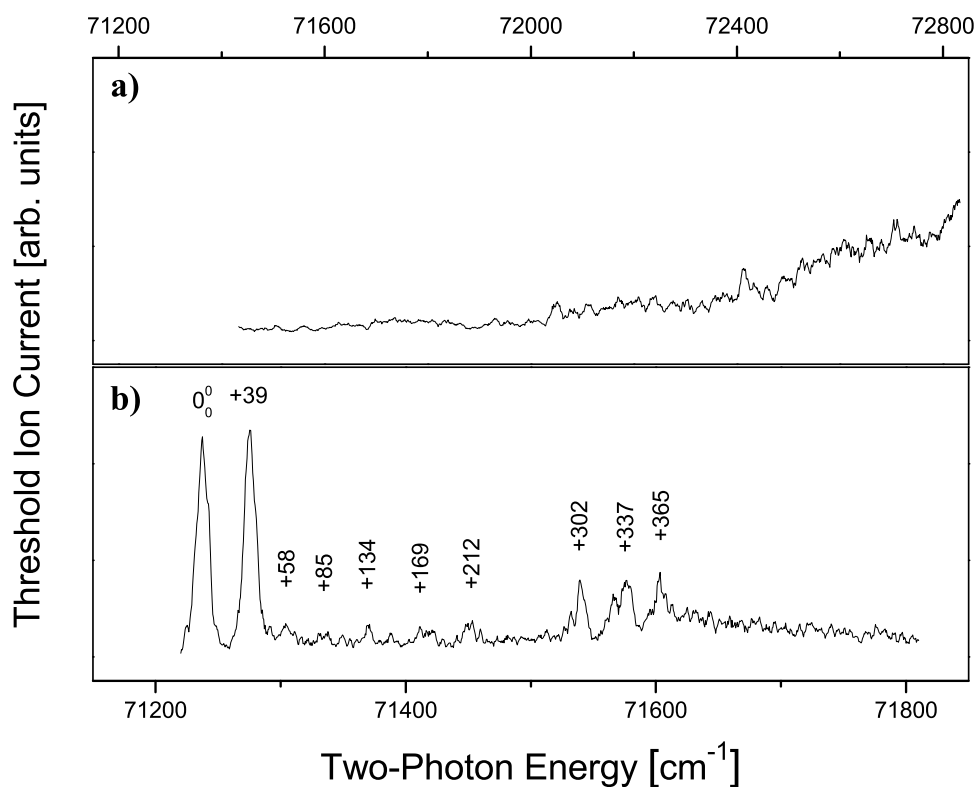
Figure 5.3: *MATI spectra of 2-pFPE measured via gauche (a) and anti (b) origins of the two conformers in the S_1 electronic state. Relative band positions are included in the lower spectrum.*

5.3.3 Computational results

Theoretical quantum chemistry calculation of the structure, energetics, electron density distribution and the vibrational frequencies without and with inclusion of anharmonicity of the 2-pFPE cationic conformers have been performed using the Gaussian 03 suite of programs. [105] We considered the most stable structures of the 2-pFPE monomer in the neutral ground, S_0, electronic state (see Chapter 4) as starting geometries for the optimizations in the cationic state. Density functional theory with the commonly used B3LYP functional, the recently developed hybrid M05 functional [106] and aug-cc-pVTZ basis set were employed for the structural optimizations, energetics, electron density distribution in the HOMO, and calculations of the normal-mode frequencies. B3LYP/cc-pVDZ and M05/cc-pVDZ level of theory was used for the computation of the anharmonic frequencies. For the most stable *gauche* conformer in the neutral we have applied also the computationally more demanding UMP2 level of theory with two different basis

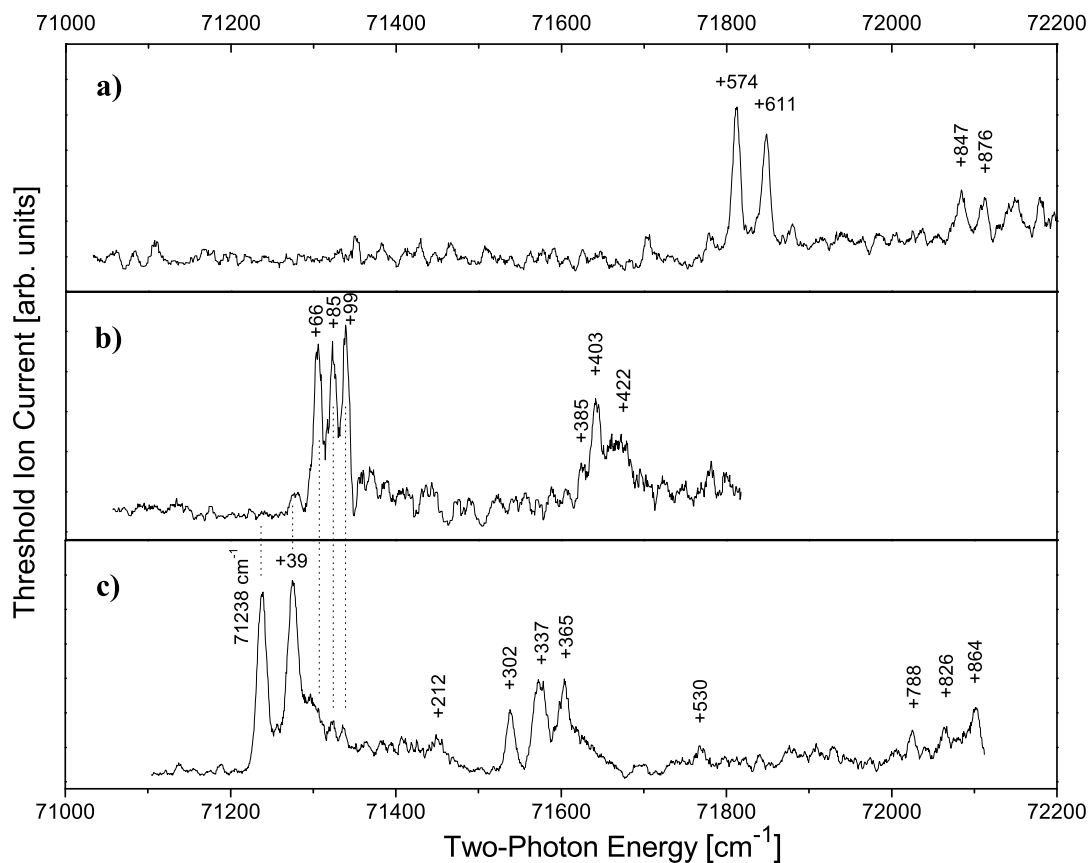**Figure 5.4:** *MATI spectra of 2-pFPE via the +632 cm^{-1} (a), the +147 cm^{-1} (b), and the anti 0_0^0 (c) bands in the S_1 intermediate electronic state. The numbers are the relative band positions to the 0_0^0 band at 71 238 cm^{-1}.*

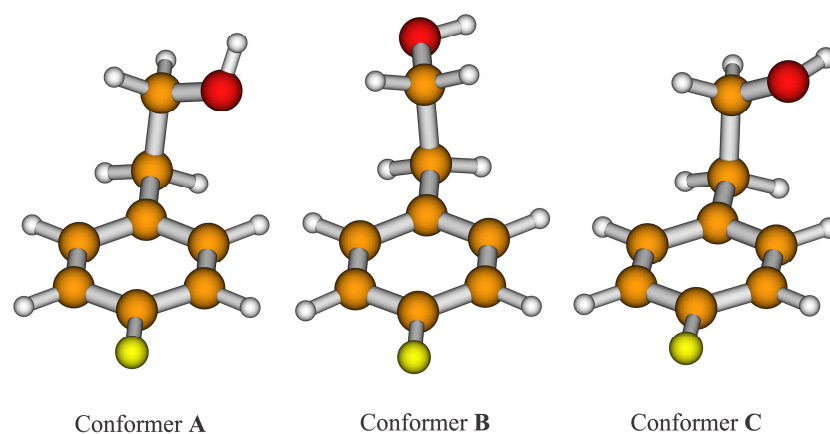sets, 6-31/G (p, d) and cc-pVDZ, respectively, to check the above calculations. [107]

Figure 5.5: *Conformations of the 2-pFPE cation obtained from ab initio quantum chemistry full structural optimisation at the DFT M05/aug-cc-pVTZ level of theory.*

All calculations predicted the same structural change in the cation. It is interesting to point out that the DFT computations with B3LYP as well as M05 functionals revealed that two of the three theoretically found *gauche* conformers and the two *anti* conformers in the neutral ground, S_0, electronic state converge to one *gauche* and one *anti* structure in the ground cationic, D_0, state, respectively, during the optimization process. Only one of the *gauche* structures retains its geometry upon ionization. Thus, the total number of the theoretically optimized conformations of the 2-p-FPE is decreasing from 5 to 3 in the cationic state: two *gauche* and one *anti* structure. It is worth noting that none of the two *gauche* conformers in the cation features a nonclassical OH· · ·π hydrogen bond between the terminal OH group of the side chain and the π electrons of the benzene ring. All three optimized conformational structures at the M05/aug-cc-pVTZ level of theory of the 2-*p*FPE cation are depicted in Fig. 5.5. The optimized structures at the B3LYP/aug-cc-pVTZ level of theory are the same as the ones shown in Fig. 5.5 with only marginal differences in some of the planar and dihedral angles. The energy ordering obtained from the B3LYP calculations is as follows: Conformer **C** (0 cm^{-1}), Conformer **A** (+18 cm^{-1}), and Conformer **B** (+517 cm^{-1}). The energy ordering resulting from the M05 calculations asserts that the most stable conformer is conformer **A** (0 cm^{-1}), followed by conformers **C** (+44 cm^{-1}) and **B** (+735 cm^{-1}). Fig. 5.6 shows a comparison between the HOMO electron density distribution in the neutral and the cationic state for the most stable conformer calculated at the M05/aug-cc-pVTZ level of theory. The normal-mode frequencies up to 1100 cm^{-1} for conformers **A**, **B**, and **C** as well as the corresponding frequencies with inclusion of anharmonic corrections for conformer **B** calculated with both B3LYP and M05 functionals are listed in Table 5.1.
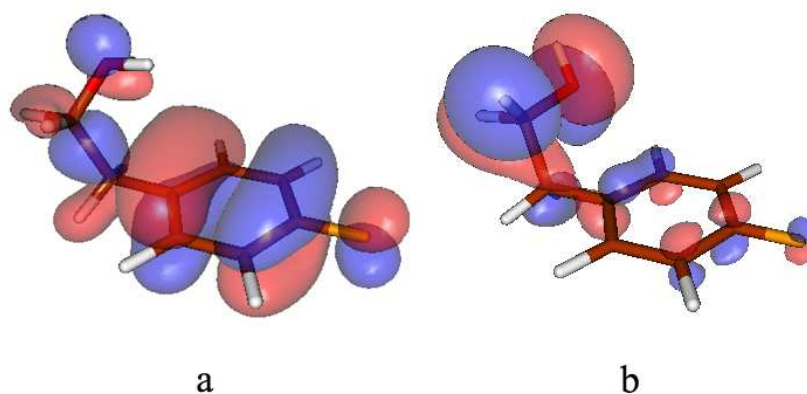
Figure 5.6: *HOMO electron density distribution of 2-pFPE in the neutral ground, S_0, electronic state for the most stable gauche conformer (a) and in the cationic ground, D0, electronic state for the most stable gauche conformer A (b) calculated at the DFT M05/aug-cc-pVTZ level of theory.*

5.4   Discussion

The MATI spectra of the 2-*p*FPE monomer measured via the origin bands of the *gauche* and the *anti* conformers in the first excited, S_1, electronic state show significantly different pattern (see Fig. 5.3): there is a well-resolved MATI spectrum only for the *anti* conformation, and an unstructured signal for the *gauche* conformer. The responsible Franck-Condon factors can be viewed upon as a probe for the structural changes of the respective species, taking place on ionization. Unfavorable Franck-Condon factors apply to the *gauche* conformer, and, for this reason, we expect that the structure of this species in the cation should be substantially different from that in the neutral state. On the contrary, the *anti* conformer produces a well-resolved MATI spectrum, which is an indication for a small or negligible structural change upon ionization. The results from our quantum chemistry *ab initio* calculations provide further arguments for these conclusions. The structural optimizations in the cation clearly demonstrate that the *anti* conformer retains its structure (see Fig. 5.5, Conformer **B**), whereas the probed most stable *gauche* conformation stabilized by a nonconventional OH$\cdots\pi$ bond in the neutral state does no longer exist in the cation, and the optimisation results in another geometry with a different arrangement of the side chain (see Fig. 5.5, Conformer **A**). Conformer **A** is the most stable conformer in the cation according to the M05 calculations. The energy gap between this and the next-in-energy conformer **C**, however, is only 44 cm^{-1}, which suggests that a reordering is not very unlikely to

Conformer A		Conformer B				Conformer C	
B3LYP Harm.	M05 Harm.	B3LYP Harm.	M05 Harm.	B3LYP Anharm.	M05 Anharm.	B3LYP Harm.	M05 Harm.
41	46	66	57	61	27	43	50
71	74	68	66	66	73	69	74
112	138	87	100	90	103	113	121
169	194	184	182	181	177	188	191
201	252	306	305	302	303	267	207
289	292	331	314	326	335	301	294
323	323	345	340	342	341	331	334
371	369	358	347	374	366	377	372
417	421	386	376	375	68	419	422
434	433	430	428	426	418	440	442
470	472	497	498	490	499	459	463
565	567	548	548	537	545	560	562
583	571	600	583	593	580	593	578
709	715	688	731	663	711	704	719
765	768	747	766	726	747	747	763
792	796	797	791	778	814	777	794
833	840	801	809	784	798	797	813
844	860	819	812	803	780	834	840
886	896	845	849	834	835	879	883
895	920	897	898	874	882	896	904
994	992	999	994	972	1022	975	982
1013	1012	1002	1002	977	960	1001	997
1014	1017	1014	1005	978	952	1012	1009
1025	1030	1017	1009	978	979	1017	1015
1047	1085	1095	1106	1081	1097	1048	1070

Table 5.1: *Theoretically predicted normal-mode vibrational frequencies (cm^{-1}) up to 1100 cm^{-1} for the three stable conformations of the 2-pFPE cation calculated at the DFT B3LYP/aug-cc-pVTZ, M05/aug-cc-pVTZ levels of theory. Frequencies including anharmonic corrections have been calculated only for conformer **B** at the DFT B3LYP/cc-pVDZ and M05/cc-pVDZ levels of theory. No scale factors have been applied to correct the normal-mode frequencies.*

occur upon changing the model theory and the basis set as already demonstrated by the B3LYP calculation where the ordering of **A** and **C** is inverted (see above). In such a case conformer **C** being the most stable conformer in the cation cannot be produced by direct ionization from its neutral counterpart since the latter is a high-energy conformation, and is not present in the cold molecular beam, but it can be produced as a result from a relaxation from the higher-energy *gauche* cation conformer **A**. Nevertheless, whichever of the two *gauche* conformations, **A** or **C**, is finally produced upon ionization of the most stable *gauche* conformer in the neutral state, no resolved MATI spectrum is anticipated since both ending structures differ considerably from the initial one in the S_1 state. With respect to the above statement, we have measured total ion current and MATI spectra via the strong peak in the intermediate, S_1, electronic state at +553 cm^{-1}, which were with unresolved peak structure. On this basis, we assigned this intermediate band as originating from the *gauche* conformer of 2-*p*FPE.(see Fig. 4.6) By contrast, the MATI spectra obtained via excitation of the vibronic bands at +147 cm^{-1} and +632 cm^{-1} in the first excited, S_1, electronic state feature similar peak pattern with the MATI spectrum of the *anti* conformer accessed via its origin band (see Fig. 5.4a and b) but with different intensity profile due to the different Franck-Condon factors corresponding to the two intermediate vibronic states in the S_1 electronic state. This result provides a clear-cut evidence that the vibronic bands at +147 cm^{-1} and +632 cm^{-1} originate from the same *anti* conformer. The AIE of the *anti* conformation of 71 238 cm^{-1} found from the MATI spectrum of Fig. 5.4a can be compared with the AIE of the parent molecule 2-PE (71 501 ±16 cm^{-1}) measured by Weinkauf *et al.*, [71][25] and thus is found to be shifted to the red by 263 cm^{-1}. The blue-shifted bands in Fig. 5.4 should correspond to vibrational excitations in the cation as shown in Table 5.2 by comparison between the experimental and the theoretical frequencies calculated at the DFT B3LYP/ cc-pVDZ level of theory with included anharmonic correction. As seen from Table 5.1 the normal-mode frequencies obtained from the DFT M05/cc-pVDZ level of theory without and with inclusion of the anharmonic correction can explain the observed band positions, especially for the lowest-frequency region where large-amplitude torsional motion is present. We were able to assign all of the experimentally observed low-frequency bands up to 365 cm^{-1}, which are sensitive to the structure of the species, either to normal modes or to combination modes of the *anti* conformer. Next, we compare the computed ionization energy with the measured one for the observed *anti* conformer. The calculated AIE for the *anti* conformer of 2-*p*FPE is 68 260 cm^{-1} at the B3LYP/aug-cc-pVTZ level of theory and 66 686 cm^{-1} at the M05/aug-cc-pVTZ level of theory. These values are lower than the experimental ionization energy of 71 238 cm^{-1} but yet they are a good estimate: the ratios of the experimental and the theoretical ionization energies are 1.044 (B3LYP) and 1.068 (M05), respectively. The calculated AIE for the *gauche* conformer of the 2-*p*FPE monomer at the same DFT B3LYP/aug-cc-pVTZ level of theory is 67 936 cm^{-1}, and 66 201 cm^{-1} at the M05/aug-cc-pVTZ level of theory. Assuming that the above ratios hold also for this case, we expect an AIE of 70 925 cm^{-1} (deduced from B3LYP) and 70 719 cm^{-1} (deduced from M05) for the *gauche* conformer whose direct experimental measurement is precluded by the unfavourable

Exp. Freq.	Theor. Freq.	Assignment
39	61	τ_1 torsion about the C2C7 bond
58	66	β_1 bending side chain *vs.* ring
85	90	τ_2 torsion about the C7C8 bond
99	-	Combination mode $\tau_1 + \beta_1$
134	-	Combination mode $\tau_2 + \beta_1$
169	181	Butterfly mode β_2 or overtone of τ_2
212	-	Combination mode $\tau_1 + \beta_2$
302	302	σ stretching along the long axis
337	342	Wagging mode
365	374	OH group torsion

Table 5.2: *Assignment of the observed vibronic bands in the MATI spectra shown in Fig. 5.3b on the basis of the theoretically predicted frequencies (cm^{-1}) with anharmonic corrections for the anti conformer of the 2-pFPE cation (conformer **B** in Fig. 5.5) calculated at the DFT B3LYP/cc-pVDZ level of theory.*

Conformer	$\mathbf{A}_{gauche}$	$\mathbf{B}_{anti}$
$S_1 \leftarrow S_0$, 0^0_0	37 068	37 148
AIE$_{exp}$	70 925*	71 238
	70 719**	
AIE$_{theo}$ (B3LYP)	67 936	68 260
AIE$_{theo}$ (M05)	66 201	66 686

Table 5.3: *Electronic origins of $S_1 \leftarrow S_0$ transitions (cm^{-1}) for conformers **A** and **B**. AIE$_{exp}$: experimental values of the adiabatic ionization energies (cm^{-1}) for conformers **A** and **B**. AIE$_{theo}$: theoretical values of the adiabatic ionization energies (cm^{-1}) for conformers **A** and **B** calculated at the DFT B3LYP and M05/aug-cc-pVTZ level of theories.*

Franck-Condon factor for the ionization step. The above results are summarized in Table 5.3. The position of the onset of the unstructured MATI spectrum of the *gauche* conformer (see Fig. 5.3a) is at ca. 72 000 cm^{-1}. This implies that the Franck-Condon factors favor transitions only to vibrational states in the cation at more than 1000 cm^{-1} above the AIE and corresponds to more than 10 quanta of the lowest-frequency torsional mode of the side chain inducing a transition from the OH$\cdots\pi$-bonded *gauche* conformer in the S_1 state to the lowest-energy structure of the cation. It demonstrates the breaking of the OH$\cdots\pi$ hydrogen bond of the *gauche* conformer followed by a significant reshaping of the side chain upon ionization. We have employed three different theoretical models to investigate the structural changes in the neutral conformers upon ionization and thus checking their suitability to account for weak intramolecular interactions, in particular the nonclassical OH$\cdots\pi$ bond. We started with the UMP2 level of theory with two basis sets (see section 5.3.3) leading to optimized structures of the neutral most stable *gauche*

conformer of 2-*p*FPE in the cation. The so-obtained cationic structures clearly demonstrate that the neutral conformer is destroyed upon ionization as a result of the breaking of the stabilizing OH$\cdots\pi$ bond. We did not consider these results in detail because the UMP2 calculations started with the neutrals of the other four conformers were not successful due to spin contamination errors in the cation. As a next step, the DFT calculations were performed with two different functionals. First, we used the standard B3LYP functional which has revealed the three stable structures in the ion, as mentioned above, but this level of theory is not expected to consider the dispersion interactions that should be important in determining the conformational structures of hydrogen-stabilized conformers. For this reason, we employed the newly elaborated hybrid functional M05, [106] which is specially designed to account for such weak interactions. It was interesting to see that the two theoretical functionals predicted the same neutral-to- cation structural changes. Unlike the very similar structures resulting from the B3LYP and M05 calculations, the energy ordering and the energy gaps between the predicted conformers is different as pointed out above, the *anti* conformer **B** being distanced away by 735 cm^{-1} from the most stable *gauche* conformer **A** in the case of the M05 calculations. As shown above, only three stable conformers are theoretically predicted for the cation: one *anti* (**B**) and two *gauche* ones (**A** and **C**). None of these geometries is favorable for the formation of an OH$\cdots\pi$ bond, and hence we can conclude that this bond does not survive the ionization process leading to the cation. A comparison between the HOMO electron distributions in the neutral [107] and in the cation calculated at the DFT M05/aug-cc-pVTZ level of theory (see Fig. 5.6) shows a significant depletion of the π-electron density in the benzene ring in the cation due to the ejected π electron, and a significant electron density relocation also in the side chain. The reduced electron density in the benzene ring thus can be rendered responsible for the weakening of the OH$\cdots\pi$ bond and ultimately for its breaking after ionization. This is an important result since it provides experimental evidence for the nature of the OH$\cdots\pi$ bond as being formed as a result of the attraction between the partial positive charge located at the terminal hydrogen atom and the partial delocalized negative π electron charge distributed over the aromatic ring in the neutral molecule.

5.5   Summary and conclusions

In this work we have investigated the effect of ionization on the structure of a prototype flexible molecule, 2-*para*-fluorophenyl-ethanol, which exists in two conformeric configurations in the cold molecular beam. By combining mass-analyzed threshold-ionization spectroscopy with high level quantum chemistry *ab initio* calculations performed at the B3LYP/aug-cc-pVTZ and the M05/aug-cc-pVTZ levels of theory, we have assigned the conformers of the 2-*para*-fluorophenylethanol cation. Our calculations predict three stable structures in the cation: two *gauche* and one *anti*. The MATI spectra via vibronic bands in the S_1 intermediate state corresponding to *gauche* and

anti conformers, respectively, are utterly different: the spectrum measured via the origin of the *gauche* conformer increases in intensity gradually but does not show resolved structure, whereas the spectra obtained via bands of the *anti* conformer are characterized by a well-pronounced peaks. We ascribe this difference to different Franck-Condon factors rather than to a fast relaxation process. This is justified by our computations, which demonstrate that the most stable *anti* conformer in the neutral undergoes a negligible structural change upon ionization and hence the ionization should have favorable Franck-Condon factors. On the other hand, the ionization of the most stable *gauche* conformer in the neutral, which is stabilized by an OH$\cdots\pi$ hydrogen bond, leads to a breaking of this bond and to a significant structural deformation resulting in the unstructured MATI spectrum in this case. These results provide further evidence for the existence of a nonclassical OH$\cdots\pi$ bond in this flexible model molecule and shed light on its nature as originating from attraction between the positive partial charge on the terminal H atom of the side chain and the delocalized negative charge of the π electrons of the neutral benzene ring. The understanding of the nature of the OH$\cdots\pi$ bond is relevant to studying the stability of secondary structures such as polypeptides and proteins held together by weak interactions. In conclusion, we have shown that MATI spectroscopy provides information particularly on weak interactions with the π electrons of aromatic molecules because a significant change in the π electron density occurs during an ionization process. This is advantageous to, *e.g.*, dispersed emission spectroscopy where during $S_1 \longleftarrow S_0$ transition no large changes in the π electron density are involved.

Chapter 6

Competition between π and σ Hydrogen Bonds and Conformational Probing of 2-*ortho*-fluorophenylethanol by High-Resolution Electronic Spectroscopy

The flexible model molecule 2-ortho-fluorophenylethanol has been investigated by low- and high-resolution resonance-enhanced two-photon ionization spectroscopy in combination with high-level ab initio quantum chemistry calculations. One dominant conformation has been identified in the cold molecular beam corresponding to the most stable theoretically predicted gauche structure stabilized by an intramolecular OH· · ·π bond. A tentative assignment of a higher-lying gauche conformer present in the molecular beam separated by high potential barriers from the most stable one has been made. The missing other higher-energy theoretically predicted conformations most likely relax to the most stable ones during the process of the adiabatic expansion. The good agreement between the experimental and theoretical results demonstrates that even in the case of a substitution with an electronegative atom at the ortho position, bringing about a significant redistribution of the electron density in the benzene ring and providing a convenient binding site for the formation of a competing OH· · · F σ hydrogen bond, the nonclassical OH· · ·π bond remains the preferred binding motif for the most stable conformer.

6.1   Introduction

The conformational preference of a flexible molecule is the outcome of a subtle interplay of non-bonded weak interactions between different groups of the molecule and with its surroundings (For review, see Refs. [3, 60, 89]). Conformational shapes determine the properties and functionality of many biologically important molecules. Toward this end, much discussion has been devoted in the past two decades to scrutinizing the relative influence of pairwise interactions between specific molecular groups [86, 87] and Chapters 3, 4. In such an endeavor, gas-phase conformational studies of small biological molecules and their convenient molecular analogs under solvent-free conditions are very well suited for investigation of the intrinsic properties of these molecules, and for this reason, have attracted the scientific interest of the spectroscopic community [20, 46, 61, 67, 75, 80, 85, 108–110] and Chapters 3, 4.
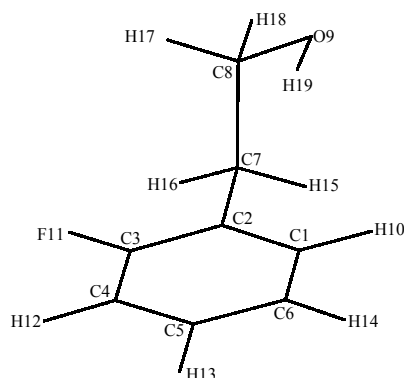

Figure 6.1: *Atom labels of 2-oFPE*

2-*ortho*-fluorophenylethanol (2-*o*FPE) is a derivative of 2-phenylethanol (2-PE), which is the hydroxyl analog of the simplest aromatic amine neurotransmitter, 2-phenylethylamine. [16, 46, 59, 60, 64, 72, 73, 111] Microwave and high-resolution electronic spectroscopy studies have conclusively established that a *gauche* geometry is the preferred conformation of the 2-PE molecule in the ground electronic state. [46, 70] The high-resolution UV spectroscopy has found also that almost no structural change in the most stable conformer occurs upon electronic excitation and that no fast isomerization processes take place. [46] The primary factor that stabilizes this conformation is a nonclassical hydrogen bonding of the terminal hydroxyl functional group of the side chain with the aromatic π-electrons. [46] The finding corroborates the predictions of quantum chemistry calculations and conclusions of earlier low-resolution laser spectroscopic measurements and microwave experiments. [16, 72, 73] Recently we used the same spectroscopic method to determine how the conformational preference is affected on binding with a foreign molecular species, such as argon [46] and water[see Chapter 3]. To shed light on the stability of the OH$\cdots\pi$

hydrogen bond and its importance for the stabilization of conformational shapes, the conformations of a number of fluorine substituted aromatic alcohols were studied in the past by measuring the low-resolution electronic spectra of those molecules under the supersonic jet expansion condition using resonance-enhanced multiphoton ionization (REMPI) spectroscopic method. [86] Direct fluorine substitution at the benzene ring sites results in a distortion of the symmetry of the aromatic π-electron distribution on the ring and the charges on the ring carbon atoms and substitutions. Im *et al.* noted that the vibrational features in the spectra of *ortho*-fluorine substituted molecules are considerably different compared to other isomeric forms. [86] They attributed the differences to the results of direct proximal interaction between the F-atom and OH group of the chain. The present study aims at understanding the relative importance of the nonclassical hydrogen bond in 2-PE compared to a classical hydrogen bond of the same terminal hydroxyl functional group of the side chain with a fluorine atom substituted at the *ortho* position of the aromatic ring, in settling to the final conformational forms of the molecule. This issue is still open because recent studies in our group with *para* fluorine substituted 2-PE show that the conformational behavior of the molecule is not very different from its unsubstituted species.(see Chapter 4) An obvious reason is the much larger separation of the *para* fluorine atom from the hydroxyl group precluding the formation of a direct OH$\cdots$F hydrogen bond. The above result also implies that the OH$\cdots\pi$ hydrogen bond remains even under the conditions of a depleted π-electron density resulting form the covalent attachment of the electronegative F atom to the aromatic ring. In this chapter, we have used the low- and high-resolution mass-selective resonance two-photon ionization (R2PI) spectroscopy supported by high-level *ab initio* theoretical calculations for determining the most stable conformational isomeric forms of 2-*ortho*fluorophenylethanol (See Scheme 6.1) in the ground state and unambiguous determination of the structures of the above isomeric species. The issues that we have addressed are whether a stable isomeric species having intramolecular OH$\cdots$F hydrogen bond can be isolated, and how the conformational distribution of the nonfluorinated 2-PE is affected because of substitution of the electronegative fluorine atom at the *ortho* position of the aromatic ring.

6.2   Experiment

The experimental apparatus and technique used for the production of the R2PI low- and high-resolution spectra have been described in details in Section 2.2. A short description will be presented here pointing out only the different experimental conditions. The 2-*o*FPE sample was purchased from Aldrich, and heated to 90 in a homemade nozzle with an orifice of 500 μm where the sample vapors were mixed with buffer gas argon at a pressure of about 3.5 bar and supersonically expanded into vacuum. A skimmer was used to collimate the molecular beam and thus to reduce the Doppler broadening. The light pulses used in the one- and two-color

experiments were produced by frequency doubling of the output pulses of a commercial broadband dye laser (Lambda Physik FL2002) operating with Coumarin 153 and the pulsed amplified output of a continuous wave single-mode ring dye laser (Coherent, CR 699-21) operating with Coumarin 334, respectively. The spectral resolution achieved ($\sim$ 70 MHz) is not sufficient to resolve single rotational lines in the congested rovibronic spectra of large molecules. Therefore, a single rotational-line assignment is not possible, and we apply a computer-based method for fitting of the experimental highly resolved spectra. The method employs genetic algorithm, which has been previously demonstrated by us [20, 46] and other groups to be a decisive tool in the determination of the molecular parameters. [112, 113] Cross correlation has been employed as a quality factor for the match between the simulated and the experimental spectra. For the production of the synthetic spectra of the 2-*o*FPE monomer, we ran the program using 300 generations with 500 individuals in a generation. [20]

6.3   Results

6.3.1   Low Resolution Spectrum

The vibrational structure of the $S_1 \longleftarrow S_0$ spectrum of 2-*o*FPE was examined by low-resolution one-color massselected R2PI spectroscopy. In Fig. 6.2, the spectra of 2-*o*FPE measured at the parent mass channel (bottom trace) and at the mass of two fragments (upper traces) are shown. Here, just like in the case of 2-*para*fluorophenylethanol (2-*p*FPE),(see Chapter 4) we observe a fragmentation of the side chain (CH2OH) resulting in a mass of mz=109. In addition, we have observed a weak signal at one more fragment at mass mz=121 that stems from detachment of the fluorine atom. In comparison to 2-*p*FPE, the fragmentation behavior of the 2-*o*FPE monomer is not so pronounced, and the intensity of the fragment signals is about six times lower compared to that of 2-*p*FPE for comparable laser intensities. The origin band of the intermediate electronic, S_1, state is detected at all mass channels,but while at masses mz=140 and mz=109 it is a prominent feature, at mass mz=121 there is another band with higher intensity located at +54 cm^{-1} from the 0_0^0 transition. There are three more bands that are observed at the parent mass channel (mz=140) and the fragment mass channel (mz =109), namely at +3, +43, and +86 cm^{-1}, which coincide with the corresponding signals in the Fluorescence Excitation spectrum. [114] To shed light on the conformational preferences of 2-*o*FPE, we measured the high-resolution two-color spectra of the above-mentioned bands at mass channel mz=140. Further, we combined the experimental results with the findings from *ab initio* computations with large basis sets.
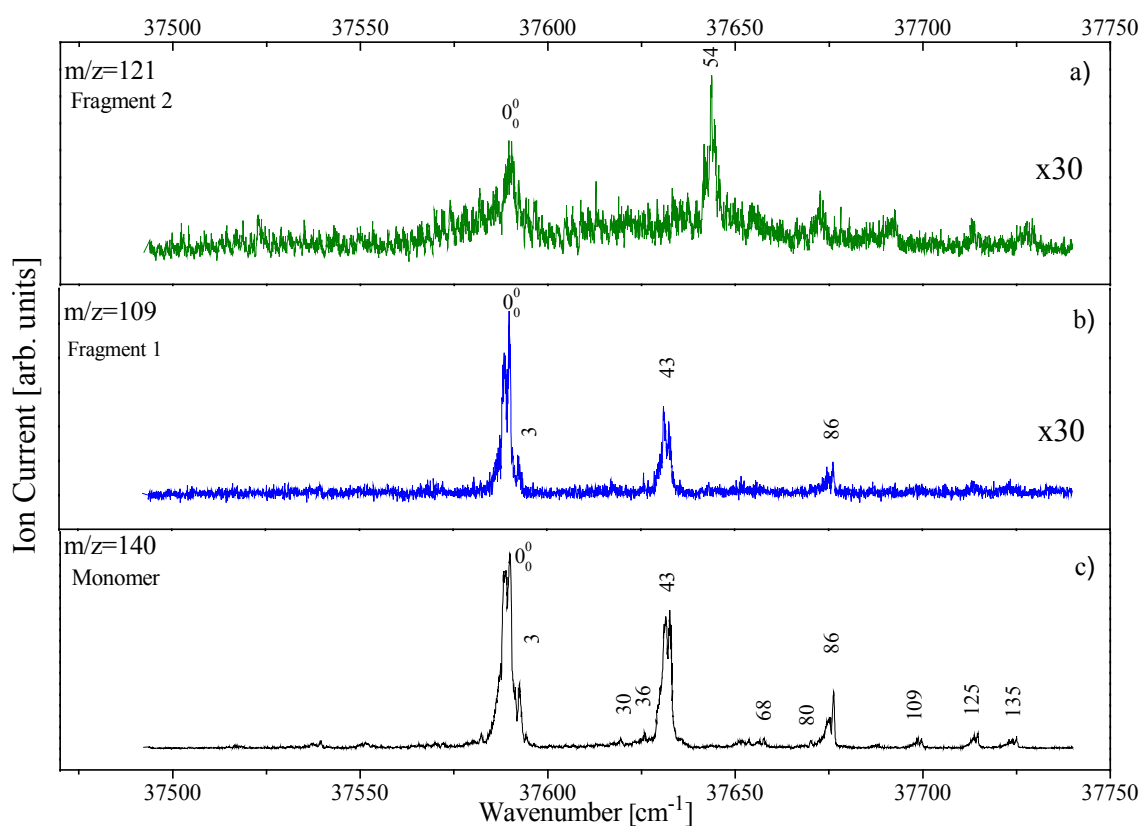
Figure 6.2: *One-color R2PI spectra of the $S_1 \leftarrow S_0$ electronic transition of the 2-oFPE monomer measured at the monomer C_8H_9OF (m/z=140) mass channel (c) and the fragment mass channels recorded at m/z=109 (b) and m/z=121 (a).*

6.3.2 High Resolution Specta

The high-resolution UV spectra of the strongest monomer band 0_0^0 and the spectra of the vibronic bands at +3, +43, +86, +109, and +125 cm^{-1} are presented in Figs. 6.3 and 6.8 (upper traces). All of them have been recorded at the monomer mass (mz=140) channel. The highly resolved spectra of the origin band and the bands at +43, +86, +109, and +125 cm^{-1}, feature very similar rotational structure, and hence, can be attributed to one and the same conformer. These bands will be discussed first.
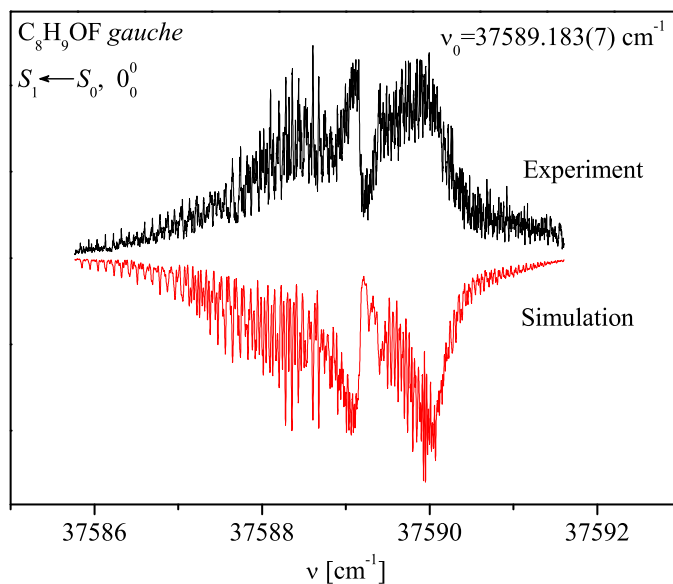
Figure 6.3: *High-resolution two-color UV R2PI spectrum of the 0_0^0 band recorded at m/z=140. The band is assigned as the origin of the gauche conformer **1** (See Fig. 6.9) of the 2-oFPE monomer with its rotationless transition centered at 37 589.183(7) cm^{-1}. Upper trace: experimental spectrum. Lower inverted trace: best-fit simulated spectrum yielding the parameters in Table 6.1 (for details, see text).*
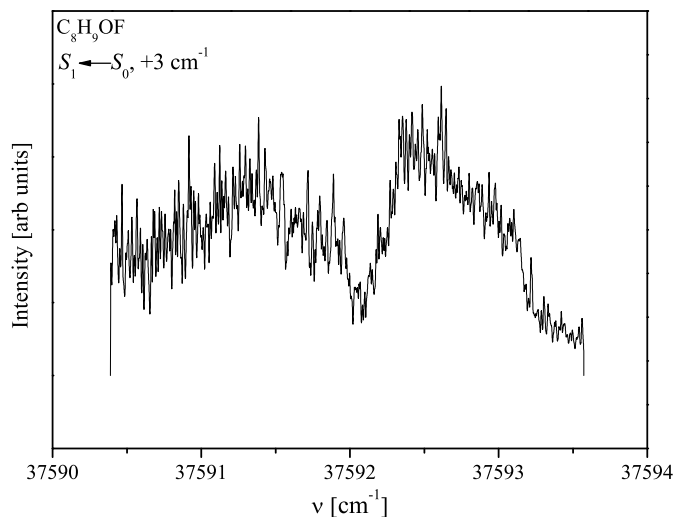

Figure 6.4: *High-resolution two-color UV R2PI spectrum of the band at +3 cm^{-1} of 2-oFPE recorded at m/z=140.*

Both the rotational constants in the ground, S_0, and the first excited, S_1, electronic state, and the transition moment ratio were determined with the computer-aided routine outlined above. As starting values for the fitted parameters, we used the results from the theoretical predictions

	Band				
Rotational constant (cm^{-1})	0^0_0 cm^{-1}	+43 cm^{-1}	+86 cm^{-1}	+109 cm^{-1}	+125 cm^{-1}
A''	0.0694(14)	0.0677(13)	0.0680(17)	0.0682(14)	0.0682(17)
B''	0.03676(79)	0.03756(88)	0.03727(53)	0.03689(78)	0.0356(12)
C''	0.02749(46)	0.02792(75)	0.02780(71)	0.02810(51)	0.02675(57)
A'	0.0681(14)	0.0666(14)	0.0664(17)	0.0665(12)	0.0668(15)
B'	0.03619(93)	0.03694(85)	0.03678(74)	0.03649(92)	0.0348(11)
C'	0.02665(49)	0.02699(61)	0.02690(69)	0.02736(56)	0.02582(51)
TM ratio $\mu_a^2 : \mu_b^2 : \mu_c^2$	60:30:10(5%)	52:29:19(9%)	82.4:17.6:0(6%)	69.4:30.6:0(4%)	74.3:20.7:5.0(6%)
Origin ν_0 (cm^{-1})	37 589.183(97)	37 631.951(11)	37 675.5306(64)	37 698.9949(74)	37 713.8964(65)
Temperature T (K)	11.0(4)	10(2)	10.1(7)	11.0(7)	11.6(6)
Best-fit cross correlation (%)	97.0(2)	93.0(3)	95.0(5)	93.0(6)	96.6(9)

Table 6.1: *Experimental rotational constants for the ground, S_0 (A'', B'', C''), and for the first excited, S_1 (A', B', C'), electronic states, the transition moment ratio, $\mu_a^2 : \mu_b^2 : \mu_c^2$, the band origin frequency, ν_0, the rotational temperature, T, and the best-fit cross correlation obtained from the rotational fit of bands 0^0_0, +43, +86, +109, and +125 cm^{-1}, shown in Figures 6.3- 6.8. The numbers in parentheses represent one standard deviation in units of the least significant quoted digit. The uncertainty for the relative values of μ_a^2, μ_b^2, and μ_c^2 in the transition moment ratio is given in parentheses.*

(MP2/cc-pVDZ and CIS/cc-pVDZ levels of theory). The resulting best-fit spectra were produced by convoluting the stick spectra with a Gaussian profile with 210 MHz full width at half maximum (FWHM), and are shown in the figures depicting the experimental spectra (lower inverted traces). The simulated spectra bear good resemblance with the experimental ones in terms of peak positions and peak intensities. The achieved cross correlations for the fits range from 93% to 96%. The experimental values of the rotational constants, transition moment ratio, rotational temperature, and band position are summarized in Table 6.1. The rotational constants for all of the discussed conformations are almost identical; there are small differences in the transition moment ratios, which are responsible for the slightly different shapes of the highly resolved spectra. The fits clearly show that the spectra consist of well-pronounced P and R branches in the wings and a prominent broad Q branch in the center. The spectra are assigned as hybrid *a*-, *b*-, and *c*-types, with dominant a contribution. The experimental spectra do not display single rotational lines but aggregations of rotational lines resulting in peaks with a FWHM of $\sim$ 250 MHz. The comparison of the experimentally found parameters with the ones obtained from the *ab initio* calculations brings the conclusion that the bands in question originate from the most stable *gauche* conformation (conformer **1**) of 2-*o*FPE (see Fig. 6.9). We present in this paper the spectra of several measured bands in detail to demonstrate that these bands can be clearly assigned to the same conformer, and rule out any interpretation stating that the bands under scrutiny descend from different conformations (see Figs. 6.3 and 6.5- 6.8). We have fitted also the high-resolution spectra of two other bands in the region above 100 cm^{-1}, namely, the bands at +109 and +135 cm^{-1}. They are very similar to the above-discussed rotationally resolved bands, and we show the bands at +109 and +125 cm^{-1} as a typical representatives for the bands in this region in Figs. 6.7 and 6.8. The vibronic band at +3 cm^{-1} in Fig. 6.4 features a conspicuously different rota-
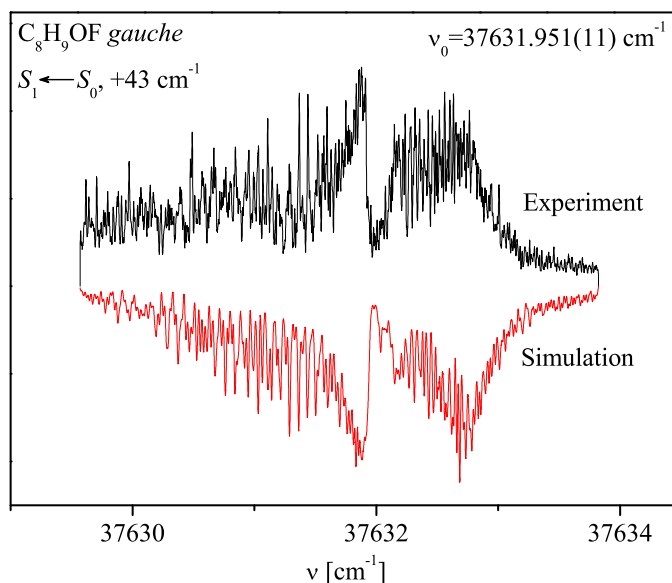
Figure 6.5: *High-resolution two-color UV R2PI spectrum of the band at +43 cm^{-1} recorded at m/z=140. The band is assigned to a progression of the origin of the gauche conformer **1** (See Fig. 6.9) of the 2-oFPE monomer with its rotationless transition centered at 37 631.951(11) cm^{-1}. Upper trace: experimental spectrum. Lower inverted trace: best-fit simulated spectrum yielding the parameters in Table 6.1 (for details, see text).*
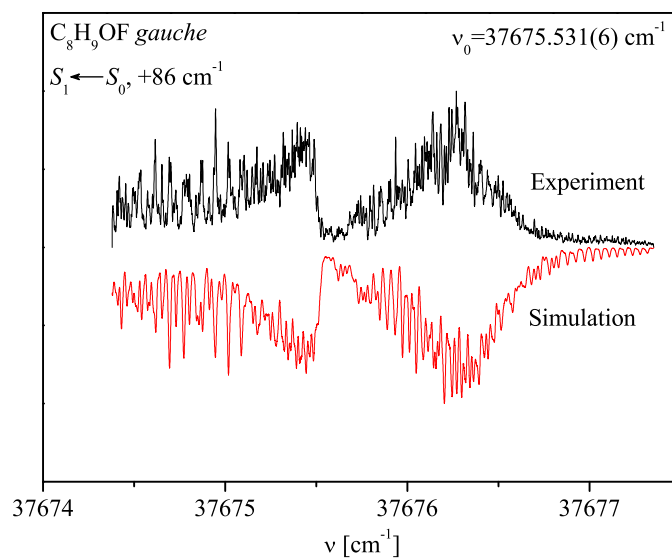

Figure 6.6: *High-resolution two-color UV R2PI spectrum of the band at +86 cm^{-1} recorded at m/z=140. The band is assigned as the second overtone of the band at +43 cm^{-1} the gauche conformer **1** (See Fig. 6.9) of the 2-oFPE monomer with its rotationless transition centered at 37 675.531(6) cm^{-1}. Upper trace: experimental spectrum. Lower inverted trace: best-fit simulated spectrum yielding the parameters in Table 6.1 (for details, see text).*

Figure 6.7: *High-resolution two-color UV R2PI spectrum of the band at +109 cm^{-1} recorded at m/z=140. The band is assigned to a combination mode of the gauche conformer **1** (See Fig. 6.9) of the 2-oFPE monomer with its rotationless transition centered at 37 698.995(7) cm-1. Upper trace: experimental spectrum. Lower inverted trace: best-fit simulated spectrum yielding the parameters in Table 6.1 (for details, see text).*
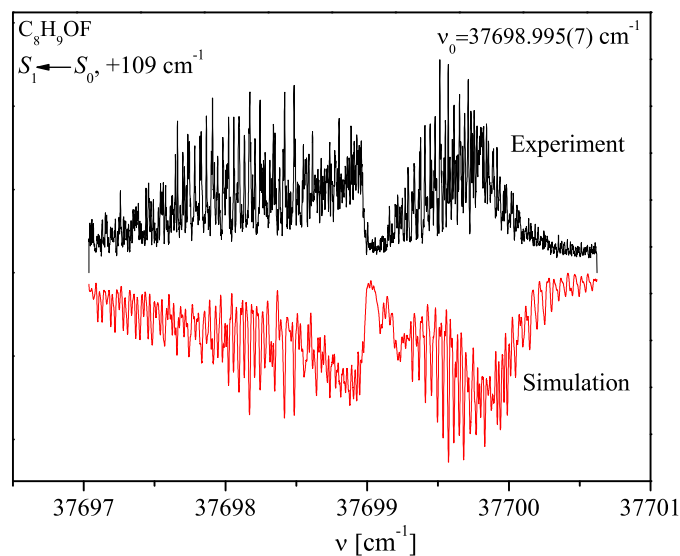

Figure 6.8: *High-resolution two-color UV R2PI spectrum of the band at +125 cm^{-1} recorded at m/z=140. The band is assigned to a combination mode of the gauche conformer **1** (See Fig. 6.9) of the 2-oFPE monomer with its rotationless transition centered at 37 713.896(7) cm-1. Upper trace: experimental spectrum. Lower inverted trace: best-fit simulated spectrum yielding the parameters in Table 6.1 (for details, see text).*
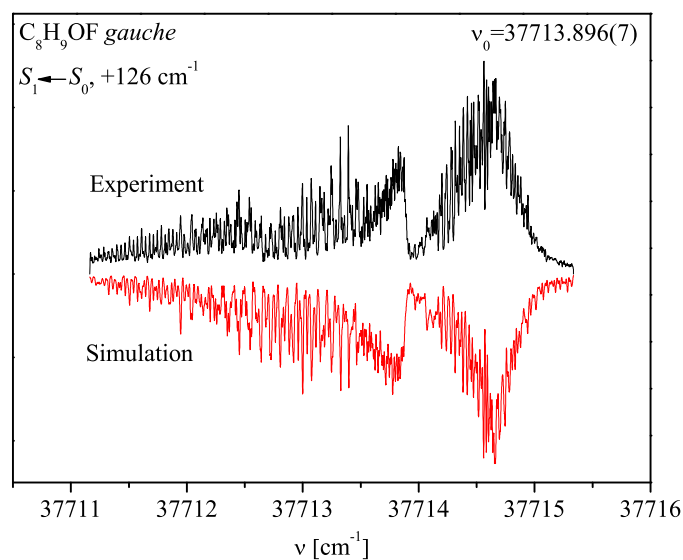
tional structure from the one of the above-discussed bands, which cannot be attributed solely to a different transition moment ratio. The spectrum consists of irregularly spaced peaks formed by bunching of single rotational lines superimposed on a broad background. It features strong P and R branches and a relatively weak Q branch. Due to its low intensity, the signal-to-noise ratio of this spectrum is smaller compared to the one of the other highly resolved spectra presented here. From the profile, the spectrum can be assigned as a mixed *a*-, *b*-, and *c*-type with significant *b* contribution in variance with the other bands presented above. To analyze the spectrum, we employed the same computer-assisted fit procedure we used also for the other bands. Presumably, this band originates from a different conformation in the cold molecular beam and for this reason, to aid-in the fit, we used as initial values for the rotational constants the ones obtained from theoretical predictions for some of the next-in-energy conformers (conformers **7** and **9**). The simulated stick spectrum was convoluted with a Gaussian profile with a FWHM of 210 MHz. The insufficient signal-to-noise ratio, however, precluded the unambiguous assignment of this band to one of the two conformations since the use of their theoretically predicted parameters as starting values for the fits yielded very similar rotational profiles. All attempted fits employing as starting values the parameters corresponding to the other theoretically predicted conformations (**1**, **2**, **3**, **4**, **5**, **6**, and **8**) failed to reproduce the experimental spectrum. That is why, the band can be attributed to either conformer **7** or conformer **9**.

6.3.3 *Ab initio* Calculations

The GAUSSIAN 03 suite of programs [82] and the TURBOMOLE program package for *ab initio* electronic structure calculations [115] have been employed to theoretically investigate the conformational structure, vibrational modes, and energetics of the 2-*o*FPE monomer. To assign the stable conformations of the species, we first performed a two dimensional grid search yielding the potential-energy surface (PES) corresponding to various shapes of the side chain. The grid search was performed at the MP2/cc-pVDZ level of theory including scans of the C2C7C8O9 and C7C8O9H19 dihedral angles from 0 to 360 with an increment of 10.The C3C2C7C8 dihedral angle was kept fixed at 90. The PES consisting of 1296 points is depicted in Fig. 6.9 (the PES is shown inverted for the sake of a better visualization). It features nine potential-energy minima (maxima in Fig. 6.9) implying nine stable conformational structures. The latter can be subsumed into three groups: *opposite gauche*, anti, and *adjacent gauche*, each of them containing three different conformations. In the*opposite gauche* conformations, the side chain is in a *gauche* geometry on the*opposite* side of the F atom and the dihedral angle C2C7C8O9 is ~ 60 for all of them (see insets in Fig. 6.9, conformers **1**, **2**, and **3**). The anti conformers (see Fig. 6.9, conformers **4**, **5**, and **6**) are characterized by an extended side chain away from the benzene ring with their dihedral angle C2C7C8O9 being ~ 180. In the case of the *adjacent gauche* conformations, the side chain is in a *gauche* geometry on the same side of the F atom and the dihedral
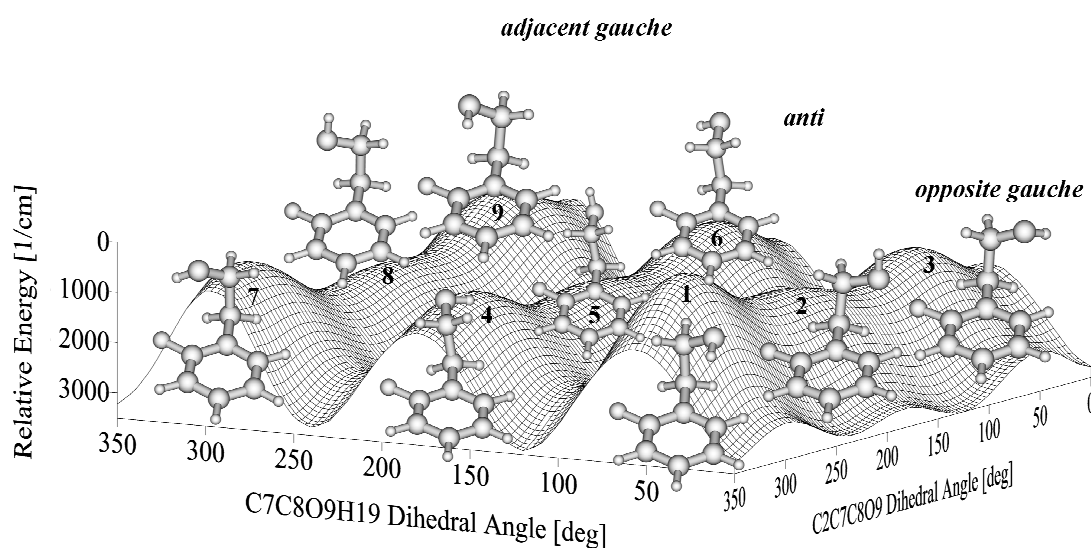
Figure 6.9: *Potential-energy surface (inverted for the sake of a better visualization) as a function of the C2C7C8O9 and C7C8O9H19 dihedral angles of the 2-oFPE monomer. The gauche and anti conformations are separated by a high potential barrier in the C7C8 coordinate. The nine energetically most favorable conformations of the 2-oFPE monomer have been fully geometrically optimized in their ground, S_0, electronic state at the MP2/ccpVDZ level of theory. The fully optimized structures are depicted on their corresponding minima (maxima in the Figure) on the potential-energy surface.*

angle C2C7C8O9 is ~ -60 for the three species in the group (conformers **7**, **8**, **9**). The species within each of the groups differ from each other by the orientation of the terminal OH group (dihedral angle C7C8O9H19). The global (deepest) minimum corresponds to the *opposite gauche* conformer (conformer **1**), in which the OH group of the side chain is away from the F atom and points to the π electrons of the benzene ring. The other two minima separated from each other and from the global minimum by low barriers also correspond to *opposite gauche* conformers. It is worthwhile pointing out that the conformations within the groups are separated from each other by low potential barriers, while high potential barriers (ridges along the C2C7C8O9 coordinate) sever the *opposite gauche*, anti, and *adjacent gauche* species from one another. All nine identified stable conformations of the 2-oFPE monomer have been further theoretically explored by performing a full structural optimization, frequency analysis, and calculation of their energetics in the ground, S_0, electronic state using MP2 level of theory with cc-pVDZ basis set. Full structural optimization and frequency analysis for all species have been carried out also for the first excited, S_1, electronic state employing the CIS/cc-pVDZ level of theory. The values of some typical interatomic distances, planar and dihedral angles defining the conformational structure of the 2-oFPE monomer, the rotational constants, the transition moment ratio, and the

Parameter	Conformer 1		Conformer 2		Conformer 3		Conformer 4		Conformer 6		Conformer 7		Conformer 9	
	S_0	S_1	S_0	S_1	S_0	S_1	S_0	S_1	S_0	S_1	S_0	S_1	S_0	S_1
r (H19C1 or H19F11) (Å)	2.63	2.77	...	...	...	...	...	...	...	...	2.33	2.63	2.70	3.20
r (C3F11) (Å)	1.36	1.32	1.36	1.32	1.36	1.32	1.36	1.32	1.36	1.32	1.36	1.32	1.35	1.31
α_1 (C1C2C7) (deg)	122.1	122.1	122.0	122.3	122.3	122.8	122.7	122.3	122.6	122.2	122.4	122.2	121.7	121.5
α_2 (C2C7C8) (deg)	110.5	113.9	112.0	114.8	111.8	115.6	111.6	113.4	111.6	113.4	111.8	113.9	110.8	113.9
α_3 (C7C8O9) (deg)	112.0	113.0	107.3	108.9	112.5	113.8	112.5	111.9	112.4	111.8	113.0	113.3	112.5	113.2
α_4 (C8O9H19) (deg)	105.7	109.1	107.0	109.6	106.1	109.1	106.2	109.4	106.1	109.3	106.6	109.6	105.9	110.0
τ_1 (C3C2C7C8)	85.1	93.3	97.0	107.5	93.0	127.8	76.8	86.3	78.2	87.2	83.8	87.3	94.8	109.6
τ_2 (C2C7C8O9)	60.6	62.9	66.2	68.4	62.1	70.5	-177.8	-179.7	177.4	176.3	-53.3	-58.0	-60.9	-65.5
τ_3 (C7C8O9H19)	-61.9	-66.7	-169.7	171.6	67.7	67.6	-64.2	-67.5	65.4	68.3	-50.9	-55.6	60.3	66.5
A (cm^{-1})	0.06645	0.06827	0.06701	0.06964	0.06672	0.07141	0.08485	0.08408	0.08439	0.08428	0.07400	0.07417	0.07078	0.07073
B (cm^{-1})	0.03631	0.03462	0.03556	0.03378	0.03543	0.03261	0.02811	0.02780	0.02811	0.02794	0.03552	0.03456	0.03528	0.03368
C (cm^{-1})	0.02676	0.02546	0.02544	0.02425	0.02567	0.02316	0.02241	0.02211	0.02240	0.02221	0.02795	0.02728	0.02785	0.02668
$\mu_a^2 : \mu_b^2 : \mu_c^2$	...	91:2:7	...	95:1:4	...	93:5:2	...	94:2:4	...	95:1:4	...	90:9:1	...	91:0:9
E_{rel} (cm^{-1})	0	...	573.2	...	666.9	...	607.6	...	503.7	...	252.6	...	413.4	...
E_{rel} (including ZPVE) (cm^{-1})	0	...	487.4	...	613.1	...	566.7	...	466.8	...	257.3	...	382.2	...

Table 6.2: *Theoretical interatomic distances, d, planar angles, α, dihedral angles, τ, and rotational constants for the ground, S_0, and the first excited, S_1, electronic state of the gauche and anti conformers of the 2-oFPE monomer calculated at the MP2/cc-pVDZ and CIS/cc-pVDZ level of theory, respectively. The electric dipole transition moment (TM) ratio $\mu_a^2 : \mu_b^2 : \mu_c^2$ has been obtained from CIS/cc-pVDZ and CIS/cc-pVDZ calculation of the optimised geometry of the 2-oFPE monomer. Relative energies, E_{rel} of the seven most stable conformational structures of the 2-oFPE monomer without and with inclusion of the zero-point vibrational energy have been obtained from MP2/cc-pVDZ level of theory.*

relative energies without and with the zero-point vibrational energy (ZPVE) are summarized in Table 6.2. The ZPVEs have been calculated using appropriate for the employed level of theory scale factors. [93, 94] A compelling argument that the theoretically predicted structures indeed correspond to potentialenergy minima is the presence of all-positive vibronic frequencies in the ground, S_0, electronic state. The normalmode frequencies up to 1000 cm^{-1} of all theoretically predicted stable conformers are listed in ascending order in Table 6.3. To ascertain the reliability of our theoretical results we performed single-point energy calculations for all already optimized nine conformations at the MP2/aug-cc-pVDZ level of theory. These results showed that conformer **1** is again the most stable structure but some reordering of the next-in-energy conformations was present, in particular, conformer **7** moved to the fourth position. Since we are concerned only with the lowest-energy conformations whose presence in the cold molecular beam can be experimentally verified, we performed a full structural optimization of conformers **1**, **7**, and **9** at the MP2/aug-cc-pVDZ level of theory. These calculations yielded the following ordering of the discussed conformations according to their energy: conformer **1**, **9**, and **7**, the latter two being spaced from the most stable one by 406 and 465 cm^{-1}, respectively. We performed also a test calculation for the excited state by optimizing the structure and calculating the normal-mode frequencies for the most stable conformer **1** at the CC2/aug-cc-pVDZ [116, 117] and MP2/aug-cc-pVDZ level of theory, respectively. The so-optimized structure does not differ much from the one optimized at the CIS/cc-pVDZ level of theory. A small discrepancy between the two levels of theory was observed only for the lowest-frequency mode, which can be attributed to the inherent anharmonicity of the torsional motion corresponding to this mode.

6.4 Discussion

Due to the reduced symmetry of the 2-*o*FPE, its potential-energy landscape (see Fig. 6.9 and Table 6.2) is more complicated compared to the ones of 2-PE and 2-*p*FPE, and it features nine potential-energy minima. The theoretically predicted most stable geometry of the 2-*o*FPE monomer without and with inclusion of the ZPVE is that of the *opposite gauche* conformer 1, in which the terminal OH group of the side chain points to the aromatic ring. The structure is assumed to be stabilized by an intramolecular nonclassical hydrogen bond between the OH group and the delocalized π electrons of the benzene ring, similarly to the cases of the nonfluorinated 2-PE (Refs. [46, 70] and Chapter 3) and the para-fluorinated 2-FPE.(see Chapter 4) The second-in-energy conformation is the *adjacent gauche* conformer **7** lying 257 cm^{-1} above the lowest-energy geometry. The skew orientation of the terminal OH group of the side chain suggests the existence of a σ hydrogen bond between this OH group and the fluorine atom at the *ortho* position of the aromatic ring stabilizing this conformer. The next-in-energy structure of the 2-*o*FPE monomer corresponds to conformer **9**, which also belongs to the group of the

adjacent gauche species. In this case, the structure resembles very much the one of conformer **1** and, for this reason, it is very likely that this geometry is also stabilized by a nonconventional intramolecular hydrogen bond between the OH group and the π electrons of the aromatic ring. The lowest-energy *anti* structure is conformer **6** with its side chain pointing to the side of the fluorine atom. It is at the fourth position and is distanced away by 467 cm^{-1} from the most stable conformer (conformer **1**), and by $\sim$ 80 cm^{-1} from the preceding geometry (conformer **9**). Conformer **6** is followed by the opposite *gauche* conformer **2** with the OH group in an upright position, the energy gap between them being only 20 cm^{-1}. The difference in the energies is small and reordering of these two conformations upon altering of the model theory and the basis set is likely to occur. The next higher-energy conformation is the *anti* conformer **4** with its OH group pointing to the opposite side of the fluorine atom, which lies 566 cm^{-1} above the most stable structure. Two closely spaced conformations follow, conformer **5** with a completely extended side chain away from the aromatic ring and the *opposite gauche* conformer **3**, lying at 610 and 613 cm^{-1}, respectively, above the most stable structure. The energy gap between these two species is very small and, for this reason, the ordering of the conformations may depend on the employed level of theory. It is interesting also to point out that the inclusion of the ZPVE correction also influences the energy ordering of the species, in variance with the case of the lower-lying conformations. The highest-energy conformation is the *adjacent gauche* conformer **8** with its terminal OH group directed upwards. This conformer is less stable by 848 cm^{-1} compared to the lowest-energy one. A preliminary identification of the observed conformations in the cold molecular beam can be made by comparison of the measured vibrational band positions in the low-resolution R2PI spectrum (see Fig. 6.2) with the theoretically predicted frequencies for the first excited, S_1 electronic state (see Table 6.3). The most prominent band at 37 589 cm^{-1} is assigned to the most stable opposite *gauche* conformer **1** as will be confirmed by the rotational analysis below. Two blueshifted vibronic bands at +43 and +86 cm^{-1} are observed in the R2PI spectra. The band at +43 cm^{-1} perfectly matches the theoretically predicted lowest frequency of 43 cm^{-1} corresponding to the torsional mode of the side chain about the C2C7 bond in conformer **1**. The band at +86 cm^{-1} can be confidently assigned to the first overtone of the above-described torsional mode. The R2PI spectrum in Fig. 6.2 features a weak band at +80 cm^{-1}, which we tentatively attribute to OH-π bending mode in conformer **1** which is theoretically predicted to be at +83 cm^{-1}. There are several weak bands at 109, 125, and 135 cm^{-1} observed in the R2PI spectra. The band at +135 cm^{-1} can be readily assigned to the low-frequency torsional mode about the C7C8 bond in conformer **1**, which is calculated to be at +134 cm^{-1}. Further, we assume that the bands at +109 and +125 cm^{-1} also originate from the same conformer though they cannot be assigned to its fundamental normal-mode vibrations (see Table 6.3). In this case, we put forward the hypothesis that these bands stem from anharmonic couplings involving overtones and frequency mixing of the normalmode vibronic bands at +43, +80, and +135 cm^{-1}. The assumption that the above bands descend from the same conformer is substantiated by the analysis of their highly resolved electronic spectra discussed below. An

interesting feature emerges from the right wing of the strongest band. This band is blueshifted by 3 cm^{-1}. Since there is no theoretically predicted conformation featuring very low-frequency vibrations, we ascribe the weak band at +3 cm^{-1} as the origin band of another conformation. Another prominent vibronic band detected in laser-induced fluorescence excitation (LIF) spectrum [114] is located at +30 cm^{-1}. The same band, however, appears only as a small bump in the R2PI spectrum (see Fig. 6.2). This suggests that this band may originate from a conformer whose relaxation dynamics is different for the different buffer gases, He and Ar, used in the LIF and R2PI experiments, respectively. It is plausible, however, to assume that this band may stem also from the conformation bringing forth the +3 cm^{-1} band in [114]. In this case the respective conformer is expected to have a lowest frequency of $\sim$ 27 cm^{-1} in the first excited, S_1, electronic state. Inspecting the table with the calculated vibrational frequencies (see Table 6.3), we can find that there are three conformers having frequencies in the vicinity above 27 cm^{-1}; these are conformers **2**, **4**, and **9**, the latter being the most likely one since it is one of the low-energy conformations. To verify or rule out this tentative assignment additional arguments will be adduced below. To corroborate the above tentative assignments as well as to complement the missing information and to make reliable implications on the structure and relaxation dynamics of the observed conformations of the 2-*o*FPE monomer, the data from the dispersed fluorescence (see our paper) and the highly resolved R2PI (see Figs. 6.3- 6.8) experiments must be analyzed and discussed. The dispersed fluorescence (DF) spectra obtained upon probing the 0_0^0, +3, and +30 cm^{-1} bands are very similar [see our paper] both in terms of band positions and band intensities. An assignment of these bands based on their DF spectra and comparison with the theoretically predicted frequencies of nine stable conformers of 2-*o*FPE is given in our combined paper with V. Ramanathan and T. Chakraborty. The DF spectra [114] produced as a result of the excitation of the bands at 0_0^0, +43, and +86 cm^{-1} feature the same peak spacing but different intensity distributions. The interpretation in this case is rather straightforward: the three bands belong to the same conformation, and hence have the same vibrational structure in the ground electronic state. The variation in the intensity distribution descends from different Franck-Condon factors for the different vibronic states in the first excited electronic state. The most rigorous and unambiguous assignment is provided by high-resolution experiments. We measured under high resolution the R2PI spectra of the bands at 0_0^0, +3, +43, +86, +109, +125, and +135 cm^{-1}. The rotational structures of all bands with the exception of the band at +3 cm^{-1} have been successfully fitted and the respective molecular parameters have been obtained. The rotational constants for the ground, S_0, and the first excited, S_1, electronic state obtained from the fits of the bands under scrutiny (see Table 6.1) are very similar pointing that all these bands originate from the same conformer. Slight differences might originate from the additional excitation of different vibrations. Comparing the experimental rotational constants obtained from the fit with the corresponding rotational constants for the theoretically predicted conformations (see Table 6.2), we find that the best match is observed for the most stable opposite *gauche* conformer **1**. This provides a compelling argument that conformer **1** gives rise to the most intense band at 37 589.18 cm^{-1} as well as to

	Conformer 1		Conformer 2		Conformer 3		Conformer 4		Conformer 5		Conformer 6		Conformer 7		Conformer 8		Conformer 9	
	S_0	S_1	S_0	S_1	S_0	S_1	S_0	S_1	S_0	S_1	S_0	S_1	S_0	S_1	S_0	S_1	S_0	S_1
	46	43	27	32	17	21	61	38	62	40	60	39	81	65	63	50	46	38
	92	83	100	89	95	97	97	79	97	80	96	80	109	81	90	71	80	68
	150	134	143	133	149	146	109	107	106	106	109	107	147	128	143	127	143	129
	201	185	202	188	198	192	207	182	208	182	207	181	213	192	205	188	202	187
	276	224	244	231	269	244	207	223	271	224	290	223	274	223	257	222	275	224
	336	308	271	263	316	257	207	297	287	286	311	307	312	297	273	270	318	316
	373	364	337	291	357	346	328	330	317	306	321	320	359	340	322	308	363	341
	417	383	408	378	411	370	355	348	333	341	360	356	419	373	417	371	423	369
	441	410	436	402	439	401	451	384	449	383	450	384	435	403	433	406	435	401
	494	423	497	423	499	429	473	419	474	417	474	417	502	429	501	428	501	430
	528	514	524	514	525	516	534	494	534	493	534	494	525	429	523	501	522	525
	551	531	548	526	550	530	546	536	546	535	545	535	553	548	550	527	549	532
	583	556	582	550	583	551	603	567	603	566	602	566	584	553	583	549	581	548
	689	628	690	618	691	617	688	617	689	617	687	616	684	626	686	581	684	622
	744	671	747	670	746	674	765	662	765	663	765	664	750	660	752	622	665	665
	766	722	764	731	761	732	775	717	780	719	777	718	765	719	765	660	768	715
	837	759	836	764	834	765	798	778	808	776	796	777	827	765	831	718	831	764
	854	782	851	779	846	784	856	810	856	811	856	811	854	777	854	766	857	781
	886	873	886	871	884	866	864	842	865	855	864	841	881	869	887	776	882	873
	926	906	924	902	919	909	928	902	929	901	929	902	926	902	925	857	931	908
	945	938	942	944	941	936	944	904	944	905	945	904	943	931	941	874	945	929
	958	1005	978	1021	976	1028	1021	1059	1035	1060	1024	1060	971	1022	974	1016	958	1007
	1038	1065	1047	1068	1023	1071	1052	1082	1044	1072	1046	1079	1034	1063	1045	1064	1039	1063

Table 6.3: *Theoretical predicted normal-mode vibrational frequencies in cm^{-1} for the ground, S_0, and the first excited, S_1, electronic state of the gauche and anti conformers of the 2-oFPE monomer calculated at the MP2/cc-pVDZ and CIS/cc-pVDZ level of theory, respectively. The vibrational frequencies for the ground, S_0, electronic state have been downscaled using the appropriate scale factor of 0.9970 [Ref. 32]. The frequencies for the excited state have not been rescaled since no reliable scale factors for the CIS/cc-pVDZ level of theory are available. All frequencies are given in cm^{-1}.*

the bands at +43, +86, +109, 125, and +135 cm^{-1}. Some discrepancy between the experimental and the observed parameters is found for the transition moment ratio, which stems most likely from the insufficient accuracy of the calculations in the excited electronic state. No convincing fit of the rotational structure of the band at +3 cm^{-1} is available due to the low signal-to-noise ratio of the experimental spectrum (see Fig. 6.4). All attempts for fitting the spectrum using as starting parameters the ones corresponding to the most stable conformer failed. The best visual agreement was achieved only when employing as starting values the parameters of the second-in-energy conformer **7** and the third-in-energy conformer **9**. From energy considerations, conformer **7** is the more favorable one. Its theoretical vibronic frequencies, however, do not match the ones experimentally observed in the DF spectrum (for details, see our paper). Though conformation **9** is energetically less favored, its rotational constants and vibrational frequencies are in a good accord with the experimental observations. That is why we tentatively assign the band at +3 cm^{-1} as originating from conformer **9**. In our experiment, we have identified two conformations and we have indications for a third one out of nine theoretically predicted stable structures. The intensity ratio of the three conformers is ∼ 94:5:1. This invokes the question why preferably only the most stable conformation is present in the beam. A plausible explanation can be found in the shape of the PES and in the relaxation dynamics during the process of the adiabatic expansion. The PES is characterized by three troughs (ridges in Fig. 6.9) hosting the three groups of conformations, the opposite *gauche*, the *anti*, and the adjacent *gauche* ones. The conformations within each of the above groups are separated by low potential barriers, which facilitates the relaxation from the higher-lying to the lowest-energy conformation in the respective group. The conformations in the different groups, however, are separated by high potential barriers, which should preclude their interconversion. Thus this mechanism reduces the total number of possibly observed conformations to three, corresponding to the lowest-energy structures within each of the three groups. Next, we have to explain why the two dominant conformations present in the cold molecular beam are *gauche* structures. This result is in striking variance with the cases of nonfluorinated 2-PE (Ref. [46]) and *para*fluorinated 2-FPE (Ref. [104]) where one *gauche* and one anti conformer have been observed. As pointed out above, due to the reduced symmetry of the species, the *ortho*fluorinated 2-FPE provides a larger number of distinct conformational structures compared to the nonfluorinated and the *para*-fluorinated counterparts. Taking into account the energy ordering, we find that the lowest-energy anti structure is at the fourth position being preceded by three *gauche* conformations (see Table 6.2). The existence of several conformations with lower energy implies more relaxation channels, which eventually leads to a depletion of the population of the anti conformation in the cold molecular beam close to the detection limit. An important aspect that deserves attention is the comparison between the considered conformers and the nonfluorinated 2-PE and the *para*fluorinated 2-FPE. As it was shown in our recent studies, the most stable structures of both 2-PE (see Chapter 3 and [46]) and the 2-*p*FPE (see Chapter 4) are stabilized by a nonclassical OH···π hydrogen bond between the terminal OH group of the side chain and the π electrons of the aromatic ring, and the stability of

this bond is almost unaffected by the *para* substitution with fluorine. The *ortho* fluorination, in addition to the OH···π bond, provides the feasibility for a σ hydrogen bond between the terminal OH group and the *ortho* substituted fluorine atom (conformer **7**). Even in this case, we have found that the lowest-energy opposite *gauche* conformer is stabilized by a nonclassical OH···π hydrogen bond rather than by a σ bond. The result clearly demonstrates that even under the conditions of a significantly distorted π electron density in the benzene ring brought about by the presence of the strongly electronegative fluorine atom and the favorable geometry enabling the formation of a competing σ bond, the nonclassical OH···π bond prevails and remains important for the sustaining of the conformational structure of the flexible molecule.

6.5   Summary and conclusions

In this chapter we have investigated the influence of fluorine substitution on the weak intramolecular forces stabilizing certain conformational structures of flexible molecules. As a prototype system, we have chosen 2-phenylethanol, which is the hydroxyl analog of the simplest neurotransmitter, 2-phenylethylamine. *Ortho* fluorinated 2-phenylethanol has been investigated by combination of low- and high-resolution resonance enhanced two-photon ionization experiments supported by high-level quantum chemistry *ab initio* calculations of the energetics, structure, and normal-mode vibrational frequencies. All vibrational bands observed in the low-resolution R2PI spectra have been preliminary assigned in a first step by comparison of the experimental band positions with the theoretically predicted frequencies in the first excited electronic state. Further arguments are provided by the comparison of the observed vibrational band positions in the DF spectra with the theoretical frequencies in the ground electronic state. [114] The final assignment relies on the comparison of the rotational constants obtained from the fits of the highly resolved spectra with the ones theoretically predicted for the optimized conformational structures. We have found that the most abundant conformer in the cold molecular beam is the theoretically predicted most stable one corresponding to a *gauche* structure stabilized by a nonclassical OH···π hydrogen bond between the terminal OH group of the side chain and the π electrons of the benzene ring. Higher-energy *gauche* and *anti* conformers have been tentatively identified, although they weakly contribute to the total concentration of 2-*ortho*fluorophenylethanol. No detectable signals stemming from other conformations have been observed in our experimental results. The most likely reason for observing predominantly only one and detecting other two out of nine theoretically predicted conformations is the complex shape of the PES and the conformational relaxation channels leading to interconversion of the higher-energy conformations to the lowest-energy ones. The results show that even in the case of the *ortho* substitution with a strongly electronegative atom leading to a significant distortion of the electron density in the aromatic ring and providing a convenient configuration for the formation of a competing σ bond, the nonclas-

sical π bond still prevails and remains the dominant intramolecular binding motif. In conclusion, this demonstrates the importance and robustness of the OH$\cdots\pi$ bonds for the stabilization of conformational structures of flexible molecules.

Chapter 7

Singly Hydrated Clusters of 2-*para*-fluorophenylethanol and 2-*ortho*-fluorophenylethanol Studied by High-Resolution UV Spectroscopy and *ab initio* Calculations

The singly hydrated complexes of the flexible prototype molecules, 2-para-fluorophenylethanol (2-pFPE) and 2-ortho-fluorophenylethanol (2-oFPE) have been investigated in a cold supersonic beam by combination of high-resolution two-color R2PI spectroscopy and quantum chemistry ab initio calculations. We have identified the conformational structures of the complexes between 2-pFPE and water, and 2-oFPE and water, which correspond to water binding to the most stable gauche conformers in both cases. No detectable structural changes of the host molecules have been observed upon attachment of a single water molecule.For the 2-oFPE·H$_2$O complex we have observed an additional structure with one of the next-in-energy gauche conformers of the monomer which pointed to the stabilizing effect of the water for monomer's conformer with lower abundance.

7.1   Introduction

Water as a biological universal solvent has attracted the attention of the scientific society. A variety of spectroscopic methods [4, 6–9, 14, 15, 76, 118] have been used in the determination of the most abundant water clusters of different biologically relevant molecules produced by microsolvation in a supersonic jet [10–13, 16, 85, 119]. A step forward in the assignment of these conformers is provided by gas phase UV high-resolution resonance enhanced two-photon spectroscopy as a sensitive tool for revealing the structural geometries of the hydrated clusters. In Chapter 3 an assignment of the dimeric water cluster of 2-phenylethanol (2-PE) was made on the basis of comparison of the parameters of the partially rotationally resolved vibronic spectrum with the predicted ones from high-level *ab initio* calculations. Here, this approach is used for the determination of the structure of the singly hydrated clusters of 2-*para*-fluorophenylethanol (2-*p*FPE) and 2-*ortho*-fluorophenylethanol (2-*o*FPE), most stable monomeric structures of which were studied in Chapters 4 and 6. As mentioned already, the main goals of such investigation are the effect of the water attachment on the monomer's conformational shape, the type of *inter*molecular interaction and the possible stabilizing effect of the water on particular conformers. The mass resolution of our experimental setup allows measuring of UV highly resolved rovibrational spectra at both mass channels: water cluster and monomer, respectively. Thus, issues as overlapping of close lying vibrational levels and fragmentation of larger clusters can be directly resolved.

7.2   Experiment and Data Processing

The mass-selected resonant two-photon ionization (R2PI) apparatus used in the present study has been thoroughly described in Section 2.1. Liquid 2-*p*FPE (97%) obtained from Aldrich and used without further purification, was vaporized at 100 °C and mixed with 30 mbar of water vapors in a stream of argon at a stagnation pressure of about 3.2 bars. Following free-jet expansion into vacuum through a pulsed-operated heatable nozzle with orifice diameters of 500 μm, the rotational temperature was found to be approximately 6-9 K under the conditions employed. For the one-color low-resolution spectra photons were used, generated by frequency doubling in a BBO I (Beta Barium Borate) crystal of the output pulses of a commercial broadband ($\Delta \upsilon$ ~ 0.4 cm^{-1} (FWHM)) dye laser (Lambda Physik FL2002) operated with a Coumarin 153 laser dye. The first color excitation photons involved in the two-color high-resolution spectra were generated by frequency doubling in a KDP crystal of the pulsed amplified output of a continuous wave (CW) single-mode ring dye laser (Coherent, CR 699-21) operated with Coumarin 334. The limited spectral resolution of our scanning UV laser pulses is not sufficient for resolution of single rotational lines in the congested spectra of large molecular complexes. For this reason

we use a computer-based method for fitting of the experimental highly resolved spectra. The algorithm and the computer program elaborated in our group have already been described in Section 2.3. Cross correlation is employed as an evaluation function. For the production of the simulated spectra of the 2-*p*FPE water complex, we ran the program using 300 generations with 500 individuals in a generation.

7.3 Results and Discussion

7.3.1 2-*p*FPE-Water Cluster

Low-Resolution Spectra

Low-resolution one-color resonant two-photon ionization (R2PI) spectra have been recorded at three different mass channels (m/z=140, 158 and 176) under water-in conditions near the S_1 ←—S_0 electronic transition of 2-*p*FPE. The spectra are depicted in Fig. 7.1, where in addition to the water-in spectra, a water-free spectrum of the monomer (m/z=140) is included for comparison (See Fig. 7.1(a)). The spectra shown in Figure 7.1(b), 7.1(c), 7.1(d), were measured under water-in conditions monitoring the 2-*p*FPE· H_2O cluster (m/z=158), 2-*p*FPE· $(H_2O)_2$ cluster (m/z=176) and monomer (m/z=140) mass channels, respectively. The most intense features of the singly hydrated complex are labeled -18 cm^{-1}, -2 cm^{-1}, 53 cm^{-1}, and 76 cm^{-1}, respectively. It has been found that most of these peaks have corresponding ones at the doubly hydrated complex mass channel (Fig. 7.1(b)).For peaks -2 cm^{-1} and 53 cm^{-1} it is clear that they originate from the fragmentation of the 2-*p*FPE· $(H_2O)_2$ complex. Peak -18 cm^{-1} coincides with the shoulder of a broad peak at the mass channel of the doubly hydrated complex. This lead us to the conclusion that -18 cm^{-1} is a mixture of two close-lying bands: one of the 2-*p*FPE· $(H_2O)_2$ and the other one of the 2-*p*FPE· H_2O complex. Only for peak 76 cm^{-1} there is no doubt that it results from the singly hydrated cluster. The clear origin of this vibronic band made it a good candidate for an insight to the conformational shape of the 2-*p*FPE· H_2O species. A comparison between the monomer mass channels spectra (see Fig. 7.1(a), 7.1(d)) recorded under different water conditions can elucidate the nature of some vibronic features observed previously under water free conditions []. All additional peaks appearing at the water-in monomer spectrum (Fig. 7.1(d)) compared to the water-free spectrum (Fig. 7.1(a)) can be easily attributed to the fragmentation of the water complexes and the small bumps in the water-free spectrum (Fig. 7.1(a)) at -40 cm^{-1} and -18 cm^{-1} are assigned as originating from 2-*p*FPE·$(H_2O)_n$ clusters fragmentation. The next level of analysis was to record the high-resolution spectra of the above-discussed bands and to compare them with the results from *ab initio* calculations to demonstrate the preferred binding moiety for the water in the singly hydrated structure.
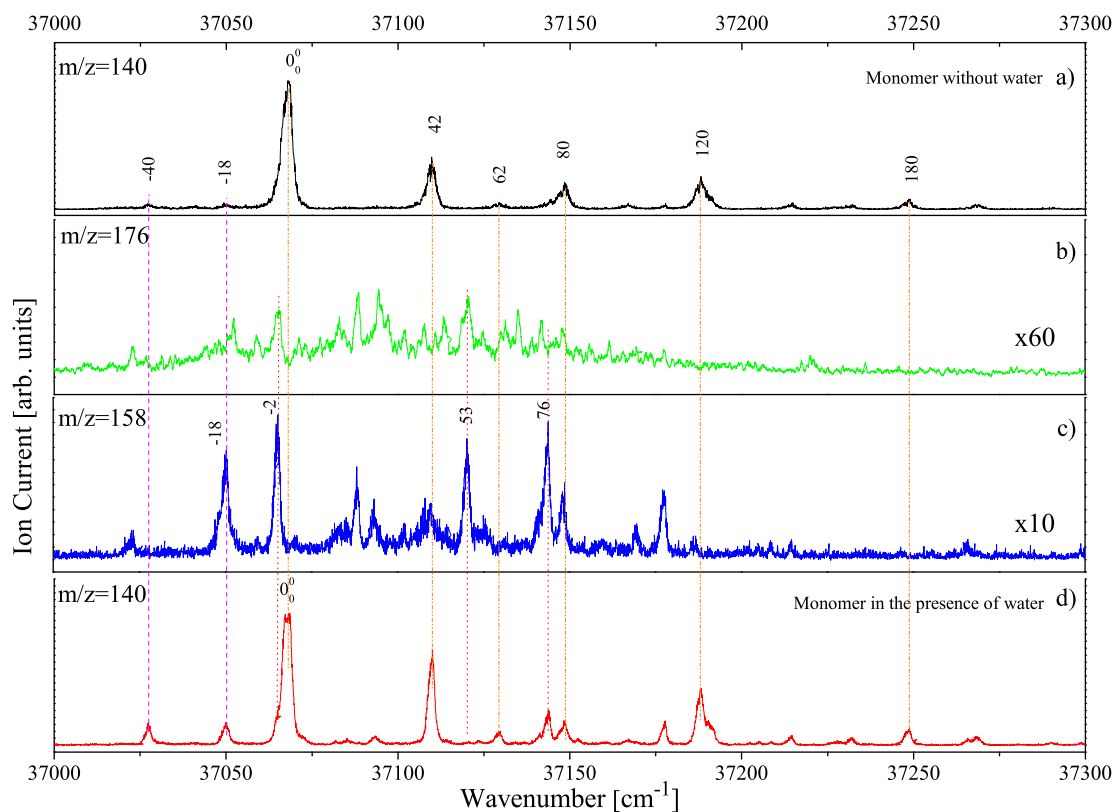
Figure 7.1: *One-color R2PI spectra of the $S_1 \longleftarrow S_0$ electronic transition of the 2pFPE water cluster measured at the monomer (m/z = 140) mass channel under water-free (a) and water-present (d) conditions. One-color R2PI spectra: (c) recorded at m/z=158 mass channel of the 2pFPE·H_2O complex, and (b) recorded at m/z=176 mass channel of the 2pFPE·($H_2O)_2$ complex.*

High Resolution Spectra

The bands at -18 cm^{-1}, -2 cm^{-1}, 53 cm^{-1}, and 76 cm^{-1} were scanned with higher resolution both at the cluster (m/z=158) and monomer (m/z=158) mass channels. The rotationally resolved spectra of the vibronic bands -18 cm^{-1}, -2 cm^{-1}, and 53 cm^{-1} are congested and with poor quality, which precludes the fitting procedure for these bands and their direct assignment to predicted cluster structures. For completeness, their experimental spectra are presented in Figs. 7.2- 7.3 and a visual assessment is made in the discussion Section. The nicely resolved spectrum of band 76 cm^{-1} allows us to perform a computer based fitting procedure and the resulting synthetic spectrum is presented as in inverted trace in Fig. 7.4. The experimental spectrum covers a frequency range of ca. 2.5 cm^{-1} and manifests a well-resolved structure built up of separate peaks
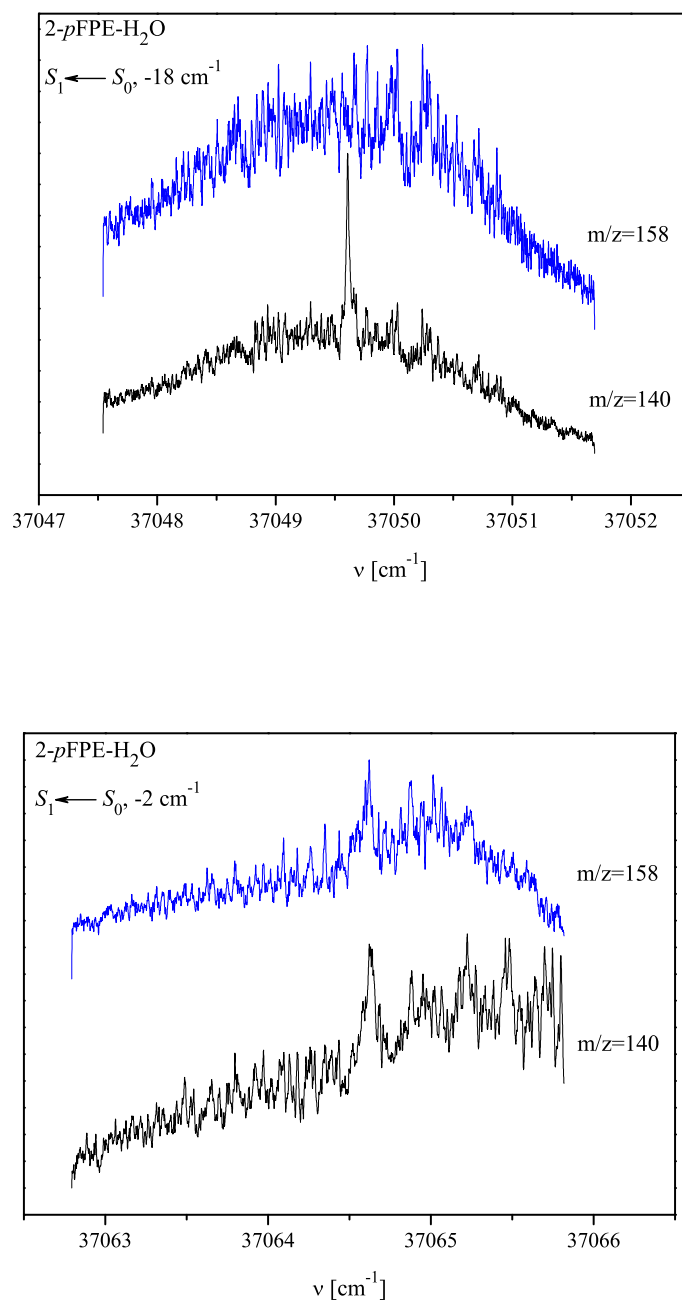
Figure 7.2: *High-resolution two-color UV R2PI spectrum of vibronic bands -18 cm^{-1} (upper picture) and -2 cm^{-1} (lower picture) in Figure 7.1, recorded at mass channels with m/z=140 and m/z=158. For plausible assignment and details, see text.*
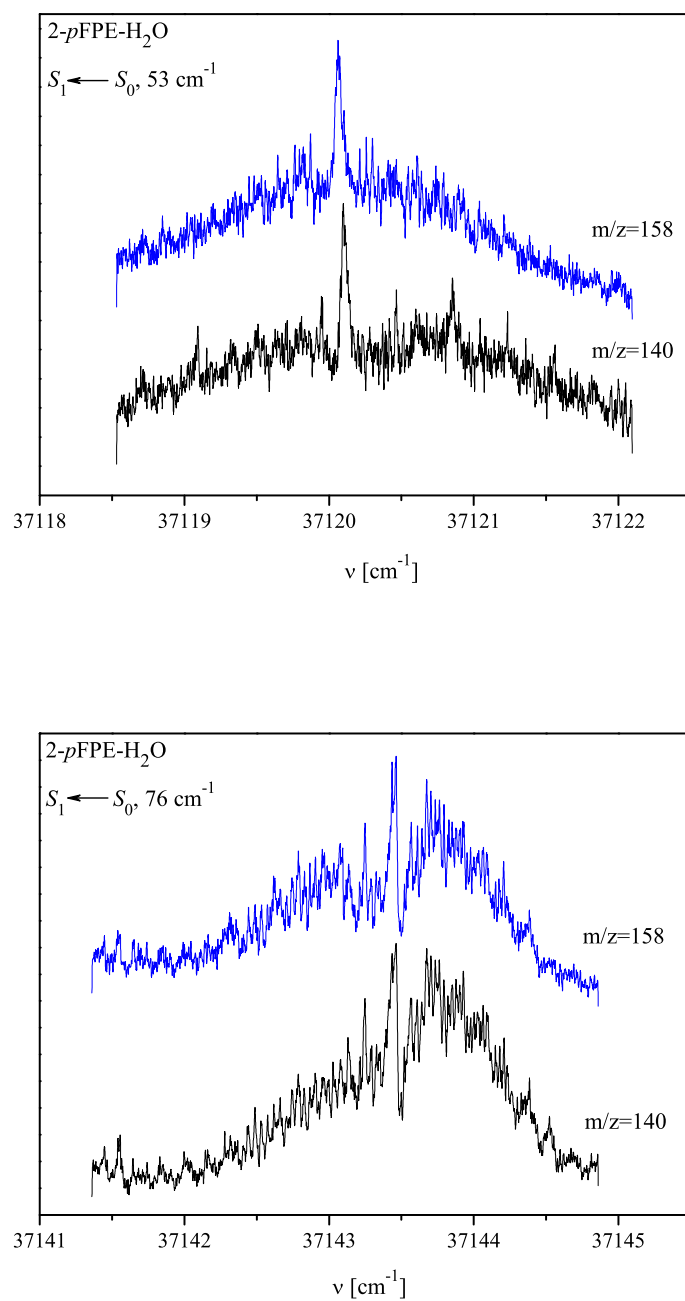
Figure 7.3: *High-resolution two-color UV R2PI spectrum of vibronic bands 53 cm^{-1} (upper picture) and 76 cm^{-1} (lower picture) in Figure 7.1, recorded at mass channels with m/z=140 and m/z=158. For plausible assignment and details, see text.*
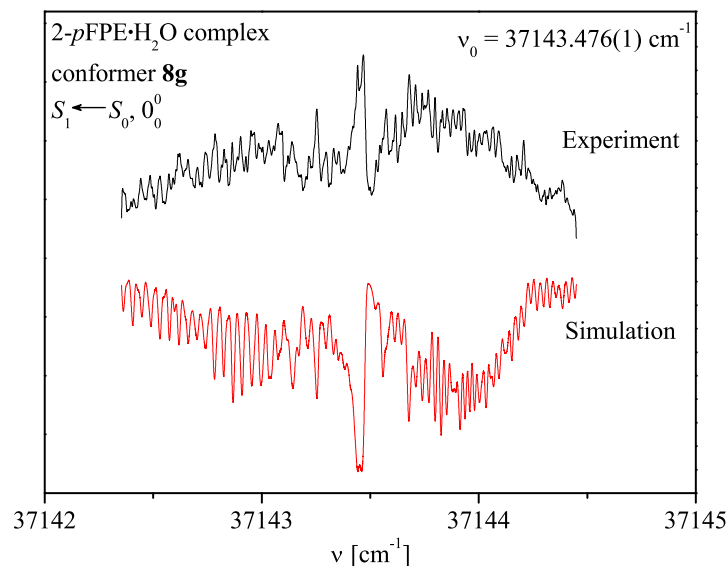
Figure 7.4: *High-resolution two-color UV R2PI spectrum of vibronic band 76 cm^{-1} in Figure 7.1, recorded at m/z = 158. The band is assigned as the 0^0_0 origin band of conformer **8g** of the 2-pFPE·H$_2$O complex with the rotationless transition centered at 37143.476(1) cm^{-1}. Upper trace: experimental spectrum. Lower inverted trace: the best-fit simulated spectrum yielding the parameters in Table 7.1 (for details, see text).*

with a line width of 250 MHz resulting from aggregations of closely situated single rotational lines. The spectrum has a pronounced Q branch in the center, an intense R branch and less intense P branch both with irregular but resolved structures. It was fitted by the routine based on genetic algorithms described in Section 2.3 which produced the molecular parameters of the searched conformeric structure. The simulated spectrum was convoluted by a Gaussian profile with a line width of 160 MHz. The simulation is in a good agreement with the experiment reproducing the individual peak positions, intensities and overall profile of the observed spectrum. The resulting rotational constants for the ground, S_0 and the first excited, S_1, electronic states, the transition moment ratio, the band origin position, ν_0, and the rotational temperature, T, are summarized in Table 7.1.

Ab initio Calculations

The Gaussian 03 program package [] was used for the optimization of various conformations of the 2-pFPE singly hydrated cluster by *ab initio* quantum chemistry calculations.The initial ge-

Parameter	cBand
	76 cm^{-1}
A''	0.0604(15)
B''	0.01934(33)
C''	0.01627(27)
A'	0.0602(12)
B'	0.01891(24)
C'	0.01607(22)
$\mu_a^2 : \mu_b^2 : \mu_c^2$	32:68:0
ν_0 , cm^{-1}	37143.476(24)
T(K)	6.1(6)
Best-fit cross correlation (%)	97

Table 7.1: *Experimental rotational constants for the ground,S_0 (A'', B'', C''), and for the first excited,S_1 (A', B', C'), electronic states, transition moment ratio, $\mu_a^2 : \mu_b^2 : \mu_c^2$, band origin frequency, ν_0, rotational temperature, T, and the best-fit cross correlation obtained from the rotational fit of the band assigned to the 0_0^0 origin of conformer **8g** of the 2-pFPE·H$_2$O complex, shown in Figure 7.5. Numbers in parentheses are standard deviation in units of the least significant quoted digit. The uncertainty for the relative values of μ_a^2, μ_b^2, and μ_c^2 in the transition moment ratio does not exceed 5(%).*

ometries of the water clusters were carefully selected by chemical intuition, exploring possible binding sites of the water molecule to the most stable *gauche* and *anti* monomer structures, observed experimentally and described in Chapter 4. The 2-*p*FPE·H$_2$O complexes were numbered by their probability for appearance. In this way, five water clusters with the *gauche* monomer and two water clusters with the *anti* monomer were optimized in the ground, S_0 and the first excited, S_1, electronic states at the MP2/6-311G** and CIS/6-311** levels of theory, respectively. As a result, five stable cluster structures were determined and subjected to further full geometrical optimizations for both ground, S_0 and and the first excited, S_1,electronic states at MP2/cc-pVDZ and CIS/cc-pVDZ levels of theory, respectively, with an improved electron correlation (see Fig. 7.5). The calculated vibrational frequencies of these five conformers are positive which verifies that they correspond to minima on the potential energy surface.All relevant theoretical parameters of these structures are summarized in Table 7.2. The most stable conformer is conformer **2g**, where the water molecule serves as a bridge between the terminal hydroxyl group and the aromatic ring forming a π-hydrogen bond with the benzene ring and accepting a proton from the OH group of the side chain. The second-in-energy conformer is conformer **8g**, in which the water molecule binds sideways to the 2-*p*FPE *gauche* structure through the formation of a single σ bond donating a proton to the hydroxyl group of 2-*p*FPE. Then the energy order, as follows from the inclusion of the basis set superposition errors (BSSE) and zero-point vibrational energies (ZPVE), is: conformer **3a**, conformer **5a**, conformer **1g**. The inclusion of these corrections

is not affecting the energy order of the first three cluster structures, which are the most probable candidates for observation in the experiment. It only increases the energy distance between the first two conformers, but still 61 cm^{-1} (see Table 7.2) is a negligible difference and may result in reordering upon the change of theoretical level and model.

Discussion

The high-resolution spectrum of band 76 cm^{-1} was recorded simultaneously at the mass channels of the monomer m/z=140 and the mass channel of the singly hydrated cluster m/z=158 (see Fig. 7.4). The two traces are identical which demonstrates the nature of this band as originating form the 2-pFPE$\cdot$ H$_2$O cluster. For our fitting procedure (see Section 2.3), the spectrum monitored at the cluster mass channel was used for further assignment. The fits were started probing the rotational constants for the ground, S_0 and the first excited, S_1, electronic states and the transition moment ratios obtained from the theoretical optimizations of conformers **2g**, **8g**, **3a**, **5a** and **1g** (see Fig. 7.5). The cross correlation ratio between experimental and synthetic spectra reached 97 % when the fit was initiated with the parameters for conformer **8g**. The so received experimental values are in a good agreement with the calculated ones for the above-mentioned conformer, which makes the assignment straightforward.Therefore, band 76 cm^{-1} corresponds to the water cluster structure where the water binds to the terminal hydroxyl group of the flexible tail of the 2-pFPE gauche structure via a single σ hydrogen bond donating a proton to the oxygen of the OH group of the side chain. This position of the water is not unusual, the same binding motif was observed for one of the high-energy water bands of 2-PE (see Chapter 3). An additional argument for the assignment is the proximity of the water molecule to hydrogen atom H10 of the aromatic ring that favors a formation of an additional σ hydrogen bond in which the water is a proton acceptor. This assumption is supported from the well-resolved rotational structure of this band (see Fig. 7.4), typical for rigid or almost rigid complexes stabilized by multiple bonds where tumbling motion is hindered. As a consequence, the predicted small energy gap of 61 cm^{-1} from the most stable conformer (conformer **2g**) can be validated.Comparing the geometrical parameters (interatomic distances, planar angles, and dihedral angles) of the 2-pFPE bare molecule (conformer **1**, see Table 4.2 in Chapter 4) and the complex with water (see Table 7.2), a conclusion for the stability of the 2-pFPE species upon complexation with water can be made. It is clear that the *intra*molecular π-hydrogen bond of the host *gauche* monomer is unperturbed by the attachment of the water by *inter*molecular σ bonds. A considerable change is observed for the transition moment ratio of the 2-pFPE$\cdot$ H$_2$O cluster compared to the one of monomer **1** (see Tables 4.2 and 7.2). The change can be attributed to a mass effect resulting from reorientation of the principle axes of inertia due to the binding of a water molecule.

On the red side of this vibronic band several other intense features measured under higher resolution at the masses of the singly hydrated cluster and the monomer at the same time are situ-

Parameter	Conformer 2g (gauche) S_0	S_1	Conformer 8g (gauche) S_0	S_1	Conformer 3a (anti) S_0	S_1	Conformer 1g (gauche) S_0	S_1	Conformer 5a (anti) S_0	S_1
r (H19–Cl), Å	2.92	3.18	2.54	2.82	-	-	2.56	2.76	-	-
α_1 (C1C2C7), deg	120.4	120.1	120.3	119.8	119.1	119.9	120.6	120.1	120.8	120.0
α_2 (C2C7C8), deg	111.1	114	110.8	113.4	110.9	111	111	113.7	111.1	113
α_3 (C7C8O9), deg	112	112.8	112.2	113	107.4	107.5	112.3	113.1	107.4	107.3
α_4 (C8O9H19), deg	105.6	109.3	105.4	109	106.9	109.5	105.8	109.3	106.8	109.4
τ_1 (C3C2C7C8), deg	90.6	84	87.5	86.7	102	82.4	91.2	92.6	89.2	89.7
τ_2 (C2C7C8O9), deg	58.5	64.7	58.4	64.1	163.6	178.9	60.7	66.5	-179.9	-179.8
τ_3 (H19O9C8C7), deg	-89	-87.4	-58.8	-65.1	173.6	177.9	-63.8	-67.1	-179.6	-179.6
r_1 (O9–H21), Å	1.87[a]	1.99[a]	1.91	2.05	1.96	2.05	2.15[b]	2.33[b]	2.15[b]	2.33[b]
α_5 (O9H21O20), deg	170.7[a]	170.1[a]	161.1	156.6	157.9	165	146.3[b]	138.1[b]	145.6[b]	137.7[b]
τ_4 (H19O9H21O20), deg	-9.9[a]	-23.3[a]	92.6	64.6	108.8	144.5	-34.7[b]	-33.6[b]	-38.3[b]	-38[b]
A, cm⁻¹	0.06218	0.05884	0.06183	0.05999	0.07421	0.08183	0.06345	0.06323	0.08034	0.08012
B, cm⁻¹	0.02249	0.02182	0.01930	0.01869	0.01612	0.01376	0.01695	0.01623	0.01381	0.01355
C, cm⁻¹	0.02049	0.01965	0.01649	0.01582	0.01389	0.01240	0.01445	0.01383	0.01228	0.01206
$\mu_a^2 : \mu_b^2 : \mu_c^2$	-	4 : 8 : 88	-	20 : 80 : 0	-	6 : 86 : 8	-	6 : 91 : 3	-	7 : 93 : 0
E_{rel}, cm⁻¹	0	-	10	-	1126	-	1678	-	2362	-
E_{rel} (BSSE), cm⁻¹	0	-	244	-	564	-	1338	-	1330	-
E_{rel} (BSSE+ZPVE), cm⁻¹	0	-	61	-	458	-	1881	-	1836	-

Table 7.2: *Interatomic distances, d, planar angles, α, dihedral angles, τ, and rotational constants for the ground, S_0, and the first excited, S_1, electronic state of the gauche and anti conformers of the 2-pFPE monomer calculated at the MP2/cc-pVDZ and CIS/cc-pVDZ level of theory, respectively. Electric dipole transition moment (TM) ratio $\mu_a^2 : \mu_b^2 : \mu_c^2$ as obtained from CIS/cc-pVDZ calculation of the optimized geometry of the 2-**pFPE**·H₂O complex. Relative energies, E_{rel} of the five most stable conformational structures of the singly hydrated complex of 2-**pFPE** without and with inclusion of the basis set superposition error (BSSE) and zero-point vibrational energy (ZPVE) as obtained from MP2/cc-pVDZ level of theory. The parent conformations of 2-**pFPE** giving rise to the respective hydrated complexes are reported in parentheses in the header of the table. For details, see text.*

*[a] For conformer **2g**: r_1 represents distance (H19–O20), α_5 represents planar angle (O9H19O20) and τ_4 represents dihedral angle (O9H19O20H21) (see Fig. 7.5).*

*[b] For conformers **1g** and **5a**: r_1 represents distance (F13–H21), α_5 represents planar angle (F13H21O20) and τ_4 represents dihedral angle (C5F13H21O20) (see Fig. 7.5).*

Conformer **2g**   Conformer **8g**   Conformer **3a**

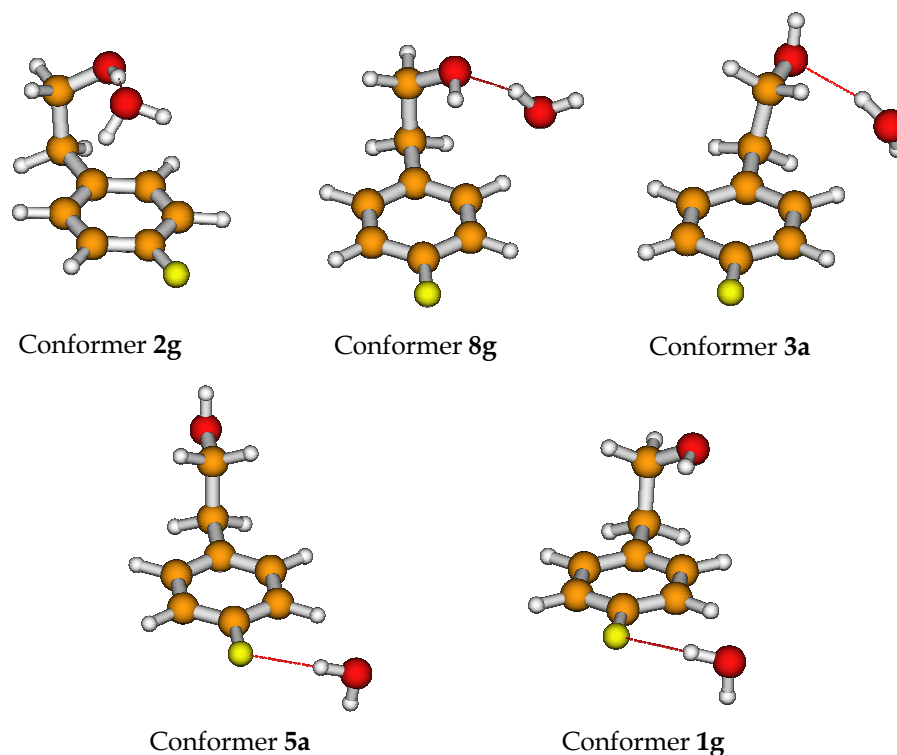Conformer **5a**   Conformer **1g**

Figure 7.5: *Electronic ground state, S_0, structures of the 2-pFPE·H_2O complex optimized at the MP2/cc-pVDZ level of theory. Typical angles, bond lengths, inertial parameters, and binding energies for these structures are listed in Table 7.2.*

ated. The spectra are presented in figures 7.2 and 7.3. The poor signal to noise ratio of these signals does not allow direct fits for these bands with our computer-assisted procedure. But looking at the low resolution traces of the doubly hydrated clusters (see Fig. 7.1) and their fragmentation pattern at lower masses we can readily assign bands -2 cm^{-1} and 53 cm^{-1} as originating from the water cluster with two water molecules attached to the 2-*p*FPE monomer. An additional argument is the similar highly resolved rotational profile of these bands, which consists in both cases of a dominant Q branch and weak P and R branches. In the case of band -18 (see Fig. 7.2) the situation is completely different. The simultaneously recorded signals at the masses of the singly hydrated cluster and monomer have mismatching rotational contours. One explanation is that the band consists of a mixture of several rovibronic features originating from different cluster sizes. The strong Q branch of the spectrum measured at mass channel m/z=140 leads to two possible conclusions. Either it is produced from a fragmentation of the doubly hydrated water cluster, as is the case for bands -2 cm^{-1} and 53 cm^{-1} or it is originating from a fragmentation of a cluster with the buffer gas argon. Investigating the profile of the R branches of the signals measured at the masses of the singly hydrated cluster and the monomer, one can see a resemblance in the

rotational contours. This points to a fragmentation of a 2-*p*FPE· H_2O cluster at the monomer mass channel and the signal at m/z=158 can be assigned as originating from the most stable theoretically predicted 2-*p*FPE· H_2O structure **2g**.

7.3.2   2-*o*FPE-Water Cluster

Low-Resolution Spectra

The one-color REMPI spectra of 2-*o*FPE and its singly hydrated cluster recorded at mass channels m/z =140 and m/z =158, respectively are depicted in Fig. 7.6. There is only one strong vibronic band in the $S_1 \longleftarrow S_0$ electronic transition of the water cluster, blue-shifted by 62 cm^{-1} relative to the monomer's origin band. There are some indications for other vibronic bands but their relatively small intensity precludes a high resolution measurement. As a next step of evaluation, to reveal the conformational geometry giving rise to the 62 cm^{-1} vibronic feature, its high-resolution spectrum was recorded.

High-Resolution Spectra

Measuring band 62 cm^{-1} under higher resolution, we have seen that it consists of two closely spaced (2 cm-1) rovibronic features, subband 62A cm^{-1} at lower energy and subband 62B cm^{-1} at higher energy. The experimental spectra of these two subbands are presented in Figures 7.7 and 7.8 (upper traces). They have completely different rotational profiles, which points out that they originate from two dissimilar singly hydrated clusters of 2-*o*FPE. Band 62A is characterized by a strong Q branch, an intense regular structure of the P branch with well resolved individual peaks and a weak R branch with poor resolution. Band 62B consists of a dominating Q branch, weak P branch and a gradually increasing R branch that ends with a characteristic sudden drop of intensity, both P and R branches having irregular rotational structure. The spectra of these two bands manifest a hybrid *a*-, *b*-, and *c*-type character with different contributions. They do not consist of single rotational lines but we observe a characteristic peak pattern produced by aggregation of several rotational lines resulting in a minimum value for the peak width of 250 MHz full width at half maximum (fwhm). To find the rotational constants for the ground, S_0 and the first excited, S_1, electronic states, the transition moment ratio, the rotational temperature, and the origin position, v_0, we used the computer-assisted rotational fit procedure based on genetic algorithm described in Section 2.3. As starting values for our fits, we used the values resulting from *ab inito* calculations of the ground state rotational constants for the first six in energy singly hydrated water clusters. The produced theoretical stick spectrum was convoluted using a Gaussian line shape with a fwhm of 160 MHz. The best-fit results for the bands are shown in the inverted spectra in figures 7.7 and 7.8. The simulated spectra (lower inverted part) agree
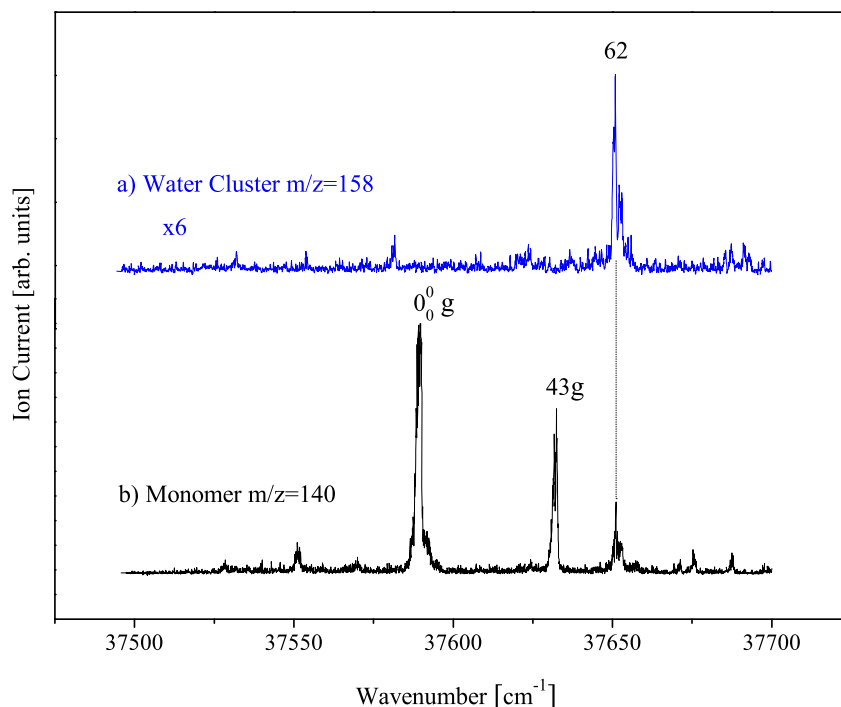
Figure 7.6: *One-color R2PI spectra of the $S_1 \longleftarrow S_0$ electronic transition of the 2oFPE monomer and its singly hydrated water cluster, measured at the monomer (m/z=140) mass channel under water-present conditions (b), and at the parent (m/z=158) mass channel of the 2oFPE·H_2O complex (a).*

well in both peak positions and peak intensities with the experimental ones (upper trace). The achieved cross correlation between the experimental and simulated spectra is as high as 95%. The experimentally obtained values of the rotational constants, the transition moment ratios, and the rotational temperatures are summarized in Table 7.3.

Ab initio Calculations

To support the structural analysis of the 2-*o*FPE· H_2O complex we performed a series of *ab initio* structural optimizations using Gaussian 03 suit of programs. The high-resolution spectra in Chapter 6 clearly demonstrate that the strongest band 0_0^0 in the UV spectrum of the monomer originates from the most stable and the most abundant conformation of 2-*o*FPE, i.e. the *gauche* structure **1**, in which the side chain is bent towards the benzene ring (see Fig. 6.9).This we used as starting structure in the modeling process of the water cluster. The water was attached to
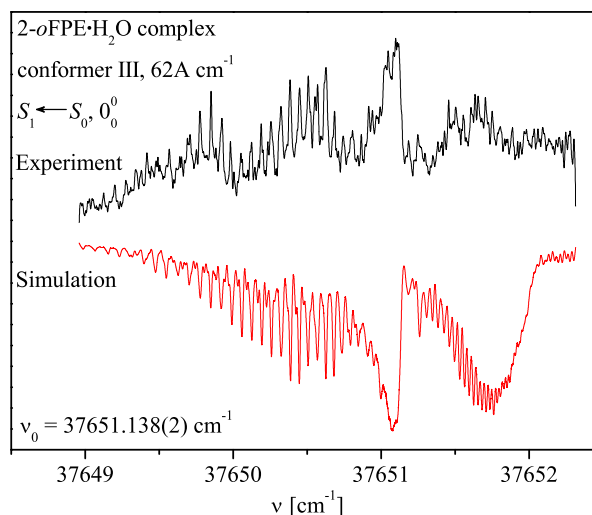
Figure 7.7: *High-resolution two-color R2PI spectrum of band 62A cm^{-1} in Figure 7.6, recorded at m/z = 158. The band is assigned as the 0_0^0 origin band of conformer **III** of the 2-oFPE·H$_2$O complex with the rotationless transition centered at 37651.138(1) cm^{-1}. Upper trace: experimental spectrum. Lower inverted trace: the best-fit simulated spectrum yielding the parameters in Table 7.3 (for details, see text).*

Parameter	Band	
	+62A cm^{-1}	+62B cm^{-1}
A''	0.0493(12)	0.0568(14)
B''	0.02486(43)	0.02511(43)
C''	0.02038(28)	0.01968(35)
A'	0.0486(11)	0.0566(14)
B'	0.02415(31)	0.02398(43)
C'	0.01996(17)	0.01937(34)
$\mu_a^2 : \mu_b^2 : \mu_c^2$	65:30:5	70:25:5
Origin ν_0 , cm^{-1}	37651.14(5)	37653.168(9)
Temperature T(K)	7.93(4)	7.5(4)
Best-fit cross correlation (%)	95	95

Table 7.3: *Experimental rotational constants for the ground,S_0 (A'', B'', C''), and for the first excited,S_1 (A', B', C'), electronic states, the transition moment ratio, $\mu_a^2 : \mu_b^2 : \mu_c^2$, the band origin frequency, ν_0, the rotational temperature, T, and the best-fit cross correlation obtained from the rotational fit of bands 62A, and +62B cm^{-1} of the 2-oFPE·H$_2$O complex, shown in figures 7.7 and 7.8. Numbers in parentheses are standard deviation in units of the least significant quoted digit. The uncertainty for the relative values of μ_a^2, μ_b^2, and μ_c^2 in the transition moment ratio does not exceed 5(%).*
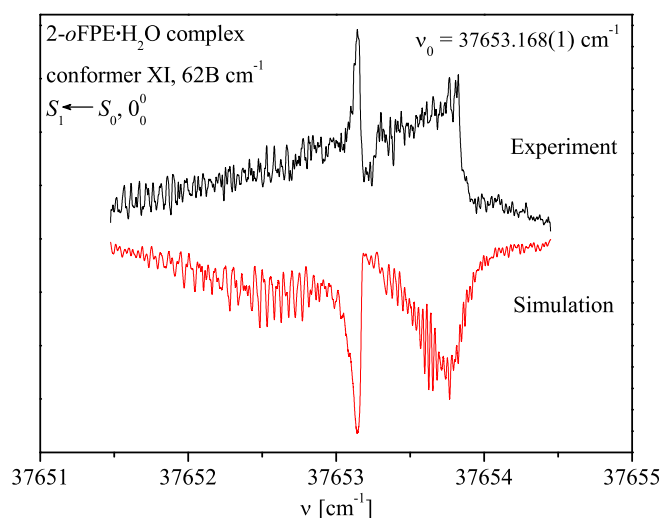
Figure 7.8: *High-resolution two-color R2PI spectrum of band 62B cm^{-1} in Figure 7.6, recorded at m/z = 158. The band is assigned as the 0_0^0 origin band of conformer **XI** of the 2-oFPE·H$_2$O complex with the rotationless transition centered at 37653.168(2) cm^{-1}. Upper trace: experimental spectrum. Lower inverted trace: the best-fit simulated spectrum yielding the parameters in Table 7.3 (for details, see text).*

various possible binding sides of monomer's *gauche* conformer **1**. The other monomer structures we probed as possible bases for the formation of singly hydrated clusters were monomer's *gauche* conformers **7** and **9**, and *anti* conformer **6**, the next in energy geometries. In this way, more than 15 water cluster conformers of 2-*o*FPE were produced and were subject to further optimization.We performed calculations at the MP2/cc-pVDZ level of theory for the ground, S_0, electronic state and CIS/cc-pVDZ level of theory for the first excited, S_1 electronic state. After the calculation of the BSSE corrections for the energies of the above structures and the inclusion of the ZPVE, only the first 6 most stable clusters were considered in the analysis of the experimental high-resolution spectra. The optimized conformational species are shown in Figure 7.9, and the results of the calculations are summarized in Table 7.4. The resulting energy order after the consideration of BSSE and ZPVE corrections is: conformer **IIIg** (0 cm^{-1}), conformer **XVIa** (21 cm^{-1}), conformer **Ig** (52 cm^{-1}), conformer **XVIIa** (128 cm^{-1}), conformer **XIg** (166 cm^{-1}) and conformer **VIg** (288 cm^{-1}). Here, in contrast to the water clusters of 2-PE and 2-*p*FPE the most stable structure is the one in which the water binds sideways to the terminal OH *gauche* of the bare *gauche* conformer **1** of 2-*o*FPE. As mentioned already, this order can change depending on the level of theory and functional used for the optimization procedure. Another difference from the singly hydrated clusters of 2-PE and 2-*p*FPE is that here we have a very stable water cluster with *anti* conformer of the monomer (**XVIa**). This is the stabilizing effect of the water

Conformer **IIIg**   Conformer **XVIa**   Conformer **Ig**

Conformer **XVIIa**   Conformer **XIg**   Conformer **VIg**
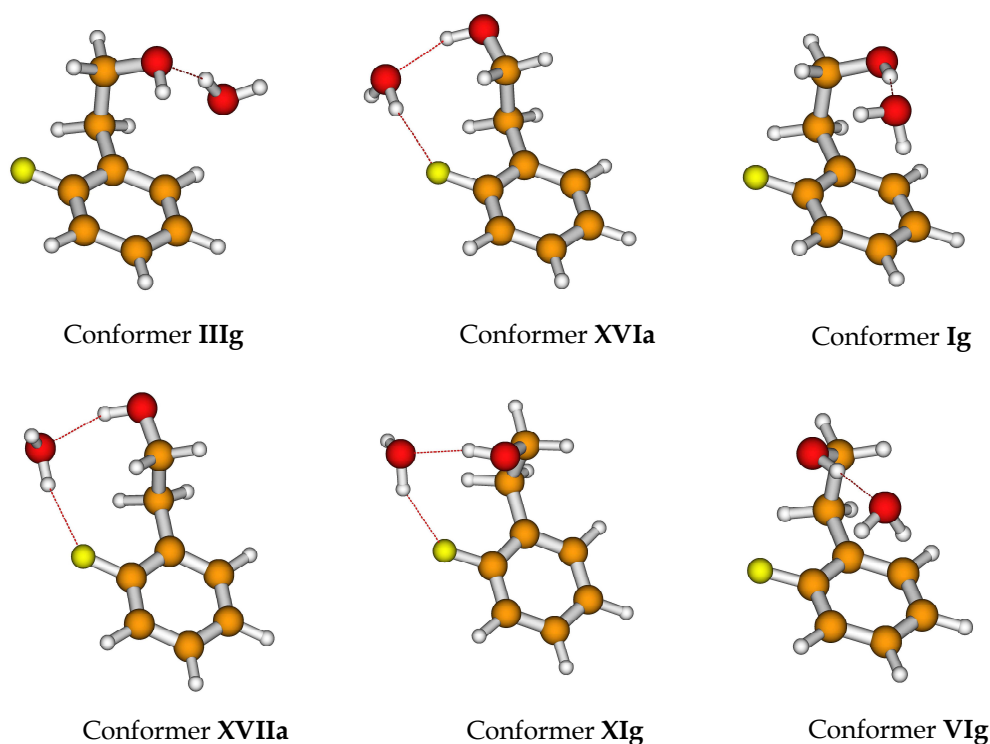
Figure 7.9: *Electronic ground state, S_0, structures of the 2-oFPE·H_2O complex optimized at the MP2/cc-pVDZ level of theory. Typical angles, bond lengths, inertial parameters, and binding energies for these structures are listed in Table 7.4.*

that selects and lowers the energy of higher energy conformers of the monomer after water attachment. These are monomer's structures which are present with negligible abundance under the conditions of free jet expansion of our experiments.

Discussion

The attempts to fit the whole rotationally resolved spectrum of band 62 cm^{-1}, starting with the predicted parameters for the fifteenth conformers of 2-*o*FPE·H_2O, were not successful. This confirms our conclusion that this band is composed of two separate close lying rovibronic bands (62A and 62B). After a comparison of the rotational constants for the ground, S_0, and the first excited, S_1, electronic states and the transition moment ratio obtained from the fit of the highly resolved spectrum with the theoretically predicted internal parameters and transition moment ratios of the optimized structures of the complex, we assigned band 62A to the 2-*o*FPE· H_2O conformer **IIIg**. This cluster is analogous to conformer B in the case of 2-PE· H_2O complex (see Chapter 3) and conformer **8g** in the case of 2-*p*FPE· H_2O complex (See Fig. 7.5). The binding of

Parameter	Conformer **Ig** S_0	S_1	Conformer **IIIg** S_0	S_1	Conformer **VIg** S_0	S_1	Conformer **XIg** S_0	S_1	Conformer **XVIa** S_0	S_1	Conformer **XVIIa** S_0	S_1
d (H15-C1), Å	2.99	3.11	2.61	2.88	3.50	3.95	4.48	4.52	5.11	5.13	5.10	5.14
α_1 (C1C2C7), deg	121.9	122.0	121.8	122.1	121.8	121.3	121.4	121.5	123.1	122.6	123.0	123.8
α_2 (C2C7C8), deg	110.6	114.2	110.5	113.8	110.6	114.3	111.1	113.7	111.5	113.5	111.5	115.1
α_3 (C7C8O9), deg	111.9	112.8	112.0	112.8	112.2	112.9	112.6	113.2	112.2	111.5	112.1	111.0
α_4 (C8O9H19), deg	106.1	109.2	105.4	109.0	106.4	109.9	105.8	109.3	103.9	107.6	103.6	108.7
τ_1 (C3C2C7C8), deg	85.6	90.1	84.3	86.4	92.3	96.3	91.8	97.1	78.9	84.4	78.9	81.5
τ_2 (C2C7C8O9), deg	60.2	62.7	58.5	61.6	-58.9	-76.7	-58.0	-61.0	-171.2	-172.9	171.7	-176.6
τ_1 (C7C8O9H19), deg	-88.6	-88.2	-59.1	-66.2	85.9	80.3	-68.7	-67.2	72.4	73.9	71.4	66.1
d(O9-H21), Å	3.16	3.36	3.15	3.23	3.20	3.42	2.93	3.13	3.17	3.37	3.18	4.10
d(H19-O20), Å	**1.85**	**1.99**	**1.91**	**2.05**	**1.86**	**2.04**	**1.87**	**2.01**	**1.95**	**2.11**	**1.95**	**3.07**
α_5 (H19O20H22), deg	**112.9**	**123.9**	**112.4**	**132.4**	**104.2**	**170.8**	**120.8**	**136.5**	**115.5**	**123.4**	**104.5**	**140.2**
α_5 (O19H21O20), deg	61.0	55.9	**161.5**	**132.4**	59.3	54.0	74.1	71.5	63.2	59.2	62.1	70.2
τ_4 (O9H19O20H22), deg	**-39.9**	**-48.3**	98.3	20.3	**-91.8**	**88.7**	**-85.6**	**-107.2**	**-109.3**	**-124.0**	**71.2**	**172.5**
τ_4 (H19O9H21O20), deg	15.4	21.7	**62.6**	**60.1**	2.1	-25.7	7.0	6.5	1.8	2.3	-19.0	26.0
A, cm^{-1}	0.04490	0.04288	0.04865	0.04803	0.04655	-	0.05784	0.05530	0.06264	0.06055	0.06273	-
B, cm^{-1}	0.03038	0.02832	0.02601	0.02459	0.02911	-	0.02464	0.02415	0.02153	0.02109	0.02156	-
C, cm^{-1}	0.02557	0.02363	0.01921	0.01809	0.02740	-	0.01952	0.01884	0.01691	0.01639	0.01684	-
TM ratio, $\mu_a^2 : \mu_b^2 : \mu_c^2$	86:11:3	-	82:12:6	-	78:12:10	-	73:18:9	-	87:10:3	-	99,9:0:0,1	-
E_{rel}, cm^{-1}	0	-	49.71	-	372.67	-	609.68	-	604.39	-	646.99	-
E_{rel} (BSSE), cm^{-1}	0	-	261	-	5	-	347	-	134	-	95	-
E_{rel} (BSSE + ZPVE), cm^{-1}	52	-	0	-	288	-	166	-	21	-	128	-

Table 7.4: *Theoretical interatomic distances, d, planar angles, α, dihedral angles, , and rotational constants for the ground, S_0, and the first excited, S_1, electronic state of the singly hydrated complexes of 2-oFPE calculated at the MP2/cc-pVDZ and CIS/cc-pVDZ level of theory, respectively. The electric dipole transition moment (TM), $\mu_a^2 : \mu_b^2 : \mu_c^2$, ratio has been obtained from CIS/cc-pVDZ calculation of the optimized geometry of the 2-oFPE·H_2O complex. The relative energies of the six most stable conformational structures of the singly hydrated complex of 2-oFPE without and with inclusion of the basis set superposition error (BSSE) correction and zero-point vibrational energy (ZPVE) have been obtained from MP2/cc-pVDZ calculations. The parent conformations of 2-oFPE giving rise to the respective hydrated complexes are indicated with small letter next to the conformer's names in the header of the table. For details, see text.*

the water molecule via a strong σ hydrogen bond to the most stable (conformer **1**) of 2-*o*FPE and the possible existence of a second σ hydrogen bond with the hydrogen atom H10 of the benzene ring in cluster's conformer **IIIg**, have been already thoroughly discussed in the cases for 2-*p*FPE· H_2O (see Section 7.3.1) and 2-PE· H_2O complexes (see Chapter 3). Here, again the structure of the host molecule (2-*o*FPE) is not changed upon the formation of the singly hydrated cluster (see Fig. 7.9 and Tables 6.2 and 7.4). The main difference from the above-mentioned water clusters of 2-PE and 2-*p*FPE is that the experimental transition moment ratio of the monomer is not changed in the presence of water. Previously, we have ascribed such change to a pure mass effect due to the attachment of a water molecule. The lack of change in the case of 2-*o*FPE·H_2O complex **IIIg** can be attributed to the compensating positions of the fluorine and the water in this conformer, which is not leading to a remarkable reorientation of the principal axes of inertia.

The more intriguing situation is observed for band 62A, where we found a very good agreement between experimental values for the rotational constants of the ground, S_0, and the first excited, S_1, electronic states, the transition moment ratio and the respective theoretical values for water conformer **XIg**. In conformer **XIg** water is inserted between the terminal hydroxyl group and the fluorine atom of the benzene ring of conformer **7** (see Chapter 6) of 2-*o*FPE through a formation of two stable σ hydrogen bonds, wherein water donates a proton to the fluorine and accepts one from the OH group of the side chain. This is not one of the most stable water cluster structures (166 cm^{-1}) according to the theoretical results. The existence of this conformer is reasonable because monomer **7** was identified in the jet (see Chapter 6). This again demonstrates the selective effect of the attached water that stabilizes conformers of the monomer, leading to a detectable 2-*o*FPE· H_2O cluster. In this indirect way, the abundance of conformer **7** of 2-*o*FPE can be proved. The presence of the other low-energy conformers (**XVIa** and **Ig**) cannot be fully excluded since there are some small red-shifted vibronic bands in the low-resolution REMPI spectrum measured at the mass channel of the singly hydrated cluster which can originate from these conformers. For our analysis they are not so important because they contribute by less than 5 to 10 % to the total cluster concentration.

7.4   Summary and Conclusions

With the combination of mass selective low- and high-resolution one- and two-color R2PI experiments supported by quantum chemistry calculations, a detailed study of the 2-*p*FPE·H_2O and 2-*o*FPE·H_2O complexes have been performed. For 2-*p*FPE·H_2O cluster an assignment of one of the vibronic bands has been made based on the comparison of the high-resolution spectrum and one of the theoretically predicted structures. Most of the other highly resolved bands have been ascribed either to fragments of the doubly hydrated complexes of 2-*p*FPE or to overlapping vibronic bands. Similar to the case of 2-PE singly hydrated clusters (see Chapter 3), here again the

most stable conformers of 2-*p*FPE· H$_2$O consist of a water molecule attached to the most stable structure of the monomer, without any detectable change of the monomer structure caused by the water attachment. For 2-*o*FPE·H$_2$O we observe a single dominant vibronic band in the low-resolution spectrum that under higher resolution shows two components. Each of these two bands has been attributed to a distinct singly hydrated complex. Due to the proximity of the fluorine atom to the terminal OH group of the 2-*o*FPE, new monomeric structures arise providing different binding sides for the water molecule. Based on comparison of the experimental parameters received from the fits of the red-shifted band of the 2-*o*FPE· H$_2$O complex with the ones received from the *ab initio* calculation we assigned this band as originating from the most stable conformer of the singly hydrated cluster. The other band was ascribed to a higher-energy conformer (according to theory) of the 2-*o*FPE· H$_2$O complex, where the water serves as a bridge between the hydroxyl group and the fluorine atom of another monomer's *gauche* structure. Here, water acts as a stabilizing solvent for the monomer's conformers present with lower abundance under the conditions of our experiment. In all the cases, we found no significant structural changes of the host molecules, which implies that in the case of *gauche* conformers of 2-*p*FPE and 2-*o*FPE, the *intra*molecular hydrogen bond prevails over the *inter*molecular hydrogen bond responsible for the water attachment.

Chapter 8

Resonance-Enhanced Two-Photon Ionization Mass Spectroscopy of Ephedrine: Indication for a State-Selective Fragmentation in a Flexible Molecule

R. Karaminkov, S. Chervenkov, P. Härter[*], H. J. Neusser, Chem. Phys. Lett.**442**, 238 (2007).

The vibronic structure of the $S_1 \leftarrow S_0$ spectrum of ephedrine was measured by resonance-enhanced two-photon ionization spectroscopy with mass resolution under cold molecular beam conditions. The spectra recorded at four different mass channels, m/z = 165 (parent), 58, and the hitherto unknown 71, 85 fragment ions show dissimilar vibronic fine structure and the observed mass pattern strongly depends on the selected intermediate vibrational state. This points to an intermediate state-selected process resulting in a different fragmentation mass pattern. ab initio calculations at the MP2/6-311++G** level demonstrate that the AG (a) conformer is more stable by 238 cm^{-1} than the next stable GG (a) conformer.

[*]*Anorganische Chemie, Technische Universität München, Lichtenbergstrasse 4, D-85748 Garching, Germany*

8.1 Introduction

The class of the ephedra molecules has attracted a lot of attention as they play an important role in the central and peripheral nervous system activities. [120, 121] The pharmacologically relevant ephedrine ($C_{10}H_{15}NO$) (EPD) molecule acts also as a neurotransmitter. [58, 122] The detection and assignment of the concentration of the neurotransmitters such as catecholamines (epinephrine, norepinephrine and dopamine), serotonine, histamine, and ephedrine in body fluids is an important marker of abnormalities in the adrenergic body functions. EPD is used as a precursor in the production of stimulants in sport, and the desire to understanding of the resulting doping properties has initiated a series of mass spectrometric studies including a variety of experimental techniques [electron impact ionization (EI), chemical ionization (CI), fast atom bombardment (FAB), collisionally induced decomposition mass analyzed ion kinetic energy (CID MIKE)]. [123–125] All these mass spectra show that the ephedrine cation undergoes an efficient fragmentation with a dominating fragment ion at mass $m/z = 58$. UV spectra of the electronic origin region of the $S_1 \leftarrow S_0$ transition of EPD, [66, 67] norephedrine, [69] and pseudoephedrine [67] in the gas phase detecting only mass 58u have been investigated by Simons and co-workers using mass-selected resonance-enhanced two-photon ionization spectroscopy (R2PI) combined with UV hole burning and ion-dip spectroscopy. In a recently published work from our group, [20] we have presented the first high-resolution spectrum of the strongest origin band of EPD monomer and we were able to determine accurate values for the rotational constants of the ground, S_0, state, the excited, S_1, state, and for the transition moment ratio of this band. Here, we present new mass-selected low-resolution R2PI UV spectra of EPD vibronic bands measured at four mass channels [parent ($m/z = 165$) and fragments ($m/z = 58$, 71 and 85)] up to 10 cm^{-1} excess energy above the electronic origin. They demonstrate a specific fragmentation behavior of the EPD cation that depends on the selected intermediate state in the resonance-enhanced two-photon ionization process. A highly state-selected fragmentation behavior has not been observed in REMPI experiments of the rigid benzene molecule, which is the aromatic basis of EPD. [126, 127] This fragmentation behavior seems to be a consequence of the flexibility of EPD because of its side chain. Experimental results are supported by high-level *ab initio* computations of the structures and energies of the two lowest energy conformers of EPD.

8.2 Experiment

The details of the experimental apparatus are described elsewhere. [10,79] The excitation scheme for producing the UV spectra employs promotion of the molecules from their ground, S_0, electronic state to the first excited, S_1, electronic state and subsequent ionization by using photons with the same frequency (one-color R2PI) generated by frequency doubling in a BBO I crystal

of the output pulses of a commercial broadband ($\sim 0.4 cm^{-1}$) dye laser (Lambda Physik FL2002) with a Coumarin 307 dye for recording spectra in the energy region from 37450 cm^{-1} to 38600 cm^{-1}. The laser pulses intersect perpendicularly the cold molecular beam which was produced by an adiabatic expansion through a pulsed nozzle of ephedrine seeded in Ar buffer gas at a backing pressure of 3.2 bar. We carefully evacuated the vacuum chamber so that the presence of water was minimized. We used a soft focused laser beam with a diameter of 2 mm in order to avoid saturation of the transitions. To determine the diameter of the laser beam in the interaction region, we deflected the beam using a prism placed in front of the vacuum-chamber entrance window and measured the beam diameter on a millimeter- grid-graph-paper screen away from the prism at a distance equal to the distance between the prism and the interaction point. In this way, the relative diameter for different focusing conditions was determined. The nozzle containing the ephedrine was heated up to 110 °C. The molecular ions were accelerated in a direction perpendicular to both the laser and the molecular beam by the ion optics of a home built Wiley-McLaren-type time-of-flight mass spectrometer and detected by microchannel plates. The ion signal in a selected time-of-flight range was integrated by a gated integrator. The absolute frequency was measured with an accurate wavemeter (Atos 007, $\nu/\Delta\nu = 10_8$). We also recorded snapshot mass spectra of different vibronic bands with an oscilloscope (Tektronix TDS 360). The data acquisition and the control of the experiment were performed by a homemade software operating in a LABVIEW environment. The purity of the sample (1*R*,2*S*)-(–)-ephedrine 99% (EPD) was additionally checked by HPLC tests.

8.3   Results

8.3.1   *Ab initio* calculations

To support the experimental results and to find the energetically most favorable geometries of the EPD monomer in the ground, S_0, electronic state *ab initio* calculations on the structures and energetics have been performed at the MP2/6-311++G** level of theory using GAUSSIAN 03 suite of programs. [82] The new calculations with extended basis set corroborate structures AG (a) and GG (a) of the EPD monomer with two distinct shapes of the side chain. [67] The A/G notation refers to the arrangement (*anti* or *gauche*) of the CCCN and OCCN atom chains, respectively. AG is the extended and GG is the folded conformational structure. The optimized geometries are shown in Fig. 8.1. The most stable conformer has been found to be the AG (a) one, our calculations predict that the energy gap between the two structures is 0.68 kcal/mol (238 cm^{-1}), which is bigger than the one computed at the MP2/6-31G* level of theory. [67] The difference most likely stems from the improved electron correlation attained with the larger basis set. The energy difference is comparable to kT at room temperature, so that the existence of both

AG (a)   GG (a)

$E_{rel.}=0.0$ $E_{rel.}=0.68$
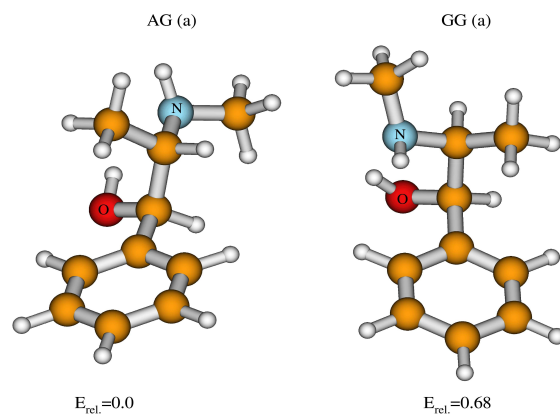
Figure 8.1: *Electronic ground state, S_0, structures of the two lowest energy AG (a) and GG (a) conformers of EPD optimized at the MP2/6-311++G** level of theory. Energies have been calculated at the same level. Relative energies are given in kcal/mol.*

conformers is possible at room temperature.

8.3.2   Experimental results

The one-color R2PI spectrum of the $S_1{\leftarrow}S_0$ electronic transition spectrum of EPD at $m/z = 58$ mass channel is depicted in Fig. 8.2d. It shows an extended scan region in comparison to our earlier work [20] by 100 cm^{-1} to the red side and more than 900 cm^{-1} to the high-energy side of the origin band of the $S_1{\leftarrow}S_0$ transition located at 37552.116(1) cm^{-1}. [20] At higher excitation energies above the electronic origin energy, two other fragment mass channels ($m/z = 71$ and $m/z = 85$) are observed, which are not known from previous mass spectra. [123–125] Two strong vibronic bands appear at about 530 cm^{-1} and 930 cm^{-1} excess energy in a close agreement with the positions of thevibronic 6_0^1 and 1_0^1 bands in the $S_1{\leftarrow}S_0$ spectrum of benzene [128]: the frequency difference is only 7 cm^{-1}. All spectra simultaneously recorded at different mass channels ($m/z = 165, 85, 71$ and 58) are presented in Fig. 8.2. We assign the small band redshifted by 25 cm^{-1} from the electronic origin observed at mass channel $m/z = 58$ to a peak resulting from the fragmentation of an EPD-Ar cluster, while the band redshifted by 8 cm^{-1} from the origin is most probably a sequence band. A magnified view of the 530 cm^{-1} spectral region of the R2PI spectrum is shown in Fig. 8.3 revealing a pronounced structure with several subbands at 519 cm^{-1}, 526 cm^{-1}, and 530 cm^{-1} with strongly differing intensity when monitored at the different mass channels. The peak at 519 cm^{-1} is only observed at $m/z = 85$ mass channel. As a
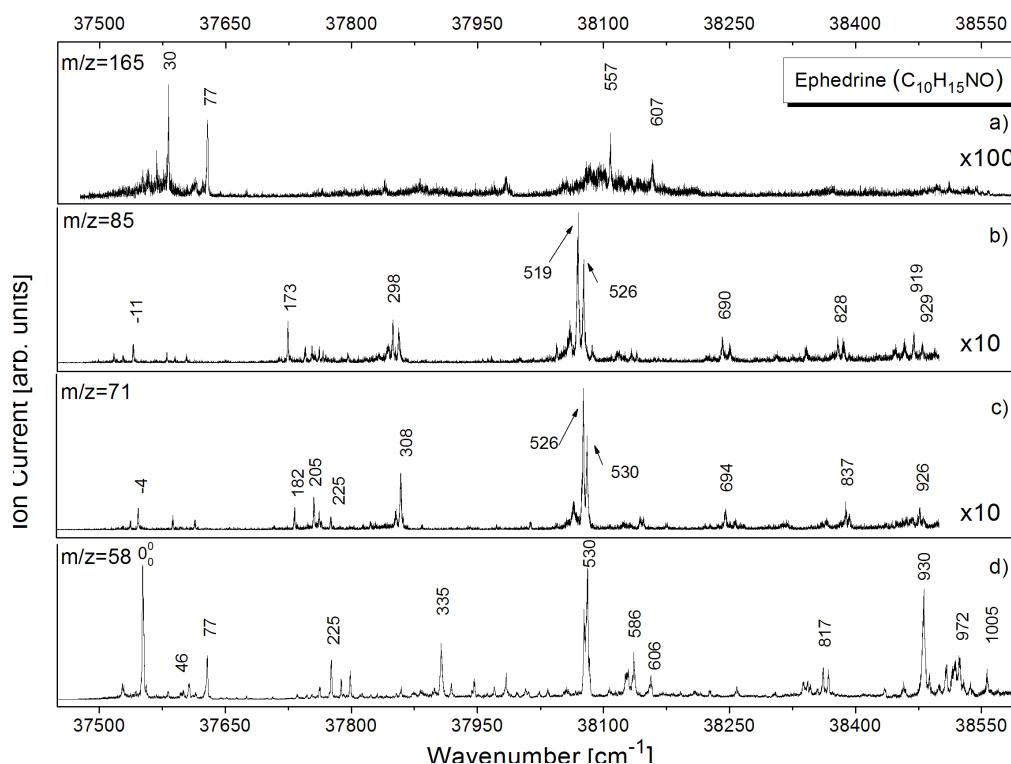
Figure 8.2: *(a) One-color (R2PI) spectra of ephedrine, measured at the parent (m/z = 165) (b-d) fragments (m/z = 85, m/z = 71, m/z = 58) mass channels,respectively. All vibronic peaks are labeled with their excess energy above the 0_0^0 band recorded at mass channel m/z = 58.*

general trend there is a red shift of the intensity maximum from 530 to 519 cm^{-1} for detection at increasing fragment masses m/z = 58, 71 and 85. A similar trend is observed for the weak bands at different positions all over the spectrum. To exclude that some of the observed peaks originate from the fragmentation of the EPD-H$_2$O cluster we recorded simultaneously a signal at m/z = 183 mass channel (i.e. the EPD-H$_2$O cluster). Since we were performing the experiments under water-free conditions the intensity at this mass channel was approximately 200 times smaller compared to the signal at the m/z = 58 mass channel. Only one broad vibronic feature slightly above the noise level is found in the +530 cm^{-1} region. It does not coincide with the peak positions observed when detecting the masses of the other fragments (m/z = 85, 71 and 58) in Fig. 8.3. To determine whether the peak ratio in the various spectra of Fig. 8.3 depends on the laser intensity we used two different laser beam focusing conditions yielding intensities differing by a factor of 16. No pronounced change in the intensity ratio of the peak heights measured at the three fragment masses (m/z = 85, 71 and 58) was observed. We have also recorded the resulting mass spectra when tuning the laser frequency to most of the bands shown in Fig. 8.2. In Fig. 8.4, four selected snapshot spectra are shown for the intermediate vibronic bands at 0_0^1, 173, 205,
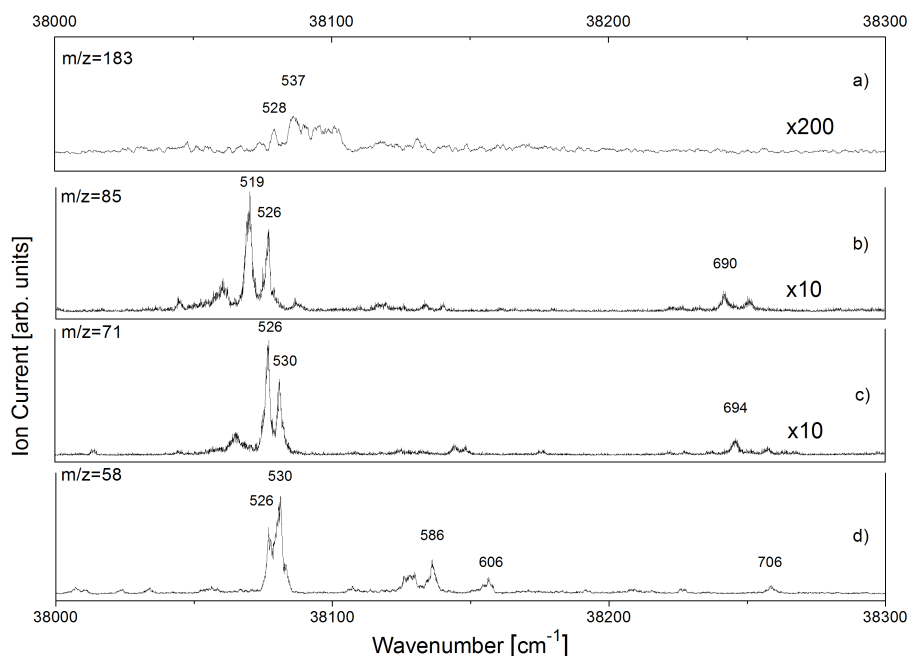
Figure 8.3: *(a) One-color (R2PI) spectra of EPD-H_2O cluster, recorded at m/z = 183 mass channel; (b-d) magnified parts of the (R2PI) spectra shown in Fig. 8.2 at the respective fragment masses.*

and 225 cm^{-1} excess energy. They demonstrate a strongly changing mass pattern depending on the selected intermediate state.

8.4 Discussion

8.4.1 Benzene-like $S_1 \leftarrow S_0$ spectrum

We excite the benzene ring chromophore which appears to be not strongly perturbed by the presence of the side chain because the measured spectrum in Fig. 8.2d is close to that of benzene, featuring several characteristic vibronic bands of the aromatic ring. The Herzberg-Teller induced vibration ν_6 is the false electronic origin in benzene (shifted by 522.4 cm^{-1} from the forbidden electronic origin), which is close to the strong band at 530 cm^{-1} excess energy in theEPD spectrum of Fig. 8.2d. In benzene, the totally symmetric CC stretch ν_1 vibration leads to a strong progression at 923 cm^{-1}, which agrees with the intense band at 930 cm^{-1} in EPD. There are,
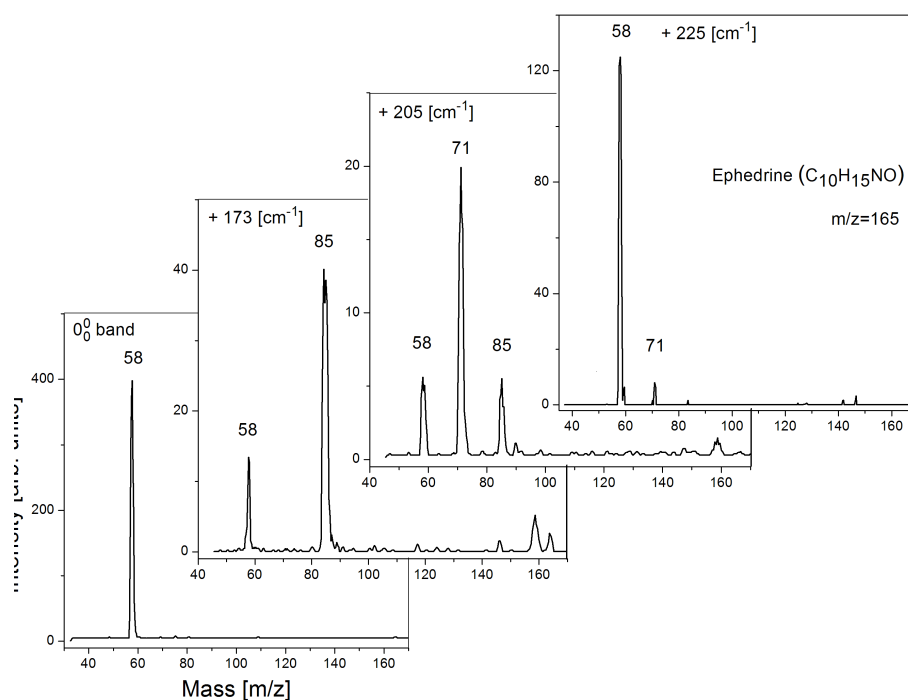
Figure 8.4: *Mass spectra recorded at vibronic bands 0_0^0, +173 cm^{-1}, +205 cm^{-1} and +225 cm^{-1}.*

however, two differences: (i) the electronic origin which is symmetry forbidden in benzene is appearing in the EPD spectrum because the C_6 symmetry is broken by the side chain; and (ii) the spectrum is shifted by 534 cm^{-1} to the red from that in benzene (38086 cm^{-1}). [129] A shift of similar size is observed for several n-alkylbenzenes: ethyl- (501 cm^{-1}), propyl- (504 cm^{-1}),and butylbenzene (511 cm^{-1}), [130] and for toluene (609 cm^{-1}). [131] This is a typical behavior for a side chain without a double bond (no mesomeric effect) when no inductive effect from an elec-tronegative substituent is present. While the deviation of the electronic origin is 534 cm^{-1}, the two prominent vibronic bands at 530 and 930 cm^{-1} excess energy differ only by 7 cm^{-1} from the excess energies of the corresponding ones in benzene though the side chain has a large mass and contains a nitrogen atom.

8.4.2 Fragmentation pathways

In our R2PI experiments the strongest ion signal is observed at the fragment mass channel $m/z = 58$ which does not originate from a fragmentation of the benzene ring as is known from previous

R2PI experiments on benzene. [126,127] As discussed in our recent work, [20] the fragmentation of ephedrine could not be avoided in a R2PI experiment. In one-color experiments the energy of the ionizing photon is fixed, this leading to a two-photon excitation energy of more than 9.3 eV, and most likely to high excess energy above the adiabatic ionization energy. From that we conclude that the fragment ions preferentially result from a fragmentation of the ionic EPD rather than from dissociation in the neutral intermediate state. The fragment at mass $m/z = 58$ is also the dominating fragment in EI, CI, FAB and CID MIKE mass spectra of EPD, [123–125] supporting the above argument of an ionic fragmentation. However, we cannot exclude fast dissociation of EPD after excitation (e.g. the ejection of an H_2) of the vibronic bands in S_1 during the laser pulse leading to a large neutral fragment that can be ionized by a second photon. The observed linewidth in our recent high-resolution experiments [20] would allow for dissociation times slower than 3 ns and thus the absorption of a further photon during the laser pulse would be possible. This could finally lead to a fragmentation of the resulting ion into the observed fragment ions. The differing ionization pathways in R2PI and EI require a closer discussion of the common fragment ion at mass $m/z = 58$ (see Fig. 8.5a). The resonant intermediate electronic state of R2PI is a $\pi\pi^*$ state of the benzene chromophore and thus the absorption of the second photon leads to the ionization of a π-electron of the benzene ring. For this reason immediately after R2PI, the positive charge is located at the benzene ring and charge transfer has to take place before the fragmentation into fragment ion with mass $m/z = 58$. This leads us to the conclusion that an electron transfer occurs from the nitrogen atom to the benzene ring. Then the dissociation into a neutral fragment of mass $m/z = 107$ and a charged side chain fragment of mass $m/z = 58$ occurs after a breaking of the single carbon bond. A similar charge transfer process has been described for the clusters of phenethylamine and amphetamine with polar, nonpolar, and hydrogen-bonding solvents studied by mass-resolved excitation spectroscopy. [100] Two possible fragmentation pathways of the EPD parent ion yielding the fragment ion with mass $m/z = 71$ originating from the two most stable conformeric structures predicted from the *ab initio* calculations are drawn in Fig. 8.5b and c. In the case of the more stable conformer AG (a), there is an electron migration from the substituent side (part c), whereas in the case of the second lowestenergy conformer GG (a) the electron transfer from the nitrogen is more likely direct because of the favorable position of the electronegative element close to the benzene ring. In Fig. 8.5d a plausible ionic fragmentation pathway yielding the fragment at mass $m/z = 85$ is shown. Here we have a typical for the benzylalcohols fragmentation with the detachment of H_2 and formation of a triple bond between the carbon and the oxygen. This fragmentation pathway is only possible for the GG (a) conformer.
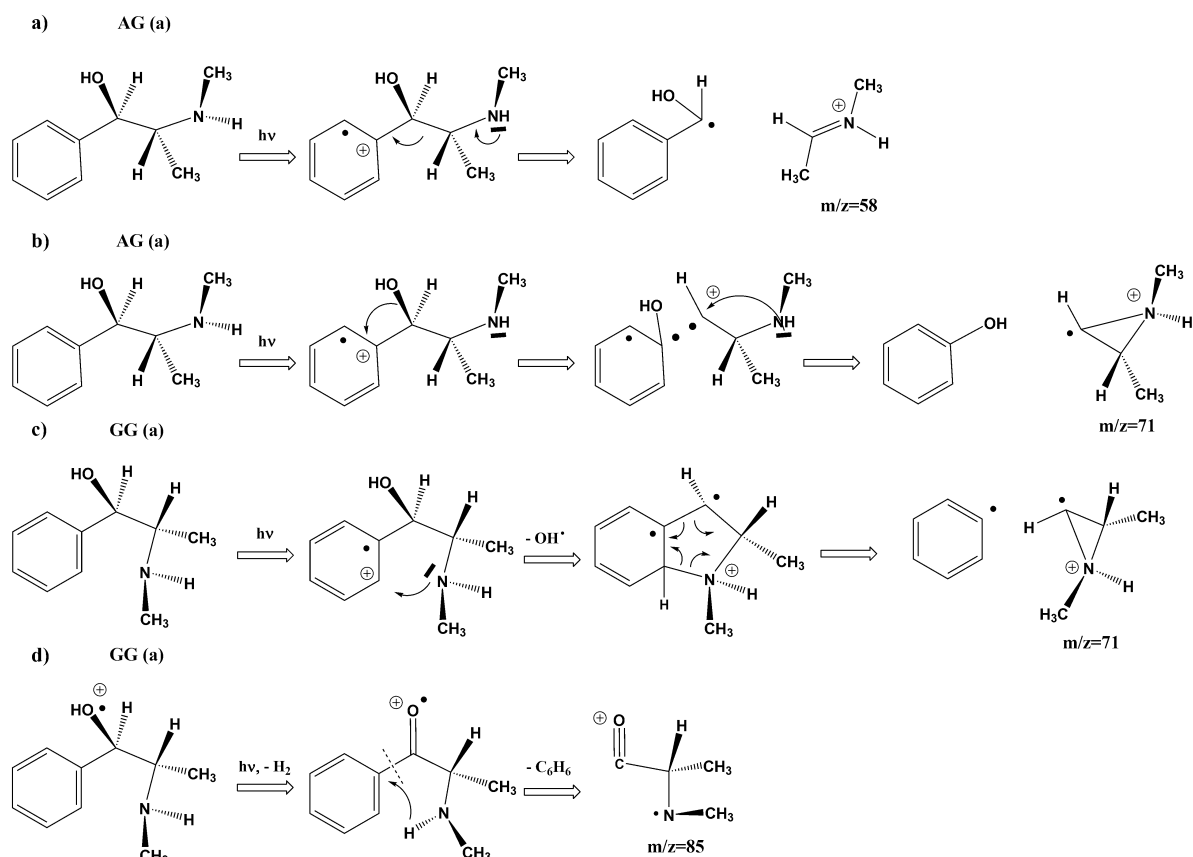
Figure 8.5: *Fragmentation pathways of the EPD cation after resonance-enhanced two-photon excitation: (a) m/z resulting from AG (a) conformer; (b) m/z = 71 resulting from AG (a) conformer; (c) m/z = 71 resulting from GG (a) conformer and (d) m/z = 85 resulting from GG (a) conformer.*

8.4.3 State-selective fragmentation

As discussed above, we have to consider more than one conformeric structure of EPD to explain the fragmentation leading to the *m/z* = 85 fragment ion. Most likely more than one conformeric structure is populated in the heated nozzle prior to the free expansion of the molecules into the vacuum chamber. However, during the expansion under our jet conditions, a relaxation from the GG (a) to the most stable AG (a) structure takes place, owing to the theoretically predicted energy gap of 238 cm^{-1} between them assuming that the potential energy barrier separating the two conformers is not too high. This is in line with our recent high-resolution experiments by analysis of the partly resolved rotational band structures of the strongest band. [20] We cannot exclude the existence of several conformers in the molecular beam but the analysis of the vibronic bands

observed at the fragment mass channels does not support their presence. The small distances of the vibronic features at -4 cm^{-1} and -11 cm^{-1} observed at fragment masses m/z = 71 and m/z = 85 (but not at m/z = 58) lead us to the conclusion that these are hot bands, rather than electronic origins of other conformeric structures. In addition, their intensity is much smaller than the intensity of the 0_0^0 band at fragment mass with m/z = 58 which is the electronic origin of the AG (a) conformer. [20] Indeed, the band at +46 cm^{-1} which has been assigned to a different conformer origin in Ref. [67] does not show any fragmentation to the m/z = 71, 85 mass channels (see Fig. 8.2). Another argument that the vibronic structure at m/z = 71 and m/z = 85 mass channels is not produced from the fragmentation of different conformers in the beam is that the fragment intensity ratio of the peaks in the 0_0^0 cm^{-1} region compared to the ratio of the corresponding peaks in the +530 cm^{-1} range is not preserved. This would be expected for the close lying origin and the 1_0^1 progression bands of different conformers. Thus two different processes leading to the observed varying fragmentation behavior of EPD are plausible: (i) an excess energy specific fragmentation in the ion after the absorption of two or three photons. Scanning to higher energies could lead to the opening of new fragmentation channels. In the ionization step, according to the Franck Condon factors, the photon energy is distributed between kinetic energy of the electron and internal energy of the ion, producing ions in different energy states, rather than leading to a sharp internal energy. For a broad energy distribution, a sudden change of the fragmentation behavior within a few cm^{-1} is not expected for a statistical unimolecular dissociation process. [127] (ii) The most likely explanation is a state-selective isomerization process in the intermediate state of the neutral vibronically excited EPD. This we would like to discuss for the bands at 530, 526, and 519 cm^{-1} (see Fig. 8.3b-d), each leading to a different fragmentation pattern. We assume that the redshifted bands at +519 cm^{-1} (m/z = 85) and 526 cm^{-1} are hot sequence bands of the AG (a) conformer leading to different vibronic states of increasing energy in the S_1 electronic state. This could lead to a state-selected isomerization or dissociation process in S_1 and to the ionization of another conformer [e.g. GG (a)] or a dissociation product with new fragmentation pathways. Another even more pronounced state-selected fragmentation is observed in the low excess energy region between 100 and 400 cm^{-1}. Here special vibronic bands can be observed only when monitoring different masses and the spectra measured at specific masses are completely dissimilar in this frequency range. This is also seen from the mass spectra which are obtained after excitation of the vibronic states at 0_0^0, 173, 205, and 225 cm^{-1} excess energy as shown in Fig. 8.4. While the mass spectra measured via the 0_0^0 and the 225 cm^{-1} bands are the ones with a dominating m/z = 58 mass peak, the mass spectra measured via 173 cm^{-1} and 205 cm^{-1} bands entirely differ from them and from each other. The identity of the vibronic states is not yet clear but future *ab initio* calculations may reveal the nature of these vibronic bands. It is particularly interesting if vibrations with a motion parallel to the benzene plane are the ones leading to the fragment masses m/z = 71 and m/z = 85. They can act as inducing modes of an isomerization process in S_1 electronic state.

8.5   Summary and conclusions

We have shown that the main features in the R2PI spectrum of ephedrine are similar to the ones in the spectrum ofbenzene. They testify that the electronic excitation takes place in the benzene chromophore. However, fine structure of the main bands and weaker additional bands originates from the flexible side chain of EPD. While the excitation of the strongest benzene-like bands in the R2PI spectrum yields the fragment with mass $m/z = 58$ known from EI and CI mass spectrometry, excitation of the additional weaker EPD specific bands results in new fragment mass channels in the R2PI spectrum. From this result, we may conclude that a state-selective primary process e.g. isomerization or dissociation takes place after excitation of the intermediate state and prior to the successive ionization with specific fragmentation channels for the different ionized conformers. To elucidate the nature of the intermediate state and the primary process high-level calculations of the excited, S_1, state potential energy surface and the vibronic frequencies of the lowest energy structures are in progress. In conclusion, we have demonstrated that flexible molecules show an intermediate state-selective fragmentation pattern after R2PI via vibronic states typical for a motion of the side chain.

Chapter 9

Mass Selective High-Resolution UV Spectroscopy of Pseudoephedrine: Evidence for Conformer Specific Fragmentation

*Using resonance-enhanced two-photon ionization spectroscopy with mass resolution, a low-resolution $S_1 \leftarrow S_0$ vibronic spectrum of pseudoephedrine was recorded at different m/z channels. The vibronic spectrum has a specific fragmentational pattern scattered over three fragment mass channels. Two of the fragments with m/z=71 and m/z=85 are observed for the first time for this molecule. Highly resolved spectra of all prominent vibronic features were measured and after a comparison with the theoretical results from high level ab initio calculations, assigned to two distinct molecular conformations **AG(a)** and **GG(b)**.The different conformers show distinct and specific fragmentational pathways, which strongly depend on the starting geometry.*

9.1   Introduction

(1S, 2S)-(+)-Pseudoephedrine (pseudoEPD) is the diastereoisomer of the (1R, 2S)-(-)-Ephedrine. The two molecules differ by the chirality of one center. This nonhuman neurotransmitters share a number of structural characteristics with the natural neurotransmitter [58, 122] adrenaline and have similar pharmacological effects on the cardiovascular system. For studying biological re-action mechanisms, it is important to know the orientation of different reactive chemical groups, since the topology of the molecule plays key role for the metabolism. The interaction between such molecules and an enzyme binding site depend on the shape of the molecule which is deter-mined by a subtle interplay between bonded and non-bonded forces.

In the last years, a number of studies have been performed to deduce the conformational prefer-ences of small biological flexible molecules [3, 4, 66, 67, 69, 85, 108, 132] (see Chapters 3, 4 and 6).In all these works, it has been shown that the combination of different UV laser spectroscopy techniques in the gas phase with time-of-flight mass spectrometry is a powerful method for prob-ing the conformational landscape. The addition of high-level quantum chemical calculations in the conformational investigations allows the assignment of discrete conformational structures to experimental features with a high degree of confidence.

9.2   Experiment and Data Processing

A detailed description of the experimental technique is given in Chapter 2. The excitation scheme for producing the high-resolution UV spectra employs promotion of the molecules from their ground, S_0, electronic state to the first excited, S_0, electronic state by scanning a narrow band pulsed laser ($\Delta v \sim 0.003$ cm^{-1}) and subsequent ionization by absorption of photons with fixed frequency from a broadband ($\Delta v \sim 0.4$ cm^{-1}) dye laser. The excitation photons involved in the two-color high-resolution spectra were generated by frequency doubling in a KDP crystal of the pulsed amplified output of a continuous wave (CW) single-mode ring dye laser (Coherent, CR 699-21) operated with Coumarin 334 dye. The substance ((1S, 2S)-(+)-Pseudoephedrine, 98 %) obtained from Aldrich was placed in a home-build heatable nozzle and heated up to 110^{0}C. The so-produced vapors of the molecule were mixed with buffer gas argon at a stagnation pressure of 2 bars. The gas mixture was expanded into vacuum through a pulsed-operated heatable nozzle with orifice diameter of 300 μm, leading to rotational temperatures for PseudoEPD of around 7-9 K. For the one-color low-resolution spectra photons with the same frequency were used, generated by frequency doubling in a BBO I (Beta Barium Borate) crystal of the output pulses of a commercial broadband dye laser (Lambda Physik, FL2002) with a Coumarin 153 dye. The congested rotational structure of vibronic bands of large floppy molecules, precludes a direct single rotational line assignment for the spectral resolution of the scanning UV laser pulses (70

MHz (FWHM)). For this reason we use a computer-based method for fitting of the experimental highly resolved spectra. The algorithm and the computer program elaborated in our group have already been described in Section 2.3. Cross correlation is employed as a penalty function. For the production of the simulated spectra of pseudoEPD, we ran the program using a 300 generations with 500 individuals in a generation.

9.3 Results

9.3.1 *Ab initio* Calculations

The Gaussian 03 program package [105] was used for the optimization of four previously introduced [67] conformations of pseudoEPD in the ground, S_0, and the first excited, S_1, electronic states at the MP2/aug-cc-pVDZ and CIS/cc-pVDZ levels of theory, respectively. The notation of the monomer's conformers is taken from the publication of Butz et al. [67]. The A/G notation refers to the arrangement (*anti* or *gauche*) of the CCCN and OCCN atom chains, respectively. AG is the extended and GG is the folded conformational structure. The optimized geometries are shown in Fig. 9.1. The improved electron correlation attained with the larger basis set results in a decrease of energy gaps between the conformers in comparison to the *ab initio* calculations at the MP2/6-311G** level of theory [67]. The relative energy order with an included zero-point vibrational energies (ZPVE) is unchanged: **AG(a)** 0 cm^{-1}, **GG(b)** 62 cm^{-1}, **GG(a)** 161 cm^{-1}, **AG(b)** 305 cm^{-1}. The inclusion of the ZPVE correction is not affecting the energy order, it only adds about 60 cm^{-1} to the uncorrected energy values. However, it may result in a reordering when the theoretical level of calculation or the model is changed. The calculated vibrational frequencies of the four conformers are all positive which verifies that they correspond to stable minima on the potential energy surface. All relevant theoretical parameters of these structures are summarized in Table 9.2.

9.3.2 Low-Resolution Spectra

Low-resolution one-color resonant two-photon ionization (R2PI) spectra in the spectral region between 37 350 cm^{-1} and 37 700 cm^{-1} have been recorded at three different mass channels (m/z=58, m/z=71 and m/z=85) under water-free conditions near the $S_1 \leftarrow S_0$ electronic transition of pseudoEPD. The spectra are depicted in Figure 9.2. The two additional mass fragments m/z=71 and m/z=85 were observed for the first time in the case of ephedrine, as discussed already in the previous chapter. It is interesting to see that the vibrational signals of fragments with m/z=71 and m/z=85 are much more intense and pronounced in the low-frequency region

AG(a) – 0 cm⁻¹

GG(b) – 62 cm⁻¹

GG(a) – 161 cm⁻¹

AG(b) – 305 cm⁻¹
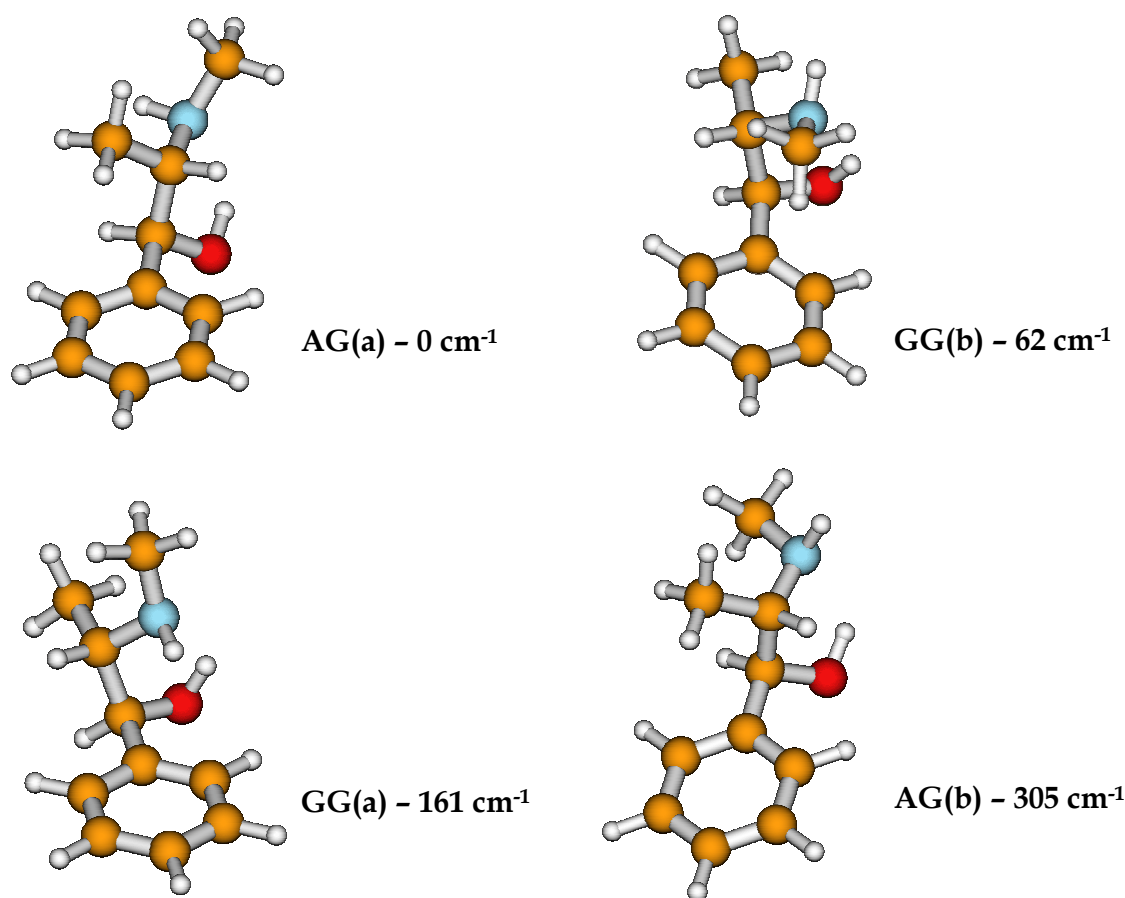
Figure 9.1: *Electronic ground state, S_0, structures of the four lowest energy conformers of pseudoEPD optimized at the MP2/aug-cc-pVDZ level of theory. Energies have been calculated at the same level. Relative energies are given in cm^{-1}.*

near to the origin band of pseudoEPD at m/z=58 in comparison to those of ephedrine (see Chapter 8). The most intense vibronic features of pseudoEPD are labeled 0_0^0 cm⁻¹, 126 cm⁻¹, 135 cm⁻¹, 181 cm⁻¹ and 212 cm⁻¹, respectively. The positions of the bands are given relative to the lowest energy band at 37417.939(1) cm⁻¹ measured at the main fragment mass channel m/z=58. To elucidate the nature of the above vibronic bands and to investigate the specific fragmentational pattern of pseudoEPD we performed high-resolution scans.

9.3.3　High-Resolution Spectra

The high-resolution UV spectrum of the lowest energy band measured at the most abundant fragment mass channel m/z=58 is presented in Figure 9.3 (upper trace). We have applied our computer-assisted fit procedure (described in details in Section 2.3) to determine the experimen-

Parameter	Band				
	0_0^0 cm^{-1}	+126 cm^{-1}	+135 cm^{-1}	+181 cm^{-1}	+212 cm^{-1}
A''	0.0665(05)	0.0541(27)	0.0655(07)	0.0675(61)	0.0548(01)
B''	0.0173(98)	0.0199(79)	0.0173(43)	0.0170(37)	0.0195(55)
C''	0.0158(61)	0.0192(94)	0.0156(34)	0.0157(31)	0.0189(11)
A'	0.0655(39)	0.0532(54)	0.0637(11)	0.0656(72)	0.0532(34)
B'	0.0173(43)	0.0201(42)	0.0167(28)	0.0169(72)	0.0192(96)
C'	0.0160(53)	0.0190(39)	0.0161(98)	0.0155(88)	0.0188(57)
$\mu_a^2 : \mu_b^2 : \mu_c^2$	68:14:18	23:60:17	26:63:11	17:67:16	42:47:11
ν_0, cm^{-1}	37417.939(1)	37545.410(5)	37553.639(2)	37597.612(3)	37631.392(1)
T(K)	8.5(2)	8.1(4)	9.2(3)	7.2(3)	11.9(4)
Best-fit cross correlation (%)	94	95	94	97	94

Table 9.1: *Experimental rotational constants for the ground,S_0 (A'', B'', C''), and for the first excited,S_1 (A', B', C'), electronic states, the transition moment ratio, $\mu_a^2 : \mu_b^2 : \mu_c^2$, the band origin frequency, ν_0, the rotational temperature, T, and the best-fit cross correlation obtained from the rotational fit of bands 0_0^0 cm^{-1},126cm^{-1},135 cm^{-1},181cm^{-1} and 212cm^{-1}, shown in Figures 9.3- 9.4- 9.5(for details, see text). The numbers in parentheses represent one standard deviation in units of the least significant quoted digit.*

tal rotational constants, transition-moment ratio, band origin and rotational temperature. The program produces a synthetic spectrum, which is compared with the experimental one on the basis of cross correlation and the values of the above parameters are determined. These artificial spectra are shown as inverted traces in Figures 9.3- 9.5. In order to reduce the searching space for the experimental rotational constants we have started the fitting procedure with theoretical values received from MP2/cc-pVDZ level of *ab initio* calculations. The best agreement for the experimental highly-resolved spectrum of the band 0_0^0 is obtained when the theoretical rotational constants for the ground, S_0, electronic state of the **AG(a)** conformer was taken as starting parameter. The simulated spectrum agree well both in peak positions and in intensity with the experimental one, when convoluting the theoretical stick spectrum with a Gaussian linewidth of 200 MHz FWHM, with an achieved cross correlation of 94 %. The fit shows that the rotational spectrum (see Figure 9.3) consists of weak, but well-resolved P- and R-branches in the wings and a prominent Q-branch in the center. It was assigned as *a*-, *b*-, and *c*-type hybrid with a significant *a*-type contribution (see Table 9.1). The structure of the highly resolved spectra of bands 135 cm^{-1}(scanned at fragment mass channel m/z=71) and 181 cm^{-1}(scanned at fragment mass channel m/z=58) differ from that of the above described band (see Figure 9.4). The latter two spectra feature nicely structured and pronounced P- and R-branches with a minor contribution from the Q-branch. From their appearance, the spectra can be assigned as predominantly b-type with small contributions also from a- and c-types (see Table 9.1). To receive the rotational constants for the ground, S_0, and the first excited, S_1, electronic states, the transition-moment ratios, the band origins and the rotational temperatures, the above-mentioned computer-aided fit rou-
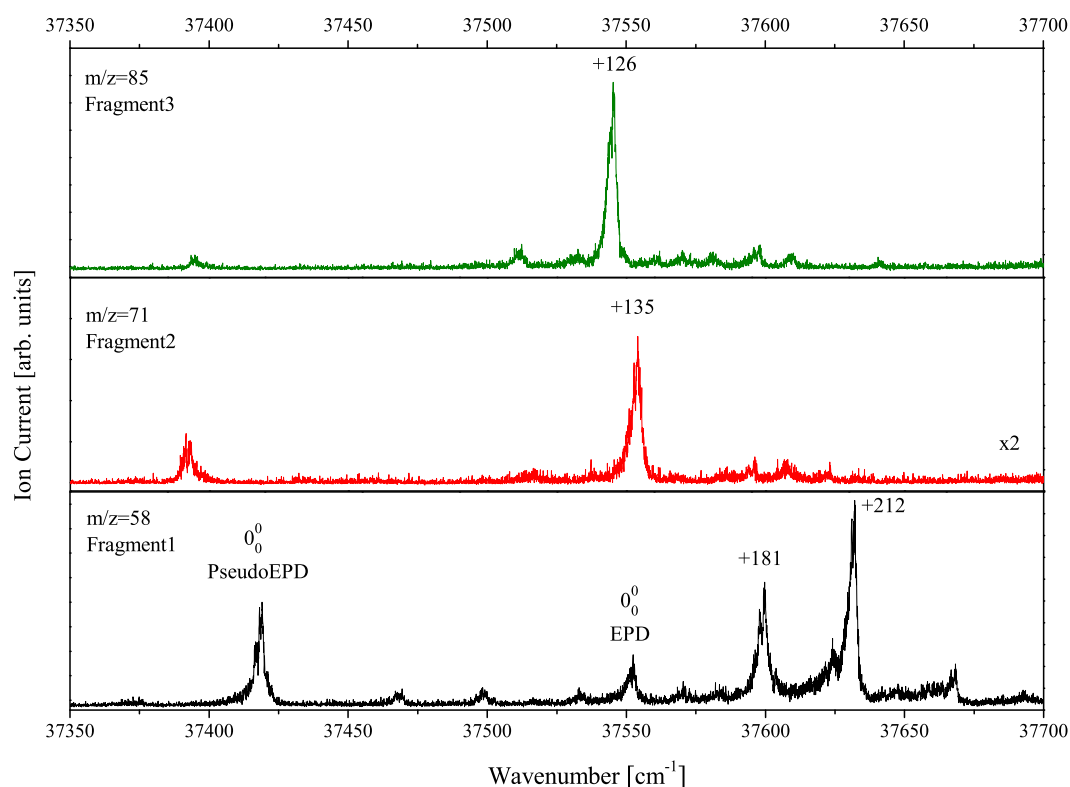
Figure 9.2: *(a) One-color (R2PI) spectra of pseudoephedrine, measured at the fragment mass channels: m/z = 85, m/z = 71, and m/z = 58,respectively. All vibronic peaks are labeled with their excess energy above the 0_0^0 band recorded at mass channel m/z = 58.*

tine was employed. In separate fit procedure the theoretical rotational constants for the ground, S_0, electronic state of all four theoretically predicted conformers of pseudoEPD were used as starting values for the fits. The resulting best-fit simulations are shown in Figure 9.4 (lower inverted traces) with an achieved cross correlation of 94% and 97%, respectively. The molecular parameters bringing forth these fits are summarized in Table 9.1. The fits were able to reproduce very well both the peak positions and the peak intensities, in particular the agreement for band 181 cm^{-1} is excellent even for the small peaks in the wings of the P- and R-branches. Here, again as in the case of the band 0_0^0 , the best fits for both bands were produced when starting the procedure with the theoretical rotational constants for the ground,S_0 , electronic state of the **AG(a)** conformer. The same approach was employed for bands 126 cm^{-1} (scanned at fragment mass channel m/z=85) and 212 cm^{-1}(scanned at fragment mass channel m/z=58), respectively. Starting the fitting procedure for both experimental spectra with the theoretical rotational con-

Parameter	Conformer **AG(a)**		Conformer **GG(b)**		Conformer **GG(a)**		Conformer **AG(b)**	
	S_0	S_1	S_0	S_1	S_0	S_1	S_0	S_1
d (OH$\cdots$N) Å	2.09	2.38[a]	2.12	2.14[a]	2.05	2.21[b]	2.05	2.21[b]
α_1 (OHN)	120.3	100.2[a]	119.9	118.4[a]	121.7	115.5[b]	122.2	110.2[b]
τ_1 (OCCN)	51.57	50.4[a]	-53	-48.96[a]	-54.98	-55.91[b]	48.44	58.77[b]
A, cm_{-1}	0.06585	0.06728[a]	0.05437	0.05416[a]	0.05391	0.05525[b]	0.06768	0.06822[b]
B, cm_{-1}	0.01699	0.01696[a]	0.02063	0.01956[a]	0.01899	0.01829[b]	0.01769	0.01751[b]
C, cm_{-1}	0.01596	0.01572[a]	0.01990	0.01910[a]	0.01824	0.01773[b]	0.01624	0.01595[b]
TM ratio, $\mu_a^2 : \mu_b^2 : \mu_c^2$	-	70:10:20[a]	-	48:8:44[a]	-	54:11:35[b]	-	1:94:5[b]
E_{rel}, cm_{-1}	0	-	9	-	96	-	241	-
E_{rel} (incl. ZPVE), cm_{-1}	0	-	62	-	161	-	305	-

Table 9.2: *Theoretical interatomic distances, d, planar angles, α, dihedral angles, τ, and rotational constants, A, B and C for the ground, S_0, and the first excited, S_1, electronic state of four conformers of the pseudoEPD monomer calculated at the MP2/aug-cc-pVDZ monomer calculated at the MP2/aug-cc-pVDZ, CIS/cc-pVDZ and CIS/631-G^{**} levels of theory, respectively. The electric dipole transition moment (TM) ratio $\mu_a^2 : \mu_b^2 : \mu_c^2$ obtained from CIS/cc-pVDZ and CIS/631-G^{**} calculation of the optimized geometries of the pseudoEPD monomer. Relative energies, E_{rel} of the four most stable conformational structures of the pseudoEPD monomer without and with inclusion of the zero-point vibrational energy (ZPVE) have been calculated at the MP2/aug-cc-pVDZ level of theory.*

[a] Values calculated at CIS/cc-pVDZ level of theory

[b] Values calculated at CIS/631-G^{**} level of theory
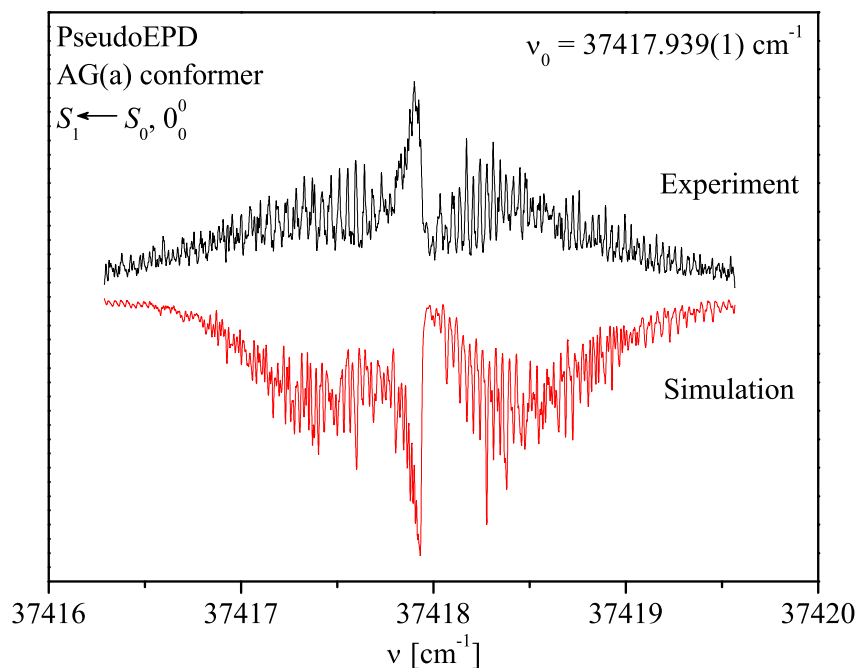
Figure 9.3: *High-resolution two-color UV R2PI spectrum of the vibronic band 0_0^0 in Figure 9.2, recorded at mass channel with m/z = 58. The band is assigned as an origin of the **AG(a)** conformer of the pseudoEDP monomer with its rotationless transitions centered at 37417.939(1) cm^{-1}. Upper trace: experimental spectrum. Lower inverted trace: the best-fit simulated spectrum yielding the parameters in Table 9.1 (for details, see text).*

stants for the ground, S_0, electronic state of the four predicted structures at the MP2/cc-pVDZ level of quantum chemical calculations, the best cross correlation (95% and 94%, respectively) between experimental and synthetic spectra was achieved for conformation **GG(b)**. The spectra are different (see Figure 9.5): for band 126 cm^{-1} one observes a resolved P-branch with several well pronounced peaks, small Q-branch and an intense R-branch with nicely defined peaks while for band 212 cm^{-1} the rotational structure consists of densely spaced rotational peaks in the P-branch, a strong Q-branch and a poorly resolved R-branch with a floating intensity of the rotational peaks. Despite the difference in rotational structure, the fitted rotational constants for both peaks are very similar; a small difference originates from the mismatching transition-moment ratios (see Table 9.1). In the case of band 126 cm^{-1} the *b*-type dominates over the *a*- and *c*-type parts, while in band 212 cm^{-1} the contributions from *a*- and *b*-type are almost equal with small *c*-type participation. As a result, we may conclude that the two bands represent different vibronic bands of the same conformer.
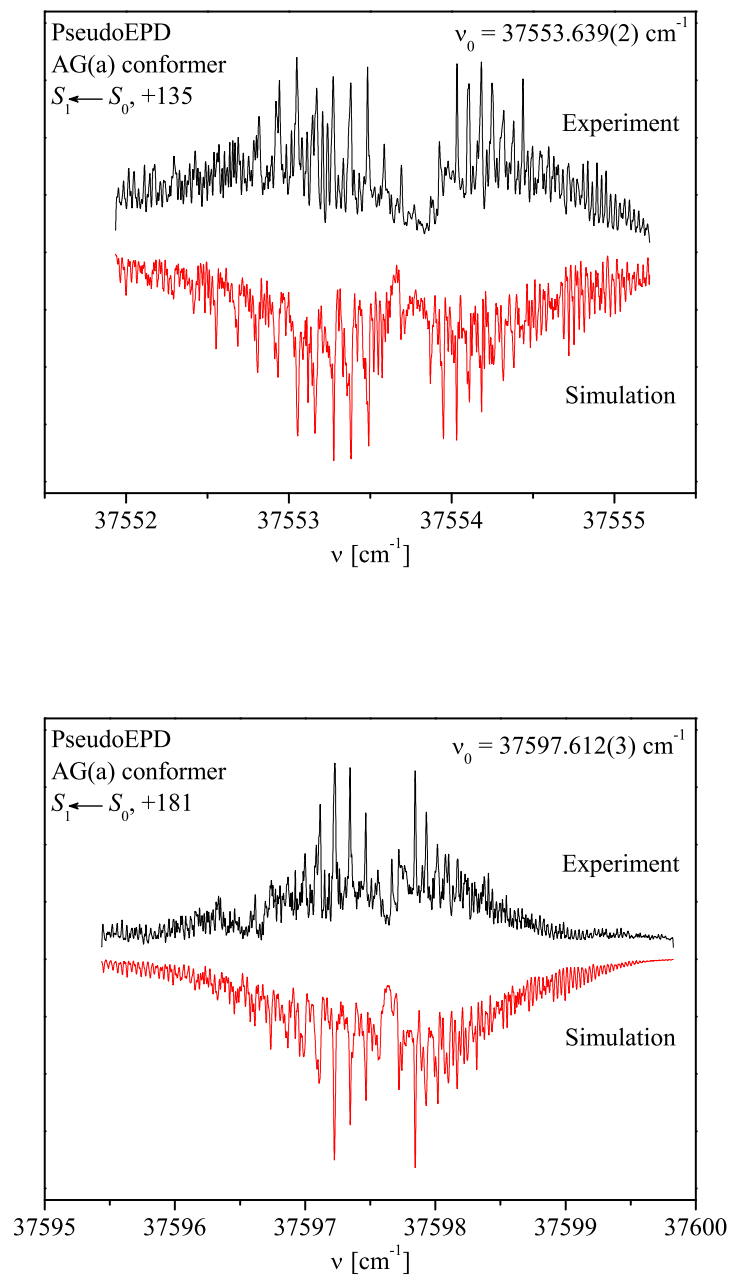
Figure 9.4: *High-resolution two-color UV R2PI spectrum of vibronic bands +135 cm^{-1} and +181 cm^{-1} in Figure 9.2, recorded at mass channels with m/z = 71 and m/z = 58, respectively. The bands are assigned as a progression of the **AG(a)** conformer of the pseudoEDP monomer with their rotationless transitions centered at 37553.639(2) cm^{-1} and 37597.612(3) cm^{-1}, respectively. Upper trace: experimental spectrum. Lower inverted trace: the best-fit simulated spectrum yielding the parameters in Table 9.1 (for details, see text).*
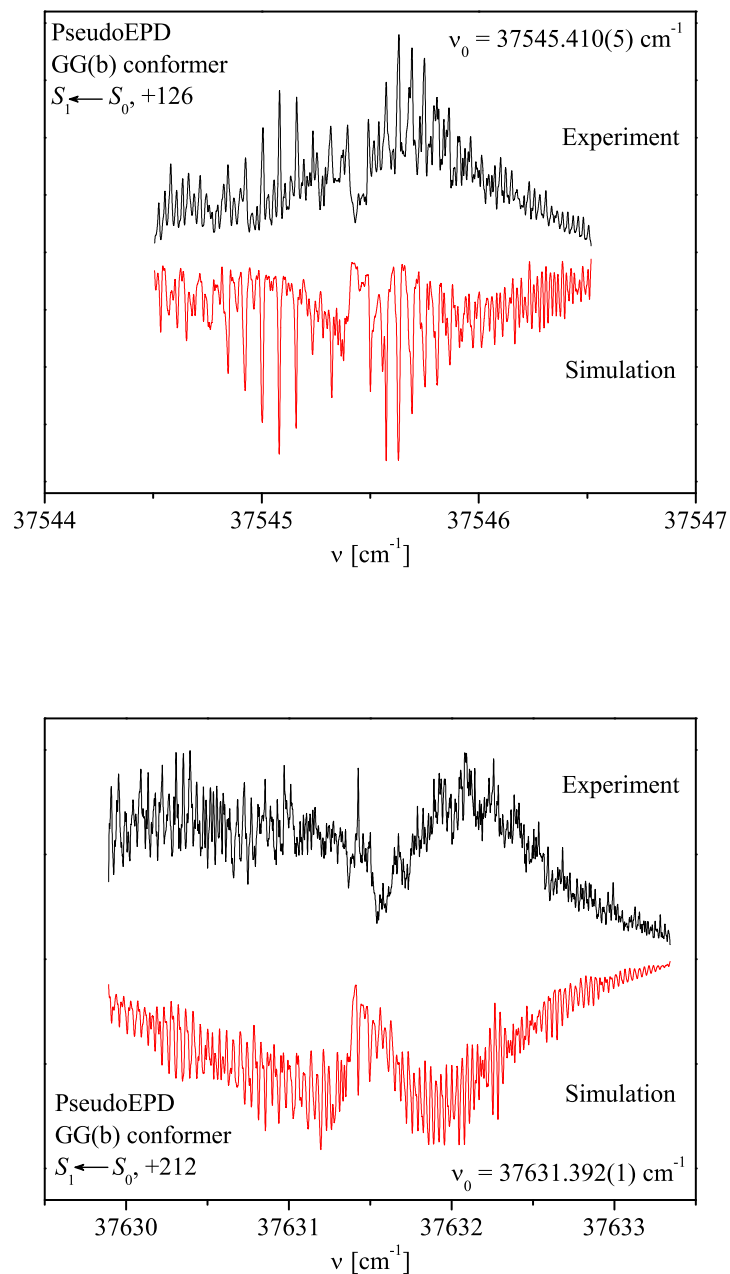
Figure 9.5: *High-resolution two-color UV R2PI spectrum of vibronic bands +126 cm^{-1} and +212 in Figure 9.2, recorded at mass channels with m/z = 85 and m/z = 58, respectively. The bands are assigned as originating form the **GG(b)** conformer of the pseudoEDP monomer with their rotationless transitions centered at 37545.410(5) cm^{-1} and 37588.040(1) cm^{-1}, respectively. Upper trace: experimental spectrum. Lower inverted trace: the best-fit simulated spectrum yielding the parameters in Table 9.1 (for details, see text).*

9.4   Discussion

The most stable calculated conformer, without and with the inclusion of the ZPVE, corresponds to the extended **AG(a)** geometry with its H atom from the OH group pointing to the neighboring (methyl) amino group. The structure is assumed to be stabilized by an *intra*molecular hydrogen bond, as is the case in the EPD monomer. [67] The next-in-energy conformer lies 62 cm^{-1} above the most stable structure and belongs to the folded **GG(b)** conformer, which differs from conformer **AG(a)** by the formation of an additional π hydrogen bond between the N-methyl group and the aromatic ring. The third-in-stability conformation correspond to the **GG(a)** geometry with its NH group pointing to the π electrons of the benzene ring which is higher by 161 cm^{-1} from the lowest-energy conformation. The stability of this structure is distorted by the competition between the formation of an *intra*molecular NH$\cdots\pi$ hydrogen bond and the possible existence of a hydrogen bond between the OH group and the N-methyl group. The highest-energy conformation at +305 cm^{-1} is the **AG(b)** conformer with a rotated terminal methyl group at 90^0 in comparison to **AG(a)**.

We assign the lowest energy peak at fragment mass m/z=58 to the 0_0^0 origin band of the most stable conformer **AG(a)**. The same conformer gives rise also to bands 135 at fragment mass m/z=71 and 181 at the main fragment mass m/z=58. The assignment has been made on the basis of the very good agreement of the theoretically predicted rotational constants for this conformer (see Table 9.2) with the ones obtained from the fit of the highly resolved spectra both for the ground, S_0, and the first excited, S_1, electronic states (see Table 9.1). It is interesting that despite the similar experimental rotational constants for these three bands, the transition-moment ratio for the 0_0^0 band (68:14:18) (which is in a very good agreement with the theoretical one (70:10:20)), differs significantly from the experimental transition-moment ratios of the other two bands 135 cm^{-1} (26:63:11) and 181 cm^{-1} (17:67:17), respectively. A trustworthy explanation for the change of the transition-moment ratio can be deduced in a closer inspection of the theoretical results for conformer **AG(a)**. It is visible from the *ab initio* optimizations in the first excited state (see Table 9.2) that a significant structural change occurs upon electronic excitation. The distance d (OH$\cdots$N) increases from 2.09 to 2.38 Å and the planar angle α_1(OHN) decreases from 120.3^o to 100.2^o, this trend can be easily induced by low-frequency vibrational modes, which include torsion of the side chain, particularly a displacement of the N-methyl group. These changes result in a redistribution of the molecular mass and interchange of the inertial moments, hence and to a change of the transition-moment ratio for the above low-frequency modes. Two such vibrational modes for the **AG(a)** conformer are predicted from the theoretical calculations in the first excited, S_1, electronic state: the β_1-bending of the N-methyl group vs. ring at 71 cm^{-1} and the β_2-bending of the N-methyl group vs. ring at 112 cm^{-1}. Both modes include a displacement of the N-methyl group and can easily lead to interchange of the inertial moments (see Table 9.2). They are in a good agreement with the experimental vibrational frequencies at

135 cm^{-1} (corresponding to β_2) and 181 cm^{-1} (corresponding to the combination mode $\beta_1 + \beta_2$). A similar situation is observed and for the experimental highly resolved spectra of the other two bands under consideration: band 126 cm^{-1} recorded at fragment mass channel m/z=85 and band 212 cm^{-1} measured at the main fragment channel with m/z=58. The assignment that these bands originate from conformer **GG(b)** is based again in the good agreement between the experimental and theoretically predicted values of the rotational constants for the ground, S_0, and the first excited, S_1, electronic states (see Tables 9.1 and 9.2). The deviations in the experimental values for the transition-moment ratio from the theoretical ones and between each of the bands can be attributed again to structural changes upon excitation due to low-frequency modes involving movement of the *N*-methyl group. The theoretical calculations for the first excited, S_1, electronic state of conformer **GG(b)** predict a bending vibrational mode at 89 cm^{-1} (β_3) which includes movement of the *N*-methyl group vs. benzene ring. This mode is in a very good agreement with the distance between the vibronic bands at 126 cm^{-1} and 212 cm^{-1} (86 cm^{-1}). Unlike ephedrine (see Chapter 8), where the pronounced fragmentation behavior was observed at excess energies larger than 500 cm^{-1} above the 0_0^0 vibration and was explained as vibrationally specific, here in the case of the diastereoisomer pseudoephedrine, for the first time, evidences for a conformer specific fragmentation are presented. As already discussed in the previous section, the relatively high intensity of the vibronic signals at fragment masses with m/z=71 and m/z=85, allowed the measurement of these bands under higher resolution. In a comparison with the theoretically predicted molecular parameters of four energetically low lying conformational structures, an assignment of the experimental spectra was made as originating from two distinct conformers: **GG(b)** and **AG(a)**. As it was shown in the previous chapter for ephedrine (see Figure 8.5) that after electronic excitation, the **AG** conformations could be observed both at mass channels with m/z=58 (the main one) and m/z=71 while in addition to the most abundant fragment channel with m/z=58 for conformations **GG** there exists a fragment mass channel with m/z=85. This clearly demonstrates a conformer specific fragmentation because mass channel with m/z=85 is only observed for the **GG(b)** conformer.

9.5   Summary and Conclusions

The flexible biological molecule pseudoephedrine, a diastereoisomer of the neurotransmitter ephedrine, has been investigated by combination of low- and high-resolution R2PI two-color mass-selective laser spectroscopy and high-level *ab initio* calculations of its structure and energetics. In this work, all prominent vibronic bands in the low-resolution spectrum of the pseudoEPD monomer up to 300cm^{-1} have been measured under high resolution of 70 MHz at the observed fragment mass channels with m/z=58, m/z=71 and m/z=85, respectively. Comparing the values of the rotational constants obtained from the fits of the highly resolved spectra with

the theoretically predicted ones for the four lowest-energy conformations, we were able to assign all of these vibronic bands to two conformational geometries: the lowest-energy structure **AG(a)** and the next-in-energy structure **GG(b)**. Different from the situation in ephedrine the mass channel with m/z=85 is more efficient with strong signals. The rotational analysis of the vibronic bands measured at different masses clearly demonstrates that m/z=85 channel is only present for the conformer **GG(b)**. We observe only two out of four predicted structural geometries, which is in indication that a relaxation of the higher energy conformers to the stable ones may occur. To estimate the potential barriers and the relaxation pathways high-level calculations of the potential energy surface are in progress. The observed deviations of the transition-moment ratios in the rotationally resolved spectra of the vibronic bands originating from the two conformers are attributed to geometrical changes during the electronic excitation accelerated by structure distorting low-frequency vibrational modes. From these results, we conclude that conformer specific processes take place after the excitation of the neutral conformers of flexible molecule. This represents a spectroscopic proof of conformer selective processes in biologically relevant molecules.

Part IV

Concluding Remarks

Summary and Conclusions

The present work contains new results on model flexible molecules, their binary water complexes and their fragmentation behavior, acquired through the powerful combination of high-resolution multiphoton UV and threshold ionization spectroscopy both with mass selectivity, genetic-algorithm-based rotational fitting procedure, and high-level *ab initio* quantum chemistry computations. These results elucidate several important phenomena: one is the effect of fluorination on the conformational preferences of biologically relevant prototype molecules; another one is the formation of *intra*molecular hydrogen bonds, which stabilize conformational structures and of *inter*molecular hydrogen bonds, which participate in the formation of water complexes. Another interesting effect that was revealed in this work is the origin of the newly observed fragmentational pattern in two important neurotransmitter molecules.

In the beginning of the thesis, a general description of the spectroscopic techniques along with the details of the experimental set up and conditions used for the investigation of the above mentioned molecular systems has been presented. Particular emphasis has been put on the excitations schemes of mass analyzed threshold ionization and resonance enhanced two-photon ionization, the attempt of pulse stretching of the laser pulses, on the production of supersonic molecular beams, the laser systems and the genetic-algorithm-based fitting routine.

The experimental section is followed by a detailed survey of the obtained results. That can be divided into three main groups. The first one considers the conformational landscape of flexible biologically prototype aromatic molecules and the effect of fluorination on the conformational behavior. The second group of results consists of the investigation of the formation of water binary complexes of these species. Finally, the third group encompasses evidences that shed light on the specific fragmentational pattern of two neurotransmitter molecules.

The nonconventional O-H$\cdots\pi$ type hydrogen bond and its stabilizing effect on the most abundant conformeric structures has been addressed through the investigation of the flexible 2-phenylethanol, 2-*para*-fluorophenylethanol and 2-*ortho*-fluorophenylethanol. The experimental high-resolution resonance enhanced two-photon ionization spectroscopic results together with fits of the rotational structure of vibronic bands and *ab inito* calculations have demonstrated that in all cases the preferred geometry is the *gauche* one in which the OH group of the bent side chain is connected and stabilized through an intramolecular hydrogen bond with the π electrons of the ben-

zene ring. For 2-phenylethanol and 2-*para*-fluorophenylethanol, presence of *anti* structures is identified. Despite of their higher energy, these conformers are available since relaxation to the lower gauche ones is not possible because of high potential barriers. The other important results is that the presence of a strongly electronegative atom in the moiety of the aromatic ring does not affect the stability of the O-H$\cdots\pi$ interaction and the *gauche* conformers of the above mentioned molecules are preserved.

The competition between σ and π hydrogen bonds, conditioned by the proximity of the F atom to the side chain, and hence to the terminal hydroxyl group in 2-*ortho*-fluorophenylethanol has been subjected to a detailed spectroscopic investigation. It showed a disappearance of the *anti* conformers, observed in the case of 2-*para*-fluorophenylethanol, and a possible presence of a new *gauche* conformer where the OH group in 2-*ortho*-fluorophenylethanol is located close to the fluorine atom, facilitating the formation of a σ hydrogen bond with nearby electronegative atom.

The fate of the O-H$\cdots\pi$ hydrogen bond during ionization has been explored by mass analyzed threshold ionization spectroscopy of the prototype system 2-*para*-fluorophenylethanol. Ionization leads to the ejection of a π electron and thus to a decrease of the π-electron density in the ring. From *ab inito* calculations with the recently developed MO5 DFT functional and threshold ion vibronic spectra, it has been found that the resulting ionic structure of the neutral *gauche* conformer is significantly influenced which leads to its transformation to a structure where the stabilizing O-H$\cdots\pi$ hydrogen bond does no longer exists.

The binding positions of the water and the resulting singly hydrated complexes of 2-phenylethanol, 2-*para*-fluorophenylethanol and 2-*ortho*-fluorophenylethanol have been elucidated through the analysis of the highly resolved rovibrational spectra of water binary clusters in the supersonic jet and theoretically by quantum chemical optimizations of the most stable conformeric structures. For 2-phenylethanol and 2-*para*-fluorophenylethanol, the theoretically most stable binary water complex is one, where the water acts as a proton acceptor from the OH group of the host and a proton donor to the π electrons of the benzene ring. These were not detected directly through their highly resolved UV spectra, but evidence for their presence was deduced from mass selective vibrational low-resolution spectra. On the other side, the next-in-energy complex structures where the water acts as a proton donor to the terminal OH group of the monomer were directly identified by rotational analysis of their high-resolution spectra. In the case of 2-*ortho*-fluorophenylethanol the theoretically predicted most stable structure was observed experimentally, together with a higher energy one that is formed through the insertion of the water molecule between the fluorine atom and the OH group of the side chain of the host molecule.

Hitherto unknown fragments of the biologically active molecules ephedrine and its diastereoisomer pseudoephedrine have been observed for the first time in our two photon ionization mass spectra. They pointed to two interesting effects: In ephedrine, the fragmentational behavior is found to depend on the nature of the vibrational intermediate state of a single conformer in the two-photon ionization process. On the other hand, in the case of pseudoephedrine the fragmen-

tational pattern depends on the different structural geometries of two conformers.

In conclusion we have shown that the correlated analysis of high-resolution R2PI and MATI spectroscopy data, supported by high-level *ab initio* calculations, provides very accurate information on the structure of medium sized monomers, and their water binary clusters and details of the *intra*molecular and *inter*molecular interaction processes, both in the excited and in the ionic state. Once the spectroscopy and conformational preferences of the monomers are available, the molecules presented here and their larger derivatives will be interesting candidates for further investigation of the effects of water attachment on their conformational preferences. As the size of the solute molecule grows, the potential for *intra*molecular hydrogen bonds also will increase. Complexation with water could lead to a competition between *intra*molecular and *inter*molecular hydrogen bonds, or to a strengthening of the *intra*molecular hydrogen bonds by water bridges. The influence of water solvation, and more particularly water bridge formation, on the conformational preferences of flexible monomers of even greater complexity will be a fascinating and challenging arena in which to apply the precise methods highlighted in this work. They also will present a particular challenge to computational chemists, and those seeking to improve semiempirical force fields.

In addition, reliable information for the cationic structures can serve as a base for the understanding of processes like charge delocalization in biologically active molecules like peptides, amino acids and neurotransmitters where ultrafast charge mobility can be highly correlated with reactivity as shown by theoretical models. As a first promising step towards this goal, we have presented threshold ionization spectra with vibrational resolution of a prototype flexible molecular cation.

Both from the experimental and theoretical points of view, the way is open to reach systems of higher dimension, starting from chromophore containing biologically relevant flexible systems with short side chains like the neurotransmitter amphetamine and the neural hormone melatonin, and continuing to larger systems like carbohydrates, including mono- and oligosaccharides, peptides and glycopeptides.

Appendices

Appendix A

Molecular Interactions

This appendix discusses the molecular interactions and their most important characteristics. It presents a classification of the weak intermolecular bonds along with examples of their typical occurrences. Stabilization of molecular structures and binding patterns of molecular clusters resulting from the subtle interplay between various weak interactions are highlighted.

A.1 Chemical Bonds

The formation of chemical bonds is a quantum mechanical phenomenon manifesting itself in the interaction of two atoms and resulting in the building of more complex objects such as molecules and solids. Chemical bonds can be subsumed into three main categories: *covalent* (homopolar), *ionic*, and *metallic* [133].

- Covalent bonds are formed by sharing an electron pair between two atoms, thus leading to a minimization of the total energy of this system. When two identical atoms form a covalent bond, for instance H_2, O_2, etc., the electron density is distributed symmetrically between them and the bond in this case is referred to as *nonpolar*. In general, however, the two atoms participating in the covalent bond formation have different electron affinities, and hence the electron density is shifted towards the one with higher electronegativity, thus resulting to a *polar* bond: HCl, HF, etc.

- In the extreme case, when the difference of electron *affinities* of the two atoms is very large, the electon pair is shifted to the strongly electronegative atom, thus giving rise to the formation of two electric charges which are held together by Coulomb electrostatic attraction. In this way the strongly polar covalent bond transforms into an *ionic* bond such

as in the case of NaCl, for instance. The border between strongly polar *covalent* and *ionic* bonds, however, is not rigorously set.

- *Metallic* bonds are strongly delocalized. They result from sharing the valent electrons, which are in the conduction band, between all atoms, thus forming the so-called electron gas.

Chemical bond energies range between 1 and 10 eV, and their typical distances are between 1 and 3 Å. They determine the 'skeletal' structure of molecules.

A.2 Weak Molecular Interactions

In isolated molecules the negatively charged electron shell shields off the positively charged molecular core, thus yielding a neutral system. When molecules are close to one another, however, their electron shells experience not only the influence of their own positive cores but also the presence of the electron shells of the surrounding molecules. This brings about a deformation and redistribution of the electron charge within the molecules, leading to an incomplete shielding of the positive cores and, respectively, to the appearance of locally charged molecular species. Thus, molecules interact with one another by electrostatic forces acting between the positively charged molecular cores and the negatively charged shells. Weak molecular interactions are also referred to as *nonbonding* or *noncovalent* to distinguish them from chemical (also called *bonding*) interactions. Nonbonding interactions are two types: *attractive* and *repulsive*. *Attractive* weak molecular interactions are classified as *electrostatic*, *inductive*, and *dispersion*. *Repulsive* interactions stem from the Pauli exclusion principle.

A.2.1 Attractive Molecular Interactions

Permanent-Charge-Distribution Interactions

Static charge distributions can be expanded in a series of multipole moments. Thus, two molecules, A and B, interact with each other through the interaction of the static multipole moments of their charge distribution. That is why, this type of intermolecular interaction is referred to as *electrostatic*, and the resulting interaction energy is designated as E_{el}. This type of intermolecular interactions is subject of the *first-order perturbation theory* . The electrostatic energy can be presented in the following way:

$$E_{el} = \frac{q_A q_B}{|\mathbf{r}|} + \frac{q_A |\boldsymbol{\mu}_B|}{\mathbf{r}^2} + \frac{q_B |\boldsymbol{\mu}_A|}{\mathbf{r}^2} + \frac{\boldsymbol{\mu}_A \cdot \boldsymbol{\mu}_B}{|\mathbf{r}|^3} + \frac{q_A Q_B}{|\mathbf{r}|^3} + \frac{q_B Q_A}{|\mathbf{r}|^3} + \frac{\boldsymbol{\mu}_A \cdot Q_B}{\mathbf{r}^4} + \frac{\boldsymbol{\mu}_B \cdot Q_A}{\mathbf{r}^4} + \frac{Q_A \cdot Q_B}{|\mathbf{r}|^5} + \cdots \quad (A.1)$$

where q, $\boldsymbol{\mu}$, Q, and $\mathbf{r}$ stand for the *electric charge*, *electric dipole moment*, *electric quadrupole moment*, and the *position vector* of the second molecule relative to the first one, respectively. It is important to emphasize that the energy, E_{el} depends not only on the magnitude of the multipoles but also on their mutual orientation (this is encoded in the dot products in Eq. A.1). That is why, in natural systems the molecules are oriented such as to minimize the total electrostatic energy. It is obvious from Eq. A.1 that the magnitude of the higher-order terms in the multipole expansion dwindles down very rapidly with the intermolecular distance (inverse power law) and for this reason, the interaction energy can be described fairly accurately only by retaining the first nonvanishing terms in the multipole series. Some molecules, due to symmetries, do not have low-rank permanent multipoles, and hence necessitate the inclusion of higher-order terms. There exist also molecular systems, e.g., complexes with rare gas atoms, that do not have permanent multipoles at all, and for them the electrostatic interactions do not come to the scene.

Induction Interactions

The induction interaction between two molecules, A and B, originates from the interaction between the permanent dipole moment of one of the molecules with the induced dipole moment (it induces) in the other one. The magnitude of the induced dipole moment depends on the magnitude of the permanent dipole moment, the spacing between the two molecules, and the *polarizability* α of the molecule in which the dipole moment is induced. This model constitutes the so-called *second-order perturbation theory* . The potential energy of induction interactions, E_{ind}, can be presented in the form:

$$E_{ind} = -\frac{1}{2}\alpha_B\left(\frac{q_A^2}{\mathbf{r}^4} + f_1(\boldsymbol{\mu}_A,\boldsymbol{\mu}_B)\frac{\mu_A^2}{\mathbf{r}^6} + f_2(\boldsymbol{\mu}_A,\boldsymbol{\mu}_B)\frac{Q_A^2}{\mathbf{r}^8}\right), \tag{A.2}$$

where α, q, $\boldsymbol{\mu}$, and Q designate the polarizability, the electric charge, the electric dipole moment , and the electric quadrupole moment , respectively. The molecule with permanent multipoles is denoted by A, and the one with induced multipoles by B. Functions f_1 and f_2 depend on the mutual orientation of the two molecules, A and B.

Dispersion Interactions

Dispersion interactions constitute the third type of attractive intermolecular interactions. They derive from the mutual polarization of the instantaneous electron density distributions of the two monomers, A and B. They were for the first time rationalized and described by London [134], and hence called also *London* inetractions. The potential energy of such an interaction, E_{disp}, can be cast in the form

$$E_{\text{disp}} = -\frac{C_6}{\mathbf{r}^6} - \frac{C_8}{\mathbf{r}^8} - \frac{C_{10}}{\mathbf{r}^{10}} - \cdots \tag{A.3}$$

C_6, C_8, C_{10}, etc. are empirical constants, and $\mathbf{r}$ is the position vector of the molecule B relative to molecule A. London [134] has discovered a relation between the above-mentioned constants and the polarizabilities α_A and α_B of the two interacting molecules, A and B, and their ionization energies. Notwithstanding it is the weakest among the attractive interactions, the dispersion interaction gains importance in nonpolar molecular complexes where it gives rise to the only binding force. Hence, it is of paramount importance in large molecules with large polarizability, and in complexes containing a noble-gas atom, as is shown in this work.

A.2.2 Repulsive Molecular Interactions

The only repulsive intermolecular interaction arising when two molecules, A and B, are close to each other stems from the *exchange* interaction. The latter is a manifestation of the fundamental Pauli exclusion principle, which precludes the penetration of electrons from one of the molecular moieties into the occupied orbitals of the other one. The description of the exchange interaction is based completely on quantum mechanics. The resulting energy, E_{exch} has been mathematically formulated by Heitler and London [133–135] through an exponential or inverse power law :

$$E_{\text{exch}} = A \cdot e^{-\frac{2r}{a_0}} \tag{A.4}$$

$$E_{\text{exch}} = \frac{B}{r^n} \tag{A.5}$$

In Eq. A.4 a_0 is the Bohr radius of the hydrogen atom, and A is an empirical constant. In Eq. A.5 B is an empirical constant, and the power n ranges between 10 and 20. The inverse-power low describes the exchange repulsion in cases of very small separation distances between the two molecules, A and B.

A.3 The Concept of Weak Molecular Bonds

Weak molecular interactions (descibed above) are not isolated but usually co-exist and act co-operatively. The net effect of the concurring weak interactions is a result of a delicate balance between them, ultimately leading to the formation of a weak bond whose nature, however, is different from the nature of chemical bonds (see Sec. A.1 above) altogether. Its strength is typically

from one to two orders of magnitude weaker compared to the one of chemical bonds, depending on the nature of the particular molecular system and the weak interactions involved. Usually, the energy of weak molecular bonds, E_{bond}, is in the range of 0.01-1 eV, and the interatomic distances are longer (2-5 Å) than the ones in the case of chemical bonds.

The total energy of a weak molecular bond, E_{bond} can be presented as a sum of the energies of the interactions involved

$$E_{\text{bond}} = E_{\text{attr}} + E_{\text{rep}} = E_{\text{el}} + E_{\text{ind}} + E_{\text{disp}} + E_{\text{exch}} \tag{A.6}$$

The interaction potential and its two constituents, the *repulsive* and the *attractive* potentials, are presented schematically in Fig. A.1
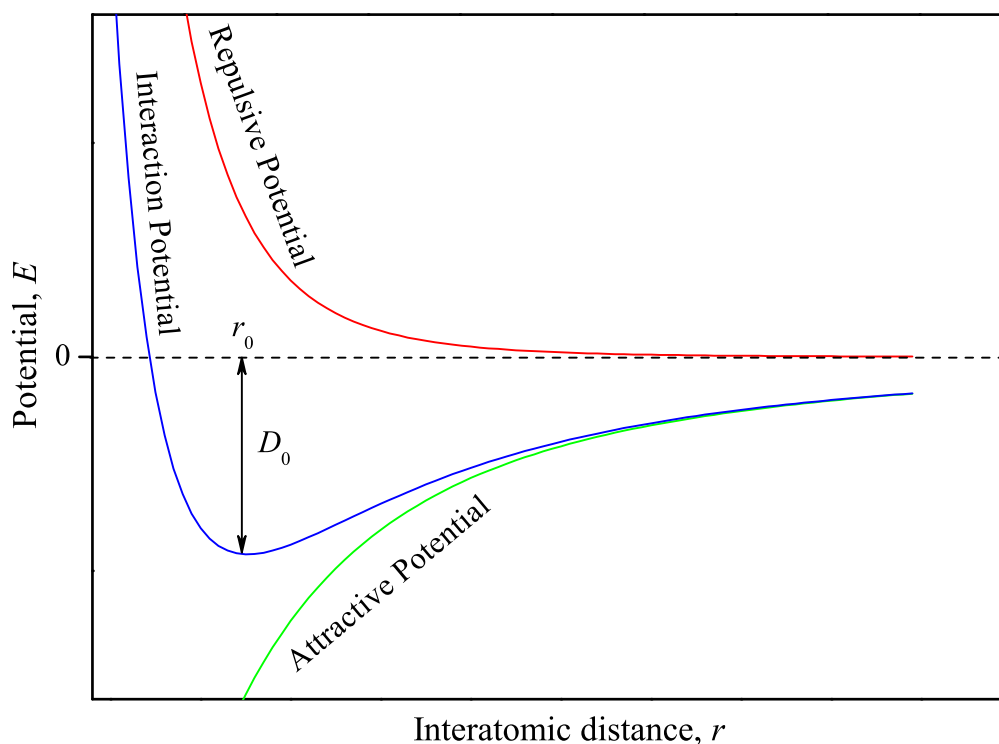
Figure A.1: *Schematic representation of a weak two-atom molecular interaction potential composed of a repulsive and attractive potentials. r_0 designates the interatomic distance corresponding to the the minimum of the potential well, and D_0 is the depth of the potential well.*

It is interesting to observe that due to the balance between the attractive and repulsive potentials, in most cases, there exists an equilibrium interatomic distance, r_0, at which the net interaction energy has minimum. It may happen, however, that the attractive potential cannot make up for the action of the repulsive potential at any point, thus leading to a nonbonding potential, i. e., a potential that do not pertain a minimum. In this case no weak bond can be formed. It is im-

portant, however, to point out that for a bond to be formed, not only must the potential have a minimum, but also the zero-point vibrational level must be below the dissociation energy.

Very often, for practical needs, the shape of the interaction potential must be known. Obtaining the shape of the potential starting from first principles and considering all types of interactions involved is quite demanding, and in most cases, untractable problem. Another approach to solving the problem is to devise a model potential, i.e., a special function containing free parameters, as the ones shown in Fig. A.1, and to fit those parameters to experimental data. The simplest, yet sustainably popular one, was suggested by Morse [136] in 1929. It is a zeroth-order approximation to experimental potentials. To more accurately describe real potentials, one has to resort to more complex potentials, the most commonly used one being the famous Lennard-Jones potential [133, 137, 138]. It includes two terms accounting for repulsive and the attractive interactions. In real systems, the interactions are not constrained to two-body ones. For an adequate description of weak molecular interactions involving more than two particles, the many-body interaction is reduced to a two-body interaction, wherein the above-discussed treatment applies.

A.4   Classification of Weak Molecular Bonds

The combination of the various types of weak molecular interactions gives rise to a big variety of bonding patterns. Though there is no rigorous borderline between them, a general classification according to the nature of the interactions involved, bond energies, and bond lengths can be made.

A.4.1   Hydrogen Bonds

Hydrogen bonds (H-bonds) are one of the most abundant and important types of weak molecular interactions in nature. They determine the properties and behavior of liquids and biological systems. Hydrogen bonds have the general motif X-H$\cdots$Y, where the X-H group is a *proton donor* , and Y is a *proton acceptor* . Usually, X is an electronegative atom (O, N, Cl, F, etc.), and Y is most typically either an atom possessing a lone electron pair or it is a π-electron system (benzene ring, or double or triple chemical bond), which has an excess of electron density. Weak hydrogen bonds involving a π-electron system have attracted scientists' attention for more than 60 years since Dewar's work [139] appeared, and their significance has been recognized in many biologically relevant systems. It was not until recently, when the importance of another specific type of hydrogen bonds was realized; these are the C-H$\cdots$Y (nonconventional) hydrogen bonds [81, 140–143], which play an important role for the stabilization of molecular structures. Usually, Y is an electronegative atom or a π system. They are much weaker compared to the conventional hydrogen bond, and with respect to the binding energy they are at the borderline

between hydrogen bonds and dispersion bonds (see below).

It has long been known that the π electrons of alkenes, alkynes, and aromatic compounds may act as hydrogen acceptors [144, 145]. Alcohols and phenols, as well as primary and secondary amines, are known as good hydrogen donors. For example, hydrogen bonds often provide the strongest *inter*molecular forces between molecules in organic molecular crystals and hence often dictate the preferred packing arrangement. The general principles underlying hydrogen-bond formation are reasonably well understood and the structures of hydrogen-bonded crystals can often be rationalized in preferred combinations of hydrogen-bond donors and acceptors [146–148]. In general, the strongest hydrogen-bond donors pair off with the strongest hydrogen-bond acceptors. Similar pairing processes are repeated until all the hydrogen-bond donors and acceptors have been utilized. However, when a system contains excess donors or acceptors, at least two hydrogen-bonding strategies are available to accommodate the mismatch [149]: (i) change in hybridization or (ii) the formation of hydrogen bonds involving the π system of an aromatic group as the acceptor. Interaction between π bases and hydrogen donors have been examined mainly by IR spectroscopy [150]. As a consequence of weakening of the OH or NH bond, the OH or NH stretching absorption of hydrogen donors show low-frequency shifts. The shifts are, however, considerably smaller than in OH$\cdots$O and other hydrogen bonds, indicating that the strength of an OH$\cdots\pi$ interaction is weaker than that of an OH$\cdots$O hydrogen bond.

Relatively few structure studies of compounds with *intra*molecular OH$\cdots\pi$ hydrogen bonds are known. In this work we have studied the formation and the role of such π hydrogen bonds as a stabilizing factor in the conformational preferences of model organic molecular systems.(See Chapters 3, 4, 6.)

The most significant features and properties of hydrogen bonds are highlighted in the following.

- Hydrogen bonds are stabilized by a subtle interplay between electrostatic, induction (charge-transfer), and dispersion interactions [89]. The most important contribution, however, is the electrostatic one, realized mainly through dipole-charge and dipole-dipole coupling. This brings about the next traits of hydrogen bonds.

- Hydrogen bonds provide a typical example of a two-body interaction. Due to the electrostatic attraction the H-bond length is shorter than the sum of the van der Waals radii of the two atoms, X, and Y.

- *Directionality*. Hydrogen bonds are strongly directional, i. e., the three atoms, X, H, and Y, lie down a straight line.

- Typical H-bond lengths range between 2 and 3 Å.

- The energy of H-bonds varies between 0.1 and 1 eV, depending on the nature of X and Y atom (groups), and consequently, on the relative contributions of the constituting interac-

tions. Thus, some H-bonds render themselves at the brink of chemical bonds

Altogether hydrogen bonds can be subsumed into three major groups: *proper* (*red-shifting*), *improper* (*blue-shifting*), and *dihydrogen* bonds.

Proper Hydrogen Bonds

Proper (red-shifting) hydrogen bonds weaken the covalent X-H bond thus leading to its elongation, and respectively, to a red shift of the X-H stretching vibrations . The nature of this effect has been explained on the basis of bond orbital analysis [89, 151]. The latter shows that a charge transfer takes place from the lone electron pair or the π-electron system of the proton acceptor to the antibonding orbitals of the proton donor. This leads to an increase of the electron density in the antibonding orbitals, which causes the weakening of the X-H chemical bond, and to its elongation.

Improper Hydrogen Bonds

Improper (blue-shifting) hydrogen bonds [89, 152] exhibit behavior opposite to the one of proper hydrogen bonds (see above), i. e., upon the formation of such weak bonds the chemical X-H bond shortens and the frequency of the X-H vibration increases. Blue-shifting hydrogen bonds were theoretically predicted for carbon-proton donor-benzene complexes [153] and later on, their existence was experimentally verified for the model system chloroform-fluorobenzene complex [154]. As in the case of red-shifting bonds, a charge transfer process underlies the observed phenomena. In this case, however, the charge transfer is directed to the remote part of the X-H bond, followed by a structural change in the proton-donor molecule.

Dihydrogen Bonds

Dihydrogen bonds [89, 155] have the pattern X-H$\cdots$H-Y, where X is an atom of a metal element, and Y is an electronegative atom. They were discovered only recently in a hydrogen-bonded complex containing Ir [156]. The mechanism of these bonds was rationalized a bit later [157], and it is quite straightforward. The metal atom donates electron density to the covalently attached to it H atom, thus creating a partial negative charge upon it. On the other hand the electronegative atom Y withdraws the electron density from the adjacent H atom so that the latter becomes positively charged. In this way the dihydrogen bond is stabilized by a multipole interaction.

A.4.2   Quadrupole-Quadrupole Bonds

The occurence of *quadrupole-quadrupole* bonds is limited to systems containing benzene rings, which do not have permanent dipole moments. They determine the T-shape structure of the benzene dimer, and play an important role for the stabilization of secondary and tertiary structures of macromolecules.

A.4.3   Charge-Transfer Bonds

Charge-transfer (CT) bonds emerge when one of the bonded moieties is a good electron donor (it has a low ionization potential), and the other one has high electron affinity. Donors pertain antibonding orbitals designated as n, σ, and π, respectively, and acceptors have vacant orbitals labelled as n^*, σ^*, and π^*, respectively. The strongest of the so-formed CT complexes are the ones of *n-v* type.

A.4.4   Ion-Mediated Bonds

Ion-mediated bonds stem from the presence of metallic cations, which have high electron affinity, and hence form polar bonds on the basis of multipole interactions.

A.4.5   Hydrophobic Interactions

Hydrophobic interactions are a special class of interactions representing associations of non-polar groups in polar solvents. It has been found [89, 158, 159] that the change of the enthalpy is almost vanishing, and the driving force for the reorganization of the molecules in a solution is the entropy. This is their most distinctive feature compared to the above-described bonds, which are formed as a result of an energy minimization.

A.4.6   Dispersion Bonds

Dispersion bonds are formed when the interacting moieties do not have permanent charge distribution, and hence only the dispersion term in the attractive potential is accounted for. Dispersion bonds lack directionality and help for the stabilization of molecules and molecular complexes. Their manifestation is most pronounced in molecular complexes containing a noble-gas atom.

A.5   Binding Motifs

Weak interactions and weak bonds can be *intra*molecular or *inter*molecular. Intramolecular weak bonds play an important role for the stabilization of molecular structures, in particular, those that have many internal degrees of freedom and can assume different conformational shapes. The most abundant intramolecular bonds are the hydrogen ones, though quadrupole-quadrupole bonds are also observed. The most typical occurrence of such bonds is in biologically relevant molecules, as is discussed in Chapters 3, 4 and 6. *Inter*molecular bonds are responsible for the formation of supramolecular structures . When benzene-ring-containing molecules are involved in the formation of a complex with another molecule, two binding patterns are possible. A bond that is formed between an atom/molecule and the π electrons of the host molecule is referred to as a π bond. A bond that is realized between an atom/molecule and a benzene-ring substituent is termed a σ bond. An example for an *inter*molecular σ bond is presented in Chap. 7.

Appendix B

Ab Initio Quantum Chemistry Calculations: Structure, Energetics, and Frequency Analysis of Isolated Molecular Species

The interpretation of the experimental results is supported by theoretical studies. The theoretical prediction of molecular properties has ever been a challenging task. Many models describing one or a few aspects of the molecular behavior have been developed over the years. Until recently, many theoretical studies even on small molecules were untractable due to their, mainly, mathematical complexity. The rapid enhancement of computational power, however, has stimulated the development of sophisticated algorithms, and enabled the treatment of medium-sized and large molecules and molecular complexes [160–162]. The existing methods for the calculation of molecular structures and properties can be grouped in four categories, which are described in the following. The main emphasis, however, is put on the quantum-mechanical methods, which will be presented in more details [163].

B.1   Semiempirical Methods

Semiempirical models use for the description of molecules a simpler Hamiltonian than the real one, and employ a set of parameters whose values are adjusted to match the experimental data, and hence the name semiempirical. A typical example of such a model is the Hückel molecular orbital model, which employs a one-electron Hamiltonian, and the bond integrals play the role of the adjustable parameters.

B.2 *Ab Initio* Quantum Chemistry Calculations

Ab initio quantum chemistry calculations are based on the use of the 'first principles' and the fundamental physical constants. They employ the true molecular Hamiltonian, which accounts for all the interactions within the molecular system. It should be pointed out, however, that due to the approximations inevitably introduced in the solving of the Schrödinger equation, *ab initio* calculations do not provide the exact solution to the treated problem. The main idea on how the Schrödinger equation can be solved along with some important concepts are described below.

B.2.1 The Møller-Plesset Perturbation Theory

The Møller-Plesset (MP) perturbation theory [164] is a particular case of the many-body perturbation theory when the interelectronic repulsion is treated as a perturbation to the interaction energy between the nuclei and the electrons of a molecular system. The first practical applications of the MP theory came to the scene only in 1975 with the work Pople and co-workers [165]. Nowadays, it is widely used for accurate modeling of molecules and molecular complexes, and it is of particular significance when electron correlations must be accounted for. The overview presented below is restricted only to closed-shell ground-state molecules. For practical reasons, the spin-orbitals, rather than the spatial orbitals, are used. For spin-orbitals, the HF equations for electron m in an n-electron molecule have the form

$$\hat{f}(m)u_i(m) = \epsilon_i u_i(m) \tag{B.1}$$

The spin-orbital Hamiltonian can be cast in the following form

$$\hat{f}(m) \equiv -\frac{1}{2}\nabla_m^2 - \sum_i \frac{Z_i}{r_{mi}} + \sum_{j=1}^{n}[\hat{j}_j(m) - \hat{k}_j(m)]. \tag{B.2}$$

$\hat{j}$ and $\hat{k}$ are the Coulomb and the exchange operators, respectively . They are defined as

$$\hat{j}_j(\alpha)f(\alpha) = f(\alpha) \int |\phi_j(\beta)|^2 \frac{1}{\mathbf{r}_{\alpha\beta}} dv_\beta \tag{B.3}$$

$$\hat{k}_j(\alpha)f(\alpha) = \phi_j(\alpha) \int \frac{\phi_j^*(\alpha)f(\beta)}{\mathbf{r}_{\alpha\beta}} dv_\beta \tag{B.4}$$

In both definitions above, the integration is performed over the whole space, f is an arbitrary function, and α and β label the electrons. The Coulomb operator shows the interaction of electron

α with the spread-out charge of electron β. The exchange operator does not have an intuitive physical meaning. It originates from the condition of the wave function upon the exchange of two electrons.

It can be proved that the sum of the zeroth- and first-order energies equals the HF energy. That is why the first significant improvement in the MP energy is introduced through the inclusion of the second-order energy correction. For a comprehensive discussion on the matter, the reader is referred to Levine's textbook on quantum chemistry [163]. The second-order correction to the energy is

$$E_0^{(2)} = \sum_{s \neq 0} \frac{| \langle \psi_s^{(0)} | \hat{H}' | \Phi_0 \rangle |^2}{E_0^{(0)} - E_s^{(0)}} \tag{B.5}$$

where the summation is performed over the excitation of the zeroth-order wave function, i. e., single, double, etc. excitations.

B.2.2 The Coupled-Cluster Method

The *coupled-cluster* (CC) method was invented in 1958 by Coester and Kümmel. A nice discussion on this method can be found in [165]. The fundamental equation the coupled-cluster method is founded on is,

$$\psi = e^{\hat{T}} \Phi_0 \tag{B.6}$$

In this formula, ψ is the exact nonrelativistic ground-state molecular electronic wave function, and Φ_0 is the normalized ground-state HF function. The exponential operator is presented by its taylorization,

$$e^{\hat{T}} \equiv 1 + \hat{T} + \frac{\hat{T}^2}{2!} + \frac{\hat{T}^3}{3!} + \cdots = \sum_{k=0}^{\infty} \frac{\hat{T}^k}{k!} \tag{B.7}$$

$\hat{T}$ is referred to as a *cluster operator*, and $\hat{T} = \hat{T}_1 + \hat{T}_2 + \cdots + \hat{T}_n$, where n stands for the number of electrons in the molecule. Only the low-order cluster operators are of practical importance. The two most commonly used cluster operators are the *one-particle excitation* operator, $\hat{T}_1$, and the *two-particle excitation* operator, $\hat{T}_2$, which are defined as

$$\hat{T}_1 \Phi_0 = \sum_{a=n+1}^{\infty} \sum_{i=1}^{n} t_i^a \Phi_i^a \tag{B.8}$$

$$\hat{T}_2\Phi_0 = \sum_{b=a+1}^{\infty} \sum_{a=n+1}^{\infty} \sum_{j=i+1}^{n} \sum_{i=1}^{n-1} t_{ij}^{ab} \Phi_{ij}^{ab} \tag{B.9}$$

In the above definitions, Φ_i^a, and Φ_{ij}^{ab} designate singly-, and doubly-excited Slater determinants, where the occupied spin-orbital u_i is replaced by the vacant orbital u_a, and the occupied spin-orbitals u_{ij} are replaced by the vacant orbitals u_{ab}, respectively. The coefficients t_i^a, and t_{ij}^{ab} are named *amplitudes*. The goal of a CC calculation is to find the amplitudes. It is worth pointing out that two important approximations are present in the CC calculations: *i*) the basis set is not infinite but has some finite number of members included; *ii*) only the first couple of terms in the cluster-operator expansion are considered. Theory shows that the main contribution to $\hat{T}$ is provided by $\hat{T}_2$, and hence the approximation

$$\hat{T} \approx \hat{T}_2 \tag{B.10}$$

is justified. With the approximations made, the ground-state wave function ψ becomes

$$\psi_{CCD} = e^{\hat{T}_2}\Phi_0 \tag{B.11}$$

Coupled-cluster methods provide very accurate treatment of electron correlations, but they are also quite computationally expensive, and hence are applied predominantly to small and medium-sized molecules. As it was shown for 2-*para*-fluoropheylethanol in Chapter 6.

B.3   Density-Functional Theory

Density-functional theory (DFT) emerged in 1964 with the Hohenberg-Kohn theorem [166]. The theorem states that the ground-state energy, E_0, the wave function, and all molecular properties are uniquely determined by the the electron probability density. Mathematically, this means that the ground-state energy is a functional of the *electron density distribution*, ρ_0. The latter depends on the three spatial coordiantes x, y, and z.

$$E_0 = E_0[\rho_0(x, y, z)] \tag{B.12}$$

This relation between the molecular properties in the ground state and the electron probability density lays the ground for the development of the DFT. The approach of the DFT is to derive ground-state molecular properties from the electron probability density.

In the DFT the potential nuclei create on electrons is considered as an external potential since it

comes from outside the electron system. It is clear that the ground-state energy depends on the types of the nuclei and on their configuration, hence the electronic ground-state energy can be presented in the following manner

$$E_0 = E_v[\rho_0] = \int \rho_0(\mathbf{r})v(\mathbf{r})\, d\mathbf{r} + \overline{T}[\rho_0] + \overline{V}_{ee}[\rho_0] = \int \rho_0(\mathbf{r})v(\mathbf{r})\, d\mathbf{r} + F[\rho_0] \qquad (B.13)$$

The index v shows that the energy depends on the nuclear potential, and F is a functional that depends on the average kinetic energy of the electrons and on the interelectronic interactions, but it does not depend on the external potential. This result as a stand-alone does not have any practical application since the functional $F[\rho]$ and the probability distribution are unknown. To harness Eq. B.13 for practical needs, Hohenberg and Kohn have proven the following theorem. Let be given a trial electron probability density, $\rho_{tr}(\mathbf{r})$, that obeys the relations $\int \rho_{tr}(\mathbf{r})\, d\mathbf{r} = n$ (n is the total number of electrons in the molecular system), and $\rho_{tr}(\mathbf{r}) \geq 0$. For every trial probability density ρ_{tr}, the following inequality holds

$$E_0 = E[\rho_0(\mathbf{r})] \leq \mathbf{E_v}[\rho_{tr}(\mathbf{r})], \qquad (B.14)$$

where ρ_0 is the true molecular electron probability density. The inequality can be also re enunciated that the true molecular electron probability distribution minimizes the energy functional $E_v[\rho_{tr}(\mathbf{r})]$. This theorem is a step ahead towards the practical implementation of the DFT since it claims that in principle all ground state molecular properties descend from the electron density distribution but, it still does not provide a recipe on *how* to do that. The practical aspect of the problem was resolved by Kohn and Sham [167]. Many functionals have been proposed for F, and they have proved themselves to be efficient in describing a great variety of molecular systems. The most typical and widely used functional is the B3LYP one [168].

The recently developed DFT functional M05 can be called a hybrid metageneralized gradient approximation , because it incorporates electron spin density, density gradient, kinetic energy density, and Hartree-Fock (HF) exchange. [106, 169, 170] The M05 functional performs well for kinetics, main-group thermochemistry, and noncovalent interactions, including those in nonpolar weakly interacting systems and charge-transfer complexes and also for transition-metal bond energies, ionization potentials (IPs), and electron affinities (EAs). This functional incorporates kinetic energy density in a balanced way in the exchange and correlation functionals; it satisfy the uniform electron gas limit, and it is a selfcorrelation-free. This makes it a preferred choice for theoretical optimizations of conformeric structures stabilized by nonconventional weak interactions. In the present work, we have used the functional for the optimization of the conformers of 2-*para*-fluorophenylethanol (see Chapter 5).

B.4   Molecular Mechanics

The *molecular mechanics* (MM) method is not a quantum mechanical method. It treats molecules as a system of atoms held together by elastic bonds characterized by force constants, and obeying the equations of classical mechanics. On the basis of the force constants, the molecular energy and the vibrational frequencies are calculated. This method is computationally cheap, and hence sometimes provides a good starting point to quantum-mechanical calculations.

B.5   Molecular Geometry

B.5.1   Equilibrium Geometry

Finding of the *equilibrium geometry* of a molecule is one of the major goals of the theoretical calculations. The equilibrium geometry of a molecule represents the arrangement of the atomic nuclei that minimizes the molecular energy, E, including also the internuclear repulsions. The task of finding the equilibrium geometry becomes more challenging with the increase of the molecular size. The problem is aggravated by the fact that polyatomic molecules have very many degrees of freedom, and often several different atomic arrangements may result in a similar molecular energy, which poses very stringent requirements on the accuracy of the energy calculations.

B.5.2   Potential Energy Surface

The geometrical structure of a molecule is uniquely determined by defining $3N$-6 independent coordinates, where N stands for the number of atoms in the molecule. As mentioned in the preceding section, the energy of a molecule depends on the atomic configuration. That is why, it is convenient to present the molecular energy, E, as a function of the $3N$-6 independent coordinates. This will result to a hypersurface (*potential energy surface* (PES)) in the $3N$-6-dimensional space. It can be formally written as $E = -E(\mathbf{r})$. The minima on this surface correspond to *stable-equilibrium* structures of the molecule. The lowest-energy minimum is referred to as the *global minimum* . All other minima are called *local minima*. The potential-surface maxima correspond to *unstable-equilibrium* structures that relax to the nearest minimum. There are also points on the PES corresponding to minima for $3N$-7 coordinates, and to a maximum for one coordinate. Such points are referred to as *saddle points*. The calculation of the energy at a fixed conformation is called a *single point* energy calculation .

The set of the *dihedral angles* about all bonds in a molecule defines its *conformation*. The conformation corresponding to an energy minimum (local or global) is termed a *conformer* . The larger the molecule, the bigger the number of conformers it has. That is why, the prediction of molecular conformers is one of the major goals of the theoretical calculations.

B.5.3   Geometry Optimizations

A *geometry optimization* or *energy minimization* is the procedure of finding the molecular conformation corresponding to an energy minimum in vicinity of some initially defined molecular geometry (conformation). From the view point of mathematics, this is the problem of the multidimensional optimization. There exist various algorithms to handle the problem. The most efficient ones are the *gradient method* , the *Newton-Raphson method*, the *steepest-descend method*, etc. To find different molecular conformers, one has to probe different starting geometries, and locally search for the energy minimum. The problem is aggravated in molecules with many internal degrees of freedom, which may have many different conformers. The finding of the global energy minimum is not a trivial task, and in general, this problem has not been solved yet. The guess of the starting conformation in the vicinity of which the global energy minimum is expected might be misleading since often it may happen that the most stable conformer (this is the conformer corresponding to the global energy minimum) is rather unconventional. This necessitates the development of algorithms for global optimization.

B.5.4   Conformational Search

Many algorithms have been invented to treat the problem of the global optimization though, none of them can provide a complete reliability. For this reason, sometimes, a combination of different algorithms is used to solve a particular problem. The general name of these algorithms is *global optimizers*. In the following, they are listed without presenting the details on how they work. A comprehensive survey of these techniques can be found in [163].

- **Systematic (grid) search method..** This is one of the commonly used techniques for global-energy-minimum search. This method samples the PES with a certain step and at each sample point it calculates the single point energy. For practical reasons usually only a few molecular coordinates are scanned (most typically dihedral angles), while the other coordinates are kept fixed at their initial values. Then a local search is applied to the lowest-energy sample point. In this way the global energy-minimum can be found.This method was used in the conformational investigation of the systems in the present work.

- **Random (Stochastic or Monte Carlo) search method.**

- **Distance-geometry method.** In this method the molecule is described as a distance matrix whose elements, d_{ij}, are the distances between atoms i and j.

- **Genetic algorithm.** This method is described in detail in Sec. 2.3 in conjunction with the analysis of highly resolved molecular spectra to find the global maximum for the cross correlation.

- **Molecular dynamics search.**

- **Metropolis (Monte Carlo) method.**

- **The diffusion-equation method.**

- **The low-mode conformational search.**

B.6   BSSE

Suppose we wish to calculate the energy of formation of a bimolecular complex, such as the energy of formation of a hydrogen-bonded water dimer. Such complexes are sometimes referred to as 'supermolecules'. One might expect that this energy value could be obtained by first calculating the energy of a single water molecule, then calculating the energy of the dimer, and finally subtracting the energy of the two isolated water molecules (the 'reactants') from that of the dimer (the 'products'). However, the energy difference obtained by such approach will invariably be an overestimate of the true value. The discrepancy arises from a phenomenon known as *basis set superpositon error* (BSSE). As the two water molecules approach each other, the energy of the system falls not only because of the favorable intermolecular interactions but also because the basis functions on each molecule provide a better description of the electronic structure around the other molecule. One way to estimate the basis set superposition error is via the counterpoise correction method of Boys and Bernardi [171], in which the entire basis set is included in all calculations. Thus, in the general case:

$$A + B \rightarrow AB \tag{B.15}$$

$$\Delta E = E(AB) - [E(A) + E(B)] \tag{B.16}$$

The calculation of the energy of the individual species A is performed in the presence of 'ghost' orbitals of B; that is, without the nuclei or electrons of B. A similar calculation is performed for B using ghost orbitals on A.The calculation can be presented and in a more detail way. Let us

consider a supermolecule AB made up of two interacting subsystems A and B. The stabilization energy can be written as:

$$\Delta E = E_{AB}^{AB}(AB) - [E_A^A(A) + E_B^B(B)] \tag{B.17}$$

Where $E_Y^Z(X)$ is the energy of a subsystem X at geometry Y with basis set Z. The stabilization energy can be spilt in the following way

$$\Delta E(AB) = \Delta E_{int}(AB) + \Delta E_{rel}(A, B) \tag{B.18}$$

The first term represents the interaction energy contribution, which depends only on the super-molecule geometrical parameters, AB

$$\Delta E_{int}(AB) = E_{AB}^{AB}(AB) - [E_{AB}^A(A) + E_{AB}^B(B)] \tag{B.19}$$

whereas the second term represents the relaxation contribution, which compensates for the geometry distortion of the subsystems in the supermolecule, $E_{AB}^A(A)$ and $E_{AB}^B(B)$, with regard to the isolated optimum geometry, $E_A^A(A)$ and $E_B^B(B)$.

$$\Delta E_{rel}(A, B) = E_{AB}^A(A) - E_A^A(A) + E_{AB}^B(B) - E_B^B(B) \tag{B.20}$$

Note that $E_{rel}(A,B)$ depends on both the supermolecule and subsystem parameters AB,A,B. According to the counterpoise idea, since the same basis set is used in the relaxation term for each subsystem, only the interaction energy contribution term brings about BSSE. Thus, the counterpoise-corrected interaction energy should be presented as:

$$\Delta E^{CP}(AB) = [E_{AB}^{AB}(AB) - E_{AB}^{AB}(A) - E_{AB}^{AB}(B)] + [E_{AB}^A(A) + E_{AB}^B(B) - E_A^A(A) - E_B^B(B)] \tag{B.21}$$

Rearranging terms of the expression above one obtains

$$\Delta E^{CP}(AB) = [E_{AB}^{AB}(AB) - E_A^A(A) - E_B^B(B)] + [E_{AB}^A(A) + E_{AB}^B(B) - E_{AB}^{AB}(A) - E_{AB}^{AB}(B)] = \Delta E(AB) + \delta_{AB}^{BSSE} \tag{B.22}$$

where the CP-correction expressed as δ_{AB}^{BSSE} presents one important property that the BSSE is not an additive term to the stabilization energy. Actually can be strongly geometry-dependent so that it should be taken into account at every point of the potential energy surface when looking for stationary points. The relevance of the basis set superposition error and its dependence upon

the basis set and the level of theory employed remains a subject of much interest (for reference see PhD thesis of SEDANO [172]).

B.7 Molecular Vibrational Frequencies

The conformational search and the geometry optimization of a molecule provide the electronic energy of this molecule. Since, however, atomic nuclei are never at rest but perform small oscillations about their equilibrium positions, it is of importance to calculate also the molecular vibronic frequencies.

The energy of a harmonic oscillator E_{vib} is

$$E_{vib} = \left(v + \frac{1}{2}\right)h\nu \tag{B.23}$$

where v stands for the vibrational quantum number that can take on values from 0 to infinity, and ν is the vibrational frequency. The vibrational energy corresponding to v=0 is known as the *zeroth vibrational energy* . For a 3N-atomic molecule there are 3N-6 vibrational modes if the molecule is not planar, and 3N-5 modes if the molecule is linear. Each of the modes has a frequency ν_n, which is called a *fundamental frequency* . In the harmonic approximation, the total vibrational energy of a molecule is the sum of the vibrational energies of all vibrational modes presented as individual harmonic oscillators

$$E_{vib} = \sum_{n=1}^{M}\left(v_n + \frac{1}{2}\right)h\nu_n, \tag{B.24}$$

where $M = 3N - 6$ in the general case, and $M = 3N - 5$ for linear molecules. The sum of all the zeroth vibrational energies yields the the so-called *zero-point vibrational energy* (ZPVE). This is the lowest energy level a molecule can occupy for a certain conformer. In practice, the fundamental vibrational frequencies of a 3N-atomic molecule are determined through the *mass-weighted force-constant matrix elements* . Force constants are also called *Hessians*,

$$F_{ij} = \frac{1}{\sqrt{m_i m_j}}\left(\frac{\partial^2 U}{\partial x_i \partial x_j}\right) \tag{B.25}$$

The real treatment of molecules requires also the inclusion of anharmonic corrections. The methodology is desribed in very detail by Wilson, Decius, and Cross [173].

B.8 Programme Packages for Theoretical Molecular Investigations

Various commercial programs for modeling of molecular structures and properties, and theoretical investigation of molecular phenomena are available nowadays. One of the most conventional program packages is GAUSSIAN [82]. It has been used also to provide the theoretical results in this work. Other, also powerful, programs are MOLPRO [174], TURBOMOL [175], GAMESS (General Atomic and Molecular Electronic Structure System), Q-CHEM, which is optimized for calculation of large molecules containing several hundred atoms, JAGUAR, ACES II, CADPAC, SPARTAN.

Appendix C

Interaction between Light and Matter

Spectroscopy deals with *transitions* between states in atoms and molecules activate by an external electromagnetic field (light, in the case of laser spectroscopy). The studied quantum systems (atoms or molecules) start from some stationary state, and as a result of the interaction with the light, they end up in some other stationary state. Quantum transitions are described by the time-dependent *Schrödinger equation*

$$i\hbar\frac{\partial\psi(q,t)}{\partial t} = [\hat{H}]\psi(q,t),\tag{C.1}$$

where q designates the $3N$ spatial and the N spin coordiantes of a system consisting of N particles, and t is time. The Hamiltonian of the joint system molecule-electromagnetic wave can be presented as the sum of the isolated-molecule Hamiltonian $H^{(0)}$ and the Hamiltonian describing the interaction between the molecule and the external field H_{int} (the lower-case index 'int' stands for 'interaction'), i. e.

$$\hat{H} = \hat{H}^{(0)} + \hat{H}_{\text{int}}(t)\tag{C.2}$$

As seen from Eq. C.2, the interaction Hamiltonian depends on time. It can be shown [176, 177] that the time-dependent wave function $\psi(q,t)$ can be expanded in terms of the time-independent (stationary-state) wave function corresponding to Hamiltonian $\hat{H}^{(0)}$,

$$\psi(q,t) = \sum_i a_i(t)\psi_i(q)\tag{C.3}$$

After some standard mathematical trasformations, and bearing in mind that the stationary-state

wave functions $\psi_i(q)$ are orthonormal, constitute a complete basis, and Eq. C.2 can be transformed into its equivalent form,

$$\frac{dc_m}{dt} = -\frac{i}{\hbar} \sum_n c_k e^{i\omega_{mn}t} \langle \psi_m^{(0)} \mid \hat{H}_{\text{int}} \mid \psi_n^{(0)} \rangle, m = 1, 2, 3, \dots \tag{C.4}$$

where

$$\omega_{mn} \equiv \frac{E_m^{(0)} - E_n^{(0)}}{\hbar} \tag{C.5}$$

Eq. C.4 is solved on the basis of perturbation theory. The interaction Hamiltonian is treated as a perturbation to the molecular Hamiltonian. If the perturbation is applied to the molecule at the time $t = 0$ in stationary state n then at $t = 0$, $\psi(q, 0) = \psi_n(0)$, and from Eq. C.3, it can be inferred that $c_n(0) = 1$, and $c_i(0) = 0$, for $i \neq n$. Assuming also that the perturbation is small and acts for short time from $t = 0$ to $t = t_1$, it is reasonable to infer that $\frac{dc_m}{dt}$ is also small, and hence the coefficient c_m is obtained as

$$c_m(t_1) = -\frac{i}{\hbar} \int_0^{t_1} e^{i\omega_{mn}t} \langle \psi_m^{(0)} \mid \hat{H}_{\text{int}} \mid \psi_n^{(0)} \rangle \, dt \tag{C.6}$$

where $c_m(0) = \delta_{mn}$. The probability for the system to commute from the initial quantum state n into a new state m is given by $\mid c_m(t) \mid^2$. This formula is the onset for the derivation of the famous Fermi's golden rule [178], which calculates the transition rate (probability of transition per unit time) from a certain energy eigenstate of a quantum system into a continuum of eigenstates, caused under the action of perturbation. This rule applies when there is no depletion of the initial-state population. Fermi's golden rule has the form

$$T_{n \to f} = \frac{2\pi}{\hbar} \delta(E_f - E_n) \mid \langle f \mid \hat{H}_{\text{pert}} \mid n \rangle \mid^2 \rho \tag{C.7}$$

In the formula above n is the initial state, f designates the continuum of states, and ρ shows the density of the final states.

Formula C.6 is irrelevant of the nature of the perturbation applied. The interaction of light with quantum systems is rationalized in the frame of the *semiclassical theory*, wherein light is treated as an electromagnetic wave. In most cases, the interaction between light and atoms/molecules can be viewed upon as an interaction between an electromagnetic wave and the dipole it induces in molecules. This is the so-called electric dipole approximation . The interaction $\hat{H}_{int}$ has the form

$$\hat{H}_{int} = -\boldsymbol{\mu} \cdot \mathbf{E}(t) \tag{C.8}$$

$\mathbf{E}(t)$ represents the electric-field vector as a function of time. It is convenient to represent a time-varying electric field as a superposition of plane-polarized waves with different frequencies, ω_i, time-dependent amplitudes, $f_i(t)$, and planes of polarization $\mathbf{e}$. The expansion in terms of plane waves is described by the next formula

$$\mathbf{E}(t) = \sum_{i=1}^{\infty} \mathbf{e}_i f_i(t) e^{-i\omega_i t} \tag{C.9}$$

On the basis of formulae C.6 and C.7, the following important for spectroscopy conclusions can be drawn.

- An optical one-photon transition is possible only when the energy of the photon equals the energy difference between the two levels, n and m. This is the so-called *resonance condition*.

- If the resonence condition is met, the intensity of the transition depends on the matrix element $| \langle \psi_m^{(0)} | \hat{H}_{\text{int}} | \psi_n^{(0)} \rangle |^2$. There are two cases when a transition may be resonance-allowed but the intensity of the transition may be zero, or very small. *i)*When the interaction Hamiltonian H_{int} is very small due to the small induced dipole moment $\boldsymbol{\mu}$ the above matrix element is also small. *ii)* Because of molecular-symmetry considerations, the matrix element may vanish even in cases when the induced dipole moment is not zero. This lays the ground for the establishment of *selection rules*, i. e., there are *allowed* and *forbidden* transitions [176]. The particular selection rules that apply to rotationally resolved spectroscopy are discussed in Appendix D.

Appendix D

Molecular Quantum Mechanical Characteristics and Molecular Structure

Molecules are complex quantum-mechanical objects. For the understanding of their structures and properties, the entangled interactions between their constituents have to be explained. The Hamiltonian of a molecule with m nuclei and n electrons is

$$\hat{H} = \hat{H}_{\mathrm{N}} + \hat{H}_{\mathrm{E}} + \hat{H}_{\mathrm{NN}} + \hat{H}_{\mathrm{EE}} + \hat{H}_{\mathrm{NE}} \tag{D.1}$$

In this formula $\hat{H}_{\mathrm{N}}$ is the kinetic energy of the nuclei, $\hat{H}_{\mathrm{E}}$ is the kinetic energy of the electrons, $\hat{H}_{\mathrm{NN}}$ is the interaction energy of the nuclei, $\hat{H}_{\mathrm{EE}}$ stands for the inetarction between the electrons, and the last term describes the interaction between the nuclei and the electrons.

The substitution of the above Hamiltonian into the Schrödinger equation (see Appendix C), and the solution of the latter, in principle, yields all the information on the energy levels and wave functions of this molecule. Due to the complicated form of the Hamiltonian, however, the so-produced Schrödinger equation does not render itself to a direct solution. That is why, some reasonable assumptions have to be made in order to make the solution tractable.

D.1 Born-Oppenheimer Approximation

The most straightforward and widely-used approximation, when treating molecules quantum-mechanically, is the *Born-Oppenheimer approximation* [179]. Electrons are 1837 times lighter than protons/neutrons. This means that for a small to medium-sized molecule containing several tens of atoms, the ratio between the mass of the electrons and that of the nuclei is in the range $10^{-3} - 10^{-5}$. Due to the higher, mass nucleons are intrinsically more inert than electrons, and

hence their response to forces is slower. This implies that at every instant of time the electrons in a molecule experience a static potential created by the nuclei. Thus, the electronic wavefunction reacts adiabatically to any change in the nuclear configuration, i. e., the nuclear configuration is "encoded" in the electronic wave function. Actually, the equilibrium configuration of the atomic nuclei in a molecule is the one that yields minimum of the sum of the energies resulting from the interaction between the nuclei, E_{NN}, between the electrons, E_{EE}, and between the nuclei and the electrons, E_{NE}. The binding of atoms to form a molecule brings forth the electronic energy of a molecule, E_{el}. The atomic nuclei in a molecule oscillate about their equilibrium positions, so these oscillations have vibrational energy, E_{vib}. Molecules also rotate with rotational energy, E_{rot}. When considering molecular properties, the overall translation of the molecule is irrelevant, and hence translation energy is omitted.

Thus, the Born-Oppenheimer approximation states that the electronic motions, the vibrations, and the rotations of a molecule can be treated separately, and the total energy of a molecule (excluding its translational component) is the sum of its electronic (the potential that keeps the atoms bound together), vibrational, and rotational energies:

$$E = E_{el} + E_{vib} + E_{rot} \qquad \text{(D.2)}$$

There is a relation between the magnitudes of the electronic, vibrational, and rotational energies:

$$E_{rot} \approx \sqrt{\frac{m}{M}} E_{vib} \approx \frac{m}{M} E_{el} \qquad \text{(D.3)}$$

The energies differ by two-three orders of magnitude from each other and that the electronic energy constitutes the largest contribution to the total energy.

It is important to point out that the Born-Oppenheimer approximation is not always valid. There are cases which cannot be described correctly within this approximation. Such cases are referred to as the Born-Oppenheimer approximation break-down. Typical examples of the Born-Oppenheimer approximation break-down are the vibration-rotation interaction through the Coriolis coupling [180], or the interaction between the electronic wave functions and the vibrations, which is known as the Herzberg-Teller effect [181].

D.2   Rotation of Molecules

The analysis and interpretation of rotationally resolved molecular spectra necessitates cognizance of the theory of the molecular rotation. This theory relates the structure of molecules with their rotational spectra.

D.2.1   Molecular Rotational Energy

If one assumes that the interatomic distances in a molecule are fixed to some *vibrationally averaged* values, then the molecule can be treated as a rigid body and hence the energy levels corresponding to its overall rotations can be calculated. The assumption of rigidity is well justified in many cases. When, however, this assumption fails due to molecular distortions, the latter are accounted for by an explicit inclusion of *distortion coefficients*.

Every rigid molecule is characterized by its *tensor of inertia* $\hat{I}$ [182, 183]

$$\hat{I} = \begin{pmatrix} I_{xx} & I_{xy} & I_{xz} \\ I_{yx} & I_{yy} & I_{yz} \\ I_{zx} & I_{zy} & I_{zz} \end{pmatrix} \tag{D.4}$$

The matrix elements are defined in the following way

$$I_{xx} \equiv \sum_i m_i(y_i^2 + z_i^2) \qquad \text{etc.,} \qquad I_{xy} \equiv \sum_i m_i x_i y_i \qquad \text{etc.} \tag{D.5}$$

where x_i, y_i, and z_i are the coordinates of atom i with respect to an arbitrary coordinate system, and m_i is the atomic mass. When this tensor is diagonalized (all off-diagonal elements I_{xy} become zeros), it yields the three principal moments of inertia , designated as I_a, I_b, and I_c, about the three principal axes of inertia, a, b, and c, respectively. The principal axes of inertia are labeled so that to produce the inequality

$$I_a \leq I_b \leq I_c \tag{D.6}$$

With respect to their principal moments of inertia molecules can be divided into four groups.

- **Spherical top.** $I_a = I_b = I_c$, for instance CH_4

- **Prolate symmetric top.** $I_a < I_b = I_c$, for instance CH_3Br. Linear molecules constitute a particular case of prolate symmetric tops, when $I_a = 0$ and $I_b = I_c$. All diatomic molecules belong to this class of molecules.

- **Oblate symmetric top.** $I_a = I_b > I_c$

- **Asymmetric top.** $I_a \neq I_b \neq I_c$, most of larger molecules

The rotational kinetic energy Hamiltonian of a rigid molecule can be expressed through its tensor of inertia and angular velocity

$$\hat{H}_{\text{rot}} = \frac{1}{2} I_{ij} \omega_i \omega_j \tag{D.7}$$

In the principal coordinate system, the rotations about the three principal axes of inertia are decoupled and the total rotational kinetic energy becomes the sum of the rotational kinetic energies about the three axes

$$\hat{H}_{\text{rot}} = \frac{1}{2}(I_a \omega_a^2 + I_b \omega_b^2 + I_c \omega_c^2) = AP_a^2 + BP_b^2 + CP_c^2 \tag{D.8}$$

The coefficients A, B, and C are called *rotational constants*, and obey the inequality $A \geq B \geq C$. They are inversely proportional to the moments of inertia, and are defined by the expressions

$$A = \frac{\hbar^2}{2I_a} \qquad B = \frac{\hbar^2}{2I_b} \qquad C = \frac{\hbar^2}{2I_c} \tag{D.9}$$

As will be shown in the subsequent chapters, rotational constants play an important role in the analysis of rotationally resolved spectra, and the assignement of molecular structures on the basis of spectroscopic data. The quantities P_α, $\alpha = a, b, c$, are the angular momenta of the molecule relative to its principal axes of inertia.

D.2.2   Molecular Rotational Energy Levels

To obtain the energy levels of a rigid molecule, it is convenient to represent the quantum-mechanical Hamiltonian through the angular momenta of the molecule as shown in the last equality of Eq. D.8. Several important properties and relations of the rigid-molecule angular momenta are highlighted in the following. The detailed derivation of these properties and relations can be found, for instance, in [176, 184, 185]. Let XYZ be a space-fixed coordinate system with its origin in the center of mass of the molecule, and abc be the coordinate system of the principal axes of inertia of the molecule. Then the following relations between the projections of the squared angular momentum, $\hat{P}^2$, onto the axes X, Y, and Z, and a, b, and c, and the rotational Hamiltonian H_{rot} hold

$$\hat{P}^2 = \hat{P}_a^2 + \hat{P}_b^2 + \hat{P}_c^2 = \hat{P}_X^2 + \hat{P}_Y^2 + \hat{P}_Z^2 \tag{D.10}$$

$$[\hat{P}_X, \hat{P}_Y] = i\hbar\hat{P}_Z \qquad \text{etc.} \tag{D.11}$$

$$[\hat{P}_a, \hat{P}_b] = -i\hbar\hat{P}_c \qquad \text{etc.} \tag{D.12}$$

$$[\hat{P}^2, \hat{P}_c] = 0 \qquad \text{etc.} \tag{D.13}$$

$$[\hat{P}^2, \hat{P}_Z] = 0 \qquad \text{etc.} \tag{D.14}$$

$$[\hat{P}_Z, \hat{P}_c] = 0 \qquad \text{etc.} \tag{D.15}$$

$$[\hat{H}_{\text{rot}}, \hat{P}^2] = 0 \qquad \text{etc.} \tag{D.16}$$

$$[\hat{H}_{\text{rot}}, \hat{P}_Z] = 0 \qquad \text{etc.} \tag{D.17}$$

It can be shown that for every rotor, there exist some fundamental relations

$$\hat{P}^2\psi = J(J+1)\hbar^2\psi, \qquad J = 0, 1, 2, \dots \tag{D.18}$$

$$\hat{P}_Z\psi = K\hbar\psi, \qquad K = 0, \pm 1, \dots, \pm J \tag{D.19}$$

where $\sqrt{J(J+1)}\hbar$ is the magnitude of the total rotational angular momentum and $K\hbar$ is its component along a space-fixed axis.

The energy levels for the different types of rotors, spherical top, symmetric top, and asymmetric top, are listed below.

Spherical-Top Energy Levels

$$E = AJ(J+1) \tag{D.20}$$

where $A = B = C$ is the rotational constant of the molecule.

Symmetric-Top Energy Levels

$$E(J, K) = BJ(J+1) + (C-B)K^2 \qquad \text{oblate top} \tag{D.21}$$

$$J = 0, 1, 2, \dots \qquad K = 0, \pm 1, \pm 2, \dots, \pm J$$

$$E(J, K) = BJ(J+1) + (A-B)K^2 \qquad \text{prolate top} \tag{D.22}$$

$$J = 0, 1, 2, \dots \qquad K = 0, \pm 1, \pm 2, \dots, \pm J$$

$$E = BJ(J+1) \qquad \text{linear} \tag{D.23}$$

As seen from the above formulae, the rotational energy of symmetric tops depends not only on J but also on a second quantum number, K, which determines the projections of the total angular momentum along a molecule-fixed axis of the symmetric top.

Asymmetric-Top Energy Levels

The formulae for the energy levels of asymmetric-top molecules are quite complicated, and the energy levels can be obtained analytically only for small values of J. For large values of J, the energy levels are calculated numerically. An important parameter in the analysis of asymmetric rotors is the *Ray's asymmetry parameter* , defined as

$$\kappa = \frac{2B - A - C}{A - C} \tag{D.24}$$

This parameter shows the deviation of the particular asymmetric top from either the prolate or the oblate symmetric top. The energy levels of an asymmetric top are, usually, designated as $J_{K_{\mathrm{pr}}K_{\mathrm{ob}}}$, where K_{pr} and K_{ob} designate the the values of K for the prolate and oblate symmetric tops, respectively, that correlate with the asymmetry-top level under consideration. It is important to emphasize, however, that K_{pr} and K_{ob} are not true quantum numbers for the asymmetric top. An alternative notation for the asymmetric energy levels is J_τ, where $\tau = K_{\mathrm{pr}} - K_{\mathrm{ob}}$.

The following table (taken from Ref. [183]) shows the analytical solutions for the first few energy levels of an asymmetric top.

$J_{K_{\mathrm{pr}}K_{\mathrm{ob}}}$	$\tau = K_{\mathrm{pr}} - K_{\mathrm{ob}}$	$E(J, K_{\mathrm{pr}}, K_{\mathrm{ob}})$
0_{00}	0	0
1_{10}	1	$A + B$
1_{11}	0	$A + C$
1_{01}	-1	$B + C$
2_{20}	2	$2A + 2B + 2C + 2\sqrt{(B - C)^2 + (A - C)(A - B)}$
2_{21}	1	$4A + B + C$
2_{11}	0	$A + 4B + C$
2_{12}	-1	$A + B + 4C$
2_{02}	-2	$2A + 2B + 2C - 2\sqrt{(B - C)^2 + (A - C)(A - B)}$

Table D.1: *Rigid asymmetric-top energy levels*

D.2.3 Electric Dipole Transition Moment

It is proved [176] in the electric dipole approximation (see Chap. C) that the transition probability of a molecule from state n to state m under the action of plane-polarized (in the x direction) monochromatic light with electromagnetic energy density u_x at frequency ν_{mn} for a time t is

$$| c_{mn}(T) |^2 = 2\pi\hbar^{-2}T \, | \langle m \, | \, \hat{\mu}_x \, | \, n \rangle |^2 \, u_x(\nu_{mn}) \tag{D.25}$$

In the above equation μ_x is the x component of the molecular dipole moment. The matrix element $| \langle m \, | \, \hat{\mu}_x \, | \, n \rangle |$ can be written in the more general form

$$| \langle m \, | \, \hat{\mu} \, | \, n \rangle |^2 = | \langle m \, | \, \hat{\mu}_x \, | \, n \rangle |^2 + | \langle m \, | \, \hat{\mu}_y \, | \, n \rangle |^2 + | \langle m \, | \, \hat{\mu}_z \, | \, n \rangle |^2 \tag{D.26}$$

where $\hat{\mu} = \mathbf{i}\hat{\mu}_x + \mathbf{j}\hat{\mu}_y + \mathbf{k}\hat{\mu}_z$. $| \hat{\mu} \rangle$ is called *transition dipole moment* or *transition moment*. The transition moment is a vector quantity, and it is usually defined with respect to the principal axes of inertia of the molecule. Depending on whether the transition dipole moment is oriented along the a, b, or c principal axis of inertia, one distinguishes between three types of transitions, $a-$, $b-$, and $c-$type.

D.2.4 Selection Rules

Not all transitions between the energy levels of an asymmetric top are possible. One-photon transitions are allowed only for transitions for which $\Delta J = 0, \pm 1$. In a set of transitions those for which $\Delta J = -1$ form the P branch, those for which $\Delta J = 0$ give rise to the Q branch, and $\Delta J = +1$ form the R branch. For two-photon transitions, the selection rules are different from those for one-photon transitions. In this case $\Delta J = -2, +2$, corresponding to O and S branches [186].

D.2.5 Transition Intensity

Rotational transition intensities are determined by statistical weights depending on the degeneracy in the quantum number K, nuclear spin, the polarization of the light inducing the transition, and on the thermal distribution of the species given by the Boltzmann formula

$$exp\left(-\frac{\Delta E_{mn}}{kT_{\text{rot}}}\right) \tag{D.27}$$

where ΔE_{mn} is the energy difference between levels m and n, k is the Boltzmann constant , and T is the rotational temperature .

D.2.6   Deviations from the Born-Oppenheimer Approximation

The discussion hitherto was on rigid molecules obeying the Born-Oppenheimer approximation (see Sec. D.1). Sometimes, however, these approximations break down, and one has to eleborate different models to treat the molecular behavior properly. The most typical deviations from the above approximations are listed here.

- **Centrifugal distortion.** When considering high values of J, molecular bonds stretch and hence molecules can be no longer treated as rigid objects. In this case, their rotational energy levels are calculated by including in the respective rigid-molecule-approximation formulae a correction for the centrifugal distortion expressed by centrifugal distortion constants [176, 184]

- **Coriolis coupling.** The Coriolis coupling in molecules results from the coupling between the molecular vibrations and the overall rotation of the molecule. The Coriolis-coupling correction in the Born-Oppenheimer approximation is introduced through the theory of perturbations.

- **Herzberg-Teller effect.** The Herzberg-Teller effect [181] is the gain of intensity by an electronically forbidden but vibronically allowed transition from another both electronically and vibronically allowed transition through vibrational coupling.

- **Jahn-Teller effect.** If at a certain symmetrical nonlinear nuclear configuration of a polyatomic molecule, two electronic states are degenerate, the latter can be lifted by some nuclear distortion. The splitting of the electronic degeneracy by a nuclear distrosion accompanied by the interaction between the rotation-vibration levels of the two electronic states is referred to as the Jann-Teller effect [187].

D.3   Rotational Constants and Structure of Molecular Species

From the rotationally resolved spectroscopy one can derive the values of molecular rotational constants, which are related to the principal moments of inertia of the studied species. Unfortunately, rotational constants do not provide unique information on the molecular structure since it may happen that different structures may have very similar rotational constants. That is why, it is necessary to find a method to assign structures on the basis of the experimentally observed rotational constants.

Molecular structures are determined by defining the interatomic distances, planar, and dihedral angles . Regarding bond lengths, the following bond-length definitions have to be distinguished [183].

- r_e is the bond legth that corresponds to a hypothetic vibrationless state of the molecule.

- r_0 is the effective bond length corresponding to a ground-state vibration. It is these distances that are involved in the measured rotational constants.

- r_s is the bond length corresponding to an isotopic substitution. The so-defined bond length is discussed in conjuction with the Kraitchman equations [188]

- $\langle r \rangle$ is an averaged bond length corresponding to some atom positions resulting from partial correction to the vibrational effects.

- r_m is the mass-weighted bond length derived from the averaging of the bond lengths of a large number of isotopically substituted species.

Kraitchman equations [183, 188, 189] are a convenient analytical tool for determining the coordinates of an isotopically substituted atom in a rigid molecule with respect to the center-of-mass (COM) principal axis system of the parent molecule (the molecule before the isotopic substitution). Kraitchman equations allow the coordinates of the substituted atom to be found on the basis of the measured rotational constants for the particular molecular species before and after the isotopic substitution. This approach has been successfully applied to the analysis of many noble-gas clusters of benzene and benzene derivatives [79, 190, 191]. The coordinates of an isotopically substituted atom with respect to the principal-axis system of the parent molecule are calculated by the formulae

$$
\begin{aligned}
\mid x \mid &= \sqrt{\frac{\Delta P_x}{\mu}\left(1 + \frac{\Delta P_y}{P_y - P_x}\right)\left(1 + \frac{\Delta P_z}{P_z - P_x}\right)} \\
\mid y \mid &= \sqrt{\frac{\Delta P_y}{\mu}\left(1 + \frac{\Delta P_z}{P_z - P_y}\right)\left(1 + \frac{\Delta P_x}{P_x - P_y}\right)} \\
\mid z \mid &= \sqrt{\frac{\Delta P_z}{\mu}\left(1 + \frac{\Delta P_x}{P_x - P_z}\right)\left(1 + \frac{\Delta P_y}{P_y - P_z}\right)}
\end{aligned}
\tag{D.28}
$$

where μ is the reduced mass of the molecular species

$$
\mu = \frac{M \Delta m}{M + \Delta m}
\tag{D.29}
$$

M is the mass of the molecule before the isotopic substitution, and Δm is difference of the masses before the substitution.

P_x, P_y, and P_z in Eq. D.3 are defined as

$$
\begin{aligned}
P_x &= \frac{1}{2}(-I_x + I_y + I_z) \\
P_y &= \frac{1}{2}(-I_y + I_z + I_x) \\
P_z &= \frac{1}{2}(-I_z + I_x + I_y)
\end{aligned}
\tag{D.30}
$$

I_x, I_y and I_z designate the principal moment of inertia of the unsubstituted molecule. Differences Δ of parameter P in Eq. D.3 are defined as

$$
\begin{aligned}
\Delta P_x &= P'_x - P_x \\
\Delta P_y &= P'_y - P_y \\
\Delta P_z &= P'_z - P_z
\end{aligned}
\tag{D.31}
$$

The primed parameters in the above definitions correspond to the molecular species after the isotopic substitution.

Bibliography

[1] F. A. Carey and R. J. Sundberg, *Advanced Organic Chemistry. Part A: Structure and Mechanisms*, 5 ed. (Springer, US, 2007), p. 169 ff.

[2] A. Schäffler and N. Mencke, *Biologie Anatomie Physiologie, Das Nervengewebe*, 4 ed. (Urban and Fischer, ADDRESS, 2000), Chap. 10, p. 145 ff.

[3] E. G. Robertson and J. P. Simons, Phys. Chem. Chem. Phys. **3**, 1 (2001).

[4] T. S. Zwier, J. Phys. Chem. A **105**, 8827 (2001).

[5] G. Scoles, *Atomic and molecular beam methods* (Oxford University Press, New York, 1988).

[6] R. N. Pribble and T. S. Zwier, Science **265**, 75 (1994).

[7] T. Ebata, A. Fujii, and N. Mikami, Int. Rev. Phys. Chem. **17**, 331 (1998).

[8] R. M. Helm and H. J. Neusser, Chem. Phys. **239**, 33 (1998).

[9] M. Gerhards, B. Kimpfel, M. Pohl, M. Schmitt, and K. Kleinermanns, J. Mol. Struct. **270**, 301 (1992).

[10] H. J. Neusser and K. Siglow, Chem. Rev. **100**, 3921 (2000).

[11] R. M. Helm, M. Clara, T. L. Grebner, and H. J. Neusser, J. Phys. Chem. A **102**, 3268 (1998).

[12] P. F. Barbara, T. J. Meyer, and M. A. Ratner, J. Phys. Chem. **100**, 13148 (1996).

[13] J. R. Carney, F. C. Hagemeister, and T. S. Zwier, J. Chem. Phys. **108**, 3379 (1998).

[14] J. R. Carney and T. S. Zwier, J. Phys. Chem. A **103**, 9943 (1999).

[15] S. Georgiev and H. J. Neusser, Chem. Phys. Lett. **389**, 24 (2004).

[16] M. Mons, E. G. Robertson, L. C. Snoek, and J. P. Simons, Chem. Phys. Lett. **310**, 423 (1999).

[17] J. P. Reilly, Mass Spectrometry Reviews **28**, 425 (2009).

[18] B. Lucas, M. Barat, J. A. Fayeton, M. Perot, C. Jouvet, G. Gregoire, and S. B. Nielsen, The Journal of Chemical Physics **128**, 164302 (2008).

[19] J. A. Stearns, S. Mercier, C. Seaiby, M. Guidi, O. V. Boyarkin, and T. R. Rizzo, Journal of the American Chemical Society **129**, 11814 (2007).

[20] S. Chervenkov, P. Q. Wang, J. E. Braun, and H. J. Neusser, J. Chem. Phys. **121**, 7169 (2004).

[21] D. H. Levy, Ann. Rev. Phys. Chem. **31**, 197 (1980).

[22] N. F. Ramsey, *Molecular Beams*, *International Series of Monographs on Physics* (Oxford University Press, New York, 1985).

[23] I. Holvan, Diplomarbeit, Aufbau einer Molekularstrahlapparatur zur Erzeugung ultra-kalter Molekülcluster für die Sub-Doppler-Laserspektroskopie (1992).

[24] R. M. Helm, Diplomarbeit, Hochauflösende Spektroskopie durch Vier-Wellen-Mischen und resonante Mehr-Photonen-Ionisation (1995).

[25] K. Siglow, Diplomarbeit, Fakultät für Chemie, Biologie und Geowissenschaften der Technischen Universität München (1996).

[26] R. Gerthner, Diplomarbeit, Hochauflösende Sub-Dopper-UV Spektroskopie zur Untersuchung der Schwingungsdynamik in molekularen Clustern (1997).

[27] R. Sussmann, Dissertation, Kohärente Ionendip Spektroskopie und rotationsaufgelöste UV-Laserspektroskopie zur Untersuchung der intermolekularen Wechselwirkung in Aromat-Edelgas Van der Waals-Komplexen (1994).

[28] S. Chervenkov, Dissertation, Investigation of Weak Intra- and Intermolecular Interactions and Conformational Structures of Flexible Molecules and Complexes by Mass Selective High Resolution Resonance Enhanced Two Photon Ionization Laser Spectroscopy (2007).

[29] D. R. Miller, *Free Jet Sources in Atomic and Molecular Beam Methods* (Oxford University Press, New York, 1988), Vol. 1, Chap. 2.

[30] M. Knerich, Diplomarbeit, Fachbereich für Chemie, Biologie und Geowissenschaften der Technischen Universität München (1990).

[31] T. Weber, Dissertation, Fachbereich für Chemie, Biologie und Geowissenschaften der Technischen Universität München (1991).

[32] W. C. Wiley and I. H. McLaren, Rev. Sci. Instr. **26**, 1150 (1955).

[33] R. Wallenstein and T. W. Hänsch, Opt. Comm. **14**, 353 (1975).

[34] R. Wallenstein and T. W. Hänsch, Phys. Rev. **A22**, 192 (1980).

[35] M. M. Salour, Opt. Commun. **22**, 202 (1977).

[36] E. Riedle, R. Moder, and H. J. Neusser, Opt. Commun. **43**, 388 (1982).

[37] A. E. Siegman, *Lasers*, 1 ed. (University Science Books, Mill Valley, CA, 1986).

[38] R. Neuhauser, Diplomarbeit. Fachbereich für Chemie, Biologie und Geowissenschaften der Technischen Universität München (1993).

[39] U. Schubert, Dissertation, Institut für Chemie, Biologie und Geowissenschaften der Technischen Universität München (1988).

[40] F. Träger, *Handbook of Lasers and Optics* (Springer, New York, 2007), Chap. 12.1, pp. 938–945.

[41] R. Wehrens and L. M. C. Buydens, Trends Analyt. Chem. **17**, 193 (1998).

[42] J. A. Hageman, R. Wehrens, R. deGelder, W. L. Meerts, and L. M. C. Buydens, J. Chem. Phys. **113**, 7955 (2000).

[43] A. E. Nikolaev, G. Miszkiewicz, G. Berden, W. Leo Meetrs, J. F. Pfanstiel, and D. W. Pratt, J. Chem. Phys. **122**, 084309 (2005).

[44] S. Chervenkov, P. Q. Wang, J. E. Braun, S. Georgiev, C. K. Nandi, T. Chakraborty, and H. J. Neusser, J. Chem. Phys. **122**, 244312 (2005).

[45] M. Schmitt, D. Krüger, M. Böhm, C. Ratzer, V. Bednarska, I. Kalkman, and W. L. Meerts, Phys. Chem. Chem. Phys. **8**, 228 (2006).

[46] S. Chervenkov, R. Karaminkov, J. E. Braun, H. J. Neusser, S. S. Panja, and T. Chakraborty, J. Chem. Phys. **124**, 234302 (2006).

[47] R. G. Neuhauser, K. Siglow, and H. J. Neusser, J. Chem. Phys. **106**, 896 (1997).

[48] T. L. Grebner and H. J. Neusser, Chem. Phys. Lett. **245**, 578 (1995).

[49] W. A. Chupka, J. Chem. Phys. **98**, 4520 (1993).

[50] W. A. Chupka, J. Chem. Phys. **99**, 5800 (1993).

[51] L. Zhu and P. M. Johnson, J. Chem. Phys. **94**, 5769 (1991).

[52] H. Krause and H. J. Neusser, J. Chem. Phys. **97**, 5923 (1992).

[53] J. E. Braun and H. J. Neusser, Mass Spectrom. Rev. **21**, 16 (2002).

[54] K. Müller-Dethlefs, M. Sander, and E. W. Schlag, Chem. Phys. Lett. **112**, 291 (1984).

[55] B. Ernstberger, H. Krause, A. Kiermeier, and H. J. Neusser, J. Chem. Phys. **92**, 5285 (1990).

[56] J. E. Braun, Dissertation, Selektive Ionisation von Wasserstoffbrücken-gebundenen Clustern und Molekülen: Bindungsenergien und Ladungstransfer (2007).

[57] M. F. Zigmond, *Fundamental Neuroscience* (Academic Press, London, 1998).

[58] S. H. Snyder, *Drugs and the Brain* (Scientific American Library, New York, 1999).

[59] P. D. Godfrey, R. D. Brown, and L. D. Hatherley, J. Am. Chem. Soc. **117**, 8204 (1995).

[60] S. Sun and E. R. Bernstein, J. Am. Chem. Soc. **118**, 5086 (1996).

[61] J. A. Dickinson, M. R. Hockridge, R. T. Kroemer, E. G. Robertson, J. P. Simons, J. Mc-Combie, and M. Walker, J. Am. Chem. Soc. **120**, 2622 (1998).

[62] S. J. Martinez III, J. C. Alfano, and D. H. Levy, J. Mol. Spectrosc. **158**, 82 (1998).

[63] N. Guchhait, T. Ebata, and N. Mikami, J.Am.Chem.Soc. **121**, 5705 (1999).

[64] M. Hockridge and E. G. Robertson, J. Phys. Chem. A **103**, 3618 (1999).

[65] Y. Lee, J. Jung, B. Kim, P. Butz, L. C. Snoek, R. T. Kroemer, and J. P. Simons, J. Phys.Chem. A **108**, 69 (2004).

[66] P. Butz, N. A. Macleod, L. C. Snoek, F. O. Talbot, and J. P. Simons, Central Laser Facility Annual Report **2000/2001**, 97 (2002).

[67] P. Butz, R. T. Kroemer, N. A. Macleod, and J. P. Simons, J.Phys.Chem. A **105**, 544 (2001).

[68] R. Karaminkov, S. Chervenkov, P. Härter, and H. J. Neusser, Chem. Phys. Lett. **442**, 238 (2007).

[69] P. Butz, R. T. Kroemer, N. A. Macleod, E. G. Robertson, and J. P. Simons, J.Phys.Chem. A **105**, 1050 (2001).

[70] P. D. Godfrey, R. N. Jorissen, and R. D. Brown, J. Phys. Chem. A **103**, 7621 (1999).

[71] R. Weinkauf, F. Lehrer, E. W. Schlag, and A. Metsala, Faraday Discuss. **115**, 363 (2000).

[72] R. D. Brown and P. D. Godfrey, J. Phys. Chem. A **104**, 5742 (2000).

[73] S. S. Panja and T. Chakraborty, J. Phys. Chem. A **107**, 10984 (2003).

[74] D. R. Borst, P. W. Joireman, D. W. Pratt, E. G. Robertson, and J. P. Simons, J. Chem. Phys. **116**, 7057 (2002).

[75] G. M. Florio and T. S. Zwier, J. Phys. Chem. A **107**, 974 (2003).

[76] M. Schmitt, M. Böhm, C. Ratzer, C. Vu, I. Kalkman, and W. L. Meerts, J. Am. Chem. Soc. **127**, 10356 (2005).

[77] T. V. Nguyen, J. T. Yi, and D. W. Pratt, Phys. Chem. Chem. Phys. **8**, 1049 (2006).

[78] L. Alvarez-Valtierra and D. W. Pratt, J. Chem. Phys. **126**, 224308 (2007).

[79] R. Sussmann, R. Neuhauser, and H. J. Neusser, Can. J. Phys. **72**, 1179 (1994).

[80] S. Chervenkov, P. Q. Wang, R. Karaminkov, T. Chakraborty, J. E. Braun, and H. J. Neusser, Proc. SPIE **5830**, 246 (2005).

[81] S. Chervenkov, P. Wang, J. E. Braun, T. Chakraborty, and H. J. Neusser, Phys. Chem. Chem. Phys. **9**, 837 (2007).

[82] M. J. Frisch, G. W. Trucks, H. B. Schlegel, G. E. Scuseria, M. A. Robb, J. R. Cheeseman, J. Montgomery, J. A., T. Vreven, K. N. Kudin, J. C. Burant, J. M. Millam, S. S. Iyengar, J. Tomasi, V. Barone, B. Mennucci, M. Cossi, G. Scalmani, N. Rega, G. A. Petersson, H. Nakatsuji, M. Haga, M. Ehara, K. Toyota, R. Fukuda, J. Hasegawa, M. Ishida, T. Nakajima, Y. Honda, O. Kitao, H. Nakai, M. Klene, X. Li, J. E. Knox, H. P. Hratchian, J. B. Cross, C. Adamo, J. Jaramillo, R. Comperts, R. E. Stratmann, O. Yazyev, A. J. Austin, R. Cammi, C. Pomelli, J. W. Ochterski, P. Y. Ayala, K. Morokuma, J. A. Voth, P. Salvador, J. J. Dannenberg, V. G. Zakrzewski, S. Dapprich, A. D. Daniels, M. C. Strain, O. Farkas, D. K. Malick, A. D. Rabuck, K. Raghavachari, J. B. Foresman, J. V. Ortiz, Q. Cui, A. G. Baboul, S. Clifford, J. Cioslowski, B. B. Stefanov, G. Liu, A. Liashenko, P. Piskorz, I. Kamaromi, R. L. Martin, D. J. Fox, T. Keith, M. A. Al-Laham, C. Y. Peng, A. Nanayakkara, M. Challacombe, P. M. W. Gill, B. Johnson, W. Chen, M. W. Wong, C. Gonzales, and J. A. Pople, Gaussian 03, Revision B.04, 2003.

[83] J. C. Pearson, K. V. L. N. Sastry, E. Herbst, and F. C. De Lucia, Astrophys. J. **480**, 420 (1997).

[84] M. R. Hockridge, S. M. Knight, E. G. Robertson, J. P. Simons, J. McCombie, and M. Walker, Phys. Chem. Chem. Phys. **1**, 407 (1999).

[85] T. S. Zwier, J. Phys. Chem. A **110**, 4133 (2006).

[86] H. S. Im, E. R. Bernstein, H. V. Secor, and J. I. Seeman, J. Am. Chem. Soc. **113**, 4422 (1991).

[87] D. W. Pratt, Annu. Rev. Phys. Chem. **49**, 481 (1998).

[88] D. W. Pratt, Science **296**, 2347 (2002).

[89] K. Müller-Dethlefs and P. Hobza, Chem. Rev. **100**, 143 (2000).

[90] R. Karaminkov, S. Chervenkov, and H. J. Neusser, J. Phys. Chem. A **112**, 839 (2008).

[91] S. S. Panja, P. Biswas, and T. Chakraborty, Chem. Phys. Lett. **411**, 128 (2005).

[92] W. Dietz, H. J. Neusser, U. Boesl, E. W. Schlag, and S. H. Lin, Chem. Phys. **66**, 105 (1982).

[93] P. Sinha, S. E. Boesch, C. Gu, R. A. Wheeler, and A. K. Wilson, J. Phys. Chem. A **108**, 9213 (2004).

[94] J. P. Merrick, D. Moran, and L. Radom, J. Phys. Chem. A **111**, 11683 (2007).

[95] R. Karaminkov, S. Chervenkov, and H. J. Neusser, work in preparation .

[96] C. M. Western, PGOPHER, A Program for Simulating Rotational Structure, 2007.

[97] G. Herzberg, *Molecular spectra and molecular structure, III. Electronic spectra and electronic structure of polyatomic molecules* (Krieger Publishing Company, Malabar, 1991), Vol. III.

[98] L. C. Snoek, E. G. Robertson, R. T. Kroemer, and J. P. Simons, Chem. Phys. Lett. **321**, 49 (2000).

[99] X. Tong, M. S. Ford, C. E. H. Dessent, and K. Müller-Dethlefs, J. Chem. Phys. **119**, 12908 (2003).

[100] J. Yao, H. S. Im, M. Foltin, and E. R. Bernstein, J. Phys. Chem. A **104**, 6197 (2000).

[101] C. E. H. Dessent, W. D. Geppert, S. Ullrich, and K. Müller-Dethlefs, Chem. Phys. Lett. **319**, 375 (2000).

[102] J. E. Braun, T. Mehnert, and H. J. Neusser, Int. J. Mass. Spectrom. **203**, 1 (2000).

[103] S. Georgiev, T. Chakraborty, and H. J. Neusser, J. Phys. Chem. A **108**, 3304 (2004).

[104] R. Karaminkov, S. Chervenkov, and H. J. Neusser, Phys. Chem. Chem. Phys. **10**, 2852 (2008).

[105] M. J. Frisch, G. W. Trucks, H. B. Schlegel, G. E. Scuseria, M. A. Robb, J. R. Cheeseman, J. Montgomery, J. A., T. Vreven, K. N. Kudin, J. C. Burant, J. M. Millam, S. S. Iyengar, J. Tomasi, V. Barone, B. Mennucci, M. Cossi, G. Scalmani, N. Rega, G. A. Petersson, H. Nakatsuji, M. Haga, M. Ehara, K. Toyota, R. Fukuda, J. Hasegawa, M. Ishida, T. Nakajima, Y. Honda, O. Kitao, H. Nakai, M. Klene, X. Li, J. E. Knox, H. P. Hratchian, J. B. Cross, C. Adamo, J. Jaramillo, R. Comperts, R. E. Stratmann, O. Yazyev, A. J. Austin, R. Cammi, C. Pomelli, J. W. Ochterski, P. Y. Ayala, K. Morokuma, J. A. Voth, P.

Salvador, J. J. Dannenberg, V. G. Zakrzewski, S. Dapprich, A. D. Daniels, M. C. Strain, O. Farkas, D. K. Malick, A. D. Rabuck, K. Raghavachari, J. B. Foresman, J. V. Ortiz, Q. Cui, A. G. Baboul, S. Clifford, J. Cioslowski, B. B. Stefanov, G. Liu, A. Liashenko, P. Piskorz, I. Kamaromi, R. L. Martin, D. J. Fox, T. Keith, M. A. Al-Laham, C. Y. Peng, A. Nanayakkara, M. Challacombe, P. M. W. Gill, B. Johnson, W. Chen, M. W. Wong, C. Gonzales, and J. A. Pople, Gaussian 03, Revision E.01, 2003.

[106] Y. Zhao, N. E. Schultz, and D. G. Truhlar, J. Chem. Phys. **123**, 161103 (2005).

[107] M. D. Patey and C. E. H. Dessent, J. Phys. Chem. A **106**, 4623 (2002).

[108] G. M. Florio, R. A. Christie, K. D. Jordan, and T. S. Zwier, J. Am. Chem. Soc. **124**, 10236 (2002).

[109] E. Nir, C. Janzen, P. Imhof, K. Kleinermanns, and M. S. de Vries, J. Chem. Phys. **115**, 4604 (2001).

[110] E. Nir, M. Müller, L. I. Grace, and M. S. de Vries, Chem.Phys. Lett. **355**, 59 (2002).

[111] J. C. Lopez, V. Cortijo, S. Blanco, and J. L. Alonso, Phys. Chem. Chem. Phys. **9**, 4521 (2007).

[112] W. L. Meerts, M. Schmitt, and G. C. Groenenboom, Can. J. Chem. **82**, 804 (2004).

[113] W. L. Meerts and M. Schmitt, Int. Rev. Phys. Chem. **25**, 353 (2006).

[114] R. Karaminkov, S. Chervenkov, H. J. Neusser, V. Ramanathan, and T. Chakraborty, The Journal of Chemical Physics **130**, 034301 (2009).

[115] TURBOMOLE, (V. 5-9-1).

[116] O. Christiansen, H. Koch, and P. Jørgensen, Chem. Phys. Lett. **243**, 409 (1995).

[117] C. Hättig and F. Weigend, J. Chem. Phys. **113**, 5154 (2000).

[118] M. Becucci, G. Pietraperzia, M. Pasquini, G. Piani, A. Zoppi, R. Chelli, and E. Castellucci, J. Chem. Phys. **120**, 5601 (2004).

[119] P. Butz, R. T. Kroemer, N. A. Macleod, and J. P. Simons, Phys. Chem. Chem. Phys. **4**, 3566 (2002).

[120] G. H. Ragab, H. Nohta, and K. Zaitsu, Analytica Chimica Acta **403**, 155 (2000).

[121] M.-H. E. Spyridaki, C. J. Tsitsimpikou, P. A. Siskos, and C. G. Georgakopoulos, Journal of Chromothography B **758**, 311 (2001).

[122] G. A. Jeffrey and W. Saenger, *Hydrogen Bonding in Biological Structures* (Springer, Berlin, 1991).

[123] T. L. Barry and G. Petzinger, Biological Mass Spectrometry **4**, 129 (1977).

[124] Y. Marde and R. Ryhage, Clinical Chemistry **24**, 1720 (1978).

[125] F. Brazzarola, M. Tubaro, P. Bravo, M. Zanda, A. Volonterio, and P. Traldi, II Farmaco **58**, 69 (2003).

[126] U. Boesl, H. J. Neusser, and E. W. Schlag, J. Chem. Phys. **72**, 4327 (1980).

[127] H. Kühlewind, A. Kiermeier, and H. J. Neusser, J. Chem. Phys. **85**, 4427 (1986).

[128] C. S. Parmenter, in *Advances in Chemical Physiscs*, 1st ed., edited by I. Prigogine and S. A. Rice (Wiley-Interscience, New York, 1978), Vol. 22.

[129] R. H. Page, Y. R. Shen, and Y. T. Lee, J. Chem. Phys. **88**, 4621 (1988).

[130] D. R. Borst, P. W. Joireman, D. W. Pratt, E. G. Robertson, and J. P. Simons, J.Chem.Phys. **116**, 7057 (2002).

[131] A. Boatwright, N. A. Besley, S. Curtis, R. R. Wright, and A. J. Stace, J. Chem. Phys. **123**, 021102 (2005).

[132] B. C. Dian, A. Longarte, S. Mercier, D. A. Evans, D. J. Wales, and T. S. Zwier, J.Chem.Phys. **117**, 10688 (2002).

[133] G. C. Maitland, M. Rigby, E. B. Smith, and W. A. Wakeham, *Intermolecular forces*, *The International Series of Monographs on Chemistry*, 2nd ed. (Clarendon Press, Oxford, 1987).

[134] F. London, Z. Phys. **63**, 245 (1930).

[135] W. Heitler and F. London, Z. Physik **44**, 455 (1927).

[136] P. M. Morse, Phys. Rev. **34**, 57 (1929).

[137] J. E. Lennard-Jones, Proc. Phys. Soc. **43**, 461 (1931).

[138] R. M. Helm, *Hochaufgelösende UV-Laserspektroskopie: Struktur und Dynamik nach elektronischer Anregung von wasserstoffbrückengebundenen Aromat-Wasser Komplexen* (Herbert Utz Verlag, München, 1998).

[139] M. J. S. Dewar, Nature(London) **156**, 784 (1945).

[140] E. Carrasquillo, T. S. Zwier, and D. H. Levy, J. Chem. Phys. **83**, 4990 (1985).

[141] M. Nishio, M. Hirota, and Y. Umezawa, *The CH/Ï Interaction: Evidence, Nature and Consequences* (Wiley-VCH, New York, 1998).

[142] S. Djafari, H.-D. Barth, K. Buchhold, and B. Brutschy, J. Chem. Phys. **107**, 10573 (1997).

[143] A. Fujii, S. Morita, M. Miyazaki, T. Ebata, and N. Mikami, J. Phys. Chem. A **108**, 2652 (2004).

[144] L. P. Hammett, *Physical Organic Chemistry* (McGraw Hill, New York, 1940), p. 294.

[145] L. J. Andrews, Chem. Rev. **54**, 713 (1954).

[146] M. C. Etter, Acc. Chem. Res. **23**, 120 (1990).

[147] M. C. Etter, J. C. McDonald, and J. Bernstein, Acta Cryst. **B46**, 256 (1990).

[148] M. C. Etter and S. M. Reutzel, J. Am. Chem. Soc. **113**, 2586 (1991).

[149] L. R. Hanton, C. A. Hunter, and D. H. Purvis, J. Chem. Soc. Chem. Commun. 1134 (1992).

[150] N. Sheppard., I. D. Hadzi, and E. H.W. Thompson, *Hydrogen Bonding* (Pergamon Press, London, 1959), p. 85105.

[151] E. Reed, Alan, A. Curtiss, Larry, and F. Weinhold, Chem. Rev. **88**, 899 (1988).

[152] P. Hobza and Z. Havlas, Chem. Rev. **100**, 4253 (2000).

[153] P. Hobza, V. Spirko, H. L. Selzle, and E. W. Schlag, J. Phys. Chem. A **102**, 2501 (1998).

[154] P. Hobza, V. Spirko, Z. Havlas, K. Buchhold, B. Reimann, H.-D. Barth, and B. Brutschy, Chem. Phys. Lett. **299**, 180 (1999).

[155] G. N. Patwari, T. Ebata, and N. Mikami, J.Phys.Chem. **105**, 8642 (2001).

[156] C. Lee Jr., Jesse, P. Eduardo, L. Rheingold, Arnold, and H. Crabtree, Robert, J. Am. Chem. Soc. **116**, 11014 (1994).

[157] Q. Liu and R. Hoffmann, J. Am. Chem. Soc. **117**, 10108 (1995).

[158] W. Kauzmann, Adv. Prot. Chem. **14**, 1 (1959).

[159] D. Chandler, Nature **437**, 640 (2005).

[160] P. Hobza and R. Zahradnik, Chem. Rev. **88**, 871 (1988).

[161] J. L. Calais and E. S. Kryachko, *Conceptual perspectives in quantum chemistry*, 1st ed. (Springer Netherland, Amsterdam, 1997).

[162] A. R. Leach, *Molecular modelling principles and applications* (Addison Wesley, Sussex, 1996).

[163] I. N. Levine, *Quantum Chemistry*, 2nd indian reprint ed. (Pearson Education, Singapore, 2004).

[164] C. Møller and M. S. Plesset, Phys. Rev. **40**, 618 (1934).

[165] R. J. Bartlett, Ann. Rev. Phys. Chem. **32**, 359 (1981).

[166] P. Hohenberg and W. Kohn, Phys. Rev. **136**, 864 (1964).

[167] W. Kohn and L. J. Sham, Chem. Rev. **140**, 1133 (1965).

[168] C. Lee, W. Yang, and R. G. Parr, Phys. Rev. B **37**, 785 (1988).

[169] Y. Zhao, N. E. Schultz, and D. G. Truhlar, J. Chem. Theory Comput. **2**, 364 (2006).

[170] Y. Zhao and D. G. Truhlar, J. Phys. Chem. A **109**, 5656 (2005).

[171] S. F. Boys and F. Bernardi, Mol.Phys. **19**, 553 (1970).

[172] P. S. Sedano, Dissertation, Implementation and Application of Basis Set Superposition Error-correction Schemes to the Theoretical Modeling Weak Intermolecular Interactions (2001).

[173] E. B. Wilson Jr, J. C. Decius, and P. C. Cross, *Molecular Vibrations*, 1955 ed. (Dover Publications, New York, 1955).

[174] H. J. Werner, P. J. Knowles, R. Lindh, F. R. Manby, and M. Schütz, MOLPRO, version 2006.1, a package of ab initio programs.

[175] R. Ahlrichs, M. Bär, M. Häser, H. Horn, and C. Kölmel, Chem. Phys. Lett. **162**, 165 (1989).

[176] I. N. Levine, *Molecular Spectroscopy*, 1st ed. (Wiley-Interscience, New York, 1975).

[177] S. H. Lin, Y. Fujimura, H. J. Neusser, and E. W. Schlag, (1984).

[178] E. Fermi, *Nuclear Physics* (Chicago University Press, Chicago, 1950).

[179] M. Born and R. Oppenheimer, Ann. Physik **84**, 457 (1927).

[180] E. Teller, Hand- u. Jahrb. Chem. Phys. **9**, 43 (1934).

[181] G. Herzberg and E. Teller, Z. Phys. Chem. **B21**, 410 (1933).

[182] L. D. Landau and E. M. Lifschitz, *Lehrbuch der theoretischen Physik I, Mechanik* (Akademie-Verlag, Leipzig, 1982).

[183] W. Gordy and R. L. Cook, *Microwave molecular spectra*, Vol. XVIII of *Techniques of Chemistry*, 1st ed. (John Wiley Sons, New York, 1984).

[184] J. E. Wollrab, *Rotational Spectra and Molecular Structure*, Vol. 13 of *A series of Monographs on Physical Chemistry*, 1st ed. (Academic Press, New York, 1967).

[185] N. Zare, Richard, *Angular Momentum. Understanding Spatial Aspects in Chemistry and Physics*, 1st ed. (Wiley Interscience, New York, 1988).

[186] H. J. Neusser, Fachbereich für Chemie, Biologie und Geowissenschaften der Technischen Universität München (1977).

[187] H. A. Jahn and E. Teller, Proc. R. Soc. London A **A161**, 220 (1937).

[188] J. Kraitchman, Am. J. Phys. **21**, 17 (1953).

[189] C. C. Costain, J. Chem. Phys. **29**, 864 (1958).

[190] T. M. Korter, J. Küpper, and D. W. Pratt, J. Chem. Phys. **111**, 3946 (1999).

[191] K. Siglow and H. J. Neusser, Chem. Phys. Lett. **343**, 475 (2001).

List of Figures

217

List of Tables

List of Publications

S. Chervenkov, P. Q. Wang, R. Karaminkov, T. Chakraborty, J. E. Braun, and H. J. Neusser, *High Resolution UV Resonance Two Photon Ionization Spectroscopy with Mass Selection of Biologically Relevant Molecules in the Gas Phase* in *13th International School on Quantum Electronics: Laser Physics and Applications, P. A. Atanasov, S. V. Gateva, L. A. Avramov, A. A. Serafetinides, eds.*,
Proc. SPIE **5830**, 246 (2005).

S. Chervenkov, R. Karaminkov, J. E. Braun, H. J. Neusser, S. S. Panja, and T. Chakraborty, *Specific and Nonspecific Interactions in a Molecule with Flexible Side Chain: 2-phenylethanol and its 1:1 Complex with Argon studied by High Resolution UV Spectroscopy*,
J. Chem. Phys. **124**, 234302 (2006).

R. Karaminkov, S. Chervenkov, P. Härter, and H. J. Neusser, *Resonance-Enhanced Two-Photon Ionization Mass Spectrometry of Ephedrine: Indication of State-Selective Fragmentation in a Flexible Molecule*,
Chem. Phys. Lett. **442**, 238 (2007).

R. Karaminkov, S. Chervenkov, and H. J. Neusser, *Identification of Conformational Structures of 2-Phenylethanol and Its Singly Hydrated Complex by Mass Selective High-Resolution Spectroscopy and ab Initio Calculations*,
J. Phys. Chem. A **112**, 839 (2008).

R. Karaminkov, S. Chervenkov, and H. J. Neusser, *Fluorine Substitution and Nonconventional OH· · ·π intramolecular bond: High-Resolution UV Spectroscopy and ab Initio Calculations of 2-(ρ-fluorophenyl)ethanol*,
Phys. Chem. Chem. Phys. **10**, 2852 (2008).

R. Karaminkov, S. Chervenkov, H. J. Neusser, V. Ramanathan, and T. Chakraborty, *Competition between π and σ Hydrogen Bonds and Conformational Probing of 2-orthofluorophenylethanol by Low-and High-Resolution electronic Spectroscopy*,
J. Chem. Phys. **130**, 034301 (2009).

R. Karaminkov, S. Chervenkov, and H. J. Neusser, *Mass Analysed Threshold Ionisation Spectroscopy of Flexible 2-para-fluorophenylethanol Conformers with and without an Intramolecular OH· · ·π Bond*,
Phys. Chem. Chem. Phys. **11**, 2249 (2009).

S. Georgiev, R. Karaminkov, S. Chervenkov, V. Delchev, and H. J. Neusser, *Mass-Analyzed Threshold Ionization Spectroscopy of 2-Phenylethanol: Probing of Conformational Changes*

Caused by Ionization,
J. Phys. Chem. A **113**, 12328 (2009).

Poster and Oral Presentations

19th Colloquium on High Resolution Molecular Spectroscopy
Salamanca, Spain, 11. 09.-16. 09. 2005
Poster
CONFORMATION ANALYSIS OF BIOLOGICAL MOLECULES IN THE GAS PHASE BY MASS SELECTIVE REMPI HIGH-RESOLUTION UV SPECTROSCOPY

19th International Conference on High Resolution Molecular Spectroscopy
Prague, The Czech Republic, 29. 08.-02. 09. 2006
Poster
FRAGMENTATION BEHAVIOR AND CONFORMATIONS OF SMALL BIOLOGICAL MOLECULES STUDIED BY MASS SELECTIVE HIGH-RESOLUTION TWO-PHOTON UV LASER SPEC-TROSCOPY

Discussion Meeting, Spectroscopy and Dynamics of Molecules and Clusters
Corbett River View Retreat, Uttarkhand, India, 23. 02.-25. 02. 2007
Poster
STATE-SELECTIVE FRAGMENTATION OF EPHEDRINE AND CONFORMATIONAL STUD-IES OF SMALL BIOLOGICAL MOLECULES AND THEIR HYDRATED CLUSTERS BY MASS SELECTIVE HIGH-RESOLUTION UV SPECTROSCOPY

Technische Universität München, Physikalische Chemie I, Kaffeeseminar
München, Germany, 10. 05. 2007
Oral Presentation
STATE SELECTED FRAGMENTATION AFTER R2PI: HOW DOES IT OCCUR?

20th Colloquium on High Resolution Molecular Spectroscopy
Dijon, France, 03. 09.-07. 09. 2007
Poster
INFLUENCE OF THE π-ELECTRON DENSITY IN 2-(ρ-FLUOROPHENYL)ETHANOL AND 2-PHENYLETHANOL ON THE CONFORMATIONAL PREFERENCES STUDIED BY MASS SELECTIVE HIGH-RESOLUTION UV SPECTROSCOPY

Gordon Research Conference, Molecular and Ionic Clusters
Centre Paul Langevin, Aussois, France, 7. 09.-12. 09. 2008
Poster
MATI SPECTROSCOPY OF A FLEXIBLE SYSTEM: GAUCHE vs. ANTI CONFORMATION OF 2-(ρ-FLUOROPHENYL)ETHANOL AND HIGH RESOLUTION UV STUDY OF ITS WATER DIMER

Discussion Meeting, Spectroscopy and Dynamics of Molecules and Clusters
Mandarmoni, West Bengal, India, 20. 02.-22. 02. 2009
Poster and Oral Presentation
MASS ANALYSED THRESHOLD IONISATION SPECTROSCOPY OF FLEXIBLE 2-PHENYLETHANOL AND ITS ortho- AND para- FLUORO-DERIVATIVES: THE EFFECT OF CONFORMATION

HIGH-RESOLUTION UV AND MASS ANALYZED THRESHOLD IONIZATION SPECTROSCOPY OF FLEXIBLE MOLECULES

Technische Universität München, Lehrstuhl f̌r Experimentalphysik E11, Institutsseminar
München, Germany, 12. 11. 2009
Oral Presentation
CONFORMATIONS AND FRAGMENTATION OF BIOLOGICALLY RELEVANT MOLECULES AND THEIR BINARY COMPLEXES WITH WATER PROBED BY HIGH RESOLUTION UV AND MASS ANALYZED THRESHOLD IONIZATION SPECTROSCOPY

Acknowledgements